Title
The Role of Quasars in the Formation of Massive Galaxies

Author
Vayner, Andrey

Publication Date
2019

Peer reviewed|Thesis/dissertation

UNIVERSITY OF CALIFORNIA SAN DIEGO

The Role of Quasars in the Formation of Massive Galaxies

A dissertation submitted in partial satisfaction of the
requirements for the degree
Doctor of Philosophy

in

Physics

by

Andrey Vayner

Committee in charge:

Professor Shelley A. Wright, Chair
Professor Farhat Beg
Professor Alison Coil
Professor Dusan Kereš
Professor Karin Sandstrom

2019

The dissertation of Andrey Vayner is approved, and it is acceptable in quality and form for publication on microfilm and electronically:

_____

_____

_____

_____

_____
Chair

University of California San Diego

2019

DEDICATION

To my family.

EPIGRAPH

I have loved the stars too truly to be fearful of the night.

—Sarah William, The Old Astronomer

TABLE OF CONTENTS

Signature Page . . . iii

Dedication . . . iv

Epigraph . . . v

Table of Contents . . . vi

List of Figures . . . x

List of Tables . . . xiv

Acknowledgements . . . xv

Vita . . . xviii

Abstract of the Dissertation . . . xix

Chapter 1 Introduction . . . 1
- 1.0.1 A brief history of AGN and quasars. . . . 6
- 1.0.2 Source of power within quasars and the unification model . . . 9
- 1.0.3 Evidence for SMBH in nearby galaxies. . . . 14
- 1.0.4 SMBH and galaxy correlations; start to the field of AGN feedback . . . 17
- 1.0.5 Discovery of small scale quasar/AGN outflows . . . 20
- 1.0.6 Galaxy scale outflows in the local Universe. Implication of feedback in nearby systems . . . 21
- 1.0.7 Galaxy scale outflows in the distant Universe. Implication of feedback at early time. . . . 22
- 1.0.8 Inter stellar medium conditions and gas photoionization in quasar host galaxies: . . . 26
- 1.0.9 Thesis outline . . . 30

Chapter 2 Providing stringent star formation rate limits of z$\sim$2 QSO host galaxies at high angular resolution . . . 34
- 2.1 abstract . . . 34
- 2.2 Observations . . . 36
  - 2.2.1 Target Selection . . . 38
  - 2.2.2 Archival Data . . . 38
- 2.3 Data Reduction . . . 42
  - 2.3.1 OSIRIS . . . 42
  - 2.3.2 NIFS . . . 43

2.4 Extraction of BH masses and PSF subtraction of the QSO 44
2.4.1 PSF construction and subtraction 44
2.5 Results 48
2.5.1 OSIRIS: SDSSJ1029+6510 50
2.5.2 NIFS: SDSSJ0925+0655 52
2.5.3 Null detections: SDSSJ1005+4346, SDSSJ2123-0050 & SDSSJ0850+5843 56
2.5.4 Unresolved QSO narrow line region emission 60
2.6 Discussion 61
2.6.1 SDSSJ1029+6510 61
2.6.2 SDSSJ0925+0655 64
2.6.3 Comparison to other type-1 QSOs at $z \gtrsim 1$ 66
2.7 Conclusions 70
2.8 Acknowledgements 72

Chapter 3 Galactic-Scale Feedback Observed in the 3C 298 Quasar Host Galaxy . . 73
3.1 Abstract 73
3.2 Introduction 74
3.3 Observations 77
3.3.1 Keck: OSIRIS 77
3.3.2 ALMA: Band 4 and 6 78
3.4 Data reduction and Analysis 80
3.4.1 OSIRIS: Data reduction 80
3.4.2 OSIRIS: PSF construction and subtraction 81
3.4.3 OSIRIS: Kinematics 82
3.4.4 OSIRIS: Nebular Emission line Diagnostics 86
3.4.5 OSIRIS: Velocity field modeling 91
3.4.6 ALMA: Data reduction 94
3.4.7 ALMA: Analysis 95
3.4.8 HST WFC3: PSF Subtraction 102
3.4.9 HST WFC3: Stellar population 105
3.5 Dynamics and energetics of outflow regions 108
3.5.1 Outflow rates 109
3.5.2 Virial parameters & gas pressure 111
3.6 Discussion 115
3.7 Conclusion 123
3.8 Acknowledgements 126

Chapter 4 A Spatially-Resolved Survey of Distant Quasar Host Galaxies: Kinematics and Energetics of Ionization Gas 128
4.1 Abstract 128
4.2 Introduction 129
4.3 Sample Selection 138

4.4 Observations . . . 138
4.4.1 Keck OSIRIS . . . 139
4.4.2 Archival VLA observations . . . 142
4.4.3 ALMA . . . 142
4.4.4 Archival *HST* imaging . . . 143
4.5 Data Reduction & Analysis . . . 144
4.5.1 OSIRIS data reduction . . . 144
4.5.2 PSF subtraction . . . 146
4.5.3 Emission Line Fitting . . . 147
4.6 Quasar sample properties . . . 149
4.7 Spatially-Resolved Regions . . . 152
4.8 Nebular Emission Line Diagnostics and Sources of Gas Excitation . 156
4.8.1 Ionization Diagnostic Models . . . 157
4.9 Outflow rates & energetics . . . 163
4.9.1 The driving source of the outflows . . . 177
4.9.2 Condition for star formation as a potential driver of outflow: 181
4.9.3 Condition for AGN as potential driver of outflow: . . . 182
4.9.4 Outflow Comparisons . . . 185
4.9.5 Sample comparison . . . 186
4.9.6 Special Note: 3C318 Outflow . . . 191
4.10 SMBH-galaxy scaling relationships . . . 196
4.10.1 Host Galaxy Velocity Dispersion . . . 196
4.11 Dynamical mass measurements . . . 203
4.11.1 Some notes on disk fitting . . . 208
4.12 Discussion . . . 209
4.12.1 Star formation and quiescent regions in the host galaxies . . 211
4.12.2 Offset from local scaling relations . . . 211
4.12.3 Galactic scale outflow, what is the main source of gas depletion? . . . 215
4.12.4 What is the main driving source of the ionized outflows and how does that compare to other galaxies in the local and distant Universe. . . . 217
4.13 Conclusions . . . 225
4.14 Acknowledgements . . . 227
4.15 Appendix . . . 228
4.16 3C 9 . . . 228
4.17 4C 09.17 . . . 230
4.18 3C 268.4 . . . 233
4.19 7C 1354+2552 . . . 234
4.20 3C 298 . . . 237
4.21 3C 318 . . . 238
4.22 4C 57.29 . . . 241
4.23 4C 22.44 . . . 242

4.24 4C 05.84 244
4.25 3C 446 245
4.26 4C 04.81 246

Chapter 5 Conclusions and Future Directions 248
5.1 The Circumgalactic Medium of Quasar Host Galaxies at z∼2 249
5.2 The Molecular Gas in Quasar Host Galaxies 254
5.3 In The Era of Extremely Large Telescopes (ELTs) 258

Bibliography 263

LIST OF FIGURES

Figure 1.1: Percentage of baryonic mass locked up in stars within galaxies of different mass 4
Figure 1.2: Unified AGN model based on (Urry and Padovani, 1995), today this the most agreed upon model of an AGN 15
Figure 1.3: The classical BPT diagnostic diagram used to distinguish between gas photoionized by stars, AGN and shocks 29

Figure 2.1: SDSS spectra of all the sources in our sample (Left). The SDSS wavelength range covers rest frame UV emission lines of QSOs at this redshift 45
Figure 2.2: Radial profiles for SDSSJ1029+6510 (left) and SDSSJ0925+0655(right). Green and blue radial profile curves are constructed from spectrally integrated images which contain both broad and narrow Hα , while the red curve is constructed from the PSF image. 48
Figure 2.3: Upper left: K-Band image of SDSSJ1029+6510 from the collapsed OSIRIS LGS-AO data cube using $0.1''$ spatial sampling. Upper right: radial velocity map (km s^{-1}) of extended narrow Hα emission detected post-PSF subtraction. 52
Figure 2.4: Upper left: K-Band image of SDSSJ0925+0655 from the collapsed NIFS Altair AO cube using $0.05''$ spatial sampling. Upper right: PSF subtracted image showing resolved extended Hα narrow line emission in contours that stretch from 1.8σ-5σ 53
Figure 2.5: Line ratio diagnostics for our detected narrow-line emission using the standard BPT diagram. 55
Figure 2.6: Limiting integrated flux in a $0.2''\times0.2''$region that was recovered at various separations from the QSO in our Monte Carlo simulation from the OSIRIS observations of SDSSJ1029+6510 58
Figure 2.7: Limiting integrated flux in a $0.25''\times0.25''$region that was recovered at various separations from the QSO in our Monte Carlo simulations from the NIFS observations of SDSSJ0925+0655 (green). Integrated fluxes of features A, B, C (red) from Figure 2.4 are over-plotted. 60

Figure 3.1: OSIRIS observations of 3C 298 nebular emission line intensities and [OIII] kinematic maps. 84
Figure 3.2: OSIRIS near-infrared spectra for distinct photoionized regions in the host galaxy of 3C 298. 87
Figure 3.3: Photoionization diagnostics of ionized gas in the 3C 298 system. 89
Figure 3.4: Photoionzation diagnostics of ionized gas in the 3C 298 system. 90
Figure 3.5: Observed and modeled galactic rotation disc, detected in the nebular [OIII] line in the 3C 298 system. 93
Figure 3.6: ALMA band 4 and 6 CO (J=3-2) and (J=5-4) observations of 3C 298. . . . 96
Figure 3.7: (TOP LEFT) Velocity field modeling of the molecular disc. 97

Figure 3.8: Local SMBH vs galactic bulge dynamical mass relationship compared to 3C 298 measured values. 100
Figure 3.9: Spectra of molecular CO (3-2) and (5-4) emission in distinct regions of the host galaxy. 103
Figure 3.10: HST WFC3 Rest-frame near-UV (F606W) and approximately rest frame V band (F140W) images of the stellar light in the host galaxy of 3C 298. . . . 106
Figure 3.11: Cartoon illustration of the merger in the 3C 298 system that includes the results from OSIRIS, ALMA, HST, and VLA. 122

Figure 4.1: OSIRIS - LGS observations of 11 quasar host galaxies in our QUART sample. 150
Figure 4.2: Line ratio diagnostics of individual resolved distinct regions. 158
Figure 4.3: We present line ratio diagnostics for spaxels in each source where at least [OIII] and Hα were detected at SNR great than 3. 159
Figure 4.4: Detection of dynamically quiescent regions in archival *Hubble Space Telescope* observation. 164
Figure 4.5: Spectra of distinct regions along with fits to individual emission lines for the 3C 9 system. 165
Figure 4.6: Spectra of distinct regions along with fits to individual emission lines for the 4C09.17 system. 166
Figure 4.7: Spectra of distinct regions along with fits to individual emission lines for the 3C268.4 system. 167
Figure 4.8: Spectra of distinct regions along with fits to individual emission lines for the 7C 1354+2552 system. 167
Figure 4.9: Spectra of distinct regions along with fits to individual emission lines for the 3C 298 system. 168
Figure 4.10: Spectra of distinct regions along with fits to individual emission lines for the 3C 446 system. 168
Figure 4.11: Spectra of distinct regions along with fits to individual emission lines for the 3C 318 system. 169
Figure 4.12: Spectra of distinct regions along with fits to individual emission lines for the 4C 57.29 system. 169
Figure 4.13: Spectra of distinct regions along with fits to individual emission lines for the 4C 22.44 system. 169
Figure 4.14: Spectra of distinct regions along with fits to individual emission lines for the 4C 05.84 system. 170
Figure 4.15: Spectra of distinct regions along with fits to individual emission lines for the 4C 04.81 system. 170
Figure 4.16: Measuring the electron density for the outflow region in the host galaxy of 3C 318. 176
Figure 4.17: Diagnostic diagram distinguishing between AGN or Star formation as the main driving mechanism of the galaxy outflows. 187
Figure 4.18: Diagnostic diagram distinguishing between different AGN components that may have driven the outflows. 188

Figure 4.19: The location of our galaxies on the velocity dispersion vs. SMBH mass plot compared to the local $M_\bullet - \sigma$ relationship. 199
Figure 4.20: We present the location of individual galaxies compared to the local scaling relation between the mass of the SMBH and mass of the galaxy/bulge shown with a blue curve. 200
Figure 4.21: Fitting an inclined disk model to the radial velocity map of the 3C9 quasar host galaxy. 207
Figure 4.22: Fitting an inclined disk model to the radial velocity map of the 7C1354 quasar host galaxy. 207
Figure 4.23: Fitting an inclined disk model to the radial velocity map of the 3C298 quasar host galaxy. 208
Figure 4.24: Measured offset of galaxies from the local $M_\bullet - \sigma$ scaling relationship . . 213
Figure 4.25: Outflow driving mechanism diagnostic diagram. We plot the $\frac{\dot{P}_{outflow}}{\dot{P}_{AGN}}$ratio vs. the radius of the outflow. 224
Figure 4.26: OSIRIS observations of 3C 9 nebular emission line distribution and kinematic maps. 230
Figure 4.27: OSIRIS observations of 4C09.17 nebular emission line distribution and kinematic maps. 232
Figure 4.28: OSIRIS observations of 3C268.4 nebular emission line distribution and kinematic maps. 234
Figure 4.29: OSIRIS observations of 7C1354+2552 nebular emission line distribution and kinematic maps. 236
Figure 4.30: OSIRIS observations of 3C298 nebular emission line distribution and kinematic maps. 238
Figure 4.31: OSIRIS observations of 3C318 nebular emission line distribution and kinematic maps. 240
Figure 4.32: OSIRIS observations of 4C57.29 nebular emission line distribution and kinematic maps. 242
Figure 4.33: OSIRIS observations of 4C2244 nebular emission line distribution and kinematic maps. 243
Figure 4.34: OSIRIS observations of 4C05.84 nebular emission line distribution and kinematic maps. 245
Figure 4.35: OSIRIS observations of 3C446 nebular emission line distribution and kinematic maps. 246
Figure 4.36: OSIRIS observations of 4C04.81 nebular emission line distribution and kinematic maps. 247

Figure 5.1: KCWI integrated $\mathrm{Ly}\alpha$ intensity maps of the six sources in our sample. . . . 251
Figure 5.2: Left: KCWI integrated $\mathrm{Ly}\alpha$ intensity map showcasing the distribution of cool gas in the CGM of the host galaxy of the quasar 3C9 (z=2.0). 253
Figure 5.3: Spectra of galaxy scale (4-21 kpc) molecular outflows detected with ALMA cycles 3 and 5 data, in the host galaxies of our quasar sample. 256

Figure 5.4: Example of our multiwavelength observations for 4C09.17 (left) and 4C05.84 (right). 257
Figure 5.5: Deriving electron densities from ratios of optical emission lines. 260

LIST OF TABLES

Table 2.1: Observational summary of Keck OSIRIS and Gemini ALTAIR-NIFS observations. 37
Table 2.2: SDSS & 2MASS photometry (Cutri et al. 2003) of the sources in our sample. 40
Table 2.3: WISE & Herschel photometry of the five sources in our sample. 41
Table 2.4: QSO General properties 46
Table 2.5: Properties of Broad-line Hα emission 46
Table 2.6: SDSSJ1029+6510: OSIRIS-AO Narrow Emission-line Properties 51
Table 2.7: SDSSJ0925+0655: NIFS-AO Narrow Emission-line Properties 54

Table 3.1: ALMA Cycle 2 and 3 observations summary 79
Table 3.2: Measured molecular line intensities 101
Table 3.3: 3C 298 Ionized Outflow Properties 112
Table 3.4: 3C 298 Properties & Results 125

Table 4.1: OSIRIS-LGS Observational Summary 141
Table 4.2: Archival VLA imaging 142
Table 4.3: Archival HST imaging 144
Table 4.4: QUART Sample properties 152
Table 4.5: Fluxes of distinct regions in individual sources 155
Table 4.6: Star formation rates and metallicities of distinct star forming regions 163
Table 4.7: Extended outflow regions properties 194
Table 4.8: Nuclear outflow regions properties 195
Table 4.9: Momentum and flux deposition from wind driving mechanisms 197
Table 4.10: Best fit values for each inclined disk model parameter 206

ACKNOWLEDGEMENTS

I want to give thanks to my advisor Shelley Wright for her guidance, and for teaching me what it means to be a scientist. Thank you for allowing me to explore my own scientific path. I am forever grateful for your support, thank you for all your life and work lessons, and for teaching me to play pool. Moving to San Diego has allowed me to start on my own, thank you for convincing me to come to California.

I wouldn't have an interest in science and astronomy if it weren't for excellent teachers in the early stages of my life. To my 9th-grade science teacher Samantha Juruc, thank you for an excellent astronomy unit that forever fortified an interested in the subject. To my 12th grade Physics and Calculus teacher Sandy Evans, thank you for believing that I could pursue a career in the physical sciences.

In the early days of graduate school I would like to thank my friends and colleagues in the Department of Astronomy & Astrophysics at the University of Toronto, especially; Charles Zhu, Robert Main, Stephen Ro, Lisa Esteves, Nick Tacik, Ari Silburt, Heidi White, Etsuko Mieda, Elliot Meyer, Suresh Sivanandam, and Paola Rodriguez-Hidalgo. A special thanks to Norm Murray, for all our discussions and for everything that you have taught me.

To the new friends I made in San Diego, thank you for the coffee breaks, chats, beer and burrito trips, hikes, bonfires, and BASH. Thanks to Greg Walth, Maren Cosens, Jeremy Chastenet, Nils Rundquist, Brooke Simmons, Arun Surya, Sibasish Laha, Jordan Runco, Caleb Choban, Cameron Trapp, Bethany Ludwig, Max Silva, and Sanchit Sabhlok.

To my friends in Toronto and throughout the world, thank you for being there. We might

not talk often, or see each other, but I treasure our friendships, thank you for being my friends. Thanks to Hans Nguyen, Ryan Cloutier, Jessica Campbell, George Stein, Jason Leung, Adiv Paradise, and Bryn Orth-Lashley.

To the wonderful staff and support astronomers and the W.M. Keck Observatory, thank you for making this thesis possible. Apologies for all the times I woke you up in the early mornings when the telescope would not cooperate. A special thanks to Jim Lyke, Randy Campbell, Luca Rizzi, and all the telescope operators. I wish to recognize and acknowledge the cultural role that the summit of Mauna Kea has always had within the Hawaiian community. I am fortunate, honored, and humbled to have had the opportunity to conduct observations from this sacred mountain.

To my mom, Elena, thank you for raising and shaping me into the person I am today. Thank you for always helping and supporting me in all my endeavors. To my father, Slava, thank you for your devoted love and support to my sister and me. To my grandma, Rimma, thank you for your life long support that you had provided your family, for moving countries to help raise my sister and me when we were younger. To my grandma, Liudmila, thank you for your assistance in my early childhood education. To my buddy and sister, Olga, thank you for always visiting and hanging out with me, thank you for sharing my interests and always listening and supporting me. To my extended family, thank you for everything.

Additionally, I would like to thank the following people; Lee Armus, Quinn Konopacky, James Graham, James Larkin, Tuan Do, Dusan Kereš, Alison Coil, and Karin Sandstrom.

Chapter 2, in part, is a reprint of the material as it appears in The Astrophysical Journal 2016. Vayner, A., Wright, S. A., Do, T., Larkin, J., Armus, L., Gallagher, S. C., 2016. The

dissertation author was the primary investigator and author of this paper.

Chapter 3, in full, is a reprint of the material as it appears in The Astrophysical Journal 2017. Vayner, A., Wright, S. A., Murray, N., Armus, L., Larkin, J. E., Mieda, E., 2017. The dissertation author was the primary investigator and author of this paper.

Chapter 4, in full, currently being prepared for submission for publication of the material in The Astrophysical Journal 2019. Vayner, A., Wright, S. A., Murray, N., Armus, L., Cosens, M., Walth, G., Boehle, A., Larkin, J. E., Mieda, 2019. The dissertation author was the primary investigator and author of this paper.

VITA

2009-2013	H.B.Sc. in Physics & Astronomy, University of Toronto, Ontario, Canada
2013-2015	M.Sc. Astronomy & Astrophysics, University of Toronto, Ontario, Canada
2019	Ph. D. in Physics, University of California San Diego

PUBLICATIONS

Vayner, A., Wright, S. A., Murray, N., Armus, L., Cosens, M., Walth, G., Boehle, A., Larkin, J. E., Mieda, E. *"A Spatially-Resolved Survey of Distant Quasar Host Galaxies: Kinematics and Energetics of Ionization Gas"*, in-prep

Lockhart, K. E., Do, T., Larkin, J. E., Boehle, A., Campbell, R. D., Chappell, S., Chu, D., Ciurlo, A., Cosens, M., Fitzgerald, M. P., Ghez, A., Lu, J. R., Lyke, J. E., Mieda, E., Rudy, A. R., **Vayner, A**., Walth, G., Wright, S. A. *"Characterizing and Improving the Data Reduction Pipeline for the Keck OSIRIS Integral Field Spectrograph"*, 2018, AJ, 157, 75

Cosens, M. Wright, S. A., Mieda, E., Murray, N., Armus, L., Do, T.,Larkin, J. E., Larson, K., Martinez, G., Walth, G., **Vayner, A.** *"Size-Luminosity Scaling Relations of Local and Distant Star Forming Regions"*, 2018, ApJ, 869, 11

Vayner, A., Wright, S. A., Murray, N., Armus, L., Larkin, J. E., Mieda, E. *"Galactic Scale Feedback Observed in the 3C 298 Quasar Host Galaxy"*, 2017, ApJ, 851, 126

Vayner, A., Wright, S. A., Do, T., Larkin, J., Armus, L., Gallagher, S. C. *"Providing stringent star formation rate limits of $z\sim2$ QSO host galaxies at high angular resolution"* , 2016, ApJ, 821, 64

ABSTRACT OF THE DISSERTATION

The Role of Quasars in the Formation of Massive Galaxies

by

Andrey Vayner

Doctor of Philosophy in Physics

University of California San Diego, 2019

Professor Shelley A. Wright, Chair

This thesis studies actively accreting supermassive black holes (SMBH) known as quasars and their impact on the formation and evolution of massive galaxies. Theoretical work predicts that quasars are responsible for regulating the growth of the SMBH and its host galaxy. Winds driven by radiation pressure from the accretion disk and quasar jets are predicted to remove a substantial amount of gas from the host galaxy. Massive galaxies are observed to form the majority of their stars when the Universe was only 3.5 billion years old. During this epoch, the most massive SMBH already grew a substantial fraction of their mass. The SMBH is predicted

to regulate the growth of the host galaxy during this co-evolutionary phase.

We have undertaken an extensive adaptive optics (AO) assisted integral field spectroscopy (IFS) survey of distant quasar host galaxies when the Universe was only 2.2-4.6 Gyr old. We conducted observations using the 10-meter W.M. Keck Observatory optical and infrared telescope. The survey aims to measure the gas-phase properties of quasar host galaxies such as metallicities, star formation rates, photoionization mechanisms, and search for galaxy-wide outflows potentially driven by the quasar. We detect outflows in all objects on scales from < 1 kpc to 10 kpc. Half the outflows are consistent with being driven by a powerful energy-conserving shock, while the rest are either driven by radiation pressure or an isothermal shock. The outflows are the dominant source of gas depletion in these distant quasar host galaxies.

For the quasar 3C298, we have also conducted observations aimed at studying the molecular gas reservoir with the Atacama Large Millimeter Array (ALMA). In addition to detecting an ionized outflow in 3C298, we detect the first molecular outflow driven by a distant quasar. These observations show clear evidence for quasar driven outflows removing the molecular interstellar medium (ISM) through negative feedback.

The gas in the host galaxies is photoionized by a combination of O & B stars, the quasar, and radiative shocks. The chemical enrichment of the ISM is lower compared to the level observed in massive local galaxies. The quasar host galaxies appear to be under-massive relative to the mass of the SMBH based on local-scaling relations between the SMBH mass and galaxy mass. Substantial stellar growth and chemical enrichment are necessary if these galaxies are to grow and evolve into the most massive present-day elliptical galaxies.

Chapter 1

Introduction

Modern cosmology has provided us with a profound understanding of the contents that make up our Universe. Ever since the discovery that we live in a non-static, expanding Universe by Edwin Hubble and Georges Lemaître, astronomers have been trying to better measure the expansion rate, size, and history of our Universe. In the young Universe when the temperatures cooled down to approximately 3000 K, protons and electrons were able to recombine. After recombination, light was able to travel freely through the Universe, producing the cosmic microwave background (CMB). As the Universe expanded the wavelength of the photons from the CMB shifted from optical to the radio. Following the discovery (Penzias and Wilson, 1965) of the CMB, ground and space-based radio observations have focused on measuring the properties of the Universe using this relic light source. Today, the CMB appears as a faint uniform background on the sky, with small anisotropies caused by early quantum fluctuations in the Universe. Precision cosmology began with balloon, rocket and space observations of the CMB in the 1970s and 80s attempting to search for and understand the fluctuations of the early

Universe giving clues about its content and expansion history. During the same time advances in precision distance measurements to stars and galaxies allowed for the use of Type-IA supernovae as standardized candles, meaning that discovery and monitoring of this type of explosion allow for accurate distance measurement to the galaxy in which it exploded. The high intrinsic luminosity of Type-IA supernovae meant that researchers could measure the distances to further galaxies than previously possible. Both CMB and supernova surveys provide us with clues on the formation, expansion rate, contents, and evolution of our Universe.

These works were critical to the formation of our current theory of galaxy formation and evolution. From these cosmological surveys, we learned that the Universe is 13.8 billion years old, and not only expanding, but today, there is an acceleration to the expansion of the Universe. The source of the acceleration is unknown and has been called “dark energy", making up 68.5% of the energy budget of the Universe. The rest of the energy content is in the matter, with 26.4% in cold dark matter and 4.9% in ordinary matter (Planck Collaboration et al., 2014). According to these cosmological surveys for any given galaxy approximately 18%, of the galaxy's content needs be in ordinary matter or Baryons. Stars, gas, and planets make up this percentage of matter. However, observations of nearby galaxies found that only at most $10 - 20\%$ of the Baryonic matter is locked up in stars (Kormendy and Ho, 2013). The rest of the matter is thought to reside in a gas phase surrounding galaxies in what we call the circum-galactic or inter-galactic medium (CGM/IGM). The CGM plays a crucial role throughout the life of a galaxy, as the majority of the gas is thought to reside there. Gas inflows from the CGM into galaxies providing fuel for star formation. The CGM extends up to radii ten times larger than the radius of a galaxy's disk while the IGM extends to even larger distances. During the lifetime of a galaxy stars form

within galaxies, inside stars Hydrogen and Helium are used up as fuel and get converted into heavier elements on the periodic table. Gas enriched with heavy elements gets expelled into the interstellar medium as stars die, enriching the ISM with heavy elements. In Astronomy, metals refer to any element on the periodic table that is not Hydrogen or Helium. Majority of metals in the Universe form either inside stars or during explosions of massive stars and mergers of stellar remnants.

Observations of enriched gas at vast distances within the CGM is puzzling, how did the gas transfer from the disk of a galaxy (8 kpc or 26,000 light years) to size scales of 100 kpc. For context, there is approximately the same mass of metals in the CGM/IGM of a typical galaxy as there is inside of it (Tumlinson et al., 2011; Werk et al., 2011). The ratio between stellar mass to total dark matter mass decreases for more massive galaxies, meaning a larger fraction of the gas content did not get converted into stars relative to less massive galaxies. In other words, the more massive the galaxy, the more inefficient star formation has been throughout its lifetime. Figure 1.1 showcases the fit to the measured ratios between the stellar mass of a galaxy to its total dark matter halo mass. Galaxies live inside halos of dark matter which constitutes the majority of the galaxy's mass. From the cosmological observations, approximately 18% of a galaxies' mass is supposed to be in stellar matter. However, observations found the percentage of ordinary within galaxies to be much lower than the measured cosmological value.

To expel material outside of galaxies to large radii requires very energetic events to occur within the galaxy. Supernova explosions are excellent sources of energy to expel material outside of galaxies (Leitherer et al., 1999; Murray et al., 2005). Other notable sources of energy are an Active Galactic Nucleus (AGN), where energy from gas accreted onto a supermassive black hole

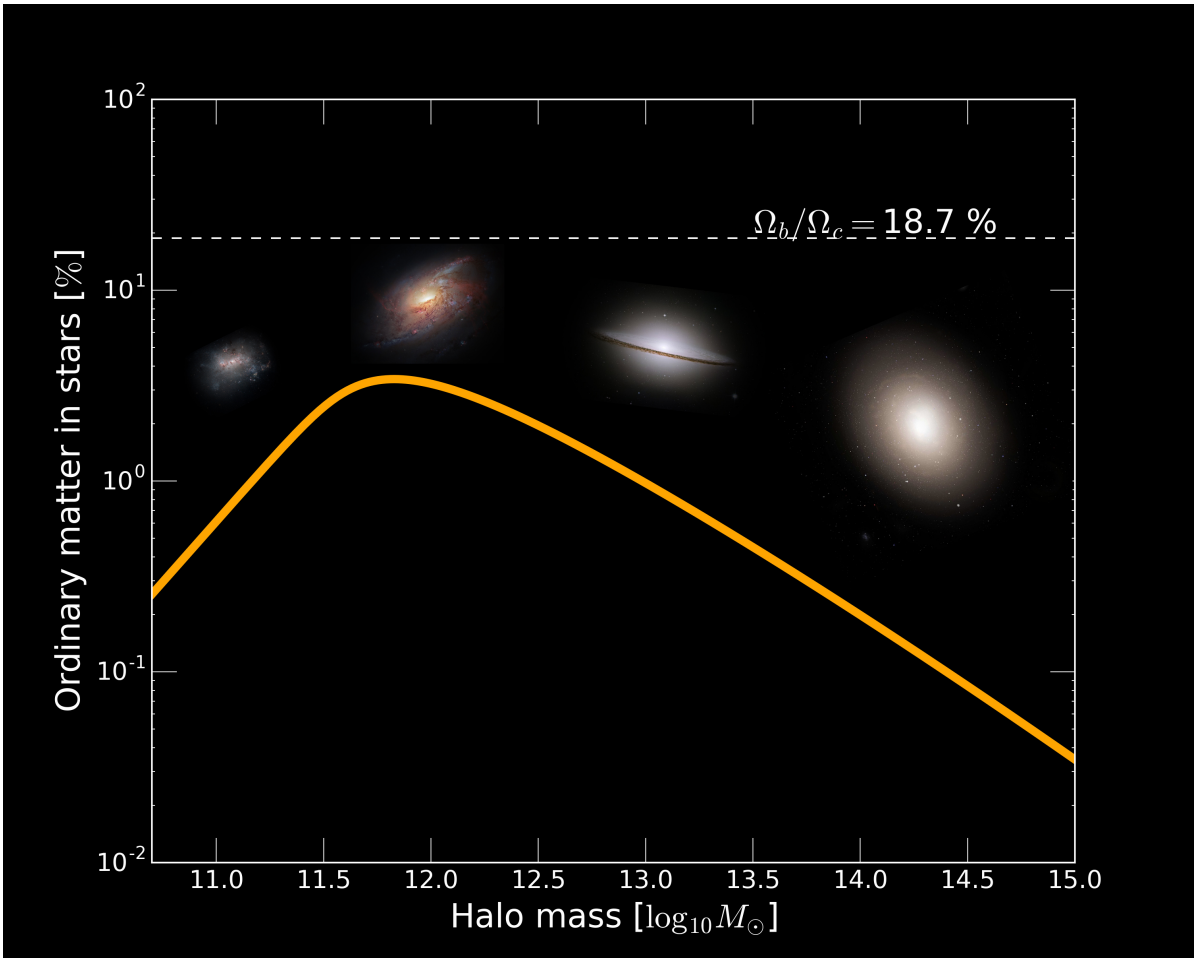

Figure 1.1 Percentage of baryonic mass locked up in stars within galaxies of different mass. Orange curve represents a fit to the ratio between stellar and total dark matter mass measured in the local Universe taken from Behroozi et al. (2010). The dashed line represents the expected value from cosmological observations. In the nearby Universe at most 10-20% of baryonic matter is locked up in stars. We show the pictures of galaxies living in the dark matter halo at their location of the x-axis. Elliptical galaxies live in the most massive dark matter halos, while irregular dwarf galaxies live in the smallest dark matter halos.

(SMBH) can turn into kinetic energy of a wind that can drive material outwards.

Over the life-time of an accreting SMBH, approximately 10% of the gravitational potential energy can be converted into light that can power a quasar. The amount of energy available in photons can be substantial, and if the energy can couple to the gas in the bulge of a galaxy, it can remove a substantial amount of fuel for star formation. As an example; the amount of available energy from the accretion of mass onto an SMBH, assuming a radiative efficiency of 10% is given by:

$$E_{BH} = 0.1 M_{\bullet} c^2, \tag{1.1}$$

while the binding energy of a galactic bulge is approximately:

$$E_{Bind,Bulge} \approx M_{bulge} \sigma^2 \tag{1.2}$$

where M_{bulge} and σ are the mass and velocity dispersion of the bulge. The ratio of E_{BH} and $E_{Bind,Bulge}$ simplifies to $5.3 \times 10^{-4} (\frac{c}{\sigma})^2$ using the average SMBH to bulge mass ratio of 5.3×10^{-3} observed in the nearby Universe. For a bulge with a velocity dispersion of 200 km s^{-1} the ratio is approximate 1000, implying that if only a small percentage $0.1 - 1\%$ of the binding energy of the SMBH is turned into an outflow, the outflow can unbind a significant fraction of the gas content within the bulge. Potentially expelling gas to very large radii into the CGM/IGM.

1.0.1 A brief history of AGN and quasars.

AGN have a fascinating history (Shields, 1999; Kellermann, 2014); the first AGN was discovered in a nearby galaxy NGC 1068 by F.A Fath in 1909 (Fath, 1909). This discovery came long before NGC 1068 was found to be an external galaxy outside of our own Milky Way, at that time it was still referred to as a nebulae which was discovered by Charles Messier (Messier, 1781). In fact, Fath's work aimed to test whether the observed nebulae were part of our galaxy such as Orion's nebula, or extra-galactic. For the majority of the objects, he found that the nebulae were a collection of stars, due to evidence of absorption lines seen in their spectra, similar to those observed in our Sun. However, in NGC 1068, he discovered strong emission lines, similar to those in Planetary Nebulae, the spectrum also showed absorption lines, similar to other objects in his sample. Higher spectral resolution observations by Slipher (1917) of NGC 1068 noted a highly redshift velocity for the object, and line broadening towards the center of the galaxy. Years later, Carl Seyfert (Seyfert, 1943) began a survey looking at galaxies with high nuclear light concentration. After taking spectra of some of these objects, he noted that some contain very broad $\sim 8,000$ km s^{-1} emission lines, as well as narrower high excitation lines similar to the planetary nebula NGC 7027. He noted that only a small fraction of the spiral galaxies showed very broad emission lines, there was no interpretation for their origin, or the high excitation narrower emission lines. Work by Woltjer (1959) was some of the first at attempting to interpret the galaxies discovered by Carl Seyfert. He pointed out that the broad emission lines discovered were very compact on the sky (<1") or about 70 pc indicating a very high mass concentration on the order of 10^9 M$_\odot$. Following World War II the 1950s brought

considerable advances in radio technology, some of the objects with peculiar emission lines were also found to emit strong radiation in the radio. Notable objects such as NGC 1068, M87 and Cyg A were found to be strong radio emitters (Bolton et al., 1949; Ryle et al., 1950; Baade and Minkowski, 1954). During the 1950s there were several radio surveys of the sky such as with the Cambridge Interferometer (2C: Shakeshaft et al. (1955) and 3C: Edge et al. (1959) surveys) that provided one of the most extensive catalogs of radio sources on the sky for that decade. Following and during these surveys, there were attempts to localize the sources better to attempt identifying them with optical counterparts.

The initial localization of radio sources focused on the brighter, more compact sources since the position for these objects were known to higher accuracy. The radio source 3C 295 was one of the first objects to be localized (Elsmore et al., 1959) within the 3C survey. First optical images with the 200-inch Hale telescope showed a cluster of galaxies. The first spectra also taken with the Hale telescope found a redshift of 0.46 (Minkowski, 1960) for the radio galaxy based on the detection of [OII] emission lines. This was the highest redshift (most distant) galaxy known at that time.

Matthews and Sandage (1963) were attempting to localize objects with the smallest angular size observed with interferometers in the radio at that time, in search of “radio stars". 3C 48 was localized in 1960 and identified with a 16th magnitude star, and a spectrum was even taken; however, the emission lines were not identified. In 1960 at the winter the American Astronomical Society (AAS) meeting, 3C48 was dubbed as the “first radio star" ever to be observed (Kellermann, 2014). Following this discovery, another object, 3C 273, was localized using lunar occultations with the 64-m Parkes Radio Telescope in Australia (Hazard et al., 1963). The

position was more accurate compared to interferometric observation at that time for this target. 3C 273 was identified with a 13th magnitude star showing a faint wisp nearby, similar to the center of the nearby elliptical galaxy M87. A spectrum was taken with 200-inch Hale telescope (Schmidt, 1963), the spectrum showed broad emission lines from Hydrogen, with similar line width to some of the objects studied by Carl Seyfert two decades earlier. The best explanation for this object was that it was a nucleus of a faraway galaxy at a redshift z=0.16, rather than a star within the Milky Way galaxy. Both the presence of the very broad emission lines, high radial velocity, and forbidden [OIII] emission lines, and lack of proper motion made it hard to explain 3C 273 as a star. Following this discovery, the spectrum of 3C48 taken in 1960 was re-examined and, it was possible to also explain all of the observed emission lines with a highly redshifted object at z=0.369. Nevertheless, the name “quasi-stellar radio sources" stuck for objects such as 3C 273 and 3C 48, later shortened to “quasar" in a Physics Today review article by Chiu (1964). Work by Kristian (1973) was the first to identify the host galaxies of some of the closer quasars, concluding that quasars live at centers of galaxies. However even in the initial imaging of 3C 48 by Matthews and Sandage (1963) they noticed faint “fuzz" or nebulosity around the quasar. From spectroscopic observation of this faint extended emission it was confirmed that it comes from gas surrounding the quasar (Wampler et al., 1975) in its host galaxy.

Following the discovery of the optical counterpart to 3C 273, it was noted that quasars show excess ultraviolet light in their spectra. A search began using optical imaging for star-like objects that show similar colors, leading to the discovery quasars that were not associated with radio emission (Sandage, 1965). Similar to their radio counter parts they showed highly redshifted broad Hydrogen lines as well as narrow forbidden lines from Oxygen, Neon, and

Nitrogen. Eventually, the agreed upon name for these objects was simply “quasi-stellar objects" or QSOs or sometimes radio-quiet quasars. Today, we know that they all belong to the same class of objects, with the only difference that some show prominent radio emission and others don’t. Throughout this thesis I will refer to quasars as the general class of luminous AGN that have a bolometric luminosity of $> 10^{45}$ erg s^{-1}. In the initial studies it was quickly noted that radio quiet quasars are far more common than quasars, today we know that roughly 10% of the entire quasar population is radio-loud. Surveys searching for quasars continued to grow since the early 1960s, at optical and radio wavelength, with the eventual addition of X-ray observations from first balloon and rocket observations (Bowyer et al., 1970) and eventual space observations with the Einstein Observatory (Tananbaum et al., 1979) and ROSAT.

1.0.2 Source of power within quasars and the unification model

For a long time, there was a debate as to what powers the emission seen in quasars. Large and rapid optical variability for some quasars implied small sizes (Matthews and Sandage, 1963). Initial theoretical work focused on very massive stars at centers galaxies as the power source. Later theoretical work introduced SMBHs as the engines powering quasars (Zel’dovich, 1964; Salpeter, 1964; Lynden-Bell, 1969). Notably, work by Lynden-Bell (1969) made an interesting prediction that if quasars are powered by accretion onto SMBHs, and with quasars having a finite lifetime, then today in the nearby Universe, the centers of galaxies should all contain SMBH with masses $> 10^6$ $M_\odot$. By counting the number of quasars as a function of distance, we learned that quasars were nearly 1000 times more prevalent in the distant young Universe compared to today (Manti et al., 2017). The consensus today is that quasars are powered through the accretion of

gas onto an SMBH. The luminosity of a quasar is given by the following equation:

$$L_{quasar} = \eta \dot{M}_{\bullet} c^2 \tag{1.3}$$

where $\dot{M}_{\bullet}$ is the accretion rate of gas onto the SMBH and (η) is the radiative efficiency in the range of 0.05-0.42, depending on the spin of the black hole (Kerr, 1963; Thorne, 1974).

In his early work, Carl Seyfert noticed that there were two types of Seyfert galaxies, ones that show both broad (5,000-8,000 km s^{-1}) Hydrogen and narrow (500-1000 km s^{-1}) forbidden emission lines which are called type-1 Seyfert galaxies and objects that only show narrow Hydrogen and forbidden metal lines with weak continuum, called Seyfert type-2. It was challenging to explain the differences between these two types of galaxies; however, a breakthrough came in 1977 (Rowan-Robinson, 1977) that proposed the central continuum source and the region from where the broad emission line arises may be obscured by dust in type-2 Seyfert galaxies. Furthermore, the dust in the vicinity of the nucleus was notable in explaining the infrared emission observed in Seyfert galaxies. Spectro-polarimetric observations of NGC 1068 a type-2 Seyfert galaxy showed broad Hydrogen lines in polarized light that were missing in the total intensity spectrum (Antonucci and Miller, 1985). The polarized flux spectrum resembled that of a type-1 Seyfert galaxy due to evidence of broad Hydrogen emission lines and a blue continuum. This early study concluded that there must be an optically thick component that is blocking the light from the broad-line region and scatters the light along other lines of sight in type-2 systems. A dusty geometric torus was introduced to the AGN phenomena to explain the difference between the two types of AGN. The dust in the torus absorbs UV photons produced in the accretion disk

and re-emits them at infrared (1-1000 μm) wavelengths. The dust sublimation temperature sets the inner radius of the dusty torus. The unification of the two types of Seyfert galaxies started the work on the AGN unification model. Seyferts and quasars were unified by merely setting an arbitrary bolometric luminosity cut at 10^{45} erg s^{-1}. Objects that are less luminous than 10^{45} erg $s^{-1}$are called Seyferts (either type 1 or type 2), and more luminous objects are called quasars (either type -1 or type -2). Eventually, with the launch of the Hubble space telescope, a torus-like object was observed in the galaxy NGC 4261 (Jaffe et al., 1993). More recently there have been observations with ALMA, a radio telescope able to detect and map the dusty torus using emission from molecular gas (Imanishi et al., 2018).

Aside from quasars emitting prominent radio emission, another class of objects known to emit in the radio were BL Lac objects; however, they showed drastically different optical properties to quasars. Unlike quasars, BL Lac objects did not show any prominent broad or narrow emission lines, simply a highly variable continuum in the optical. During a conference on BL Lac Objects, Blandford and Rees (1978) proposed that these are simply radio galaxies, where the viewing angle is along the axis of the jet. The highly beamed synchrotron emission produces a continuum emission seen at all wavelength. The beamed synchrotron emission from the jet outshines the isotropic emission from the gas, stars, accretion disk, and broad-line region. If these objects were viewed from the side, they would show jets and lobes, similar to quasars and radio galaxies. The generally accepted unification model of today (Figure 1.2) is presented in Antonucci (1993); Urry and Padovani (1995) based on the earlier works listed above.

The unification model is developed from observations of nearby AGN. In the more distant Universe, galaxy evolution can play an essential role in causing the apparent differences in type

1 and type 2 AGN. Since the discovery of Ultra-Luminous Infrared Galaxies (ULIRGs) and their association with quasar activity, there have been several proposed models that link AGN and quasar obscuration to galaxy evolution (Sanders et al., 1988; Hopkins et al., 2008). In these models typically the quasar is triggered in a gas-rich merger between two galaxies. As the galaxies pass close to each other, the gas and dust within them begin to lose angular momentum and spiral towards their centers. As the gas moves inwards, a nuclear star-burst is triggered along with rapid accretion of gas onto the SMBH, which triggers quasar activity in the center. However, because of the large gas and dust content in the inner regions of the galaxy, majority of the light coming from either the accretion disk or from young stars in the nucleus are obscured by dust. Of course, some of the light from the quasar can also be obscured by a torus-like phenomenon, but just as equality, it can be absorbed by the infalling gas and dust and tidal debris from the merger on larger scales. Eventually, the quasar drives a wind that clears the gas and dust from the inner regions and the UV light from the accretion disk can escape, at this point the quasar becomes apparent in UV and visible light.

The key generally agreed upon structures of an AGN/quasar are listed blow:

- **Supermassive black hole:** In the center there is a SMBH with a mass range of 10^{6-10} $M_{\odot}$
- **Accretion disk:** In the center gas accreting onto the SMBH forms a thin optically thick disk of temperature $T \sim 10^{4-5}$ K which primarily emits in the UV. The typical size of a quasar accretion disk is on the order of $10^{14} - 10^{16}$ cm. (Mudd et al., 2018)
- **Broad-line region:** Beyond the accretion disk, there are high-density clouds with electron

densities $> 10^9$ cm^{-3} , and temperatures of 10^4 K. The clouds rapidly orbit the accretion disk, producing Doppler-broadened lines seen at UV and optical wavelength with line widths of 5,000-20,000 km s^{-1} . The typical size of a broad line region is on the order of 10^{17} cm. (Gravity Collaboration et al., 2018)

- **Hot Corona:** Close the SMBH and surrounding the accretion disk there is a hot optically thin corona. The corona up-scatters photons produced in the accretion disk through inverse Compton scattering. The up-scattered photons are seen in high-energy X-ray spectra of AGN/quasars as a power-law continuum.

- **Torus:** A dusty torus surrounds the accretion disk, with an inner radius at a distance where UV and X-ray photons no longer sublimate dust. The dusty torus dominates the emission at mid-infrared wavelength.

- **X-ray reflection:** Some of the up-scattered photons produced by the hot corona are reflected of the dusty torus, producing a reflection component seen in the X-ray spectra of quasars and AGN.

- **Narrow-line region:** Even further from the dusty torus, there are lower density clouds that are photoionized by the accretion disk and produce recombination radiation seen in Hydrogen, Helium and forbidden metal lines (e,g [OIII] , [NII]). The velocity widths of these emission lines are on the order of 500-1000 km s^{-1} . The size of this narrow-line region (NLR) can vary drastically, spanning from a few tens of pc to a few kpc. An extended narrow line region (ENLR) refers to gas photoionized by the accretion disk on kpc scales.

- **Quasar jets:** Jets are evident in about 10% of quasars, extending from scales of a few pc to Mpc scales. The jets produce synchrotron emission seen at nearly all wavelength.

1.0.3 Evidence for SMBH in nearby galaxies.

As noted by Lynden-Bell (1969), if quasars were common phenomena in the distant Universe, today the remnants of quasars should be dormant SMBH at centers of most galaxies. One of the ways to search for SMBH at centers of galaxies in the nearby Universe is through measuring the motion of stars or gas within the sphere of influence of an SMBH given by the equation below.

$$R_{influence} = \frac{GM_{SMBH}}{\sigma^2_{Bulge}} = 48\left(\frac{M_{SMBH}}{1 \times 10^9\ M_\odot}\right)\left(\frac{\sigma}{300km\ s^{-1}}\right)^{-2} pc \tag{1.4}$$

For an SMBH with a mass of 1×10^9 $M_\odot$ and a galaxy where stars are moving at 300km s^{-1} in the bulge, the sphere of influence is only 48 pc. At the distance of the Virgo cluster, this translates to an angular scale of 0.4" on the sky. The sphere of influence subtends a small angle, which is difficult to probe from the ground due to turbulence in the atmosphere, which blurs images from space. Astronomical seeing refers to the amount of blurring that is caused by the earth's atmosphere, which is the effective resolution of a telescope. On the best astronomical sites on earth, the typical median seeing is about 0.7" in the visible; this is larger than the gravitational sphere of influence of an SMBH at the distance of the Virgo cluster. The first SMBH mass measurements focused on two nearby galaxies; M31 and M32 for which the sphere of influence on the sky is 5.75" and 0.46", respectively. The SMBH in M32 was measured first under seeing

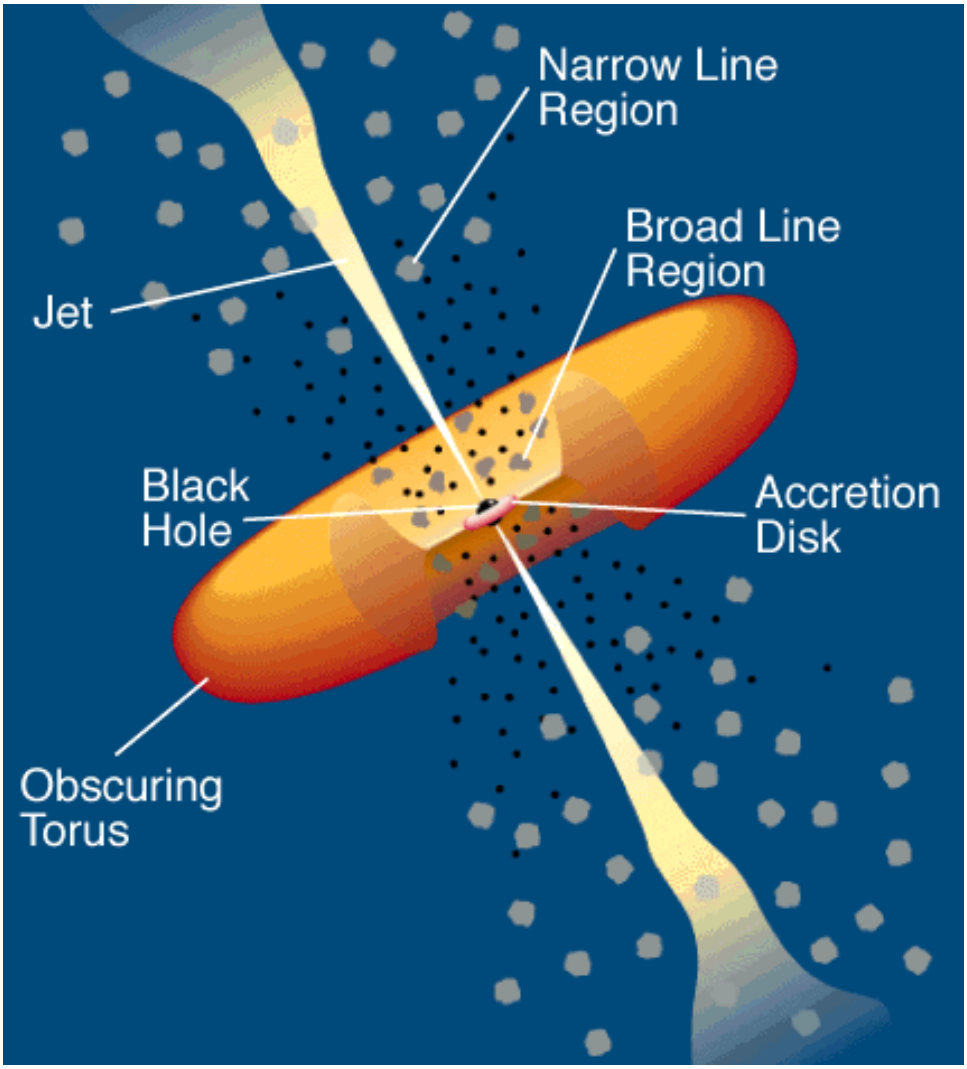

Figure 1.2 Unified AGN model based on (Urry and Padovani, 1995), today this the most agreed upon model of an AGN. At the center, there is an SMBH with gas accreting on it in a thin accretion disk. Dense clouds orbit in the broad-line region outside the accretion disk. A dense torus consisting of dust and molecular gas surrounds the broad-line region and the accretion disk. Above the plane of the accretion disk/torus low density gas is photoionized by the accretion disk in the narrow-line region. Jets from the accretion disk extend perpendicular to the accretion disk/torus. Lines of sight through the dusty torus produce quasar and AGN spectra lacking broad emission lines from the broad-line region and do not show continuum from the accretion disk. Lines of sight perpendicular to the dusty torus produce quasar spectra with both broad and narrow line emission and, continuum emission emitting in the UV. For radio-loud quasars, view along the jet produces BL Lac or Blazer synchrotron spectrum that outshines the rest of the AGN and galaxy structure. When the viewing angle is away from the axis of the jet, radio lobes and extended jet emission are visible as in radio galaxies and radio-loud quasars.

conditions that barely matched the size of the sphere of influence (Tonry, 1987). The mass of the SMBH in M31 was published a year later by Dressler and Richstone (1988), and this study also confirmed the mass measured for M32 under better seeing conditions. Following the launch of the Hubble Space Telescope, weighing the masses of SMBHs shifted towards space observations which are unaffected by the blurring effects of the atmosphere and many more SMBH masses were measured for galaxies in the nearby Universe, see Kormendy and Ho (2013) for review. The projected sphere of influence for the SMBH within the Milky Way galaxy is much larger than M31 and M32 at about 41". Measuring the SMBH mass at the center of the Milky Way galaxy was challenging because of the high obscuration by dust towards the center. It was not until advancement in infrared detectors which allowed to see the stars in the galactic center at near-infrared wavelengths where the dust attenuation is minimal. The first evidence for a massive compact object within 0.6 pc of the galactic center was by Sellgren et al. (1990) from the evidence of an increase in the mass to light ratio in the inner 0.6 pc. Eventually, with the advancement in adaptive optics (AO) technology, it was possible to resolve the individual stars within the galactic center and track their orbits over time and measure the mass of the SMBH (Ghez et al., 2008; Genzel et al., 2010). Adaptive optics (AO) corrects for the blurring effects of our atmosphere, making the images much sharper. Starting from the year 2000, AO assisted observations were used to measure the masses of many more SMBHs.

The theory of general relativity predicts the existence of an “Event Horizon" around a black hole. Within this region, even light cannot escape the gravitational potential of the black hole. Even for nearby galaxies the size of the event horizon is very small on the sky, requiring telescopes with nearly the diameter of our planet to resolve. For emitting gas near the SMBH,

the theory of general relativity predicts an image with a central depression and a ring due to light being bent by the strong gravitational potential of the black hole. The Event-Horizon Telescope (EHT) using an assembly of millimeter-wavelength radio telescopes around our planet took the first image of the event horizon around the SMBH in the galaxy M87 in 2017 (Event Horizon Telescope Collaboration et al., 2019). The reconstructed images agree with the prediction for the size and shape of the event horizon around a massive black hole. These observations provide an independent proof for the existence of SMBH at centers of galaxies, and that SMBHs are responsible for powering central engines of active galactic nuclei. The profound conclusion provided by these observations is that there is an SMBH at the center of every galaxy in the nearby Universe. These SMBHs must be the remnants of quasars seen in the distance Universe.

1.0.4 SMBH and galaxy correlations; start to the field of AGN feedback

With a large enough sample of black hole masses, a tight correlation between the mass of the SMBH and the velocity dispersion, luminosity, and mass of the bulge emerged (Magorrian et al., 1998; Gebhardt et al., 2000; Ferrarese and Merritt, 2000). These results were very puzzling because the gravitational sphere of influence of the SMBH is so much smaller than the size scales over which these quantities are correlated. How does the galaxy know about the presence of the SMBH? How does the SMBH know about the mass of the entire galaxy? Theoretical papers attempting to explain these correlations quickly developed, starting with Silk and Rees (1998) which proposed that if a small fraction of the quasar's bolometric luminosity is converted into kinetic energy of an outflowing gas shell, it may be possible to expel a significant fraction of the gas from the galaxy. They proposed the accretion disk surrounding the SMBH drives the

wind once the galaxy has reached the critical ratio of 5.3×10^{-3} between SMBH and galaxy mass observed in the nearby Universe. The seminal paper by Silk and Rees (1998) along with the observed correlation in nearby galaxies effectively started the field of AGN feedback. AGN feedback generally refers to a process that can either inhibit star formation in the host galaxy due to AGN (quasar) activity or expel the gas from the inner regions of the galaxy, removing the fuel necessary for star formation. The only time that the galaxy knows about the existence of the SMBH and vice-versa is during the feedback process, which effectively establishes the observed correlations. Furthermore, during episodes of AGN feedback, the expelled gas from the galaxy is highly enriched as it processed through stellar evolution. The velocities predicted from quasar driven winds are fast enough to escape the gravitational potential of the galactic disk, meaning that gas from the ISM can be transferred deep into the CGM/IGM, helping explain the missing baryon problem discussed earlier. Over the years, the theoretical models of AGN feedback have evolved. Today, theoretical work predicts that feedback happens in two stages. First, the wind is driven in the vicinity of the SMBH, the generally accepted mechanism for driving this wind is through radiation pressure or a jet from the AGN accretion disk. Once the SMBH and galaxy evolve to the critical ratio seen in the nearby Universe, this wind becomes powerful enough to expand deeper into the ISM, eventually heating the gas and driving a secondary outflow that sweeps material out of the galaxy (Hopkins and Elvis, 2010a; Faucher-Giguère et al., 2012; Zubovas and King, 2012, 2014). This mode of feedback is often referred to as transformative, where the galaxy generally goes from being star-forming to quiescence.

To address the cooling problem in nearby galaxy clusters, “maintenance mode" feedback has also been introduced into galaxy evolution. In the early 1990s, it was noted that massive

galaxies and galaxy clusters show an overabundance of X-ray emission. Given our understanding of gas cooling mechanisms, the X-ray gas surrounding massive galaxies should have cooled quickly in the absence of any energy input. This gas should have then accreted onto the galaxy and contributed to star formation. However, observations indicate both lack of large reservoirs of cold gas and any evidence for recent star formation at a rate consistent with the available hot gas reservoir. The slower cooling timescale for the hot X-ray gas indicates a heating mechanism in the halos of massive galaxies. With the launch of the ROSAT and eventually the Chandra Space Telescope it was noted that some clusters show cavities in their X-ray emitting halos (Boehringer et al., 1993; Carilli et al., 1994; McNamara et al., 2000; Hlavacek-Larrondo et al., 2013). Such cavities are most notable in NGC 1275 and M87 which are the brightest cluster galaxies (BCGs) in the Perseus and Virgo galaxy clusters. Radio emission from jets often fills the X-ray cavities, indicating that jets might be responsible for carving them, hence providing the turbulence, which keeps the X-rays gas from cooling. The required energy to vacate the X-ray gas in the cavities is consistent with the energy deposition from powerful quasar jets (Bîrzan et al., 2008; Fabian, 2012), indicating a balance between the heating and cooling mechanisms in halos of massive galaxies. In the current feedback paradigm, maintenance feedback follows sometime after transformative feedback, in order to keep the galactic halos hot, preventing future gas from accreting onto galaxies and providing fuel for future star formation. This mode of feedback effectively keeps the galaxies on the local scaling relations, preventing the SMBH and galaxy from growing further. Maintenance-mode feedback addresses the cooling-flow problem, by keeping the baryons locked up in the hot gas halo further helping to explain the significantly lower ratio between total stellar and dark matter halo mass ratio in massive galaxies (Figure 1.1.

Other terms often used to describe this mode of feedback is “radio-mode" or “hot-halo-mode."

1.0.5 Discovery of small scale quasar/AGN outflows

The first outflows in quasars were discovered from the presence of broad blueshifted absorption lines in rest-frame ultraviolet spectra. These outflows were found to be moving fast, away from the accretion disk at velocities up to 20% the speed of light. These types of outflows are found in approximately 40% of optically selected AGN (Ganguly and Brotherton, 2008; Allen et al., 2011); however, the intrinsic value may be higher. Outflows detected from absorption lines in rest-frame UV spectra are called Broad Absorption Line winds or BAL. To explain the BALs, Murray et al. (1995) applied similar mechanisms for driving outflows from massive O and B stars to quasars, which similarly show very broad blueshifted absorption lines in their spectra. The generally accepted mechanism for driving the outflows is through radiation pressure from the accretion disk on gas in the vicinity. Recently X-ray spectra of nearby AGN show the presence of broad blueshifted absorption lines. The outflows detected in X-rays are referred to as Ultra-Fast Outflows or UFOs. Theoretical work proposes that on small scales in the vicinity of the AGN, BAL, UFOs, and jets from the accretion disk are responsible for driving the large scale outflow on galaxy scale. However, observationally linking these phenomena to the expulsion of gas and quenching of star formation in quasar host galaxies has been challenging.

1.0.6 Galaxy scale outflows in the local Universe. Implication of feedback in nearby systems

The primary method for detecting galaxy-scale outflows has been through the use of nebular emission lines such has [OIII] , Hα , and [NII] , by looking for evidence of broad asymmetric profiles. Some of the initial work was done in the late 1960s by Burbidge and Burbidge (1965); Walker (1968); Weedman (1970), which detected asymmetric profiles in the 500.7 nm [OIII] emission line with a width reaching a few thousand km s^{-1} . There was even attempts to link the nuclear activity in these sources to the ejection of gas from the inner regions of these galaxies. As detector technology improved and larger more powerful telescopes were constructed along with bigger samples of AGN and quasars (e.g., from the Sloan Digital Sky Survey) to study, it became clear that broad asymmetric nebular emission profiles are typical in galaxies with quasars and AGN. With the advent of integral field spectroscopy (IFS), it became possible to study the two-dimensional structure of outflows in galaxies hosting powerful AGN. IFS provides a spectrum for each spatial location in the field of view of the instrument. This enables the measurements of the motion of stars and gas at a discrete location in the two-dimensional field of view. Previously, the majority of spectroscopic observations were done with long-slit observations which only provided a one-dimensional view of the galaxy. In the nearby Universe z$<$ 0.3 IFS observations of both type-1 and type-2 quasars primarily selected from the SDSS sample reveal evidence for ubiquitous galaxy-scale outflows (Liu et al., 2013b; Harrison et al., 2014). In several objects, the galaxy-wide outflows were detected in other gas phases such as neutral (Rupke et al., 2002; Rupke and Veilleux, 2011), and molecular Feruglio et al. (2013);

Cicone et al. (2014) revealing that powerful outflows driven by quasar activity can remove the molecular reservoir in galaxies, which is the direct fuel for star formation. However, the number of galaxies showing direct evidence for molecular outflows is still very small in the nearby Universe. Furthermore, it has been a challenge to link the small scale winds in the vicinity of the SMBH to the larger scale outflows detected with ionized, molecular, and neutral gas tracers. Attempts have been made for Mrk273 and IRAS F11119+3257 which show both nuclear winds and galaxy-scale molecular and ionized outflows (Feruglio et al., 2015; Tombesi et al., 2015). However linking the small and large scale outflows has been tricky, as the two outflows have drastically different time scales. The galaxy-scale outflows in these systems have been propagating on the order of millions of years, while the nuclear wind in the vicinity of the SMBH has a time scale on the order of thousands of years. Making the causal link is henceforth difficult.

1.0.7 Galaxy scale outflows in the distant Universe. Implication of feedback at early time.

The ages of stars in massive local galaxies indicate that the bulk of them formed when the Universe was younger than 8 billion years (Gallazzi et al., 2008). If the local scaling relations are a consequence of AGN feedback, the stellar populations in massive elliptical galaxies today must have existed during episodes of powerful AGN feedback. From studying the demographics of both star-forming galaxies and AGN, the majority of SMBH and stellar growth happens in the early Universe with both star formation and AGN activity peaking when the age of the Universe was only 2.6-5 billion years Delvecchio et al. (2014); Madau and Dickinson (2014). To under-

stand the effects of AGN feedback on star formation, we have to study galaxies hosting luminous AGN in the early Universe. The challenge with studying distant galaxies is their small angular size on sky $\sim$1" together with surface brightness dimming as a function of redshift, proportional to $(1+z)^{-4}$ where z is the redshift of the galaxy. Furthermore, quasars can outshine the light from their host galaxy by several orders of magnitude, hence require observations with high contrast capabilities. Due to the expansion of the Universe, all of the vital emission lines that are used to detect outflows and study the conditions (e.g., metallicity, density, and temperature) of the ISM get shifted out of the optical waveband. For galaxies in the redshift range of z=1-3, the typical nebular emission lines (Hβ,[OIII] ,Hα ,[NII] ,[SII]) are redshifted to the near-infrared. To study distant galaxies through similar methods to local systems requires observations at the longer wavelength. Large format infrared detectors allowed for the construction of integral field spectrographs operating at 0.8-2.5 μm on 8-10 m class optical/infrared telescopes. Advances in laser-guided star adaptive optics (LGS-AO) allowed for the correction of atmospheric blurring of distant galaxies. By pairing LGS-AO with near-infrared IFS provided the necessary contrast to study the host galaxies of AGN and quasars in the distant Universe.

Initial studies found outflows in ULIRGs hosting quasars (Alexander and Hickox, 2012; Harrison et al., 2012), star-forming galaxies (Genzel et al., 2014), radio galaxies (Nesvadba et al., 2008; Steinbring, 2011; Nesvadba et al., 2017a,b,c), type-2 quasars (Brusa et al., 2016) and un-obscured type-1 quasars (Cano-Díaz et al., 2012; Carniani et al., 2015, 2016). Linking these ionized outflows to star formation properties has been quite challenging. Some objects show outflows with energy rates consistent with the theoretical prediction of AGN feedback that is necessary to establish the local scaling relations. In these cases, the energy rates are on

the order of 0.1-5% of the total quasar or AGN luminosity. However, it is difficult to interpret whether these outflows are affecting the star-forming properties of these galaxies. In specific cases, studies found that galaxies hosting powerful AGN show lower gas fraction and shorter depletion time for the gas reservoir (Kakkad et al., 2017; Brusa et al., 2018). In other systems, outflows driven by quasars are found in regions with no recent star formation, while in regions away from the outflows star formation is still ongoing (Cano-Díaz et al., 2012; Cresci et al., 2015; Carniani et al., 2016). The concern for some of these galaxies is that the observations are taken at seeing limiting resolution, which might not be high enough to resolve the outflow geometry. In some systems, these outflows can simply be expanding perpendicularly to the disk of the galaxy, and we are seeing them above the plane of the galaxy, where star formation is not expected to occur. Alternatively, star formation can still be occurring in regions with outflows; however, it may be heavily obscured by dust.

All near-infrared IFS studies have focused on ionized gas in galactic outflows. Lower than expected energy rates of outflows in the distant Universe ($z > 1$) are attributed to unaccounted mass, which is in either a molecular or neutral gas phase. Numerous studies (e.g., Cano-Díaz et al. (2012); Maiolino et al. (2012); Richings and Faucher-Giguère (2018)) discuss the possibility for the majority galactic outflows to be in a molecular state, inspired by both theoretical work and observations of nearby galaxies (Cicone et al., 2014). The molecular gas in the outflow arises either from shock-heated gas that cools and forms molecules or directly from molecular clouds inside the galaxy being over-pressured by a hot outflow from within. The added benefit of detecting outflows directly in the molecular gas phase means direct proof for removal of the gas reservoir from the galaxy. Detection of warm molecular ($T > 200$ K)

gas indicates that gas is being heated, meaning it will not collapse and form stars on a regular timescale. Detection of warm molecular gas at mid-infrared from the Hydrogen molecule (H_2) in the outflow of M82 supports the idea of molecular gas heating by shocks in galactic outflows. Work with the Spitzer Space Telescope found evidence for an increased presence of warm molecular gas in galaxies with both intense star formation or AGN activity in nearby galaxies (Hill and Zakamska, 2014; Guillard et al., 2015; Petric et al., 2018; Lambrides et al., 2019). The poor angular resolution of the Spitzer telescope made it impossible to resolve the gas within the outflows. Before 2012 there was no telescope powerful enough to detect and resolve outflows in distant galaxies (z$>$ 1, look-back time $>$ 8 Gyr) in the molecular gas phase. The Atacama Large Millimeter Array (ALMA) provided the necessary collecting area, and resolution to both detect molecular outflows in distant galaxies as well as resolve them from the rest of the galactic structure. However, the number of detected molecular outflows at the peak epoch of galaxy and SMBH formation is still very limited.

In the luminous radio-loud quasar host galaxy of 3C 298 Vayner et al. (2017) finds a multi-phase outflow driven by the quasar. Ionized gas in the outflow is detected through nebular emission lines with the Keck telescope and the OSIRIS instrument paired with the laser guide star adaptive optics system. A molecular outflow is detected through emission from rotation transitions of the CO molecule with ALMA. Both outflows are emanating from a disk centered on the quasar. The energy rates of both the ionized and molecular gas phase are consistent with the theoretical predictions (e.g., Zubovas and King (2012)), with the molecular gas containing the larger fraction of the gas in the outflow. Furthermore, the rest of the molecular gas in the system is stable against collapse, meaning at present it will not form stars.

In the host galaxy of the obscured AGN XID 2028 (Brusa et al., 2018) also detects a molecular outflow through CO emission using ALMA, in addition to an ionized outflow that was detected previously with Very Large Telescope (VLT) and the SINFONI instrument. The majority of the gas in the outflow is also in the molecular gas phase, similar to 3C 298. The depletion time scale for the gas within the galaxy is shorter than typical galaxies of similar mass. In a lower luminosity AGN; zC400528 Herrera-Camus et al. (2019) detects a multi-phase outflow with similar results and conclusions as with 3C298 and XID 2028. To understand the demographics of molecular gas in outflows driven by the most powerful AGN and starbursts still requires further observations. The sample today is very limiting, and it is hard to understand the dominant mechanism for driving both the ionized and molecular outflows. Furthermore, to understand the impact of AGN activity and whether it matches with theoretical predictions requires more detection and characterization of molecular gas within distinct regions of distant galaxies.

1.0.8 Inter stellar medium conditions and gas photoionization in quasar host galaxies:

Ever since the discovery of extended ionized emission around distant quasars (Matthews and Sandage, 1963; Wampler et al., 1975), there have been numerous studies interested in understanding the mechanisms for gas ionization. In 1981 a diagnostic system was proposed by Baldwin et al. (1981) to separate different photoionization mechanisms by taking a ratio of four nebular emission lines — the classical diagram on y-axis plots a ratio of log([OIII] /Hβ) against

log([NII]/Hα) on the x-axis. Using photoionization models the diagram was later updated by Veilleux and Osterbrock (1987) to incorporating a separation between star formation and AGN ionization. They also introduced additional diagnostic line ratios between log([OIII] /Hβ) and log([SII]/Hα) or log([OI] /Hα) . The Sloan Digital Sky Survey (SDSS) brought a revolution to our understanding of photoionization diagnostics. Due to the increase in the number of line ratios measured from high signal to noise ratio spectra the two sequences on the BPT diagram became more apparent. The two sequences are star-forming abundance sequence and the starburst-shocks-AGN mixing sequence. With the increased number of objects, it became possible to characterize the shape of the two sequences on the BPT diagrams. Kewley et al. (2001) using stellar population synthesis and photoionization models revised the boundary between gas photoionized by star formation and AGN. Figure 1.3 shows the classical BPT diagram with the two mixing sequences highlighted. The star-forming sequence provides information about the metallicity of star-forming regions, the stellar ionizing radiation field as well as information on the gas condition in star-forming regions (e.g., density, temperature). The mixing sequence, on the other hand, consists of gas photoionized by AGN and shocks and can provide information on the hardness of the AGN ionizing radiation and the metallicity of the gas photoionized by the quasar/AGN. Models of radiative shocks predict line ratios that are consistent with the location of the mixing sequence (Allen et al., 2008; Newman et al., 2014; Dopita et al., 2015). Galaxies with powerful outflows and systems within mergers often show evidence for shocked emission (Rich et al., 2015). Gas with harder ionization tends to lie at higher log([OIII] /Hβ) values, while gas with lower metallicity at lower log([NII]/Hα)regions on the BPT diagram. The BPT diagram is a powerful tool in selecting galaxies with AGN, particularly type-2 AGN which do not show

characteristic broad emission lines and strong UV continuum. At redshift > 0.5 Hα and [NII] get redshifted out of the spectral range of optical spectrographs. Luckily, the log([NII]/Hα) ratio correlates with both stellar mass and rest-frame galaxy colors. For systems at z> 0.5 stellar mass and galaxy colors can be used as a proxy for the log([NII]/Hα)line ratio. Modified diagnostic diagram use log([OIII] /Hβ) and galaxy stellar mass (Juneau et al., 2011) or rest-frame galaxy color (Yan et al., 2011) for photoionization diagnostics at z> 0.5 which are calibrated to the traditional SDSS z=0.1 BPT diagram. "Color-excitation" (CEx), refers to the diagrams using galaxy colors while "stellar mass-excitation" (MEx) refers to diagrams using stellar masses as a proxy for log([NII]/Hα).

Theoretical work has predicted evolution in both sequences on the BPT diagram as a function of redshift. Lower gas-phase metallicity, harder ionization conditions in the ISM, and presence of denser gas in higher redshift galaxies cause a shift in both sequences. At z> 1 all the nebular emission lines are redshifted into the near-infrared, to understand the demographics of photoionization conditions in higher redshift galaxies requires spectroscopic observations at a wavelength of 1-2.4μm. Near-infrared multi-object spectrographs assembled large samples of nebular emission lines (Hβ,[OIII] ,Hα ,[NII] ,[SII]) data that can be used for ionization diagnostics similar to low redshift galaxies, using the log([OIII] /Hβ) vs log([NII]/Hα) diagnostic diagram. In a large sample of star-forming galaxies at z$\sim$2 Steidel et al. (2014); Strom et al. (2017) find elevated line ratios compared to the local star-forming sequence on the BPT diagram. The elevated values are consistent with the theoretical predictions made by (Kewley et al., 2013a). Similarly, in a large sample of AGN, there is tentative evidence for systems lying outside the local mixing sequence (Juneau et al., 2014; Coil et al., 2015; Strom et al., 2017; Nesvadba

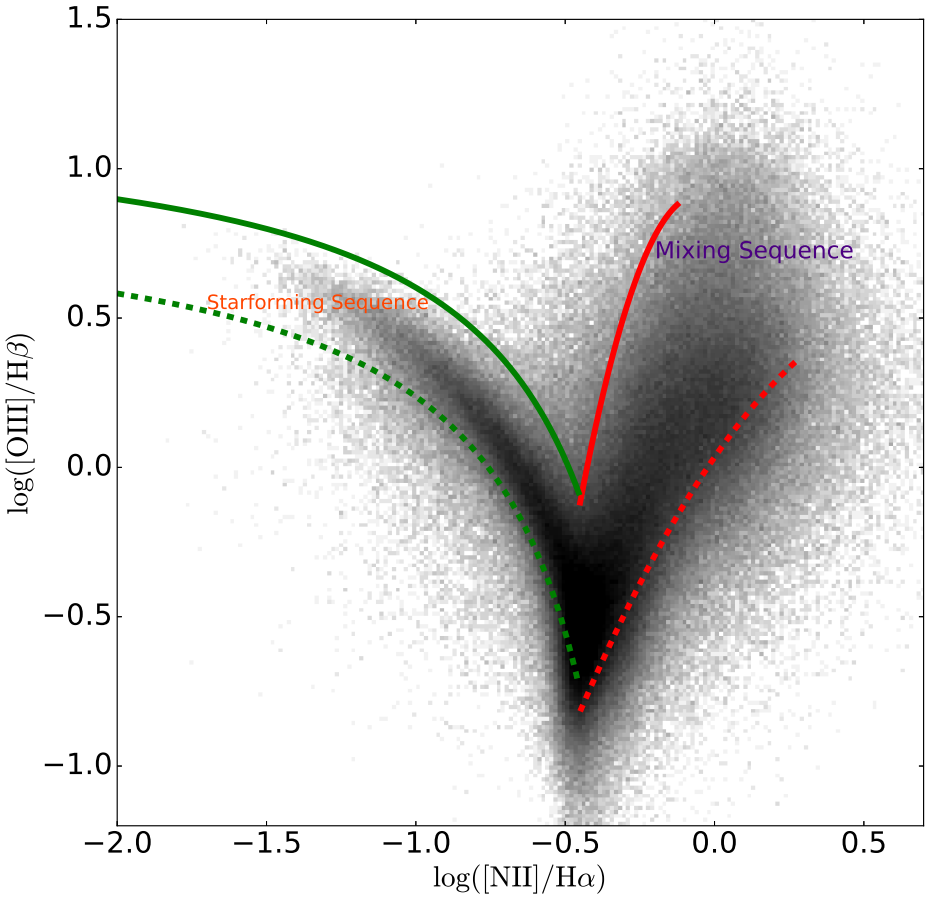

Figure 1.3 The classical BPT diagnostic diagram used to distinguish between gas photoionized by stars, AGN and shocks. Green curves represent the boundary of the star-forming sequence, where points photoionized by massive O and B stars lie. The mixing sequence contains points where shocks and AGN photoionize gas. The outline of the sequences is taken from Kewley et al. (2013a). In the background, we show line ratios from the Sloan Digital Sky Survey.

et al., 2017c; Law et al., 2018). Given the numerous sources of ionization in quasar host galaxies (star formation, quasar and shocks) it is crucial to spatially resolve the quasar host galaxy to understand the various contributions to gas ionization. In both nearby and distant AGN/quasar host galaxies studies have found regions with distinct photoionization mechanisms (Davies et al., 2014; Williams et al., 2017; Vayner et al., 2017). The question remains whether the condition of the ISM in high redshift quasar host galaxies is different from local AGN and other lower luminosity AGN at high redshift.

1.0.9 Thesis outline

The aim of this thesis is to understand the fundamental processes governing massive galaxy formation. To meet this objective, I have conducted high spatial resolution and high contrast observation of a representative sample of $1.4 < \mathrm{z} < 2.6$ radio-loud quasar host galaxies. Observations were conducted for 11 objects with the OSIRIS IFS and the facility laser-guide-star adaptive optics system at the W.M. Keck Observatory. By observing nebular emission lines in distant quasar host galaxies, I was able to map the distribution, kinematics, and dynamics of the ionized gas. From these observations, I was able to search for outflows and understand their dynamics and impact on the host galaxy, understand the sources of gas photoionization and measure star formation rates and masses of the quasar host galaxies. For select objects, I have also conducted mm-radio interferometric observations with the ALMA to understand the distribution, kinematics, and dynamics of the molecular gas.

To date, this is the largest adaptive optics and IFS survey of quasar host galaxies at the peak epoch of galaxy and SMBH growth. The selected quasars are some of the most bolometri-

cally luminous objects in the Universe, with measured spectral energy distributions from gamma rays to cm waves. At redshift ~ 2 these objects already contain SMBH with masses on the order of 10^9 $M_\odot$, indicating that these systems are the most likely progenitors to the massive elliptical galaxies (e.g., M87) seen in the nearby Universe. The sources are selected from the historic 3C and 4C catalog of radio sources and contain heritage multi-wavelength observations in radio, optical and X-rays. For all the objects the conducted IFS observation are some of the first to resolve the two-dimensional structures of the host galaxies at high SNR.

In chapter 2, I present our technique developed to remove the luminous quasar to detect and study the faint extended host galaxy. We apply the technique on a pilot survey of luminous type-1 quasars at z$\sim$2. We demonstrate that we can successfully remove the quasar and detect extended emission as close as 0.2" from the quasar down to a flux of 1×10^{-17} erg s^{-1}.

In chapter 3, I present results on the first object; 3C298 observed within the radio-loud sample. 3C298 is a late-stage merger system between two disc galaxies with a projected separation of 8 kpc. The quasar lives in a disc galaxy with powerful quasar driven outflows that are emanating from the disc. In the merging galaxy 8 kpc away from the quasar an outflow is also detected. Narrow nebular emission lines with ratios consistent with star formation and a detected a molecular reservoir suggest recent star formation in the tidal tail feature, 21 kpc away from the quasar. ALMA observations for this object reveal the first molecular outflow detected at the peak epoch of galaxy and SMBH growth. The dynamical mass of the galactic disc centered on the quasar as measured from molecular gas observations with ALMA reveals that the SMBH mass is overly-massive compared to the mass of the galaxy. This implies that the galaxy resides away from the local scaling relation between the mass of the SMBH and the mass of the

galaxy. At present, there is not enough molecular gas in the 3C 298 system to grow the stellar mass to the expected value based on the local scaling relations. The system requires substantial gas accretion from the CGM/IGM or dry mergers with galaxies in the quasar's environment to provide fuel for star-formation or grow the stellar mass through mergers. This object challenges the paradigm of merger-induced AGN activity and the stage at which feedback is supposed to occur relative to the merger time scale.

In chapter 4, I present the results of the entire radio-loud sample. I find that the host galaxies of the quasars appear to be metal-poor relative to galaxies hosting AGN in the nearby Universe. For sources where we could measure the velocity dispersion and mass of the host galaxy, I find them to be offset from the local scaling relation, similar to 3C 298. The under-massive metal-poor galaxies indicate that they require significant growth from $z \sim 2$ to present day if they are to evolve into the most massive galaxies seen in the local Universe. Powerful outflows are detected in most objects, however only four show energy rates consistent with the prediction of AGN feedback. Galaxy-scale outflows line up with the projected extent of the radio jets in these systems; however, the jets are not doing any work on the outflows at the present time. If the jets were to drive the outflows, it would have had to happen in the past in very dense environments close to the SMBH. On the other hand, the outflows can be driven by either radiation pressure on dust or through a BAL type wind, and if the jets turned on at later times, they would proceed in the path of least resistance, along the path of the outflow. These results disagree with the typical assumption that type-1 quasar appears near the end of massive galaxy formation and that feedback occurs once the galaxies have assembled onto the local scaling relations.

In chapter 5, I outline future projects that address the evolutionary path of massive galaxy formation from z$\sim$ 2 to the present day. A consequence of the results presented in chapters 2 and 3 is that the galaxies harboring the most massive SMBH at z$\sim$ 2 need to go through substantial growth to increase their stellar mass and enrich their ISM. The first project looks at the gas reservoir in the CGM of these quasar host galaxies, to understand the amount of available gas and its transport into the quasar host galaxies to fuel future star formation. The project will also address the role of dry mergers from quiescent galaxies in growing the stellar mass of the quasar host galaxies.

A second project looks at the molecular gas reservoir in these systems, mainly searching for evidence of molecular outflows or putting stringent limits on the molecular gas mass in quasar driven outflow regions.

I then predict the state of the field in five years with the addition of James Webb Space Telescope, and ten years with the addition of the next generation large ground-based facilities such as TMT, GMT, EELT, and ngVLA. I also discuss future multi-messenger astronomy with the LISA spacecraft in helping understand the co-evolution of galaxies and SMBH in the distant Universe.

Chapter 2

Providing stringent star formation rate limits of z$\sim$2 QSO host galaxies at high angular resolution

2.1 abstract

We present integral field spectrograph (IFS) with laser guide star adaptive optics (LGS-AO) observations of z$\sim$2 quasi-stellar objects (QSOs) designed to resolve extended nebular line emission from the host galaxy. Our data was obtained with W. M. Keck and Gemini-North Observatories using OSIRIS and NIFS coupled with the LGS-AO systems, respectively. We have conducted a pilot survey of five QSOs, three observed with NIFS+AO and two observed with OSIRIS+AO at an average redshift of z=2.2. We demonstrate that the combination of AO and IFSs provides the necessary spatial and spectral resolutions required to separate QSO

emission from its host. We present our technique for generating a PSF from the broad-line region of the QSO and performing PSF subtraction of the QSO emission to detect the host galaxy emission at separation of $\sim$0.2$''$ ($\sim$1.4 kpc). We detect Hα narrow-line emission for two sources, SDSSJ1029+6510 ($z_{H\alpha}$=2.182) and SDSSJ0925+0655 ($z_{H\alpha}$=2.197), that have evidence for both star formation and extended narrow-line emission. Assuming that the majority of narrow-line Hα emission is from star formation, we infer a star formation rate for SDSSJ1029+6510 of 78.4 $M_\odot$ yr^{-1} originating from a compact region that is kinematically offset by 290 - 350 $km\,s^{-1}$. For SDSSJ0925+0655 we infer a star formation rate of 29 $M_\odot$ yr^{-1} distributed over three clumps that are spatially offset by $\sim$ 7 kpc. The null detections on three of the QSOs are used to infer surface brightness limits and we find that at 1.4 kpc from the QSO the un-reddened star formation limit is $\lesssim$ 0.3 $M_\odot$ yr^{-1} kpc^{-2}. If we assume typical extinction values for z=2 type-1 QSOs, the dereddened star formation rate for our null detections would be $\lesssim$ 0.6 $M_\odot$ yr^{-1} kpc^{-2}. These IFS observations indicate that while the central black hole is accreting mass at 10-40% of the Eddington rate, if star formation is present in the host (1.4 - 20 kpc) it would have to occur diffusely with significant extinction and not in compact, clumpy regions.

2.2 Observations

We used the near infrared integral field spectrographs OSIRIS (Larkin et al. 2006) on the Keck telescope and NIFS (McGregor et al., 2003) on the Gemini north telescope (program identification GN-2012B-Q-53) coupled with the observatories' laser guide star adaptive optics systems. We present K-Band spectra of 5 quasars at an average redshift of z $\approx$ 2.2 (angular size scale, 8.5 kpc per arcsecond) with an average total on-target integration time of 3600s. On each night we observed an A type standard star for telluric correction and flux calibration. Table 2.1 summarizes our observational parameters and setup.

Table 2.1 Observational summary of Keck OSIRIS and Gemini ALTAIR-NIFS observations.

QSO SDSSJ	R.A J2000	DEC J2000	Observation Date	Integration $N_{frames} \times s$	PSF FWHM $''$	Tip/Tilt sep ($''$)	Tip/Tilt r [mag]
085022.63+584315.0	08:50:22.63	58:43:15	2013Jan04	4x600	0.15	14.1	10.4
092547.47+065538.9	09:25:47.47	6:55:38.9	2013Jan08	6x600	0.13	6.2	13.0
100517.43+434609.3	10:05:17.50	43:46:10.9	2011Dec31	16x300	0.202	21.5	13.1
102907.09+651024.6	10:29:07.09	65:10:24.6	2011Dec30	12x300	0.177	43.8	13.8
212329.46-005052.9	21:23:29.46	-00:50:52.9	2012Aug06	6x600	0.11	0	16.4

2.2.1 Target Selection

We selected these QSOs from the fifth edition of the SDSS quasar catalog based on the seventh data release (Schneider et al. 2010). For this pilot survey we selected sources that would have optimal AO performance to aid in the PSF subtraction. Criteria for the Keck and Gemini North observations were: (1) all objects must be observable with the ALTAIR and Keck AO systems based on tip/tilt magnitude and separations (R mag $<$ 16.5 within 25$''$ for ALTAIR system and R mag $<$ 18.5 within 45$''$ for Keck-AO), and (2) objects must have redshift between 2.016 and 2.427 where Hα falls in the prime K-band wavelength regime ($<$ 2.2 μm). Using these constraints at K-band allowed only $\sim$30 observable QSOs. We made our final selection based on available tip/tilt stars that are bright and close in separation: one with on-axis tip-tilt source correction (R=16.4 mag), and four for off-axis tip-tilt correction. Table 2.1 contains all the information on the tip/tilt stars. All of our selected sources are Type 1 radio-quiet QSOs with 1.4 GHz flux $<$ 0.15 mJy (Becker et al. 1995) with no availible near-IR spectroscopy, making our sample less biased towards QSO hosts with high star formation rates. Host galaxies with high star formation rates presented in Alexander et al. 2010, Cano-Díaz et al. 2012 were pre-selected based on long slit spectra of the [OIII] 5007 Å line or far-IR observations.

2.2.2 Archival Data

For multi-wavelength analysis of our objects we include archival observations on our sources. Table 2.2 contains optical to near-infrared archival photometric information on our QSO sample, encompassing archival data from the SDSS for the optical magnitudes and 2MASS

for near-infrared. As of Data Release 10, SDSS has incorporated WISE and 2MASS photometric data into their catalog, made available in web format on the object explorer website that can be accessed through sdss3.org. In Table 2.3 we present photometry for the four WISE bands at 3.4μm, 4.6μm, 12μm and 22μm. All five sources are detected in the 3.4-12μm bands however only three sources have reliable photometry, where the other two suffer from confusion of flux from the bright nearby tip/tilt stars. Three sources are detected in the 22μm band, one is undetected and one doesn't have reliable photometry due to confusion; please see Table 2.3 for details on the individual sources. Two of our sources, SDSSJ1029+651 and SDSSJ2123-005 were observed with the Herschel space telescope's SPIRE instrument[1] in the 250μm, 350μm& 500μm bands. We downloaded the fully reduced level 2 maps from the Herschel data archive (http://irsa.ipac.caltech.edu/applications/Herschel/), we converted the maps from Jy/beam to Jy/pixel by dividing the maps by the beam size found in the SPIRE Handbook, available at herschel.esac.esa.int and applied standard aperture photometry over the beam size (17.6$''$, 23.9$''$, 35.2$''$) of the telescope in each of the bands at the optical location of the QSOs from Table 2.1. The two sources are undetected in all of the bands and we provide the three sigma limits in Table 2.3.

[1]PIs: D.Weedman, observation ID:1342270222 & H.Netzer, observation ID:1342270338

Table 2.2 SDSS & 2MASS photometry (Cutri et al. 2003) of the sources in our sample.

QSO	u	g	r	i	z	J	H	K
SDSSJ0850+5843	19.301	19.071	18.939	18.977	18.619	–	–	–
SDSSJ0925+0655	21.583	20.745	19.888	19.493	19.197	–	–	–
SDSSJ1005+4346	16.985	16.803	16.631	16.469	16.249	15.474	15.041	14.271
SDSSJ1029+6510	17.150	16.938	16.833	16.757	16.602	15.881	15.413	14.566
SDSSJ2123-0050	17.194	16.648	16.434	16.338	16.121	15.180	14.616	13.904

Table 2.3 WISE & Herschel photometry of the five sources in our sample.

QSO SDSSJ	W1 3.4μm mJy	W2 4.6μm mJy	W3 12μm mJy	W4 22μm mJy	SPIRE 250μm mJy	SPIRE 350μm mJy	SPIRE 500μm mJy
0850+5843	–[a]	–[a]	–[a]	$<$6.8	–	–	–
0925+0655	–[a]	–[a]	–[a]	–[a]	–	–	–
1005+4346	1.32	2.21	8.01	13.83	–	–	–
1029+6510	0.87	1.49	6.82	12.91	$<$21.8	$<$13.3	$<$16.5
2123-0050	1.48	2.37	9.82	23.85	$<$13.8	$<$8.67	$<$11.6

[a] No reliable photometry due to source confusion

2.3 Data Reduction

2.3.1 OSIRIS

The OSIRIS observations were reduced using the publicly available OSIRIS data reduction pipeline[2]. Dark frames were median combined to produce a master dark frame using the OSIRIS pipeline routine "combine frames". Each science and calibration frame then had the master dark subtracted from it and the following pipeline routines were performed: "adjust channel levels", "remove crosstalk", "clean cosmic rays", "extract spectra", "assemble data cube", "correct dispersion". For sky subtraction, each science frame had the nearest in time sky frame subtracted using the "scaled sky subtraction" routine that accounts for the temporal variability of the OH sky lines (Davies 2007). The science and telluric frames were stacked together using a 3σ mean clip algorithm in the "mosaic frames" routine to remove large bad pixels that occur from the "extract spectra" routine . A 1D telluric spectrum was then extracted from the highest signal-to-noise spaxels in the telluric cube using the "extract star" routine. Strong hydrogen absorption lines were masked using the "remove hydrogen lines" routine, and the blackbody of the star was subtracted using the "divide blackbody" routine. The spectra were normalized and used to correct for atmospheric absorption and the instrumental footprint in the mosaiced science frame. The final science data was flux calibrated using standard star observations that were taken closest in time, at similar air mass and were reduced in the same manner as described above.

[2]http://www2.keck.hawaii.edu/inst/osiris/tools/

2.3.2 NIFS

The NIFS observations were reduced using the Gemini NIFS IRAF reduction pipeline that operates within Pyraf [3]. Some modifications were applied to the standard pipeline and additional routines were written to match our science goals. For each night we reduced the Xe, Ar lamp observations to establish the wavelength solution for each of the targets using the Gemini NIFS Pyraf baseline calibration routine. Dark frames for the science observations were median combined and subtracted from each of the science and sky frames. The science, telluric, and sky frames were then reduced using the NIFS science reduction routine. The end result is a data cube which has been flat fielded, bad pixel masked and reformatted into a 3D cube, which was spatially re-sampled from the native spatial sampling of $0.1 \times 0.04''$ to square pixels with a size of $0.05''$. The science and telluric frames had the nearest sky frame in time subtracted, with OH emission line scaling between the sky and science frames. The centroids of the QSO and telluric stars were obtained through a 2D Gaussian fit to a spectrally collapsed image, and the dithered observations were shifted and stacked using a 3σ mean clipped algorithm. The 1D telluric star spectrum was extracted by averaging spatially over the highest signal-to-noise spaxels, its blackbody was subtracted, and the strong hydrogen absorption line were masked. The 1D telluric spectrum was then divided into the science cube to correct for atmospheric and instrumental absorption features.

[3] http://www.gemini.edu/sciops/instruments/nifs/data-format-and-reduction

2.4 Extraction of BH masses and PSF subtraction of the QSO

Using the SDSS spectra (Figure 2.1, left) we derive the bolometric luminosity (L_{Bol}) from the rest-frame 1450Å continuum using methodology presented in Runnoe et al. 2012. We obtain the black hole mass (M_{BH}) using equation (7) presented in Vestergaard and Peterson 2006, utilizing the 1350Å continuum value together with 1549Å CIV FWHM, derived by fitting a Gaussian profile using the curve_fit function that is part of the scipy package, written for python based on non-linear least squares routine. Table 2.4 contains the above information. Using our K-band QSO spectra (Figure 2.1, right side) we derive luminosity of the broad Hα emission line, black hole mass and the equivalent width (Table 2.5). We fit the line using a Gaussian profile which assisted in deriving the broad Hα luminosity, redshift and equivalent width. In deriving the line luminosity and equivalent width we integrate over $\pm 1.3\times$ the FWHM of the fitted profile. The black hole mass was then estimated using equation (6) from Greene and Ho 2005. The presented near infrared spectra were extracted from our data cubes using a spatial aperture of approximately the seeing halo.

2.4.1 PSF construction and subtraction

The broad Hα emission originates from gas located in a compact disk within the central few parsecs making this emission essentially point-like in our observations. We use spectral channels that confine the broad line emission for PSF construction. Our algorithm finds the highest signal-to-noise spectral channels that do not coincide with OH emission lines to be com-

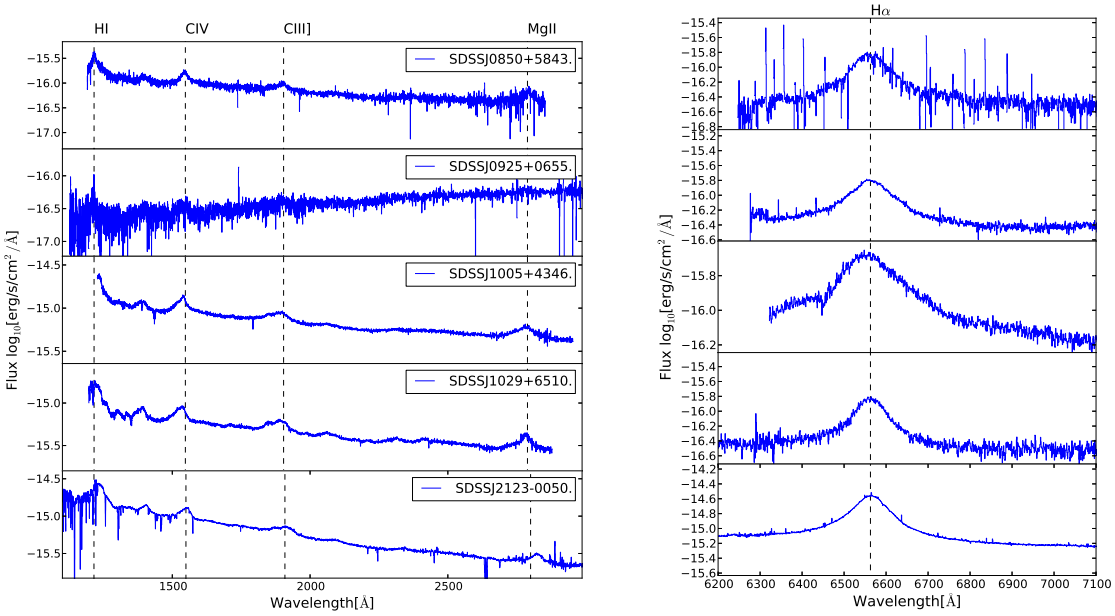

Figure 2.1 SDSS spectra of all the sources in our sample (Left). The SDSS wavelength range covers rest frame UV emission lines of QSOs at this redshift. Vertical dashed lines indicate emission from Lyα, CIV, CIII], MgII. Near-IR spectra are presented on the right side, where the broad Hα line is present. These were extracted from the data cubes, integrating over the spaxels within the seeing halo.

bined to create a master PSF image. Generally the selected PSF regions are 2.5-3 nm (10 - 15 spectral channels) in size and tend to sit near the peak of the broad Hα line. We hypothesised that the majority of the extended narrow line emission will be within 400km s^{-1} from the QSO's redshift, where the PSF has the highest signal to noise and the greatest potential for contamination from the NLR, so we also select spectral regions that are offset from the peak of the broad emission line (not including OH sky lines), that should have minimal contribution from extended narrow-line emission. We combine all spectral regions using a 3σ clipping routine, to mitigate contamination from the extended narrow-line emission. This way spaxels that do contain narrow emission would be weighted less since spectral channels offsets by 2000 - 3000km s^{-1} are less

Table 2.4 QSO General properties

QSO	z_{UV}	L_{Bol} erg $s^{-1}\times10^{47}$	M_{BH} $M_\odot\times10^9$	Eddington Ratio
SDSS0850+5843	2.211	0.216±0.029	1.75±0.13	0.098
SDSS0925+0655	2.197	0.059±0.008	...	...
SDSS1005+4346	2.086	1.98±0.06	10.2±0.4	0.14
SDSS1029+6510	2.163	1.39±0.06	8.0±0.5	0.14
SDSS2123−0050	2.261	2.57±0.07	8.5±0.5	0.24

Column 3 is the bolometric luminosities (L_{Bol}=4.2×L_{1450}) obtained from rest frame 1450Å continuum with corrections from Runnoe et al. 2012. Column 4 is the black hole mass obtained from rest frame 1549Å CIV emission line (Vestergaard and Peterson 2006). Column 5 is the ratio of the bolometric luminosity to the Eddington luminosity obtained from the measured black hole mass.

Table 2.5 Properties of Broad-line Hα emission

QSO	$z_{H\alpha}$	$L_{H\alpha}$ erg s^{-1}	M_{BH} $M_\odot\times10^9$	Equivalent Width (Å)
SDSS0850+5843	2.212	3.16×10^{44}	1.49±0.38	384±6
SDSS0925+0655	2.196	3.58×10^{44}	1.94±0.5	352±1
SDSS1005+4346	2.105	7.42×10^{44}	5.43±1.47	230±1
SDSS1029+6510	2.183	3.12×10^{44}	0.90±0.22	289±2
SDSS2123−0050	2.281	3.84×10^{45}	5.0±1.41	281±1

Column 3 is the luminosity of the broad Hα line. Column 4 is black hole mass derived from Hα FWHM and its luminosity as in Greene and Ho 2005. Column 5 is equivalent width of the broad Hα line.

likely to contain NLR. The end result is a 2D image of our observed PSF that gets normalized to the flux at the peak pixel. We then go through individual channels in our data cube, scale the image to the maximum value of the PSF at the particular channel and subtract the image. This routine provided the best residuals post PSF subtraction. Some studies have additional steps with PSF construction, by initially fitting and subtracting the nuclear continuum with a low or-

der polynomial (Inskip et al. 2011). The purpose of the linear fit is to remove any continuum emission from the host galaxy. In our work, extensive studies of the final PSF subtracted cube using both methods does not reveal a continuum emission from the host galaxy at the 3σ level (average K mag > 20.9), hence we decided not to include this additional step in our QSO PSF construction routine since it adds at least 1.2 times more noise in the PSF subtracted cubes.

To test the quality of our PSF subtraction, we constructed radial profiles at different wavelength channels, before and after PSF subtraction, to verify whether the final cube had the central core and seeing halo successfully removed. Figure 2.2 shows the results of these tests for two of our targets. The green and blue radial profile curves are constructed from a spectrally-summed image which contains both broad and narrow Hα emission ($\Delta\lambda$ =2.5 nm or Δv=1142km s^{-1}). The green curve is constructed from the data cube before PSF subtraction, the blue is after the PSF is removed and the red curve is constructed from just the PSF image ($\sim \Delta\lambda$ =2.5 nm, spectrally offset 1-5nm). The points are constructed by taking an average in an annulus with Δr=0.1$''$ at a range of separations from the centroid of the QSO. The radial profile in the post PSF subtracted data cube (blue curves) have little slope and significantly less flux, and do not strongly correlate with the general shape of the green and red curves. This demonstrates that the PSF subtracted data has a significant portion of the QSO flux removed, with only the inner 0.2$''$ being strongly dominated by noise from PSF subtraction. Averaging over the data cube along the spectral axis, we find that generally within 0.2$''$ the QSO still contributes to about 10-20$\%$ of the total data counts, while only 2-5$\%$ outside 0.2$''$. As expected, observations with the smallest PSF FWHM showed the best post PSF subtraction data cubes producing the best contrast. However it should be noted that leftover QSO continuum/BLR light does not affect

measured values derived from narrow line emission, since they are derived by fitting the line and any underline continuum left over from PSF subtraction simultaneously, at which stage the continuum contamination can be calculated.

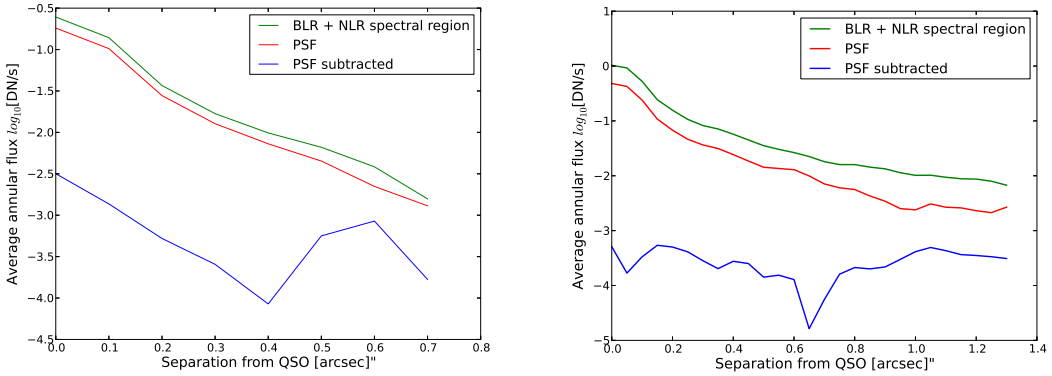

Figure 2.2 Radial profiles for SDSSJ1029+6510 (left) and SDSSJ0925+0655(right). Green and blue radial profile curves are constructed from spectrally integrated images which contain both broad and narrow Hα , while the red curve is constructed from the PSF image. The blue curve is constructed in the same spectral regions as the green curve however post PSF subtraction, indicating that our PSF removal technique is capable of removing both the AO corrected core as well as the seeing halo.

2.5 Results

To find narrow line emission we searched all of the individual $\sim$ 3,000 spaxels in each of the cubes using an algorithm that searches for flux above a predefined threshold, in combination with visual inspection of each cube. When a line feature is identified we calculated the signal-to-noise by obtaining the standard deviation in the surrounding spatial and spectral pixels, and divided it into the fitted peak of the emission line. For cases where a faint emission feature is found we bin the data using nearby spaxels to increase the signal-to-noise to distinguish between a faint noise spike versus real emission. We confirm a detection if the peak of the emission line is

greater than 3σ from the neighboring spaxels and the spectral width is greater than the intrinsic instrumental width of 0.35 nm and 0.20 nm for OSIRIS and NIFS respectively. For bright noise spikes we wrote a routine that parses through the cube and removes them if their counts are 5σ or higher from the surrounding region (one spaxel in each spatial direction, and 2 spectral channel two the left and right of the spike), some of these features have a FWHM greater than instrumental but given their spatial isolation and significantly higher counts than the surrounding region we quantify them as being "noise spikes". Majority of them are associated with locations of OH sky lines, hence we believe these spikes are residuals caused by sky subtraction. This routine also confirms faint extended structure in the case of SDSSJ0925+0655 to be real rather than a combination of separated noise spikes. After searching through the five observed data cubes we identify narrow line emission in two of the systems, SDSSJ1029+6510 and SDSSJ0925+06. For the given QSO redshift, the identified emission lines are likely narrow Hα . If [NII] 6584Å were assumed instead the flux ratio between it and undetected Hα would be $\gtrsim$30 in some regions, this is well beyond what has been found in other galaxies (e.g, Kauffmann et al. 2003). Once an Hα line is identified we searched for [NII] 6548,6584 Å and [SII]6718,6733 Å at a similar velocity offset from the broad Hα line. The detected narrow Hα emission lines all lie within 600 km s^{-1} from of their respective QSOs broad Hα redshift, however the full spectral axis in each spaxel was examined for potential narrow emission lines that could be associated with structure surrounding our QSOs. All of the line fits were done with a single Gaussian function using the non-linear least squares routine provided through scipy. The initial guess for the peak is the value at the location of the maximum flux, the initial guess on wavelength offset is the location of the maximum flux, and initial guess on σ was 80 km s^{-1} , no further constraints were

put on the parameters. The radial velocity map is derived from the measured line offset in each spaxel relative to the redshift of the broad Hα line. The velocity dispersion map of the gas is derived after removing the instrumental width in quadrature from σ at each spaxel. Velocity dispersion map is used to dictate the region over which the spectra need to be summed to derive total flux.

2.5.1 OSIRIS: SDSSJ1029+6510

Figure 2.3 (panel I) shows the K-band image of the SDSSJ1029+6510 QSO from the collapsed data cube (1.99-2.4 μm). Figure 2.3 (panel II) and Figure 2.3 (panel III) show the 2D kinematics of the extended narrow line emission relative to the broad Hα emission and the spectra of the individual components.

The PSF subtracted data cube reveals three extended narrow line emission regions, labeled A, B and C in Figure 2.3 (panel II). These emission-line regions have a blue-shifted velocity offset of 10-500 km s^{-1} with respect to broad Hα emission, and a maximum projected separation of $\sim 0.6''$(4.2 kpc) from the QSO. We bin the individual spaxels in regions A and C to detect a hint of Hα emission at a signal-to-noise of 3.1 and 2.1, respectively. Individual spaxels in region B reach a signal-to-noise of $\gtrsim$2, with the central 3 pixels reaching a signal to noise $\gtrsim$ 7. In Table 2.6 we present the extracted emission-line properties of the individual regions. Using [N II] & Hα we adopt the the line ratio separation between star formation and AGN to be at log([NII]/Hα)=-0.5 in the HII diagnostic or "BPT" (Baldwin et al., 1981) diagram (Figure 2.5). The majority of the objects in the region log([NII]/Hα)<-0.5 are star forming galaxies (Kauff-

mann et al. 2003, Kewley et al. 2001, Groves et al. 2006). While low metallicity regions ionized by an AGN can be a contaminant at these line ratios, all of the QSOs in our sample (particularly SDSSJ1029+6510) show strong UV emission lines in CIV,SIV+OIV and MgII (Figure 2.1) that are typical of solar to super-solar metallicity QSOs; hence for this particular system we are not concerned about low metallicity contamination in the region log([NII]/Hα)<-0.5. Our limits allow us to discard shock contributions to the emission for regions A and B, line ratios of emission due to shocks tend to reside in log([NII]/Hα)>-0.4 on the BPT diagram (Allen et al. 2008) from a gas that is moving at the recorded velocities of our extended emission. Based on the ratio of log([NII]/Hα) for A, this region can reside in the transition zone between AGN/SF, assuming no extinction, the star formation rate limit for Hα flux in region A is 11.0$\pm$2.3 $M_\odot$ yr^{-1} using the Schmidt-Kennicutt law ($SFR_{H\alpha} = \frac{L_{H\alpha}}{1.26\times10^{41}}$, Kennicutt 1998), this is a limit because AGN photo ionization contribution will increase the observed flux, hence the star formation rate is lower than what is quoted. Region B is located well in the star formation position on the BPT (log([NII]/Hα)<-1.5) diagram with a star formation rate limit of 67.4$\pm$5.7$M_\odot$ yr^{-1} . Region C resides well inside the AGN component of the diagram, and therefore is likely narrow line emission from the QSO, at a projected radial distance of $\sim$2.8 kpc.

Table 2.6 SDSSJ1029+6510: OSIRIS-AO Narrow Emission-line Properties

Component	$F_{H\alpha}$	$F_{[NII}$]6584Å	[NII]/Hα	SFR $M_\odot$ yr^{-1}	V_r km s^{-1}	V_σ km s^{-1}	M_{dyn}
A	4.22 $\pm$ 0.75	<0.951	<0.2310	$\cdots$	-778$\pm$16	163$\pm$36	$\cdots$
B	22.6 $\pm$ 1.92	<0.71	<0.0319	67$\pm$6	-355$\pm$19	34$\pm$12	0.9$\pm$0.07
C	4.14$\pm$ 1.95	2.34$\pm$0.73	-0.24$\pm$ 0.32	$\cdots$	-39$\pm$42	36$\pm$40	$\cdots$

Column 2 and 3 units are erg s^{-1} cm^{-2} $\times$ 10^{-17}. Column 8 is in units of $M_\odot \times 10^9$.

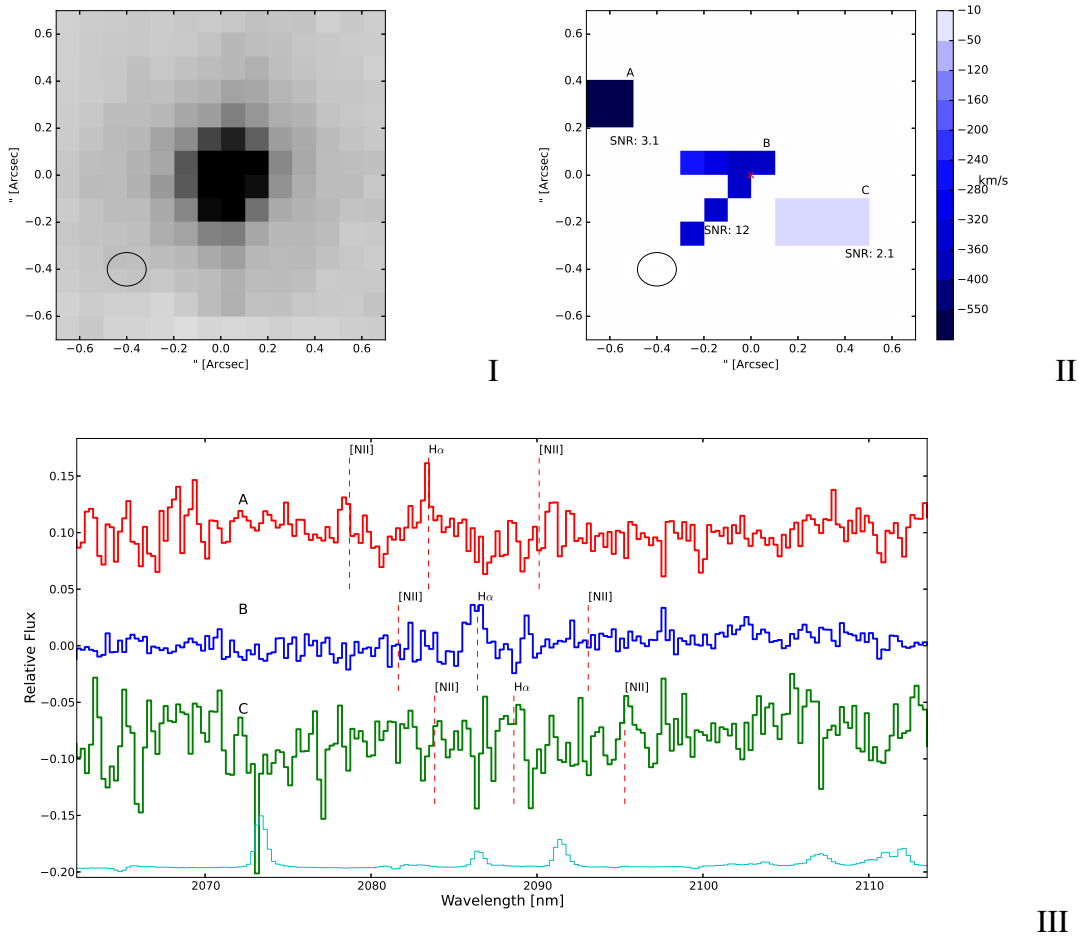

Figure 2.3 Upper left: K-Band image of SDSSJ1029+6510 from the collapsed OSIRIS LGS-AO data cube using 0.1″ spatial sampling. Upper right: radial velocity map (km s^{-1}) of extended narrow Hα emission detected post-PSF subtraction. Radial velocity measurements are obtained by fitting narrow Hα emission line in the individual regions with a Gaussian function. The spatial resolution of each observation is reprsented by the ellipse in the lower left corner obtained through 2D Gaussian fitting to the PSF image. Bottom: Averaged per spaxel spectra of each of the labeled components with some relative flux offset. The light blue curve shows the wavelength dependence of the noise and OH sky emission. Dashed red lines represent the expected wavelength of narrow emission lines. North is up, east is left.

2.5.2 NIFS: SDSSJ0925+0655

Figure 2.4 (panel I) is a K-Band image of the QSO constructed by summing the flux across the entire data cube (1.99-2.4 μm). Figure 2.4 (panel II and III), show the 2D kinematics

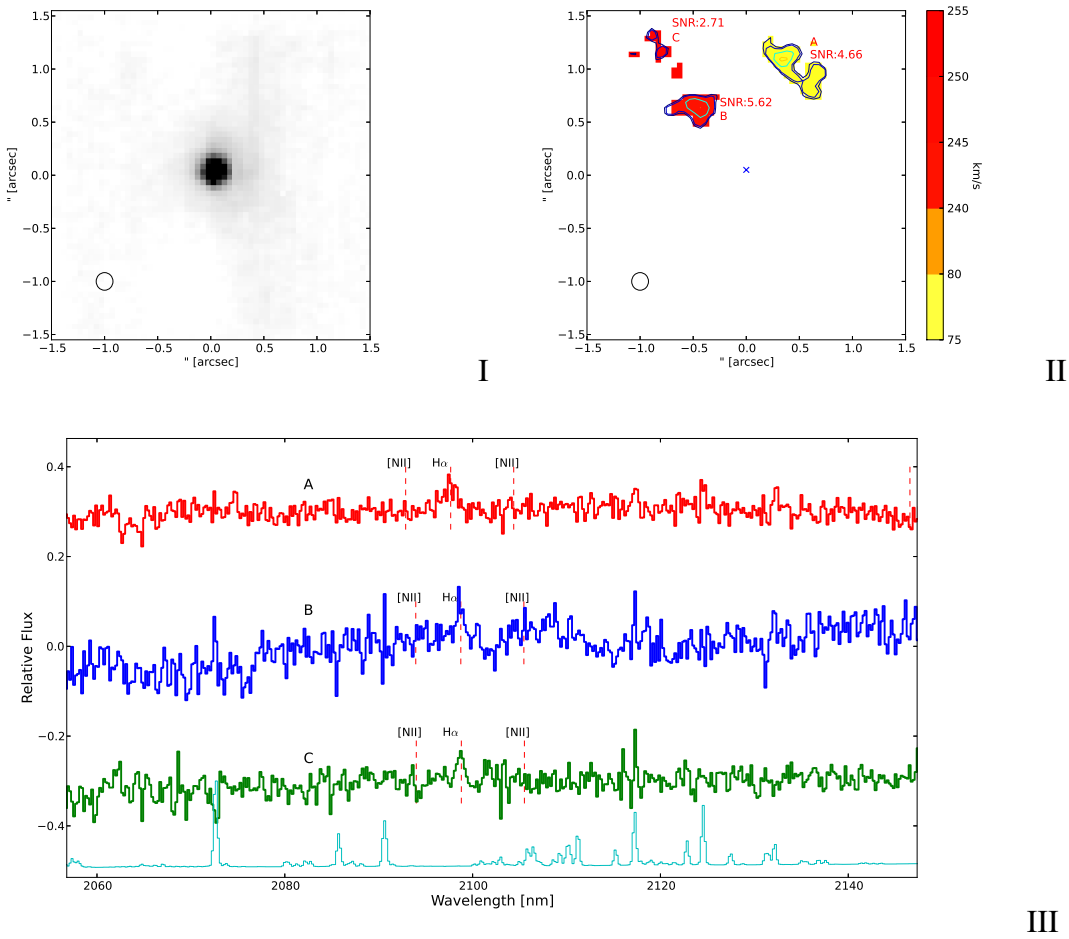

Figure 2.4 Upper left: K-Band image of SDSSJ0925+0655 from the collapsed NIFS Altair AO cube using 0.05″ spatial sampling. Upper right: PSF subtracted image showing resolved extended Hα narrow line emission in contours that stretch from 1.8σ-5σ and the velocity map (km s^{-1}) obtained from fitting the Hα line in the individual regions using a Gaussian function. The spatial resolution of each observation is represented by the aperture in the lower left corner obtained through 2D Gaussian fitting to the PSF image. Bottom: Averaged per spaxel spectra of each of the labeled components with some relative flux offset. The light blue curve shows the wavelength dependence of the noise and OH sky. Dashed red lines represent the expected wavelength of narrow emission lines. North is up, east is left.

of the extended narrow line emission relative to the redshift of the broad Hα emission and the spectra of the individual components, respectively. The post-PSF subtracted data cube reveals resolved narrow Hα emission originating from three distinct regions (A, B, and C), that are

both spatially offset (0.5″-1″) and redshifted (80-250 km s^{-1}) from the QSO, see Table 2.7 for extracted parameters on individual regions. We bin by 0.25″×0.25″ for each of these regions to increase the signal-to-noise for kinematic analysis. Using ([N II] & Hα) ratio diagnostic, we put the separation between star formation and AGN at log([NII]/Hα)=-0.5, with star formation being the dominant photoionization mechanism in log([NII]/Hα)<-0.5 (see, section 2.5.1 for further discussion). Limits on the log([NII]/Hα) ratio places regions A,B and C inside the star formation region on the BPT diagram. Our limits allow us to discard shock contributions to the emission for regions A,B, and C, line ratios of emission due to shocks tend to reside in log([NII]/Hα)>-0.4 on the BPT diagram (Allen et al. 2008) from a gas that is moving at the recorded velocities of our extended emission. Using the Schmidt-Kennicutt law (Kennicutt 1998) we obtain un-reddened upper limit star formation rates of 13±2.3, 12.0±0.5, 4.0±0.4 M$_\odot$ yr^{-1} for regions A, B and C, respectively. Assuming these three clumps have virialized we obtain dynamical masses of 8.7, 1.0, 0.3 ×10^{9}M$_\odot$ (Table 2.7 using the standard virial mass equation $M_{virial} \approx \frac{5R\sigma_r^2}{G}$)

Table 2.7 SDSSJ0925+0655: NIFS-AO Narrow Emission-line Properties

Component	$F_{H\alpha}$	$F_{[NII]}$6584Å	[NII]/Hα	SFR	V_r	V_σ	M_{dyn}
				M$_\odot$ yr^{-1}	km s^{-1}	km s^{-1}	
A	4.33±1.22	<0.245	<0.0565	13±2.3	88.4±19.6	103.1±19.3	8.7±4.1
B	4.11±0.163	<0.58	<0.1410	12±0.5	242.6±15.4	37.7±14.5	1.0±0.8
C	1.20±0.126	<0.148	<0.1222	4±0.4	250.5±15.6	42.44±14.7	0.3±0.05

Column 2 and 3 units are erg s^{-1} cm^{-2} × 10^{-17}. Column 8 is in units of M$_\odot$ × 10^9.

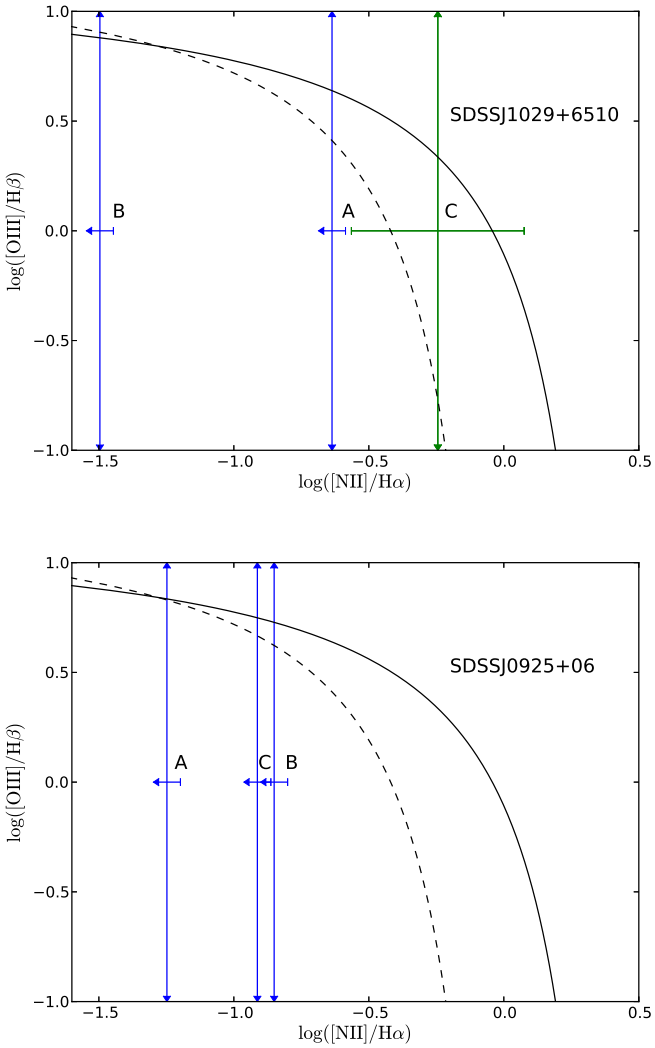

Figure 2.5 Line ratio diagnostics for our detected narrow-line emission using the standard BPT diagram. Limits for log([OIII] /Hβ) and log([NII] /Hα) for SDSSJ1029+6510 regions A,B & C (TOP) and regions A,B, & C for SDSSJ0925+0655 (BOTTOM) are over-plotted. Dashed curve represents the empirical boundary between star formation and AGN from SDSS (z<0.1) by Kauffmann et al. 2003. The solid curve is the theoretical star formation boundary from Kewley et al. 2001. Our limits indicate that the narrow-line emission that we detect is not strongly dominated by AGN or shocks, with the possible exception of the low-signal to noise region C in SDSSJ1029+6510.

2.5.3 Null detections: SDSSJ1005+4346, SDSSJ2123-0050 & SDSSJ0850+5843

The remaining three targets reveal no narrow-line Hα emission offset spatially or spectrally from the QSO. Null detections may be due to two possibilities: (1) these sources have heavy extinction azimuthally around the QSO $\gtrsim$1 kpc; and/or (2) these sources have sufficiently low star-formation rates that reside below the sensitivity limit of these observations.

We perform a Monte-Carlo simulation in which we generate star forming regions with narrow-line Hα emission surrounding the QSO at various spatial separations. The purpose of this simulation is to find the limiting flux (and unreddened star-formation rate limits) of our observations and determine how our PSF removal techniques affect our sensitivity versus distance from these QSOs. For our simulations, individual star-forming regions occupy $0.2'' \times 0.2''$ in the OSIRIS data cube and $0.25'' \times 0.25''$ in the NIFS data cube, with each spaxel containing a spectrum consisting of an emission line resembling narrow Hα with a fixed full width at half maximum of 80 km s^{-1} (not convolved with an instrumental profile). We select a FWHM of 80 km s^{-1} to match the widths of some of our detected extended narrow line emission, to further test their validity. In a given data cube the star forming regions have a spatially uniform flux, the integrated flux over all the simulated regions vary between cubes. We insert these regions uniformly surrounding the QSO in a cross shape to resemble resolved extended structure, which ranges from $0.1''$ to $1.5''$ in separation from the QSO in the NIFS data cubes and $0.1''$-$0.7''$in the OSIRIS cubes. The star forming regions are always centered on the quasar whose position we obtain by fitting a 2D Gaussian to an image of a collapsed data cube along the spectral axis. The

spacing between the star forming regions is $0.1''$ to allow signal-to-noise estimates surrounding each individual region. We vary the star formation rates from 0.5 $M_\odot$ yr^{-1} to 40 $M_\odot$ yr^{-1} in each of the narrow-line emission regions. For the OSIRIS data, we insert the simulated star forming regions into a data cube that is created by running the extract spectra routine that simply transforms the two dimensional data into a 3D cube. For the Gemini data we run the standard iraf reduction pipeline that extracts the 2D spectra and constructs the 3D data cubes, into which we insert the star forming regions. We then process the data cubes through the rest of the reduction pipeline as described in §2.3. Finally we run our PSF subtraction routine on the reduced data cubes as described in §2.4. We attempt to recover each of the narrow-line Hα emission regions that were artificially inserted. Just as for the real data, emission must be detected with a minimum of 3σ confidence, and emission lines must have a FWMH greater than the instrumental width.

Recovered star-forming regions with minimum star-formation rates at various angular separations are presented in Figures 2.6 and 2.7, and fluxes of Hα from SDSSJ0925+0655 and SDSSJ1029+6510 regions A,B, and C are over-plotted for comparison. In general we find that our data reduction procedure is not the main factor for missing narrow Hα flux; the dominant effect is the sensitivity of the detector and PSF removal within $0.2''$ from the QSO. At separations $> 0.2''$, limiting star-formation rates are an average of 1.4 $M_\odot$ yr^{-1} (0.7×10^{-17}erg s^{-1} cm^{-2}) integrated over a star-forming region for the NIFS instrument and 1.5$M_\odot$ yr^{-1} for OSIRIS. This translates to 0.32$M_\odot$ yr^{-1} kpc^{-2} and 0.53$M_\odot$ yr^{-1} kpc^{-2} in the NIFS and OSIRIS data cubes respectively.

For SDSSJ1029+6510, we show the integrated flux of region B as well as its individual

components in Figure 2.6, and find they are detected without binning. These simulations and the limiting fluxes for both of these sources indicate low Hα flux at near and far angular separations from the QSO. For SDSSJ0925+0655, fluxes of the observed components sit well above the star formation distribution (Figure 2.7), and in principle we are able to detect fainter emission at smaller separations. The other three QSOs do not show any signs of Hα narrow-line emission.

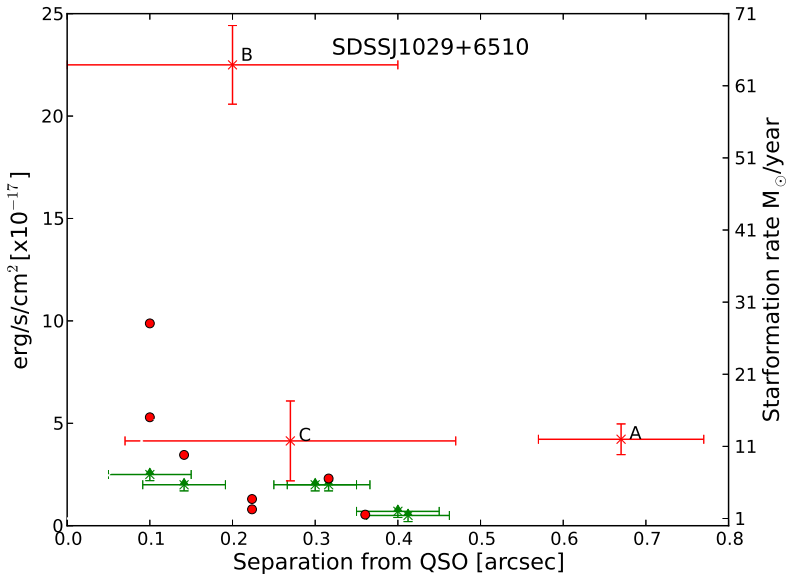

Figure 2.6 Limiting integrated flux in a $0.2''\times0.2''$region that was recovered at various separations from the QSO in our Monte Carlo simulation from the OSIRIS observations of SDSSJ1029+6510 (green). Fluxes and distribution of features A, B, C (light red) from Figure 2.3 are over plotted. In addition, flux from individual spaxels of region B are plotted in dark red. The three inner spaxels surpass the $0.2''\times0.2''$ box flux limit, while integration of the additional 4 outer spaxels builds a spectrum with a signal-to-noise that is significantly above the noise floor. Note: although the spatial size of region B is greater than $0.2''\times0.2''$, 90% of the flux sits in the central 3 spaxels, who individually contain a signal to noise ratio > 3.

We use the bolometric luminosities of our sources to make estimates of dust extinction. The Bolometric luminosities of our sample all sit near 1×10^{47}erg s^{-1} cm^{-2}, the maximum value for a z$\sim$2 QSO is around 1×10^{48}erg s^{-1} cm^{-2} as has been found by studies such as Croom

et al. 2009. This limit only allows us to correct for 2.5 magnitudes of extinction at 1450Å , so the limiting star formation rates get as large as 2.03 $M_\odot$ yr^{-1} ($0.5M_\odot$ yr^{-1} kpc^{-2}) or 2.2 $M_\odot$ yr^{-1} ($0.8M_\odot$ yr^{-1} kpc^{-2}, using a Small Magellanic cloud extinction curve from Gordon et al. 2003) for NIFS and OSIRIS respectively (see §2.6.1, 2.6.2). Note that for SDSSJ0925+0655 the limits may be higher as the QSO is intrinsically redder than the rest of our sample (see §2.6.2). We acknowledge that the dust in these scenarios is uniformly distributed, hence the same dust properties that we find along the line of sight to the QSO are elsewhere in the galaxy. Most studies that quote star formation rates give them integrated over some angular scale, typically the beam size of their instrument if the sources they are referencing are not resolved. At the angular resolution of our observations we are capable of resolving a typical z$\sim$2 galaxy with an angular scale of $\sim 1''$. Integrating these limits over a $1''$ box we obtain for NIFS: $22M_\odot$ yr^{-1} ($33M_\odot$ yr^{-1} with maximum dust extinction), OSIRIS: $37M_\odot$ yr^{-1} ($54M_\odot$ yr^{-1} with maximum dust extinction). These limits are a sum of the lowest flux that we detected around the QSOs in a $1''^2$ box in our simulations with the addition of possible dust obscuration. We believe these are hard limits on the upper value of the star formation rate in these host galaxies. Derived SFR limits include contamination from dust in the AGN. There is a possibly that most of the dust is surrounding the nuclear region rather than distributed in the host galaxy. Archival WISE photometry of our sources (Table 2.3) shows that 3 of our sources are detected at 22μm(rest frame $\sim 7\mu$m), all of the sources are detected in the other 3 WISE bands that range from 1-3.75 μm at an average redshift of z=2.2, however only 3 sources have reliable photometry due to confusion of flux from the nearby bright tip/tilt stars. For the sources that were detected at an observed wavelength of 22μm we find that the average flux density is 16.8mJy indicating that

the dust is AGN heated (Rowan-Robinson 1995). Limits closer to the value with minimum dust ($22M_{\odot}$ yr^{-1} for NIFS and $37M_{\odot}$ yr^{-1} for OSIRIS) may be more realistic, as some previous studies of dust in type-1 luminous QSOs near z$\sim$2 have found a number of sources with very little (A_V <0.01) to no extinction (see, Fynbo et al. 2013).

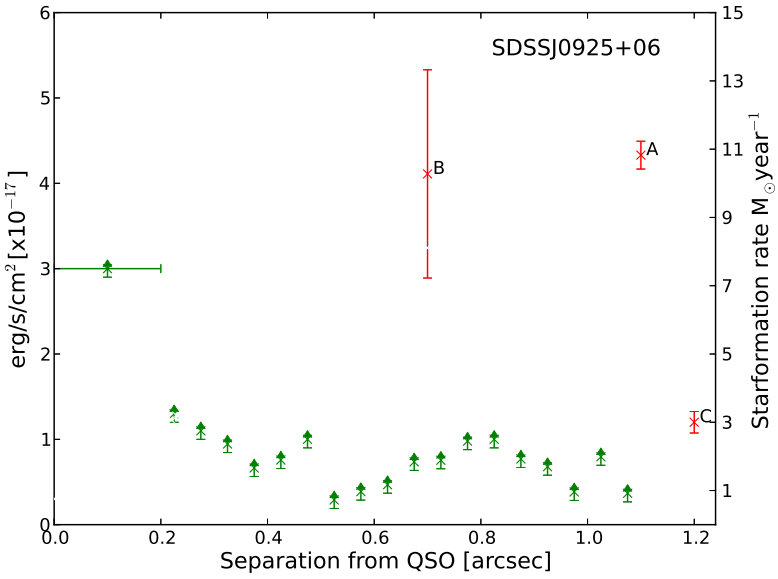

Figure 2.7 Limiting integrated flux in a $0.25'' \times 0.25''$region that was recovered at various separations from the QSO in our Monte Carlo simulations from the NIFS observations of SDSSJ0925+0655 (green). Integrated fluxes of features A, B, C (red) from Figure 2.4 are over-plotted.

2.5.4 Unresolved QSO narrow line region emission

Examining QSO spectra extracted over the PSF halo (Figure 2.1, right side) we do not detected any unresolved narrow line region emission in any of our sources. We find that generally the spectra are well fitted with a single Gaussian profile and inclusion of narrow emission is only required for the case of SDSSJ1029+65 due to narrow Hα emission associated with star

formation within $0.2''$ of the QSO. We place a flux limit of 3-4$\times10^{-17}$ erg s^{-1} cm^{-2} which converts to 1-1.5$\times10^{42}$ erg s^{-1}, assuming the NLR emission line has a FWHM of 80 km s^{-1} .

2.6 Discussion

There are two explanations for the null narrow-line Hα emission detections for three of the sources in our sample. This could be caused simply by the lack of star formation and/or significant extinction in the host galaxy. We argue that the main reason we do not see a significant amount of narrow Hα is likely due to the lack of star formation rather than extinction. Multi-wavelength observations can help estimate the amount of obscuration that is present in the galaxy due to dust. Using available multi-wavelength data we find that our sources do not contain sufficient amounts of dust to cause the observed Hα limits. The QSOs in our sample are all luminous type-1 AGN representing some of the most powerful QSOs at z$\sim$ 2. As we will argue in the following sections, even a small dust correction to these systems will increase the bolometric luminosities of our objects above the observed values at this redshift. This indicates that the majority of QSOs in our sample are hosted inside galaxies that are either transitioning from star forming to quenched galaxies or already reside in quiescent galaxies.

2.6.1 SDSSJ1029+6510

The host galaxy of this object shows compact vigorous star formation within 2 kpc from the QSO. The rest of the galaxy seems to show no narrow Hα which we attribute to low star formation rates. SDSSJ1029+6510 is the second most powerful QSO in our sample with a

bolometric luminosity of $1.39\pm0.06 \times 10^{47}$erg s^{-1}(Table-2.1), in addition to the second longest observation time in our sample. Note that some of the emission in individual spaxels of region B are at the 3σ level, near the limit of our observations. The ratio of log([NII]/Hα) < -1.5 is located in the HII star formation portion of the diagram (Figure 2.5) for region B making it a strong candidate for star formation with a formation rate of 67.4 ± 5.7M$_\odot$ yr^{-1} . This indicates rapid star formation within 2kpc of the QSO.

For region C, a ratio of 0.57 ± 0.3 for log([NII]/Hα) puts this source partly in the AGN ionization region of the diagram (Figure 2.5), and detection of [NII] emission with higher signal to noise than Hα suggests this emission is due to the AGN. Lastly for region A, the measured ratio of log([NII]/Hα)=-0.6 places it partially inside the star-formation region on the diagram.

This source has a lack of extended star-forming regions, with 90% of the star formation activity within 2 kpc from the QSO. This is in stark contrast to other resolved host galaxies in Inskip et al. 2011, Cano-Díaz et al. 2012 and Alexander et al. 2010, which have extended star forming regions over several kiloparsecs with star formation rates of $\sim$100 M$_\odot$ yr^{-1} . Our limiting flux simulations indicate that we should detect star formation rates as low as 1.4 M$_\odot$ yr^{-1} or down to a flux level of 0.6-0.8$\times10^{-17}$erg s^{-1} cm^{-2}, at separations $>0.2''$ from the QSO. Instead, we detect two "streams" (region B at SNR$>$3) of narrow Hα and nothing else significant around it (regions A and C are $\sim 3\sigma$). This indicates that the surrounding ($>$2 kpc) regions have narrow Hα flux that is below the sensitivity of the instrument.

Dust can cause extinction of Hα flux by re-radiating it at longer wavelength. QSOs in early stages of evolution are thought to be heavily obscured. After the AGN inputs energy/momentum during the “blow out" phase, gas and dust can get pushed out allowing the

AGN & galaxy to be detected in the optical, which otherwise would be obscured. Observations at other wavelengths can provide clues about the level of obscuration. A strong detection in the far-IR can indicate dust heating due to UV radiation from recent birth of massive stars. This would indicate that some portion of the UV radiation is absorbed (suppressed) and re-emitted at longer wavelength. QSOs that show reddening in their rest-frame UV spectra are good candidates for systems with a considerable level of obscuration, including a number of systems with indicators of outflows through blue shifted broad absorption lines in their rest-frame UV spectra, or broad blue-shifted components in the 500.7nm [OIII] emission line, indicating that some of these systems might be in the “blow-out" stage (Farrah et al. 2012; Urrutia et al. 2012).

For the case of SDSSJ1029+6510 we are able to put some constraints on the level of obscuration from both far-IR photometry and rest-frame UV-spectrum. This QSO was observed as part of a program with the Herschel space telescope to target some of the brightest optical QSOs with the SPIRE instrument. Examining the archival data we find that at the optical position of the QSO nothing is detected above 3σ level in the 250 μm, 350μm, and 500μm bands. The flux density limits are ($\sim$10mJy, see Table 2.3), indicating that this QSO's host galaxy is not in a star-burst phase ($L_{ir} < 10^{13} L_{\odot}$). The rest frame UV spectrum obtained from SDSS shows (Figure 2.1) a continuum slope typical of a type 1 un-obscured QSO (steep blue continuum), and a bolometric luminosity of 1.39×10^{47}erg s^{-1} (Table-2.4), which is about an order of magnitude above the average QSO bolometric luminosity. Any correction for dust will start pushing the bolometric luminosity beyond the typical value for bright QSOs at z$\sim$ 2 ($\sim 10^{48}$erg s^{-1}). Assuming we need to correct an order of magnitude of flux at rest frame wavelength of 1450Å due to dust we would only push the limiting star formation rate to 0.7 $M_{\odot}$ yr^{-1} kpc^{-2} (using a Small

Magellanic cloud extinction curve from Gordon et al. 2003), not sufficient to explain the lack of Hα flux. We therefore favor the low star formation rate model as the main explanation for the observed Hα flux in the case of SDSSJ1029+6510 at separations greater than 2 kpc.

2.6.2 SDSSJ0925+0655

The extended Hα emission surrounding SDSSJ0925+0655 is a strong candidate for active star formation. The ratio of log([NII]/Hα) for region A is within the star formation region on the diagram (Figure 2.5) while our limits on regions B and C place them near the ambiguous regions between star formation and AGN. The total flux from all these implies an integrated star formation rate of 29 ± 2.4 $M_\odot$ yr^{-1} . The detected narrow Hα emission regions are compact ($\sim$2kpc) and we only detect narrow Hα in these three regions. In other regions of the data cube we are able to reach a sensitivity limit of 0.8×10^{-17}erg s^{-1} or a star formation rate of 1.4 $M_\odot$ yr^{-1} at separations $\gtrsim 0.2''$ from the QSO. All of the detected regions are at separations $\gtrsim$ $0.5''$ (4 kpc). This implies the narrow Hα flux sits below the sensitivity of the detector at separations between 1.4 to 4 kpc. We propose that the primary reason for lack of Hα flux is either from star formation halting, or from obscuration due to dust in the host galaxy (as introduced in the §2.6.1). The bolometric luminosity (5.9×10^{45}erg s^{-1}) of this QSO as calculated from the 1450Å continuum is about an order of magnitude below the average value of a QSO at this redshift, due to the continuum being heavily reddened. However the broad Hα emission of this source agrees with the rest of the objects in our sample (similar equivalent width and luminosity, see Table 2.4) that do not show any signs of reddening in their rest-frame UV spectra (see Figure 2.1 and Table 2.5). The average bolometric luminosities of our sample is 1.24×10^{47}erg s^{-1}(see

Table 2.4). The agreement between broad line Hα properties (velocity dispersion & intensity) hints that the bolometric luminosity should be consistent with other members of our sample. As found in Fynbo et al. 2013 most reddened QSOs are red due to dust in their host galaxies rather than the inter-galactic medium or dust inside the Milky Way. For this source we estimate the amount of reddening by invoking the condition that the bolometric luminosity should be at the average value for a QSO with such a strong broad Hα emission (at least $\sim 3\times10^{46}$erg s^{-1}). This implies that the flux at 1450Å needs to be boosted by $10^{0.94}$ implying that $A_{1450} = 2.35$. Using extinction curve from Gordon et al. 2003 assuming Small Magellanic Cloud (SMC) like extinction (R_v=2.74) we obtain $A_{H_\alpha} = 0.38$. This implies that the flux at Hα needs to be corrected by at least $10^{0.15}$, yielding a de-reddened star formation rate limit of 0.45 $M_\odot$ yr^{-1} kpc^{-2} , and the combined de-reddened star formation rate on A, B, and C of 41 $M_\odot$ yr^{-1} . This implies that dust attenuation only removes 0.1 $M_\odot$ yr^{-1} kpc^{-2} if we only correct the bolometric luminosity such that it sits at the average. Overall this level of dust obscuration is not enough to be the primary reason for low Hα flux.

Even assuming an extreme case where the bolometric luminosity is near the maximum value for a type-1 QSO at z$\sim$2 ($\sim 10^{48}$) would only imply a limit of 0.9$M_\odot$ yr^{-1} kpc^{-2}. This could imply that there is a low star formation rate in the host galaxy, where the star formation has been nearly shut off within 0.2″$-$0.5″(1.4-4 kpc) from the QSO. These distant regions (A, B and C) are still forming stars at rates that are detectable. Our observations indicate that the host could be in a process of transitioning from a star-forming into a quiescent galaxy. However the less unlikely possibility is that the star formation is active in a diffuse region at separations of 1.4-4kpc rather than in the clumpy regions that we see in regions A, B, C and in other star

forming galaxies at this redshift.

2.6.3 Comparison to other type-1 QSOs at z$\gtrsim$1

There have been a number of multi-wavelength surveys of radio quiet type 1 QSOs at z$\sim$2 that have presented a range of conclusions about host galaxy star formation properties. High redshift QSO studies have either implied high star formation rates in concurrent high-z type-I QSOs or have argued for a lack of star formation activity. In this section we summarize and compare surveys that share similar QSO properties to our sample (i.e., SMBH mass, bolometric luminosity, unobscured type 1).

Herschel PACS observations of AGN and QSOs in the COSMOS extragalactic survey indicate a correlation between their bolometric luminosity and rest-frame 60μm host galaxy emission (Rosario et al. 2013). Using the mean 60μm flux (3.4×10^{45}erg s^{-1}) in the 10^{46-47}erg s^{-1} z=1.5-2.2 bin in Table 1 from Rosario et al. 2013 indicate that the mean star formation rate should be of order 200 M$_\odot$ yr^{-1} , using the 70μm star formation rate law presented in Calzetti et al. 2010. This is nearly an order of magnitude greater than the mean star formation rate in our sample, as indicated by narrow Hα emission line detection (78M$_\odot$ yr^{-1} and 29M$_\odot$ yr^{-1}) and limits (22M$_\odot$ yr^{-1} for NIFS and 37M$_\odot$ yr^{-1} for OSIRIS, integrated over a $1''^2$ box. See Section 2.5.3 for the discussion). The disagreement between our sample and the Herschel results could be due to just the limited-number of sources observed (14 in Rosario et al. 2013 at a similar bolometric luminosity ($10^{45.5-47}$erg s^{-1}) as the 5 QSOs in our sample). It is worth noting that the QSOs may be responsible for a significant portion of the total 60μm luminosity, so derived 60 μm star formation rates should be considered as upper limits.

HST observations of radio quiet QSOs at z$\sim$2 in Floyd et al. 2013 indicate an average star formation rate of 100$M_{\odot}$ yr^{-1} derived from rest-frame UV emission originating from the host galaxy. In their study they use both stellar and artificial PSFs to remove the bright QSO. The number of QSOs in our sample is similar to Floyd et al. 2013, which are type-1 and radio quiet. The star formation rate differences between our sample and Floyd et al. 2013 could be due to strong QSO contamination from residual emission from their PSF subtraction, or that star formation in our hosts are quite diffuse.

In contrast, studies such as Villforth et al. 2008 and Kotilainen et al. 2009 find quiescent galaxies that host radio quiet high-z QSOs. These observations are from seeing-limited (0.4-0.5$''$) near-infrared imaging and are limited to disentangling the host galaxy at close angular scales ($\lesssim$ 4 kpc). SDSSJ0925+0655 and SDSSJ0850+5843 share similar rest frame UV photometry to their samples, however the other half of the QSOs in our study are 1 to 1.5 magnitudes brighter. Including our results with these two other papers only yields a total of 15 high-z QSO that are observed to reside in "quiescent" z$\sim$2 galaxies in current literature.

At even higher redshifts, recent ALMA observations of z$\sim$6 QSOs (Wang et al., 2013; Willott et al., 2013) using the 158μm [CII] emission line reveals a detection in nearly 90% of the sources observed. The targets in their samples have similar properties to ours (i.e., BH mass, bolometric luminosities & Eddington ratios). In Willott et al. 2013 they reach a star formation limit of 40 $M_{\odot}$ yr^{-1} assuming the [CII] emission emanates solely from star formation. Yet sources in Wang et al. 2013 reach star formation rates as high as 1000 $M_{\odot}$ yr^{-1} , which implies that sources with detected [CII] have extreme star formation rates in comparison to our detections and sensitivity limits at z=2. These z$\sim$6 sources are all near the peak of their starburst

phase, assuming that most of the [CII] emission originates from star formation and not the QSO. According to present day $M_{stellar,bulge}$-M_{bh} relation and theoretical work (e.g., Somerville et al. 2008) there is an expectation of simultaneous SMBH and galaxy growth, presumably via mergers at these high ($> 1 \times 10^{46}$erg s^{-1} cm^{-2}) bolometric luminosities (Treister et al. 2012). In contrast, our observations show star formation rates that are well below this expected initial burst and below the typical star-forming galaxies at z$\sim$2 (Erb et al., 2006b; Förster Schreiber et al., 2009; Steidel et al., 2014).

The essential difference and advantage of our study compared to previous studies, is that our detection and limits of star formation rates can be made at differing spatial and velocity locations away from the QSO. In contrast, the majority of all studies we have discussed have integrated star formation rate limits over a large range of PSF and beam sizes. Based on our detection limits, it is clear that we do not detect the clumpy (1 kpc^2), strong star formation regions (up to $\sim$10 M$_\odot$ yr^{-1} kpc^{-2}) in current IFS observed z$\sim$2 star forming galaxies (Förster Schreiber et al., 2009; Law et al., 2009; Genzel et al., 2011; Law et al., 2012). If there is underlying star formation undetected in these host systems, then the surface brightness profiles of the star formation has to be diffuse and integrated across a large area of the galaxy. If our limits are to match previous inferred star formation rates of z$\sim$2 QSO hosts, then it would need to be diffuse with significant extinction.

The sample selection in our pilot survey is albeit random, since we were selecting based on achieving the best AO performance for PSF subtraction, therefore it is interesting that we would happen to select 3/5 type-I QSOs that are quiescent. The majority of our sample is similar to only a small number of observations of high-z QSO hosts residing in quiescent galaxies,

and are in disagreement with other work that indicate simultaneous high star formation rates and AGN activity. QSO duty cycles are still poorly understood, however it does seem to appear that in a number of cases the QSO can still be active while star formation in the host has been effectively turned off. These results agree well with AGN feedback models that require that the feedback mechanism only carry a small portion of the total bolometric luminosity of the QSO (5-10$\%$) to effectively turn off star formation (Hopkins and Elvis, 2010b). On the other hand this also agrees with non-causal evolution of SMBH and their host galaxies (Jahnke and Macciò 2011; Peng 2007), where the growth of the SMBH and star formation are unrelated and AGN feedback is not the main constituent in formation of local scaling relations, possibly because AGN and star formation activity happen on different time scales. Our study, Kotilainen et al. 2009 and Villforth et al. 2008 are consistent with star formation time scales being significantly shorter than that of the QSO. There are likely numerous high angular resolution observations from HST and ground-based observations that have had null detections of high-redshift QSO host galaxies, that would benefit being released to the community to improve these global statistics. Interestingly, this means there is likely a social selection bias of high-z QSO host galaxies, where authors typically only publish detections (hence QSO hosts with higher star formation properties) rather than their null detections. In any case, it is obvious that there are a large number of selection effects that need to be taken account, but clearly a larger sample of high-redshift QSOs would greatly benefit from IFS+AO observations and aid in our understanding of the demographics of high-z QSO host galaxies.

2.7 Conclusions

We have presented LGS-AO assisted integral field spectroscopy observations of five z = 2 QSOs targeted at resolving Hα nebular emission lines from their host galaxies. Using the broad emission line region of the QSO we were able to construct a PSF to remove the QSO continuum and emission to achieve the necessary contrast to detect Hα and [NII] host galaxy emission (see §2.4).

- For two out of five sources (SDSSJ1029+6510 & SDSSJ0925+0655) we are able to resolve extended narrow line emission surrounding the QSO.

- In SDSSJ1029+6510 we detect narrow Hα (regions A and B) that likely originates from star formation at close separations (2 - 4 kpc) from the QSO. If we assume the Hα flux is from star formation the integrated star formation rate from region A and B is 78.4$\pm$6.2 $M_\odot$ yr^{-1} (110 $M_\odot$ yr^{-1} with dust correction).

- For SDSSJ0925+06 we detect three distinct star forming regions that are separated from the QSO by $\sim$ 4 kpc. The upper limit star formation rate for all three regions combined is 29.0$\pm$2.4 $M_\odot$ yr^{-1} (40.7 $M_\odot$ yr^{-1} with dust corrections).

- Careful examination of the other three sources in our sample do not detect any narrow Hα emission post PSF subtraction, even in the cases of SDSSJ1005+4356 & SDSSJ2123-0050 for which we spent the most integration time per source.

- We ran a Monte Carlo simulation on our data by inserting extended narrow Hα at various separations from the QSO with varying Hα fluxes (star formation rates). We find that we

can detect star formation rates down to 1.4 $M_\odot$ yr^{-1} (see §2.5.3) as close as 0.2″ from the QSO. Incorporating dust obscuration this value can vary from 2.6$M_\odot$ yr^{-1} -9$M_\odot$ yr^{-1} (see §2.6.1 & §2.6.2) depending on the value of A_V. At the 9$M_\odot$ yr^{-1} limit, after correcting the SDSS spectra for dust reddening we are pushing the bolometric luminosities for some of our sources past the typical values for type 1 QSOs at this redshift. Even with a star formation rate of 9 $M_\odot$ yr^{-1} it would be difficult to explain the missing narrow Hα to be due to dust obscuration inside the host galaxy. Hence for these sources low star formation rate is the likely reason for lack of narrow Hα originating from the host galaxy.

- Four sources show low star formation rates at close angular separation of the QSO, with no dereddened star formation $\gtrsim$ 9 $M_\odot$ yr^{-1} within 2 to 4 kpc of the QSO.

- We do not detect any strong evidence for NLR emission (region C of SDSSJ1029+6510 is only 2.1σ) in any of our sources. We place a luminosity limit of 1-1.5$\times 10^{42}$erg s^{-1} cm^{-2} on an emission line originating from the QSO's NLR.

- Compared to other z=2 QSO host galaxy surveys our sample is unique by having little-to-no star formation in high redshift type-I QSOs. This is in agreement with a large fraction of nearby (z $\lesssim$ 0.5) QSO host galaxies being quiescent. Yet at comparable and higher redshifts to our sample the majority of surveys have found simultaneous star formation activity with QSO activity. Clearly a larger z=1-3 QSO IFS+AO sample will be critical in developing a more coherent picture of QSO host galaxies during this important epoch.

2.8 Acknowledgements

Based on observations obtained at the Gemini Observatory, which is operated by the Association of Universities for Research in Astronomy, Inc., under a cooperative agreement with the NSF on behalf of the Gemini partnership: the National Science Foundation (United States), the National Research Council (Canada), CONICYT (Chile), the Australian Research Council (Australia), Ministério da Ciência, Tecnologiae Inovação (Brazil) and Ministerio de Ciencia, Tecnología e Innovación Productiva (Argentina). The authors would like to give our thanks to Eric Steinbring who served as our Gemini phase II liaison for planning this program (GN-2012B-Q-53). Data was also obtained at W.M. Keck Observatory, which was made possible by generous financial support from the W.M. Keck Foundation. The authors would like to acknowledge the dedicated members of the Keck Observatory staff, particularly Jim Lyke and Randy Campbell, who helped with the success of our observations. The authors wish to recognize the significant cultural role and reverence that the summit of Mauna Kea has always had within the indigenous Hawaiian community. We are most fortunate to have the opportunity to conduct observations from this “heiau" mountain. SCG thanks the Natural Science and Engineering Research Council of Canada for support.

Chapter 2, in part, is a reprint of the material as it appears in The Astrophysical Journal 2016. Vayner, A., Wright, S. A., Do, T., Larkin, J., Armus, L., Gallagher, S. C., 2016. The dissertation author was the primary investigator and author of this paper.

Chapter 3

Galactic-Scale Feedback Observed in the 3C 298 Quasar Host Galaxy

3.1 Abstract

We present high angular resolution multi-wavelength data of the 3C 298 radio-loud quasar host galaxy (z=1.439) taken using the W.M. Keck Observatory OSIRIS integral field spectrograph (IFS) with adaptive optics, Atacama Large Millimeter/submillimeter Array (ALMA), Hubble Space Telescope (HST) WFC3, and the Very Large Array (VLA). Extended emission is detected in the rest-frame optical nebular emission lines Hβ, [OIII] , Hα , [NII] , and [SII], as well as molecular lines CO (J=3-2) and (J=5-4). Along the path of 3C 298's relativistic jets we detect conical outflows in ionized gas emission with velocities up to 1700 km s^{-1} and outflow rate of 450-1500 M$_{\odot}$ yr^{-1} extended over 12 kpc. Near the spatial center of the conical outflow, CO (J=3-2) emission shows a molecular gas disc with a rotational velocity of $\pm$150km s^{-1} and

total molecular mass ($\mathrm{M_{H_2}}$) of 6.6$\pm$0.36 $\times$ 10^9 $\mathrm{M_\odot}$. On the molecular disc's blueshifted side we observe broad extended emission due to a molecular outflow with a rate of 2300 $\mathrm{M_\odot}$ $\mathrm{yr^{-1}}$ and depletion time scale of 3 Myr. We detect no narrow Hα emission in the outflow regions, suggesting a limit on star formation of 0.3 $\mathrm{M_\odot}$ $\mathrm{yr^{-1}}$ $\mathrm{kpc^{-2}}$. Quasar driven winds are evacuating the molecular gas reservoir thereby directly impacting star formation in the host galaxy. The observed mass of the supermassive black hole is $10^{9.37-9.56}$ $\mathrm{M_\odot}$ and we determine a dynamical bulge mass of $\mathrm{M_{bulge}}$ = 1-1.7$\times 10^{10} \frac{\mathrm{R}}{\mathrm{1.6kpc}}$ $\mathrm{M_\odot}$. The bulge mass of 3C 298 resides 2-2.5 orders of magnitude below the expected value from the local galactic bulge - supermassive black hole mass ($\mathrm{M_{bulge}} - \mathrm{M_{BH}}$) relationship. A second galactic disc observed in nebular emission is offset from the quasar by 9 kpc suggesting the system is an intermediate stage merger. These results show that galactic scale negative feedback is occurring early in the merger phase of 3C 298, well before the coalescence of the galactic nuclei and assembly on the local $\mathrm{M_{bulge}} - \mathrm{M_{BH}}$ relationship.

3.2 Introduction

Quasars are the most luminous active galactic nuclei (AGN), whose supermassive black holes (SMBHs) are often fueled by large galaxy mergers (Treister et al., 2012). AGN accretion discs are thought to drive energetic winds (Murray et al., 1995) and/or relativistic jets that suppress star formation (Hopkins and Elvis, 2010a; Zubovas and King, 2014; Costa et al., 2015), thereby impacting galactic structure and evolution. This is one of the leading theoretical (Di Matteo et al., 2005; Faucher-Giguère et al., 2012; Barai et al., 2017; Anglés-Alcázar et al., 2017b)

pictures used to explain correlations between SMBH masses and galactic stellar masses (Magorrian et al., 1998; Gebhardt et al., 2000; Ferrarese and Merritt, 2000; Kormendy and Ho, 2013) and luminosity function of local massive galaxies (Benson et al., 2003). The sphere of influence of SMBHs, inside of which their gravity dominates that of the stars, gas, and dark matter, range from a few 10s to 100 pc, while the local scaling relations of $M_{bulge} - M_{BH}$ apply on stellar bulge scales, i.e., several kpc. The SMBH energy output can be orders of magnitude higher than the binding energy of galactic bulges; therefore energy injected by active SMBHs into the interstellar medium (ISM) could be efficient at impacting the stellar mass history of its host galaxy. Since the bulk of stellar mass is formed at high-redshift ($z > 1$) (Gallazzi et al., 2008), it is critical to study the effects of AGN activity during the assembly periods of their host galaxies at high-redshift.

Observational studies have found that nearby quasars and ULIRGs (Ultra-Luminous Infrared Galaxies) show evidence of large scale ionized (Greene et al., 2012; Rupke and Veilleux, 2011; Liu et al., 2013a; Harrison et al., 2014) and molecular outflows (e.g., Cicone et al. 2014; Sun et al. 2014; Stone et al. 2016; Veilleux et al. 2017) allowing for detailed studies of feedback physics. However the computed outflow rates in nearby systems are not sufficient to impact the stellar mass assembly history since these galaxies have already done the bulk of their growth. In contrast, there is minimal observational evidence for AGN activity directly affecting star formation at the peak epoch ($1<z<3$) of galaxy formation and black hole accretion (Delvecchio et al., 2014; Madau and Dickinson, 2014). Recent studies of distant quasars and radio-loud galaxies have shown evidence of large scale (5-20 kpc) outflows driven by AGN activity that theoretically should be powerful enough to quench star formation (Nesvadba et al., 2008; Steinbring, 2011;

Cano-Díaz et al., 2012; Harrison et al., 2012; Brusa et al., 2016; Carniani et al., 2015). Although it has still remained challenging to directly associate large scale outflows with the suppression of star formation of AGN host galaxies (Cano-Díaz et al., 2012; Cresci et al., 2015; Carniani et al., 2016). These studies have provided intriguing clues as to the nature of quasar feedback. Yet compared to nearby quasars there is little known about $z > 1$ host galaxies (i.e., stellar mass, dynamics, and morphologies) and the true effects of feedback on host galaxy star formation. A key missing result is one that connects quasar and jet driven outflows with the observed galactic scale winds, star formation activity, and molecular gas properties.

Quasars outshine their host galaxies by an order of magnitude or more, making it observationally challenging to detect and study their faint underlying galaxies (Lehnert et al., 1999; Hutchings et al., 2002; Jahnke et al., 2004a; Falomo et al., 2005; Floyd et al., 2013; Glikman et al., 2015). The sizes of distant ($z > 1$; look-back time of 9.25 Gyr) galaxies are small ($\sim 1''$), roughly the same angular size as ground-based “seeing" and space-based instrument resolution and contrast sensitivity. The combination of near-infrared integral field spectroscopy (IFS) with laser-guide star adaptive optics (LGS-AO) allows for the effective separation of quasar emission from the host galaxy. This is achieved by using a pristine point spread function (PSF) generated by the quasar broad-line and continuum emission from the IFS data cube (Inskip et al., 2011; Vayner et al., 2016).

We have started the QUART (Quasar hosts Unveiled by high Angular Resolution Techniques) survey of high-redshift ($1.3<z<2.6$) quasars using W.M Keck Observatory laser guide star adaptive optics (LGS-AO) observations to resolve and study quasar host galaxy properties with a rich multi-wavelength data sets. Herein we present the first paper of this survey on the

individual z=1.439 (look-back time 9.3 Gyr) radio loud quasar 3C 298. We combine high spatial resolution observations to reveal the complex morphology, dynamics, and energetics of the 3C 298 host galaxy. Using OSIRIS and Keck LGS-AO, we are able to map the kinematics and intensity of galactic nebular emission lines Hβ, [OIII] , Hα , [NII] and [SII] at$\sim$1.4 kiloparsec (kpc) resolution. We present the multi-wavelength data sets in §3.3 and describe the data reduction and analysis techniques for each instrument in §3.4. We discuss the dynamics and energetics of ionized and molecular gas in §3.5, and in §3.6 we discuss our results and overall interpretation. We suggest the reader refers to Figure 3.11 while reading the manuscript, which summarizes the observed structure and properties of the 3C 298 host galaxy. Throughout the paper we assume a Λ-dominated cosmology (Planck Collaboration et al., 2014) with Ω_M=0.308, Ω_Λ=0.692, and H_o=67.8 km s^{-1} Mpc^{-1}

3.3 Observations

We present new observations of 3C 298 using Keck OSIRIS AO and ALMA band 4 and 6. These observations are coupled with archival Hubble Space Telescope (HST) WFC3 and Very Large Array (VLA) imaging data.

3.3.1 Keck: OSIRIS

Observations were taken using the integral field spectrograph OSIRIS (Larkin et al., 2006) with the upgraded grating (Mieda et al., 2014) behind the laser guide star adaptive optics (LGS-AO) system at W.M. Keck Observatory on May 19 and 20, 2014 (UT). The quasar was

used for tip/tilt correction while the laser tuned to 589.2 nm created an artificial star on-axis for higher order corrections. We used the Hn3 (May 19) and Jn1 (May 20) filters with a plate scale of 100 milli-arcseconds (mas) per lenslet with a position-angle of 103°. In these modes OSIRIS has a field of view of $3.2'' \times 6.4''$in Jn1 and $4.8'' \times 6.4''$in Hn3. We took four 600s exposures on-source in each filter, plus an additional 600s pure-sky frame. Each night immediately after the quasar observations we observed the standard star HD136754 for telluric and flux calibrations. Both nights were photometric with near-infrared seeing of 0.4-0.5$''$.

3.3.2 ALMA: Band 4 and 6

Early ALMA science (cycle 2, 3) band 4 and 6 observations (2013.1.01359.S, 2015.1.01090.S, PI: Vayner) were aimed at observing the rotational molecular transition of CO J=3-2 and J=5-4 in emission to map the distribution and kinematics of the molecular gas in 3C 298. One 1.8745 GHz spectral window was centered on CO (J=3-2) (141.87 GHz) and CO (J=5-4) (236.43 GHz) while three additional spectral windows set up to map the continuum in each band. The effective velocity bandwidth per spectral window was approximately 4,000 $\mathrm{km\,s^{-1}}$ for band 4 and 2,400 $\mathrm{km\,s^{-1}}$ for band 6. Observations were taken in an extended configuration with an approximate angular resolution of $\sim$0.4$''$ and $\sim 0.3''$ for band 4 and 6, respectively. In Table 3.1 we summarize the observational setup for each band.

Table 3.1 ALMA Cycle 2 and 3 observations summary

Date	Band	Central frequencies (GHz)	Integration Time (min)	PWV (mm)	Antennae #	Beam Size	Line σ/beam (mJy)	Continuum (mJy)
2015 Aug 6	4	141.86	27.84	4.5	39	$0.44'' \times 0.41''$	0.5	48
2016 Sep 9	4	141.85, 140.00, 129.97, 128.01	24.19	2.5	37	$0.39'' \times 0.30''$	0.22	46
2016 Sep 17	6	236.42, 234.5, 220.99, 219.11	19.65	0.7	38	$0.28'' \times 0.18''$	0.37	44

3.4 Data reduction and Analysis

3.4.1 OSIRIS: Data reduction

The data was reduced with the OSIRIS data reduction pipeline version 3.2, which performs standard near-infrared IFS reduction procedures: dark subtraction; adjust channel levels; remove crosstalk; glitch identification; clean cosmic rays; extract spectra; assemble data cube; and correct dispersion. We used the *scaled sky subtraction* routine for the Jn1 data cubes, which uses families of atmospheric OH-emission lines between multiple frames for a cleaner subtraction. For Hn3 data we used our own custom sky subtraction routine that scales only the nearest three OH lines in proximity to the quasar Hα emission line. This produced better residuals compared to the pipeline's scaled sky routine in Hn3. Inspection of individual spaxels in the scaled sky subtracted data cubes still revealed strong OH-sky line residuals, typically over 2-3 spectral pixels in the wings of the Hα emission line. These spectral pixels were linearly interpolated using the slope from the neighboring two pixels around the strong residuals. The telluric spectrum of the calibration star was extracted over the seeing halo and had its continuum divided by a 9400K blackbody function with its hydrogen absorption lines removed. The 1D telluric spectrum was normalized and divided into the quasar data cubes. Individual data cubes were then shifted to a common position and combined using a 3σ clipping algorithm, which is part of the OSIRIS data reduction pipeline. Finally we applied flux calibration to all quasar data cube by using the telluric corrected standard star spectrum and scaling the DN/s/channel to match the expected Jn1 and Hn3 band flux (erg/s/cm^2).

3.4.2 OSIRIS: PSF construction and subtraction

Both the quasar broad line emission (Hβ and Hα) and quasar continuum originate from gas on parsec scales from the SMBH, and are therefore spatially unresolved in our OSIRIS observations. Wavelength channels of the broad line emission and/or continuum can be used to construct a pristine quasar image that can then be used for PSF subtraction in the reduced data cube. In Vayner et al. (2016) we discuss in greater detail our PSF subtraction routine and its performance on a set of luminous type-1 radio quiet quasars at z$\sim$2. In brief, we used broad emission line/continuum channels that should not overlap with the host galaxy emission with spectral channels offset by 5,000-10,000 km s^{-1} from the quasar redshift. We carefully select spectral channels that do not coincide with OH-emission lines or regions of low transparency in the near-infrared. PSFs are generated by combining individual data channels and are scaled to the peak pixel values. This empirical PSF is then subtracted from the entire data cube while re-scaling to the peak pixel value of the quasar emission per wavelength channel.

After data reduction, the 100 mas mode in OSIRIS suffers from flux mis-assignment between adjacent spaxels given its enlarged pupil size in the instrument. The reductions still conserve the integrated flux of the source, but neighboring pixels can receive a $\sim$10% mis-assignment of flux. This effect is seen in bright stars (H $<$ 16 mag) with excellent AO correction, where flux is mis-assigned from the bright central spaxel to the row above and below the centroid position of the point source. This effect can be easily identified by evidence of spaxels with an inaccurate spectral shape. Our PSF subtraction routine removes a significant portion of flux from the PSF in these spaxels but they generally have stronger post-PSF subtraction

residuals. We masked the affected spaxles with background flux values calculated by taking a standard deviation in a $1'' \times 1''$sky region. We fit a 2D Gaussian to the PSF image and measure a full-width half-maximum (FWHM) of $0.127''$and $0.113''$in Hn3 and Jn1, respectively. After PSF subtraction of the quasar data cubes, we smooth the Hn3 and Jn1 data sets to a common resolution with a beam FWHM of $0.2''$ to improve the signal-to-noise (SNR) in the diffuse parts of the host galaxy.

3.4.3 OSIRIS: Kinematics

In this section we investigate the kinematics properties of nebular emission lines in the host galaxy of 3C 298. We inspect *all* individual spectra that overlap between the two observing modes (Jn1 and Hn3), which amounts to approximately 2,640 spectra. An emission line is identified to be real if the peak intensity is at least $3\times$ greater than the noise per wavelength channel, and the emission line dispersion is larger than the instrumental resolution (0.206 nm for Hn3 and 0.174 nm for Jn1).

A single Gaussian profile provides a good fit to the 486.1 nm Hβ emission line that is redshifted into Jn1 at an observed wavelength of 1186 nm. The 495.9, 500.7 nm [OIII] lines are redshifted into Jn1 band at an observed wavelength of 1210 and 1221 nm. The 495.9, 500.7 nm [OIII] lines are fit simultaneously, each with a single Gaussian profile. The position and width of the 495.9 nm line are held fixed to the redshift and width of 500.7 nm line at each spaxel. The line ratio between the [OIII] lines are held fixed at 1:2.98 (Storey and Zeippen, 2000). The 495.9, 500.7 [OIII] lines in several spaxels in the north-west and south-east regions require two Gaussian profiles for a good fit. The [NII] 654.9, 658.5 nm, Hα 656.3 nm, and

[SII] 671.7 673.1 nm are redshifted into the Hn3 filter. Spaxels with detected Hα and both [NII] emission lines are fit together with three Gaussian profiles. The position and width of the [NII] lines are fixed to the Hα redshift and width, with a flux ratio between [NII] 654.9, 658.5 nm of 1:2.95. Generally a single Gaussian profile fit to Hα and each [NII] line provide a satisfactory fit ($\chi^2_R \sim 1-2$), with the exception of several spaxels in the south-east region, where an additional broad Hα component is necessary. The Hα , Hβ and [OIII] broad-line components have similar velocity dispersions and offsets. The lower SNR of the [SII] doublet make it challenging to fit a single Gaussian profile to each emission line, therefore each spaxel where [SII] is detected we fit a single Gaussian profile to the combined signal. Regions where no [NII] or [SII] lines are detected have only a single Gaussian fit to Hα . Limits on [NII] and [SII] lines are derived by inserting a Gaussian profile with the same width as Hα at the expected location of the emission line based on Hα 's redshift, with a peak flux $2\times$ greater than the standard deviation of the noise. Similarly to a real detection we integrate the inserted emission line to obtain a limit.

To construct 2D flux maps we integrate each emission line from -3σ to $+3\sigma$, where σ is derived from the line fit. Error on the line flux is calculated by taking a standard deviation of every 3 spectral channels and summing in quadrature over the same spectral region where the nebular emission line is integrated. Velocity maps for each emission line are relative to the redshift of the quasar's broad line region, which is calculated by fitting a single Gaussian profile to the broad Hβ line constructed by spatially integrating the cube over the seeing halo before PSF subtraction. The velocity dispersion map has the instrumental PSF subtracted out in quadrature using the width of OH emission sky lines. Errors on velocity offsets and dispersions are based on 1σ errors associated with the least squares fit.

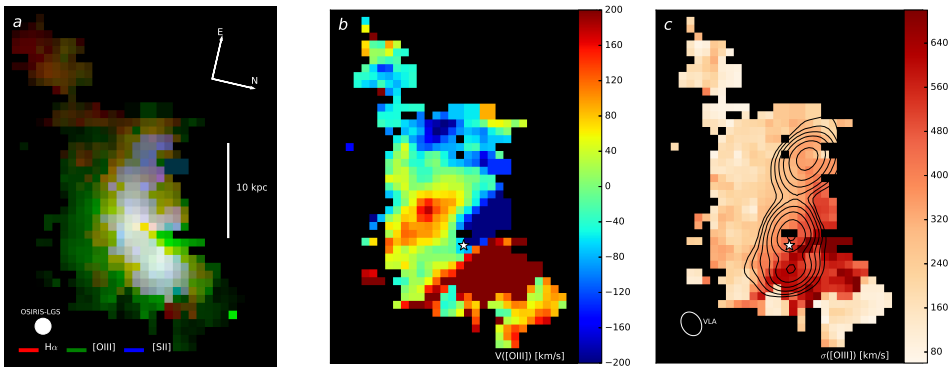

Figure 3.1 OSIRIS observations of 3C 298 nebular emission line intensities and [OIII] kinematic maps. (a) Three colour intensity map of nebular emission lines: Hα (red), [OIII] (green), and [SII](blue). FWHM of the OSIRIS beam is shown as a white circle on the bottom left. (b) Radial velocity offset (km s^{-1}) of the [OIII] line relative to the redshift of the quasar. The white star shows the location of the subtracted luminous quasar. (c) Velocity dispersion (km s^{-1}) map of [OIII] emission. The black contours are 8485.100 MHz VLA observations of radio synchrotron emission from the quasar jet and lobes. The largest velocity offset and dispersion corresponds to the location of jet and lobes. This spatial correspondence provides evidence of a quasar driven outflow in the ionized ISM with an ionized outflow rate of 450-1500 M$_\odot$ yr^{-1} .

In Figure 3.1 we show the line integrated emission of Hα , [OIII] and [SII] in a three colour image composite alongside the [OIII] radial velocity and dispersion maps of 3C 298. A distinct extended broad velocity emission region is co-spatial with radio synchrotron emission emanating from extended jet/lobes. The radio VLA observations are taken from Mantovani et al. (2013) (Project code: AJ206). We downloaded fully reduced clean map of 3C 298 at 8485.100 MHz [1]. The centroid of the point source with the flattest spectral slope is associated with the optical location of the quasar. We extract the image centered on the quasar and rotate to a position angle of 103° to match our OSIRIS observations.

We generate integrated spectra for three distinct outflow regions identified based on their

[1] http://db.ira.inaf.it/aj206-fm/

radial velocity ($\pm$400 km/s) and dispersion (V_σ >500km s^{-1}), see Figure 3.1. For the purposes of the figure, the north-western outflow will be identified as the redshifted outflow or "Outflow-R", and the north-eastern outflow will be identified as the blueshifted outflow or "Outflow-B", and the third outflow in the south-eastern direction will be identified as "AGN-Outflow". We believe AGN-outflow belongs to a secondary nucleus in the 3C 298 system due to its isolated nature, and since the ionized emission does not extend from the quasar and does not coincide with the quasar jet/lobes. The AGN-outflow is in close proximity to the dynamical center of a rotating disc in the 3C 298 system that belongs to a second merging galaxy (see section 3.4.5 for further discussion). Each spectra are then fit with multiple Gaussian profiles. *Outflow-R* is best fit with a combination of two relatively broad (V_σ $\sim$500 km/s) Gaussian profiles in both [OIII] lines, Hα , and [NII] , which we interpret as a signature of outflowing gas along the line of sight. The 500.7 nm [OIII] line requires an additional relatively narrow (V_σ $\sim$ 80 km/s) component for a good fit that has no counterpart in Hα , [NII] , or [SII]. A faint Hβ line is detected, and is fit with a single Gaussian component that potentially matches the broad components of [OIII] and Hα . See the top row of Figure 3.2 for the integrated spectrum in J and H band along with the fit. Components A (green curve) and B (red curve) are the broad lines, while component C (blue curve) is the narrow line found only in [OIII] . The white contour in the right column shows the region over which the data cube is spatially integrated. The spectrum of the blueshifted outflow (*Outflow-B*) region is best fit with a single broad Gaussian component in Hβ, [OIII] , Hα and [NII] ; second row of Figure 3.2 shows the spectra along with the fit. In the redshifted outflow region the lines are very broad, so the [SII] doublet blends together, making it very hard to fit the individual lines. The lines are slightly narrower in the blueshifted outflow region, and each

emission line in [OIII] and Hα require only a single Gaussian component. This made it possible to fit the [SII] doublet using a single Gaussian profile for each emission line.

We construct a high SNR spectrum over the entire *AGN-Outflow* region. Hα and [OIII] are fit with two components: a broad-line blueshifted Gaussian for the outflow and a narrow component that we interpret as part of the AGN/quasar narrow-line region. Hβ, [NII] , and [SII] are fit with a single Guassian narrow-line component.

3.4.4 OSIRIS: Nebular Emission line Diagnostics

In this section we investigate potential ionizing sources for distinct regions of the host galaxy. Line ratio maps are constructed by taking ratios of integrated flux maps [OIII] , Hα , [NII] , and [SII]. The Hβ line is only detected in a small number of individual spaxels; sensitivity and dust obscuration prohibits us from detecting this line over similar sized regions to other detected nebular emission lines. We construct an Hβ map over the region where Hα is detected by assuming case B recombination ($F_{H\beta} = F_{H\alpha}/2.89$).

We create three line ratio maps log([OIII] /Hβ) , log([NII]/Hα), and log([SII]/Hα) . In Figure 3.3 we plot the line ratios on a standard BPT diagram, log([OIII] /Hβ) vs log([NII]/Hα). Empirical (Kauffmann et al., 2003) and theoretical (Kewley et al., 2001) curves separating photoionization by O-stars versus quasar ionization are shown. Generally, values that lie above these curves represent photo-ionization by an AGN, while points below represent photoionization by newly formed O-type stars, tracing regions of active/recent star formation. Points on the BPT diagram are colour coded to match the line ratio map of log([OIII] /Hβ) (middle Figure 3.3). The 1$''$ central region (red and orange in Figure 3.3) is mainly photoionized by the quasar in

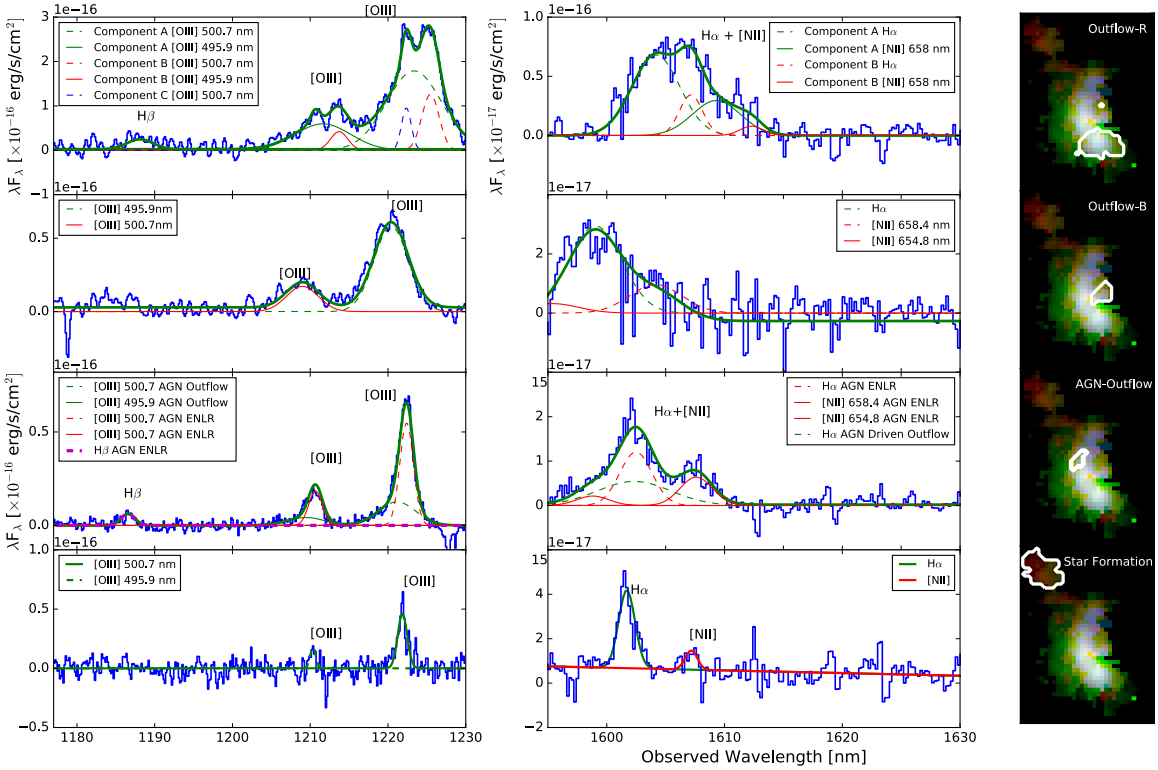

Figure 3.2 OSIRIS near-infrared spectra for distinct photoionized regions in the host galaxy of 3C 298. J and H band spectra are shown in the left and middle panels, respectively, with observed wavelengths (nm) and calibrated flux (F_λ). The three-colour composite image (right) shows the regions over which the spectra were extracted. Multiple Gaussian functions are fit to each of the emission lines: Hβ, [OIII], Hα , and [NII] in all the spectra. The green curves show the combined fit to each spectrum, and each dotted line represents an individual component of the fit. The redshifted outflow region is best fit with a double Gaussian component (labeled A and B in top panel) to each nebular emission line, that suggests conical expansion of the gas along the line-of-sight. The blueshifted outflow region is best modeled with a single Gaussian component to each emission line. The presence of broad, blueshifted emission lines in [OIII] and Hα (labeled 'AGN Outflow', third panel from top), indicating outflowing gas, roughly coincident with the dynamical center of the secondary galaxy in the merger. This outflow region is not associated with strong star formation, based on line ratio diagnostics in Figure 3.3. The star forming region is best fit with a single narrow Gaussian component to each emission line.

an extended narrow line region (ENLR), as shown by very high log([OIII] /Hβ) $\gtrsim$ 0.8 values. 658.5[NII] is detected over the red region in individual spaxels while over the orange region we place a 2σ flux limit. Even within the limits the orange region fall in the AGN photoionzation portion of the BPT diagram due to very high log([OIII] /Hβ) values. The star formation region (blue) has low log([OIII] /Hβ) <0.8 and log([NII]/Hα)<0.5 values, corresponding to ionization from newly formed stars. We generate a spectrum over the *Star Formation* region and easily identify and fit a single Gaussian to [OIII] , Hα , [NII] and a Hβ line with a SNR of 2 identified (bottom panel of Figure 3.2).

Star forming regions are spatially offset from the large outflows, and their kinematics and morphologies agree with a potential tidal feature induced by the merging galaxies. Outflow regions (yellow and green) correspond to the highest log([OIII] /Hβ) line ratios. These regions are inconsistent with ionization by young stars, and are photoionized by quasars and shocks. Gas in outflow regions is moving at sufficiently high velocity so the Mach number of the wind is high and strong radiative shocks are expected. Using shock models from (Allen et al., 2008) we find that a large portion of observed line ratios agree with shock models for gas with electron density between $10^2 - 10^3 \mathrm{cm}^{-3}$ and shock velocities of 1000 km/s. In Figure 3.4 we plot the log([OIII] /Hβ) vs log([SII]/Hα) values over regions where [SII] was detected in individual spaxels. We overlay shock models on this BPT diagram, a large fraction of the nebular line ratios in the redshifted outflow region (green) and blueshifted outflow region (yellow) are consistent with these models. Dark red/blue lines in the model represent higher velocity gas and stronger magnetic parameter (see Allen et al. (2008) for further details). Furthermore the region photoionized by AGN shows a spatial profile that drops off as $1/\mathrm{R}^2$ in nebular emission, while

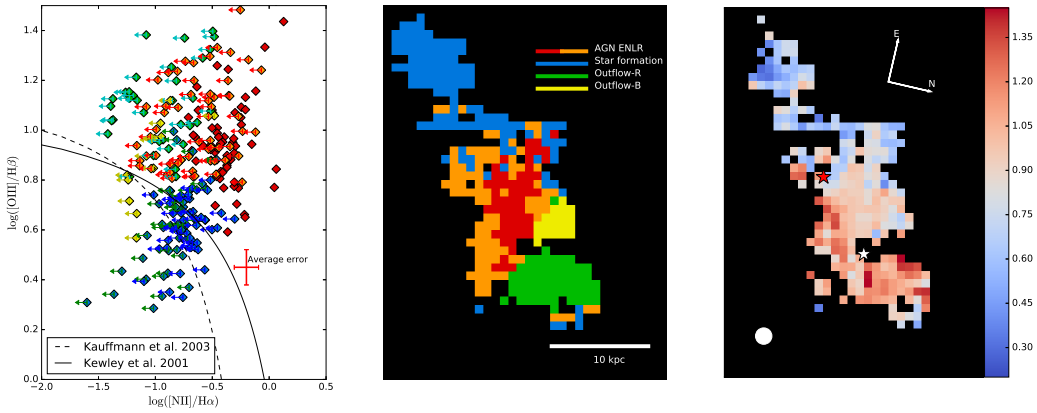

Figure 3.3 Photoionization diagnostics of ionized gas in the 3C 298 system. (LEFT) The log([OIII] /Hβ) vs log([NII]/Hα) nebular line ratio diagram of the 3C 298 host galaxy with empirical (Kauffmann et al., 2003) and theoretical (Kewley et al., 2001) curves that delineate the separation between star formation and AGN. Nebular line ratios that lie above and to the right of the curves are considered to be photoionzed by a hard radiation source such as a quasar/AGN or shocks, and values below the curves are considered to be ionized by O-stars in HII regions. (MIDDLE) Galaxy map coloured to match the line ratio diagnostic diagram. Red and orange colours represent regions photoionization by the quasar and secondary AGN in an extended narrow line region (ENLR). Regions with upper limits on log([NII]/Hα) are labelled orange, while red regions have directly measured 658.4nm [NII] line. The blue region shows gas whose line ratios are consistent with ionization by young massive stars. The green region is the redshifted outflow, and the yellow region is the blueshifted outflow. The redshifted outflow (green) shows a blend of photoionization from the quasar and radiative shocks due to interactions of the ISM with large scale outflows. This is further confirmed with the log([OIII] /Hβ) vs. log([SII]/Hα) diagnostic diagram as seen in Figure 3.4. (RIGHT) The log([OIII] /Hβ) ratio map illustrating different photoionization levels across the galaxy. The colours clearly cluster in distinct regions in the resolved host galaxy. The beam size is given by the solid white circle. The white star represents the location of the quasar and the red star and circle represents the location of the dynamical center of the secondary galaxy, where a potential secondary obscured, AGN exists.

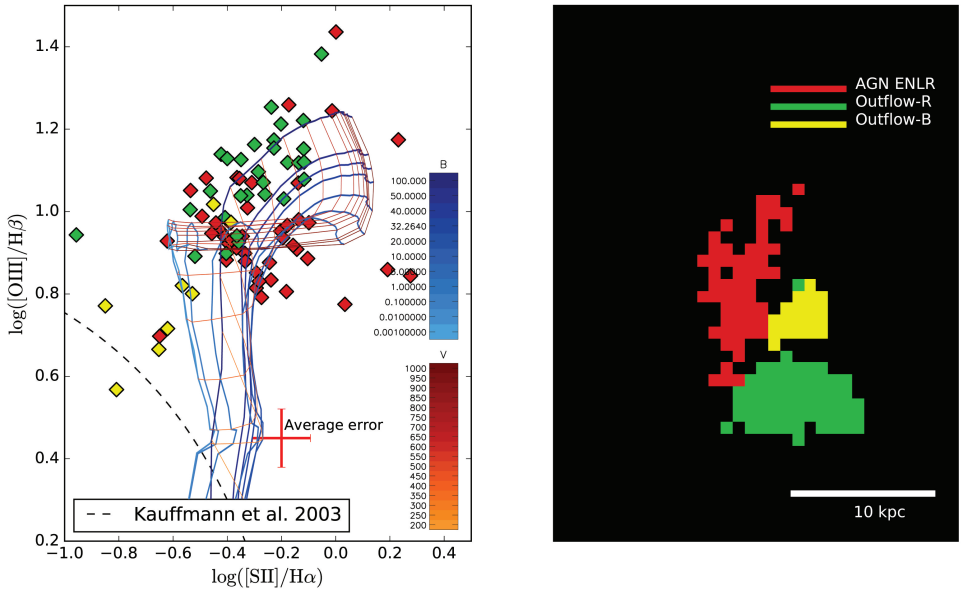

Figure 3.4 Photoionzation diagnostics of ionized gas in the 3C 298 system. (LEFT) We show diagram of log([OIII] /Hβ) vs log([SII]/Hα) with empirical dash curve(Kauffmann et al., 2003) that separates photoionization of star forming regions and AGN. The theoretical position of shocked ionization is overlaid on the BPT diagram (Allen et al., 2008). Dark red/blue lines in the model represent higher velocity gas and stronger magnetic parameter. (RIGHT) Coloured values match the spatial regions of the host galaxy, where the green and yellow points are from the redshifted and blueshifted outflow regions. Ionization in these outflow regions are due to shocks moving at speeds of $\sim$1000km s^{-1} . The red region is consistent with values primarily ionized by AGN.

in the region where we see powerful outflows the profile is more complex suggesting multiple ionizing sources. Both regions show similar extinction values as we discuss below.

In order to investigate how dust can alter our photoioniziation measurements, we construct a high SNR spectrum over the ENLR (red in Figure 3.3) to estimate the amount of dust obscuration from the Hα /Hβ ratio. Using the Calzetti et al. (2000) law, we find an average $A_v = 0.07$ over the ENLR (the red region in Figure-3.3), based on an Hα /Hβ ratio of 2.9. This would on average increase the ratio of log([OIII] /Hβ) only by a factor of 1.05 for the ENLR;

this is not large enough to alter our results. We find that in portions of the the ENLR and red-shifted outflow region the A_v value is consistent with zero extinction in the ionized gas. Similar results are found over the outflow regions suggesting negligible extinction in the ionized gas. Over the star forming region (blue region in Figure-3.3) we measure an A_v value of 1.2 based on Hα /Hβ ratio of 4.0. The observed non-detection of Hβ in individual spaxels is consistent with the derived integrated extinction value and given the expected Hβ SNR relative to [OIII] and Hα emission lines.

3.4.5 OSIRIS: Velocity field modeling

To the south-east of the quasar there is a kinematic feature resembling a rotating galactic disc that is offset by $\sim$ 200 km s^{-1} from the quasar BLR, with a projected rotational velocity of $\pm$170 km s^{-1} . In this section we outline the modeling done on the radial velocity map of [OIII] emission to confirm the rotating disc nature of this feature. We isolate this feature for the disc fitting, using a box size of 0.7″×1.7″centered on the gradient feature in the [OIII] radial velocity map. The boxed region is selected to not include any strong broad emission from the conical outflow. The [OIII] velocity field is modelled by fitting a two dimensional arc-tangent disc model given by

$$V(r) = \frac{2}{\pi} V_{max} \arctan\left(\frac{r}{r_{dyn}}\right), \tag{3.1}$$

where V(r) is rotation velocity at radius r from the dynamical center, V_{max} is plateau velocity, and r_{dyn} is the radius at which the arc-tangent function has a turn over to a decreasing slope. The

measured line-of-sight velocity from our observations relates to V(r) as

$$V = V_0 + \sin i \cos \theta V(r), \tag{3.2}$$

where

$$\cos \theta = \frac{(\sin \phi(x_0 - x)) + (\cos \phi(y_0 - y))}{r}. \tag{3.3}$$

Radial distance from the dynamical center to each spaxel is given by

$$r = \sqrt{(x - x_0)^2 + \left(\frac{y - y_0}{\cos i}\right)^2}, \tag{3.4}$$

where x_0, y_0 is spaxel location of the dynamical center, V_0 is velocity offset at the dynamical center relative to the redshift of the quasar broad line region, ϕ is position angle in spaxel space, and i is the inclination of the disc.

We fit the seven parameter velocity field model to a selected region of our observed [OIII] velocity map using a non-linear least squares routine. The selected box region tries to exclude broad emission from the extended quasar outflow and a tidal feature that seems to show its own distinct kinematic structure. Our best fit has a χ^2_R =0.7 with the following values: x_0, y_0 = -0.49″, +0.94″ relative to the centroid of the quasar, V_{max}= 209±33 km s^{-1} , r_{dyn} = 2.2 ±0.98 kpc, $i = 72 \pm 4°$, $\phi = -109 \pm 6°$, and $V_0 = 170 \pm 9$ km s^{-1} relative to the redshift of the quasar broad line region. Figure 3.5 shows the region selected for disc fitting with the modeled 2D velocity profile and residuals between the model and observed velocities. The disc is offset

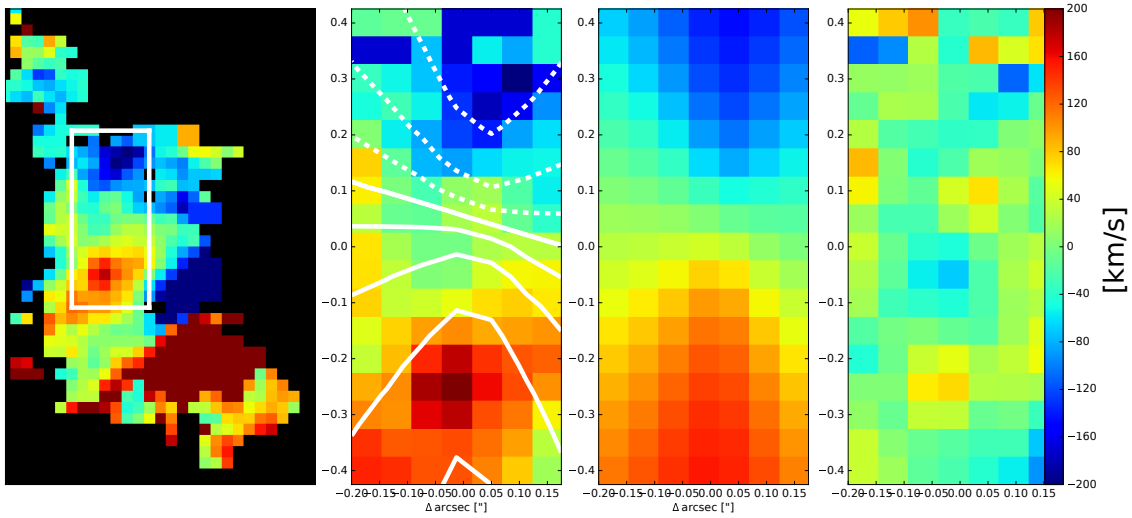

Figure 3.5 Observed and modeled galactic rotation disc, detected in the nebular [OIII] line in the 3C 298 system. (LEFT) The entire [OIII] radial velocity map with overlaid region used for the modeled disc fit. (MIDDLE LEFT) Observed [OIII] velocities with the spider diagram overlaid from the disc model. (MIDDLE RIGHT) The best fit 2D disc model. (RIGHT) The residual map shows the observed velocities subtracted by the disc model fit. The dynamical center is at 0,0.

from the quasar by 1.06 $''$ or $\sim$ 9 kpc, which is evidence of a merging disc system in 3C 298. We obtain a dynamical mass of $1.3 \pm 0.8 \times 10^{10} \mathrm{M}_{\odot}$ within a radius of $r_{dyn} = 2.2$ kpc. The dynamical center of this disc is in the vicinity of the isolated AGN outflow identified in Figure 3.2. With currently available archival Chandra ACIS observations we are unable to explore the X-ray properties of this secondary AGN candidate. Unfortunately there is strong asymmetry in the Chandra PSF along this position angle from the quasar. Future Chandra observations at a specific spacecraft roll angle will allow us to search for X-ray emission from this secondary AGN and explore the potential dual AGN nature of this system.

3.4.6 ALMA: Data reduction

Data reduction was performed using CASA (Common Astronomy Software Applications (McMullin et al., 2007)) version 4.4 and 4.7. At the observed frequencies, synchrotron emission from the quasar dominates over molecular CO or dust emission, and has sufficient SNR to perform self calibrations directly on the science source. We used the CASA *CLEAN* function to establish a model for the synchrotron continuum through several interactive runs with clean masks centered on high SNR features. Cleaning is performed with Briggs weighting using a robust value of 0.5 with a pixel scale of $0.05''$. We used the *gaincal* function to perform phase corrections. The self-calibrated data was then cleaned again with further phase corrections until we did not see a significant improvement in the SNR on the continuum. The final root mean square (rms) improved by a factor of 6-8 in the continuum images. We perform continuum subtraction in UV-space by fitting a first order polynomial to channels free of line emission from the host galaxy, and subtract this fit from the rest of the channels.

Data cubes were imaged using clean with a plate scale of $0.05''$ per pixel, spectral channel size of 34 $\mathrm{km\,s^{-1}}$ and natural weighting to improve SNR in diffuse structure of the host galaxy at cost of angular resolution. For cycle 3 data, clean masks were placed on CO emission with SNR$>$5 with the same mask applied to all channels. The resulting beam sizes and rms values are reported in Table 3.1.

We find the cycle 2 band 4 data cube is a factor of 2 noisier due to poorer weather conditions at the time of observations. Faint emission is detected with a peak SNR of 3.6σ for CO (J=3-2) emission over a number of spaxels in the east/north-east direction from the quasar. Ap-

plying UV tapering to a resolution of $0.98'' \times 0.8''$with Briggs weighting (robust = 0.5) improves the SNR to 5 however the line is not spatially resolved. Therefore for the analysis of CO (J=3-2) we defer to cycle 3 data taken under superior weather conditions.

We align the ALMA and OSIRIS data cubes by matching the position of the optical quasar emission to the unresolved quasar synchrotron emission centroid in the continuum map. The centroid of the quasar matches the location of the unresolved point source with the flattest spectra seen using high resolution cm observation of 3C 298 with MERLIN (component B1/B2 in (Fanti et al., 2002)). This location is typically associated with the quasar core. Finally, we rotate the ALMA data cube to a position angle of 103° to match the OSIRIS observations.

3.4.7 ALMA: Analysis

In this section we describe the analysis of resolved CO (3-2) and (5-4) 3D spectroscopy. Initial inspection revealed high SNR $\gtrsim 5$ detection of CO (J=3-2) and (J=5-4) emission. We extracted spectra over the beam size centered on the detected regions. We then collapsed the data cube over spectral channels where the CO features are detected, and constructed SNR maps by dividing the integrated emission by the standard deviation computed in an empty sky region. Spaxels that showed an emission line with a SNR ≥ 3 are fit with a Gaussian profile. We constructed a flux map by integrating over the line (-3σ to $+3\sigma$). We created a velocity map by computing the Doppler shift of the emission line centroid relative to the redshift (z=1.439) of the broad line region (calculated from Hβ), and generated a velocity dispersion map from the Gaussian fit. Figure 3.6 shows the CO emission, radial velocity, and dispersion maps.

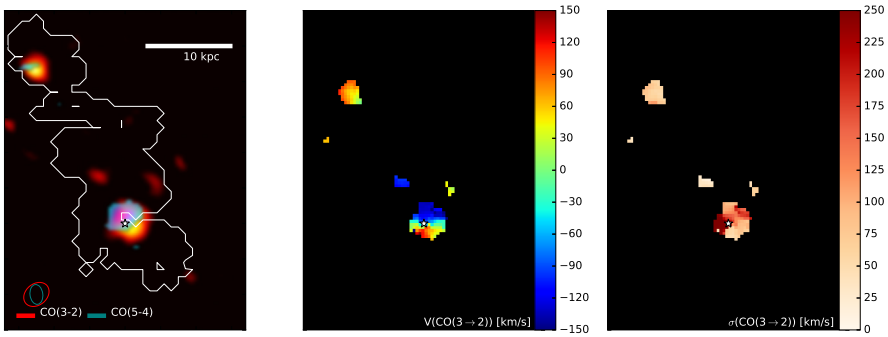

Figure 3.6 ALMA band 4 and 6 CO (J=3-2) and (J=5-4) observations of 3C 298. (LEFT) Integrated emission shown in red for CO (3-2) and teal for CO (5-4) with white contours representing the lowest surface brightness of the integrated Hα map. (MIDDLE) Radial velocity map (km s^{-1}) for CO (3-2) data relative to the redshift of the quasar. (RIGHT) Radial velocity dispersion map (km s^{-1}) of CO (3-2) emission. We find that majority of the molecular gas resides in a disc centered on the quasar and in a molecular clump 16 kpc away from the quasar where active star formation is present as indicated by the log([OIII] /Hβ) and log([NII]/Hα) line ratios (blue region in Figure 3.3). The synthesized beam is shown in the lower left corner. White star marks the location of the quasar

Molecular gas velocity field modeling

In this section we outline modeling performed on the CO (3-2) radial velocity map to derive a dynamical mass for the inner $\sim$2 kpc of the host galaxy. We find the majority of the CO emission to be concentrated at the spatial location of the quasar and with a secondary peak offset by 16 kpc spatially coincident with the recent star formation from OSIRIS BPT analysis (see Figure 3.3 and section 3.4.4). CO (3-2) emission concentrated on the quasar shows a distinct velocity gradient resembling a rotating disc, with an extent of about 0.8$''$ with a velocity difference of $\pm$150 km s^{-1} . Similar to section 3.4.5 we model the molecular disc with a hyperbolic arctangent function and derive the following properties about the disc: χ^2_R =0.6: $x_0, y_0 =$ 0.05$''$, 0.0$''$ relative to the centroid of the quasar, V_{max}= 392$\pm$65 km s^{-1} , r_{dyn} = 2.1 $\pm$0.9 kpc, $i = 54.37 \pm 6.4°$, $\phi = 5.3 \pm 1.28°$, and $V_0 = -13.0 \pm 3.15$km s^{-1} . Fit of the disc along with

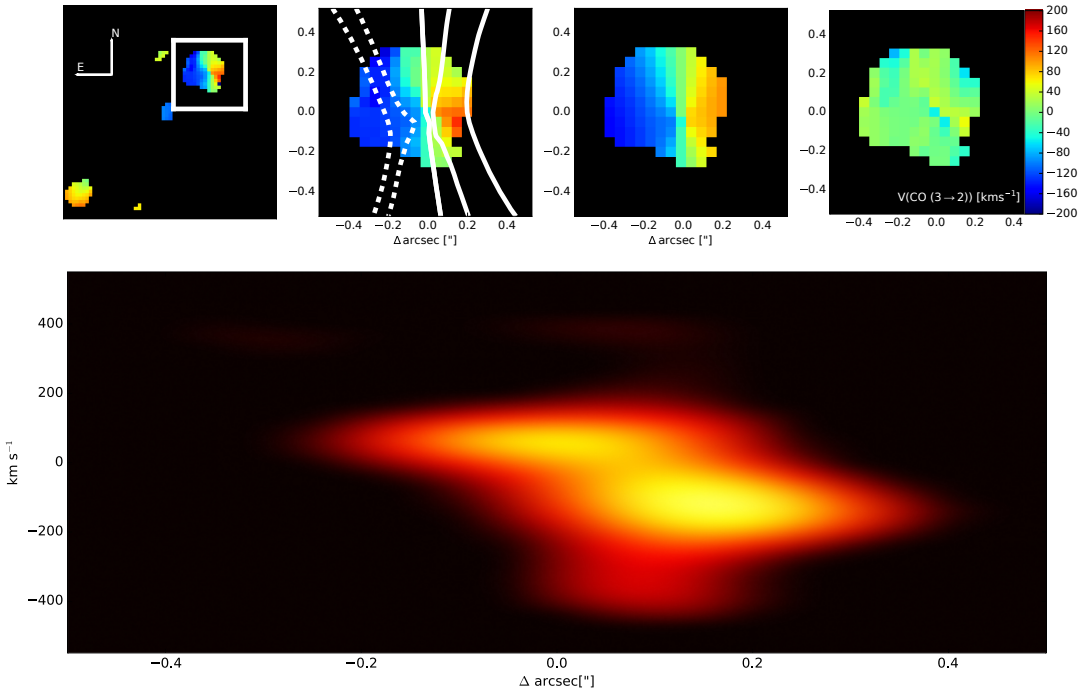

Figure 3.7 (TOP LEFT) Velocity field modeling of the molecular disc. CO (3-2) radial velocity map with a box highlighting the location of the molecular disc. (MIDDLE LEFT) Boxed region with spider diagram of the disc model. (MIDDLE RIGHT) The best fit rotating disc model. (RIGHT) The residuals between the observed velocity and model fit. The quasar is located at 0,0. The fitting was done on data at the ALMA observation position angle of 0° to avoid any pixel interpolation that may cause a difference in the fitting results. (BOTTOM) Position velocity (PV) diagram along the major axis of the ALMA disc, which illustrates the the velocity field and plateau velocity on kiloparsec scale. Broad blue shifted emission that is not associated with the disc's rotation is observed in the PV diagram from -400 to 200 km s^{-1} as the large molecular outflow.

the residuals are shown in Figure 3.7. We derive a dynamical mass $1.7\pm0.9 \times 10^{10}$M$_{\odot}$ within r_{dyn} =2.1 kpc using the disc inclination derived from the velocity modeling.

Alternatively, we collapsed the data cube along the spectral direction from -150 km s^{-1} to +150 km s^{-1} to produce a CO (3-2) image of the molecular disc. Using a 2D Gaussian we obtain a major axis value of $0.374\pm0.05''$and a minor axis of $0.155\pm0.098''$ corrected for the beam size. Assuming the molecular disc can be approximated by an oblate spheroid we derive

the inclination angle using the following formula (Holmberg, 1946):

$$\mathrm{i} = \cos^{-1}\sqrt{\frac{(\mathrm{b/a})^2 - \mathrm{q_0^2}}{1 - \mathrm{q_0^2}}}, \tag{3.5}$$

where a and b are the major and minor axes, and $\mathrm{q_0}$ is the axial ratio for an edge on disc taken to be 0.13. We derive a dynamical mass of $1.0 \pm 0.5 \times 10^{10}$ $\mathrm{M_\odot}$ using a major axis radius of 1.6 ± 0.215 kpc and an inclination angle of $66.6 \pm 17.8°$. The dynamical masses and disc inclination angles obtained with these two methods agree within the error. With two distinct galactic discs (see section 3.4.5) in the 3C 298 system we are finding evidence for an intermediate-late stage merger.

Shen et al. (2011) determined a single epoch black hole mass for 3C 298 using three calibration methods: $10^{9.57\pm0.03}$ $\mathrm{M_\odot}$ using the MgII-black hole mass relationship calibrated from their study; $10^{9.37\pm0.03}$ $\mathrm{M_\odot}$ using the Vestergaard and Osmer (2009) calibration; and $10^{9.56\pm0.01}$ $\mathrm{M_\odot}$ using McLure and Dunlop (2004) relation. The systematic differences between black hole mass measurements are typically due to differing quasar samples, and properties of the emission lines (e.g., Hβ) used for the SMBH mass calculation.

With both the derived dynamical and black hole mass we can compare the nuclear region of 3C 298 to the local black hole $\mathrm{M_{bulge}} - \mathrm{M_{BH}}$ relationship. In Figure 3.8 we plot the 3C 298 black hole and bulge dynamical mass relative to the local scaling relation from Häring and Rix (2004); Sani et al. (2011); McConnell and Ma (2013). Compared to all three relationships the 3C 298 bulge dynamical mass is either ∼2-2.5 orders of magnitude lower than what is expected or the black hole is $\sim$ 2 orders of magnitude higher than what is expected for its bulge mass.

If one assumes the 3C 298 bulge is more extended than what is measured by ALMA, then we can use the tidal feature at 21.5 kpc as an estimate for the total enclosed mass. To do this, we integrate all spaxels with a detected CO (3-2) line and remove the outflow contribution by simultaneously fitting a broad and a narrow Gaussian component to the outflow region. We measure a maximum line width of 369.3 $\mathrm{km\,s^{-1}}$ at 90% intensity, and find the maximum circular velocity of 184.6/$\sin(i)$ $\mathrm{km\,s^{-1}}$ at 21.5 kpc from the quasar. Using this maximum circular velocity, we obtain a total enclosed mass at this radius of $\sim 2.7 \times 10^{11}$ $\mathrm{M_{\odot}}$ assuming the smallest measured inclination angle from the molecular disc. This value should be considered as a maximum limit for the total enclosed mass of the 3C 298 system. This enclosed dynamical mass at 21.5 kpc from the quasar still places 3C 298 an order of magnitude above from the local scaling relation. Also, the radius used for this calculation is significantly larger than the typical bulge radius at this redshift (Bruce et al., 2014; Sachdeva et al., 2017), and there is no guarantee that the entire enclosed stellar mass will end up in the newly created bulge once the merger is finished. This implies a delay in growth of the galactic bulge for the 3C 298 host galaxy with respect to its SMBH. Averaging SMBH masses and dynamical masses determined for 3C 298 we obtain the following values: $\mathrm{M_{dyn,bulge}} = 1.35 \pm 0.5 \times 10^{10}$, $\mathrm{M_{SMBH}} = 3.23 \pm 1.1 \times 10^{9}$. Errors are added in quadrature with the SMBH mass standard deviation included to address the systematic uncertainty associated with using various calibration methods.

Molecular gas mass

In this section we derive the molecular gas mass from spatially integrated CO (3-2) and (5-4) emission presented in Table 3.2.

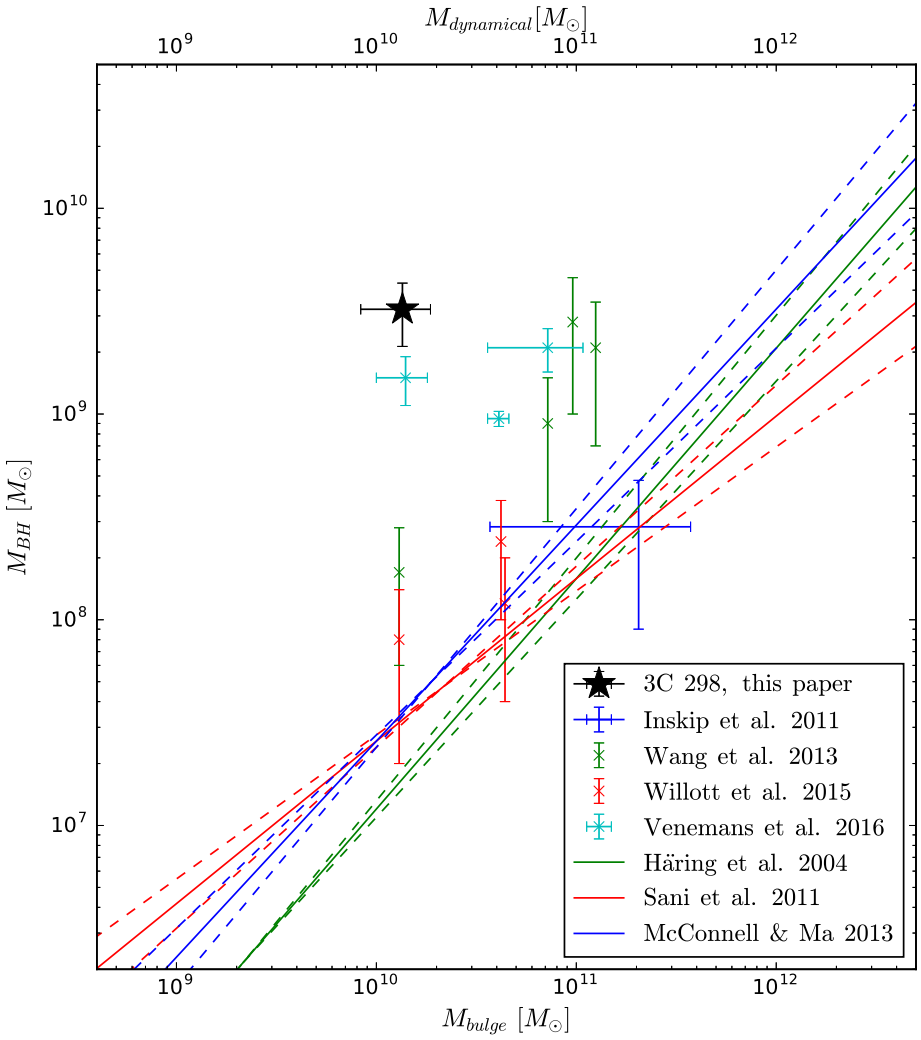

Figure 3.8 Local SMBH vs galactic bulge dynamical mass relationship compared to 3C 298 measured values. The black star represents the average dynamical mass derived from the intensity and kinematic molecular gas disc modeling and the average black hole mass derived with McLure and Dunlop (2004); Vestergaard and Osmer (2009); Shen et al. (2011) relationships. Errors are added in quadrature from the various methods used to derive the dynamical mass of the disc and the black hole mass. Local scaling laws from various studies (Häring and Rix, 2004; Sani et al., 2011; McConnell and Ma, 2013) are shown in solid lines with their respective 1σ errors shown with dotted curves. The observed black hole mass and dynamical mass of the bulge of 3C 298 resides $\sim$2-2.5 orders of magnitude away from the local scaling relation. Points from literature (Wang et al., 2013; Willott et al., 2015; Venemans et al., 2016) for z$>$ 5.7 quasars are also included. There is line of evidence that some of these high redshifts systems also reside off the local scaling laws.

Table 3.2 Measured molecular line intensities

Region	$I_{CO(3-2)}$	$I_{CO(5-4)}$
Molecular disc	0.63±0.035 Jy km s^{-1}	1.26±0.063 Jy km s^{-1}
Tidal Feature[a]	0.13±0.013 Jy km s^{-1}	0.1±0.025 Jy km s^{-1}

[a]Molecular gas associated with star forming region labeled in blue in Figure 3.3

In order to measure the molecular gas in the 3C 298 system we convert the CO (3-2) flux into $L^{'}_{CO(3-2)}$ using the following equation from Carilli and Walter (2013),

$$\mathrm{L}^{'}_{\mathrm{CO(3-2)}} = 3.25 \times 10^{7} \mathrm{S}_{\mathrm{CO(3-2)}} \Delta \mathrm{v} \frac{\mathrm{D}_{\mathrm{L}}^{2}}{(1+\mathrm{z})^{3} \nu_{\mathrm{obs}}^{2}} \mathrm{K\ km\ s^{-1}\ pc^{2}}. \tag{3.6}$$

We convert to CO (1-0) luminosity ($\mathrm{L}^{'}_{CO(1-0)}$) using a ratio $L^{'}_{\mathrm{CO(3-2)}}/L^{'}_{\mathrm{CO(1-0)}}$ of 0.97 (Carilli and Walter, 2013). Using the typical α_{CO} value from nuclear star bursts and quasars (0.8 K km s^{-1} pc^{2})$^{-1}$), we derive a total molecular gas mass equal to $8.75 \pm 0.4 \times 10^{9} \mathrm{M}_{\odot}$. The total molecular gas includes all regions with a fitted CO (3-2) line in Figure 3.6. The molecular gas disc contains $6.6 \pm 0.36 \times 10^{9} \mathrm{M}_{\odot}$, while the active star formation region that resides 16 kpc away contains $1.44 \pm 0.14 \times 10^{9} \mathrm{M}_{\odot}$. We measure a 2σ molecular gas limit of $1 \times 10^{9} \mathrm{M}_{\odot} (\frac{\alpha_{\mathrm{CO}}}{0.8})(\frac{\mathrm{V_{FWHM}}}{200 \mathrm{kms^{-1}}})$ per beam. This corresponds to a molecular gas surface density of 104 $\mathrm{M}_{\odot}\ \mathrm{pc}^{-2}(\frac{\alpha_{\mathrm{CO}}}{0.8})(\frac{\mathrm{V_{FWHM}}}{200 \mathrm{kms^{-1}}})$. These estimates are valid for the inner few arcseconds around the phase center (quasar).

CO (3-2) and (5-4) emission in some spaxels shows relatively broad ($V_{\sigma} > 270 \mathrm{km\,s^{-1}}$) emission, greater than the escape velocity $\sqrt{2} V_{rotational} \sim 270$ km s^{-1} at the observed edge of the rotating disc. In the position-velocity diagram (Figure 3.7) broad blue-shifted emission is seen with velocities ranging from -400 to 200 km s^{-1} that spatially resides away from the ordered

$\pm$150km s^{-1} rotation profile. Integrating over these spaxels the CO (3-2) and (5-4) emission profiles resemble both an outflow with broad emission, and narrow emission that is likely emanating from the molecular disc. We fit a double Gaussian component to the CO (3-2) line and a single Gaussian to the CO (5-4) data. We measure FWHM of 624$\pm$49 km s^{-1} for the broad line emission in CO (3-2) and 687$\pm$18 km s^{-1} in CO (5-4). The broad emission line represents either an extended outflow originating from the nuclear region of 3C 298 quasar or from the molecular disc itself. Figure 3.9 shows spectra of the CO (3-2) and (5-4) emission regions with their corresponding Gaussian fits. The broad emission in both lines is predominantly found on the blue shifted side of the rotating disc. The total molecular gas in the outflow is $3.3\pm0.1 \times 10^9$ $M_\odot$. In section 3.5 we measure the molecular gas outflow rate, kinetic energy, and momentum to understand its impact on the galaxy.

3.4.8 HST WFC3: PSF Subtraction

We obtain archival Hubble Space Telescope (HST) observations of 3C 298 to quantify properties of the stellar populations of the host galaxy (GO13023, P.I. Chiaberge). Detailed description of the observations are available in (Hilbert et al., 2016). In summary, observations were taken in the F606W (λ_p=588.7 nm, width = 218.2 nm) and F140W (λ_p=1392.3 nm, width=384.0 nm) filters which cover the rest frame wavelength range of 196.6 nm - 286.1 nm and 492.1-649.6 nm, respectively. These wavelength ranges bracket the 4000Å break feature in galaxy spectra. Two observations were taken in each filter for a total exposure time of 1100.0s (F606W) and 498.46s (F140W).

We utilize the nearby star SDSS J141908.18+062834.7 to construct a PSF for the F606W

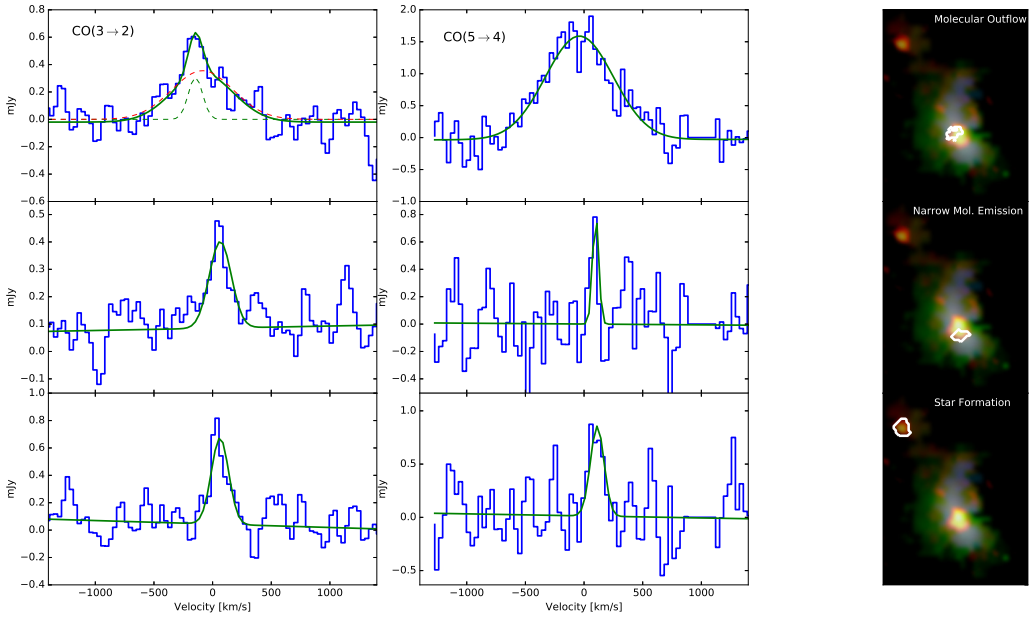

Figure 3.9 Spectra of molecular CO (3-2) and (5-4) emission in distinct regions of the host galaxy. Left and middle columns show CO (3-2) and (5-4) emission spectra respectively, while the right column showcases a three colour composite from nebular emission lines [OIII] , Hα , [SII] with an overlay of CO (3-2) emission in orange. White contours represent the region over which the cubes were spatially integrated to construct the spectra. (TOP) Spectrum constructed by integrating over region with broad ($V_\sigma > 270 \mathrm{km\,s^{-1}}$) emission implying a molecular outflow. Both lines are fit with a broad Gaussian profile, CO (3-2) requires a second narrow component that is likely emission from the disc. (MIDDLE) Spectrum constructed over region with narrow emission in the molecular disc, both spectra are well fit with a single Gaussian component. (BOTTOM) Integrated spectrum over the molecular reservoir in the star forming region identified in Figure 3.3. Both CO (3-2) and (5-4) spectra are fit with a narrow component.

filter. The PSF star and quasar have a similar magnitude in the F606W filter with a similar g-r colour as measured in SDSS. Both the PSF star and quasar are saturated, so they share similar bleeding and diffraction patterns on the detector. In the F140W filter the quasar is unsaturated and is about 0.8 magnitudes brighter, so we combine two unsaturated stars in the field to produce a final PSF with matching SNR in the diffraction spikes structure. We extract a $12'' \times 12''$ box centered on the quasar and the PSF, and scale the flux of the PSF image to match the peak of the quasar emission and then subtract the two images. We also tried to match only the flux in the diffraction spikes that do not overlap with the structure in the host galaxy, and obtained a similar scaling factor. In both filters the inner $1''$ is dominated by noise from the PSF subtraction, the diffraction spikes at position angles of 0°, 180°, 225° and along the bleeding pattern in the F606W filter that extends about 0.5" along PA 0° from the quasar. However, the majority of the host galaxy lies between position angles of 45° and 170° where the structure is least affected by residual noise. The quoted residual structure are for an image at a PA of 103° matching the observations of OSIRIS and ALMA.

We convert electron counts at each pixel into flux density (Jy) using the 'PHOTFNU' header value. We resize the pixels to 100 milliarcsecond plate scale to match OSIRIS and ALMA data by using the flux conserving IDL *frebin* routine. We convert the maps into AB magnitude/arcsec^2 and construct a colour map of the host galaxy. Reliable colours are extracted down to a surface brightness limit of 23.5 AB mag/arcsecond^2 for the majority of the host galaxy, with the exception of the redshifted outflow region that falls in the area dominated by residual noise from PSF subtraction.

Figure 3.10 presents the WFC3 F606W (left) and F140W (middle) after PSF subtraction

in 0.1″/pixel scale. The right panel shows the resolved host galaxy colours (F606W-F140W). Overlaying Hα contours on the colour map shows that the star forming regions identified in OSIRIS (blue region in Figure 3.3) nicely aligns to regions with bluer colours. Additionally we overlay the ALMA CO (3-2) observation. The molecular clump offset 16 kpc from the quasar matches with bluer regions where clumpy structure is seen in the F606W observations, yielding evidence for young stellar populations over these regions as would be expected from on-going star formation.

3.4.9 HST WFC3: Stellar population

Two available filters for the 3C 298 system are ideally placed to bracket the break feature at rest-frame wavelength of 4000Å found in galaxy spectra. Thus we can easily identify young ($<$100 Myr) stellar populations without any ambiguity, as we attribute blue colours (F606W-F140W $<$1.5) in these filters to stellar populations dominated by young O and B stars. Redder colours in these filters can come from older stellar populations (100 Myr - 1 Gyr) or from young dusty star forming regions, and thus we are unable to say much about older stellar populations without additional filters.

HST colours provide strong constraints on the resolved star formation and stellar population history across the 3C 298 system. We approximate the HST colour map with the flexible stellar population synthesis (FSPS) code (Conroy et al., 2009; Conroy and Gunn, 2010), using a five parameter star formation history model. We start the FSPS code with an exponential star formation history that is followed by a burst of star formation 2 Gyr later, using a solar metallicity and Salpeter IMF. Using the FSPS code, we find that varying the star formation history and

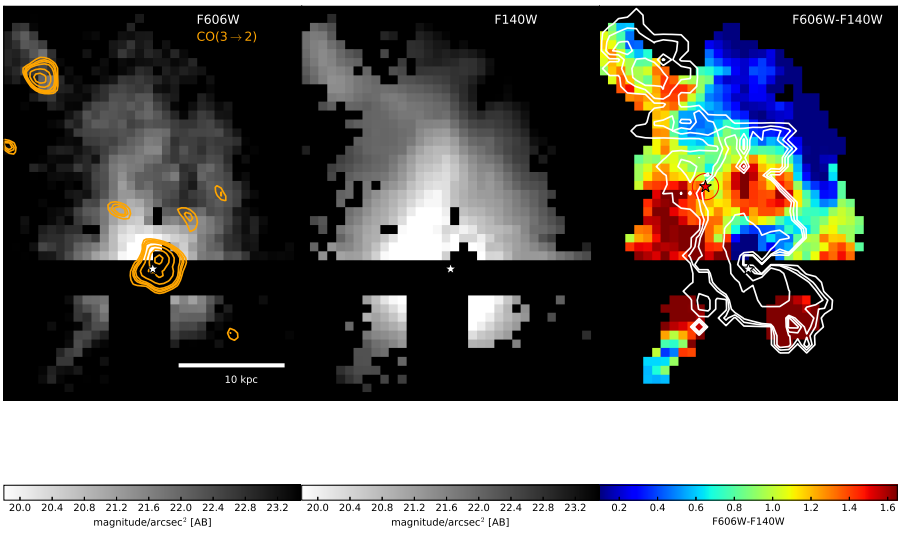

Figure 3.10 HST WFC3 Rest-frame near-UV (F606W) and approximately rest frame V band (F140W) images of the stellar light in the host galaxy of 3C 298. The images have had the bright unresolved quasar emission subtracted from them. (LEFT) Rest frame near-UV image representing light from young massive stars in the 3C 298 system. Orange contours represent the CO 3-2 ALMA observations of the molecular gas. The UV morphology appears clumpy as in Hα , indicating regions heated by young stars. (MIDDLE) Rest frame V band image which traces light from a combination of young and older stellar populations. The units are in AB magnitude/arcsec^2. (RIGHT) Colours (F606W-F140W) of stars in the host galaxy of 3C 298 representing the ages of the stellar populations. White contours represent integrated Hα luminosity tracing the ionized gas; note the similarity between the morphology of the ionized emission and the stellar light. Bluer regions contain younger stars, and are typically found where clumpy structure exists in Hα , CO and UV light; these regions are sights of active star formation. Red star represents the location of the dynamical center of the second merging galaxy in the system.

e-folding time scale τ from 0.1 to 10^2 prior to the starburst does not significantly affect the age of the stellar population post starburst.

The average F606W-F140W colour over the blueshifted outflow region is best explained with a stellar population that has an age of 25 Myr after the burst. According to ionized gas emission, dust does not affect the age estimated in this region since the Hα and Hβ ratio suggests a low E(B-V)$\sim$0 value. However ALMA observations reveal that part of the molecular disc centered on the quasar has extened emission into the blueshifted outflow region suggesting that a part of the region can have higher dust extinction. The age of the outflow region and the modelled rest frame U-V colour imply that the stellar population resides in the transition zone between the red sequence and blue cloud in the U-V vs M_V colour diagram (Hopkins et al., 2008; Sánchez et al., 2004; Bell et al., 2004). Furthermore u-r modelled colours at this age suggest that the region lies where post starburst galaxies reside in the u-r vs $M_{stellar}$ diagram (Wong et al., 2012). The extracted 3C 298 model spectra shows strong Balmer absorption lines with a strong 4000Å break, characteristic of a post-starburst galaxy. Stellar colours over the blueshifted outflow region are consistent with a strong episode of star formation that was abruptly halted.

In the region where star formation is identified in Figure 3.3 based on BPT diagnostics and in the molecular gas clump found in CO, using the same initial conditions in the FSPS code with the outflow region, we find a stellar population with an age of 20 Myr after a burst of star formation. Without any dust correction this age should be taken as an upper limit. Ahead of the jet/blueshifted outflow we find an even younger stellar population. From the Hα emission we can place a limit of 0.3 $M_\odot$ yr^{-1} kpc^{-2} across this region. ALMA observation of the CO (3-2) transition yields a limit of $1\times10^9 M_\odot$ on the molecular gas. This suggests that the current star

formation rate is relatively low. However the blue colours indicate recent star formation activity. The stellar populations in this region would then be associated with a young age of 7 Myr after the burst. It is likely that the star formation event was very recent and short (6-10 Myr) due to lack of Hα emission that would otherwise be present if star formation persisted for a time longer than 6 Myr.

Ages quoted in this analysis could be altered by additional quasar emission from light scattered off dust grains or electrons in the ISM making the colours systemically bluer. However polarimetric observations of 3C 298 reveal that the source is not heavily polarized, with an optical polarization of only $0.77\pm0.39\%$ (Stockman et al., 1984). Given that the bluest regions also show star formation from other indicators (e.g, Hα and CO (3-2) emission), this implies that the majority of UV emission comes from young massive stars and not from scattered quasar light. The young stellar population observed $>$16 kpc beyond the blueshifted outflow is even further away than the region photoionized by the quasar, indicating that ionizing radiation from the quasar does not reach this region.

3.5 Dynamics and energetics of outflow regions

In this section we explore the dynamics and energetics of the ionized and molecular outflows identified in sections 3.4.3, 3.4.4, and 3.4.7. We explore the energy budget from a broad absorption line (BAL) wind and from the quasar jets to investigate the origin of the galactic scale winds.

3.5.1 Outflow rates

The redshifted and blueshifted outflow regions resemble a cone-like structure. For a conical outflow with constant density ($\overline{\rho}$) we use the outflow rate equation from (Cano-Díaz et al., 2012),

$$\dot{M} = vR^2\Omega\overline{\rho}, \tag{3.7}$$

where v is the velocity of the material in the outflow assumed to be moving at a constant rate over the cone, R is the radial extent of the cone and Ω is the opening angle of the cone. For $\overline{\rho} = M/V = \frac{3M}{R^3\Omega}$ the outflow rate equation simplifies to

$$\dot{M} = 3\frac{Mv}{R}. \tag{3.8}$$

Assuming individual ionizing clouds in the outflow have the same density, we can derive an ionized gas mass from line-integrated Hα luminosity and average electron density over the outflow using (Osterbrock and Ferland, 2006),

$$\mathrm{M_{gas\ ionized}} = 0.98 \times 10^9 \left(\frac{\mathrm{L_{H\alpha}}}{10^{43}\ \mathrm{ergs^{-1}}}\right)\left(\frac{\mathrm{n_e}}{100\ \mathrm{cm^{-3}}}\right)^{-1}. \tag{3.9}$$

The electron density is derived from the line ratio of the [SII] lines in the blueshifted outflow region through using a Gaussian fit to each component of the doublet. We find a ratio of ([SII] 6717/[SII]6731=1.14), which yields an electron density of 272 cm^{-3} using the *getTempDen* code part of *PyNeb* (Luridiana et al., 2015) package. We calculate the ionized gas mass from the [OIII]

line using methodology presented in (Cano-Díaz et al., 2012). This method requires knowledge of the ionized gas-phase metallicity at the site of the outflow region. We assume a metallicity value set to solar for a conservative estimate (i.e., for less than solar the gas mass increases). For the outflow velocity we use the v_{10} parameter, which is the velocity value where 10% of the line is integrated. This value is calculated from the model fits to the spatially integrated [OIII] and Hα lines for each outflow region. The wings of the emission lines most likely give the true average velocity of the outflow, as the lower velocities seen in the line profiles are probably due to projection effects of the conical structure (Cano-Díaz et al., 2012; Greene et al., 2012). Measured properties of the the outflow regions are presented in Table 3.3.

For the redshited and blueshifted outflow regions we obtain a combined outflow rate of 467 $M_\odot$ yr^{-1} and 1515 $M_\odot$ yr^{-1} for [OIII] and Hα , respectively, while for the AGN outflow region we obtain an outflow rate of 9 $M_\odot$ yr^{-1} and 115 $M_\odot$ yr^{-1} for [OIII] and Hα . The Hα outflow rate is likely a better representation of the ionized outflow rate, since Hα is capable of probing denser regions where [OIII] would be collisionally de-excited. The observed Hα outflow rate is similar to what is observed in other quasar surveys (Carniani et al., 2015), where they measure a larger outflow rate in Hα compared to [OIII] . The total kinetic energy and luminosity of the ionized outflow are 3.5×10^{58} erg and 1.2×10^{45} erg s^{-1}. The kinetic luminosity is consistent with the value usually invoked in theoretical models (Hopkins and Elvis, 2010a) as necessary to affect star forming properties in the host galaxy. Over the outflow regions we measure a 2σ star formation rate upper limit of 0.3 $M_\odot$ yr^{-1} kpc^{-2}, by using a Gaussian profile with 2σ peak flux and FWHM of 200 km s^{-1} , with the multi-Gaussian fit of the outflowing gas subtracted. The properties of the multiple outflow components are summarized in Table 3.3

Similarly using equation 3.8 we compute the molecular outflow rate. As found in section 3.4.7 the extent of the broad molecular emission from CO (3-2) and (5-4) lines is approximately 1.6kpc, the total molecular gas mass in the outflow region is 3.3×10^{9}M$_{\odot}$ with an outflow velocity of 400km s^{-1} as measured by V_{10} parameter. This yields a total molecular outflow rate of 2300M$_{\odot}$ yr^{-1} . The kinetic energy and luminosity of the molecular outflow are 5.1×10^{57} erg and 1×10^{44} erg/s.

3.5.2 Virial parameters & gas pressure

Using the virial parameter, a ratio of the free fall time scale to the dynamical time scale we can investigate whether the gas is gravitationally bound or unbound in the outflow regions and molecular disc. A value of unity or below would suggest that the gas is bound and is able to collapse to form stars. A value much greater than one would suggest that the gas is unbound and therefore at present time should not be collapsing to form stars. Over the outflow region we measure a virial parameter

$$\alpha_{\rm vir} = 5\frac{\sigma^2 R}{GM} \approx 164 \left(\frac{\sigma}{500\,{\rm km\,s^{-1}}}\right)^2, \tag{3.10}$$

using an average velocity dispersion of $\sigma = 500\,{\rm km\,s^{-1}}$ seen in the ionized outflow, a radius of $R = 3$ kpc, and the ionized gas mass (1.32×10^{9} M$_{\odot}$). Using the molecular gas mass of 6.6×10^{9} M$_{\odot}$ an average velocity dispersion of 270 km s^{-1} seen in the molecular outflow and a radius of 1.6 kpc yields $\alpha_{\rm vir}$ of 20.5. Both of these virial parameter estimates suggest that at the present time, the physical conditions in the ionized and molecular outflow regions and in the

Table 3.3 3C 298 Ionized Outflow Properties

Region	$L_{H\alpha}$ $\times 10^{44}$ erg s^{-1}	$L_{[OIII]}$ $\times 10^{44}$ erg s^{-1}	$M_{H\alpha}$ $\times 10^{8} M_{\odot}$	$M_{[OIII]}$ $\times 10^{8} M_{\odot}$	v km s^{-1}	R kpc	$\dot{M}_{H\alpha}$ $M_{\odot}$ yr^{-1}	$\dot{M}_{[OIII]}$ $M_{\odot}$ yr^{-1}
Outflow-R	0.29	1.8	10	3.5	1703	4.7	1110	390
Outflow-B	0.09	0.3	3.2	0.6	1403	3.4	405	77
Outflow-AGN	0.03	0.04	0.8	0.064	1400	3	115	9

molecular disc are stable against gravitational collapse, hindering star formation. In contrast, the molecular gas clump in the star forming region observed in CO (3-2) yields a virial parameter value of $\alpha_{\rm vir} \approx 0.7$. A value close to unity suggests that star formation should be able to proceed in this region, where there are no powerful outflows.

If the quasar-driven wind does not efficiently cool and adiabatically expands, then the initial driving mechanism is capable of transferring its kinetic energy into mechanical energy in the galactic-scale outflow. The momentum flux of the outflow should therefore be greater than $L_{\rm bol}$/c (Zubovas and King, 2012). We measure total momentum flux ($\dot{P}_{\rm outflow} = \dot{M} \times v$) of 2.1×10^{37} dynes over the entire outflow region. We use the 3000Å quasar luminosity to compute a bolometric luminosity value of 1.04×10^{47} erg s^{-1} (Runnoe et al., 2012). Comparing the outflow momentum flux to the quasar radiation momentum flux ($L_{\rm bol}$/c) of 3.5×10^{36} dynes, yields a ratio $\dot{P}_{\rm outflow}/\dot{P}_{\rm quasar}$ (loading factor) of 6. In principle this ratio is a lower limit, since there can still be diffuse molecular gas in the ionized outflow regions whose CO emission is below the sensitivity of ALMA. Based on theoretical work by Faucher-Giguère et al. 2012; Zubovas and King 2012 the measured loading factor of $>$6 suggests that the wind is energy-conserving. The total kinetic luminosity of the outflow is also about 2% of $\rm L_{bol}$, consistent with the above theoretical prediction. 3C 298 observed extended outflow properties strongly suggests that radiation pressure by itself is unable to drive the outflow. Star formation is also incapable of driving the observed outflow as the expected terminal velocity for a supernova driven galactic scale wind is only σ $\sim$200 km s^{-1} (Murray et al., 2005), far lower than the observed velocities ($\sigma \sim 500$km s^{-1}) seen in the bi-conical wind.

The outflow could be induced by either the jet and/or broad-absorption line (BAL) winds

from the quasar. We infer a jet pressure

$$\mathrm{P_{jet}} \approx \frac{\mathrm{L_{jet}} \times \mathrm{t}}{3\mathrm{V}}, \tag{3.11}$$

of 3×10^{-8} dynes cm^{-2} using the jet kinetic luminosity of $1.4{\times}10^{47}$ erg/s, derived using the 1.4 GHz (570 MHz observed) radio flux-jet power relation (Bîrzan et al., 2008; Cavagnolo et al., 2010), assuming spherical volumes at a radius of 9 kpc and a time scale of 3 Myr. This is an order of magnitude calculation given the approximations in the jet luminosity, lifetime (t) of the jet, and volume. Observations of other BAL quasars indicate that the kinetic luminosity of outflows can get as high as 10^{46} erg s^{-1}(Chamberlain et al., 2015), which is close to the kinetic luminosity for the 3C 298 jet and would exert a pressure of 10^{-8} dynes cm^{-2}. This means that a BAL-type wind could potentially drive the extended 3C 298 outflow. However, there is no observed BAL in the optical and infrared spectra of 3C 298. The lack of an observed BAL in 3C 298 could be due to an orientation effect where our line-of-sight does not overlap with the absorbing outflowing gas. If this is not the case, and there is no BAL, the jet of 3C 298 still has the necessary ram pressure capable of inducing a large scale outflow.

The gas pressure ($P = nkT$) in the ionized ([SII]) gas is $\sim 4 \times 10^{-10}$ dynes cm^{-2}. From the ALMA CO (3-2) observations we measure a molecular gas surface density of 490 M$_\odot$ pc^{-1} indicating a molecular gas pressure ($P = (\pi/2)G\Sigma^2_{molecular}$) of $\sim 1{\times}10^{-9}$ dynes cm^{-2}. Both the BAL wind and quasar jet pressures are 2-3 orders of magnitude higher than the current pressure of the ionized and molecular ISM. The fact that the ionized gas pressure is comparable to or smaller than the weight per unit area of the molecular gas shows that the jet is not currently

producing an overpressure (which would be reflected in the thermal gas pressure of the ionized gas in the ISM) relative to the overburden of the molecular gas. This suggests that the jet is now venting out of the galaxy. The interaction between the ISM and the jet and/or BAL wind in the past was likely in a denser environment, and thus confined to a smaller volume with a higher pressure, to initially generate the outflows.

Both a BAL quasar wind and jet have enough kinetic energy to drive galactic scale winds. These large outflows in 3C 298 supply the necessary energy and momentum to hinder star formation along their path and expel large amounts of gas out of the galaxy. If the sources of turbulence were to halt at the present time, the shocks would dissipate on a dynamical time scale of 3-6 Myr. By that time the majority of the gas in the ionized outflow will have already escaped into the intergalactic medium with most of the molecular gas in the disc removed from the inner few kpc and potentially swept up into the ionized outflow. Any left over gas in the galaxy would quickly cool back into a molecular state. Taken together this shows both negative and ejective feedback occurring along the outflow region, thereby impacting the stellar mass growth of the quasar host.

3.6 Discussion

To generate a comprehensive picture of 3C 298, we combine multi-wavelength data to spatially resolve the ionized gas, molecular gas, and stellar light distribution of the host galaxy. This allows a unique comparison between the star formation histories, photo-ionization mechanisms, and gas-phase properties in a high-redshift quasar host galaxy. In Figure 3.11 we gener-

alize the multi-wavelength analysis of the 3C 298 system in a schematic diagram and summarize its properties in Table 3.4.

We make use of observations from VLA to probe the quasar radio jets, WFC3 data from HST to study the stellar contribution, ALMA to measure the resolved molecular gas morphology and dynamics, and Keck LGS-AO to determine the resolved ionized gas properties. These data show clear evidence of a conical outflow in the host galaxy of 3C 298, driven by quasar jets and/or winds, that directly impact the ISM of the host galaxy. VLA images of 3C 298 reveal synchrotron radio jets feeding lobes that extend over $\sim$ 18 kpc from the quasar in the east-west direction (Figure 3.1). Along the radio lobes, OSIRIS kinematic maps reveal broad ($\sigma \sim 800$ km/s) emission lines that are offset up to 600 $\mathrm{km\,s^{-1}}$ from the quasar's systemic redshift, indicating an outflow extending over a significant swathe of the galaxy.

We find direct evidence of negative feedback along the path of the jet and outflow regions of the host galaxy. The term "negative feedback" has been used loosely in the astronomical literature; herein we define negative feedback as injected energy and momentum in the ISM that inhibits the normal thermal cooling and/or decay of turbulence, thereby extending the time scale for star formation to occur. Galactic-scale feedback may also occur when high velocity outflows remove large fractions of the ISM, thereby impacting the star formation and stellar mass history of the host galaxy. The latter might be called "ejective feedback". Both negative and ejective feedback may occur simultaneously. The 3C 298 ionized outflow region has a bi-conical shape with a primarily blueshifted approaching side and redshifted receding side of the cone (Figures 3.1 and 3.3). Emission line ratios (e.g., [NII] /Hα and [OIII] /Hβ) allow us to distinguish between various photo-ionization modes of 3C 298's ISM, which is illustrated in the nebular diagnostic

diagram Figure 3.3. In both of the outflow regions we detect high nebular emission-line ratios that imply a combination of hard photoionizing radiation from the quasar and shock ionization. We find a total ionized mass outflow rate ($\dot{M}$) of 450-1500 $M_\odot$ yr^{-1} combined for both outflow regions. ALMA observations of molecular gas reveal a disc centered on the quasar. A large fraction of gas in the molecular disc reveals broad emission associated with a molecular outflow with a rate of 2300$M_\odot$ yr^{-1} . Unlike the ionized outflow the molecular outflow emanates in a single direction from the blueshifted side of the molecular disc. The molecular outflow either originates from the 3C 298 quasar nuclear region or from the disc itself. In the rest-frame of the redshifted ionized receding cone, two broad Gaussian functions are required to fit the profiles of the nebular emission lines (Figure 3.2). This indicates an approaching and receding component corresponding to the front and back of a hollow cone that suggests expansion of the outflow along our line-of-sight.

Combining kinematic maps from OSIRIS and ALMA reveals that the ionized outflow gas most likely originates from the molecular disc since the blue/red-shifted outflow matches the blue/red-shifted region of the disc. Furthermore the blueshifted molecular outflow is on the same side as the ionized. We find no narrow (σ <200 km/s) Hα emission in either of the outflow regions, suggesting that the majority of the ionized gas is in a turbulent phase. The outflow carries a significant amount of kinetic energy and it is capable of removing the majority of the galaxy's gas on a time scale of 3 Myr. The virial parameter deduced from the ionized and molecular gas over the outflow regions are much greater than one, implying that the ISM is not self-gravitating, and hence will not collapse to form stars. Similarly, the molecular outflow is both stirring the molecular gas and removing it from the inner regions of the galaxy. Ionization

occurring over the outflow region is dominated by shocks, which drives intense heating into the ISM that further inhibits star formation. Over the conical outflow region we derive a conservative limit for Hα emission due to star formation of < 14 M$_\odot$ yr^{-1} (2σ), or $\sim$0.3 M$_\odot$ yr^{-1} kpc^{-2} using the empirical Hα luminosity-star formation rate (Kennicutt, 1998). Colours of the stellar light as seen in HST data projected on the blueshifted outflow region are also consistent with a stellar population that had its star formation abruptly halted within the last $\sim$25 Myr (see Figure 3.10).

In the 3C 298 host galaxy we observe star forming regions that are offset from the outflows. The youngest (7 Myr) stellar populations observed with HST (Figure 3.10) imply that a recent burst of star formation has occurred. These regions are found 10-16 kpc east of the quasar. In addition, beyond the extended narrow-line and outflow regions, using OSIRIS and HST we resolve star forming clumps that reside $\sim$10-22 kpc (blue in Figure 3.3) away from the quasar. These clumps have an integrated star formation rate of 88$\pm$9 M$_\odot$ yr^{-1} , based on the observed Hα luminosity and empirical star formation rate relation (Kennicutt, 1998). ALMA CO (3-2) and (5-4) data reveal a molecular clump in the vicinity of this region with a total molecular gas mass of 1.4×10^9M$_\odot$. Using the HST-measured colours, we find a young stellar population with an age of $\sim$20 Myr in these star forming regions. Therefore, combining results from the resolved molecular gas, stellar populations, and ionized gas yields a consistent picture; we find star formation occurring away from large scale outflows, where the quasar winds and/or jets are stirring the ISM and removing gas.

The kinematic map of the ionized gas in 3C 298 shows a systematic velocity gradient across a large portion of the system. We fit this region with a rotating disc model (Figure 3.5). We find evidence for a second rotating disc in the system that is offset by $\sim$8.6 kpc and $\sim$170

km s^{-1} from the quasar centroid and central velocity of the broad line region. The dynamical center of the second disc is in the vicinity of a secondary outflow region, suggesting for the presence of a candidate second nucleus. The offset between the dynamical center of the second disc and the secondary outflow is on the order of 3kpc. We note that this is a typical separation that is found between the stellar centroid and AGN location in local late stage mergers (Liu et al., 2013b; Comerford et al., 2015; Barrows et al., 2016). We infer that the 3C 298 system likely has two massive galaxies with distinct rotating discs that are currently experiencing a close passage, where their galactic nuclei and SMBHs have yet to merge.

We calculated the enclosed dynamical mass of the molecular disc at the location of the quasar to be 1-1.7$\times10^{10}$M$_{\odot}$. With the measured SMBH mass ($10^{9.37-9.56}$M$_{\odot}$) 3C 298 resides off the local scaling $\mathrm{M_{bulge}} - \mathrm{M_{BH}}$ relationship, which indicates that black hole growth must occur earlier than stellar mass assembly. These results are similar to what has been recently observed in nearby ultraluminous infrared galaxies (ULIRGs) in gas-rich merger stages by Medling et al. 2015, where they find that these ULIRGs predominantly have early black hole growth and have yet to form the bulk of their stellar mass. Similar results have been found for a small number of z$>$ 6 quasar host galaxies observed with ALMA, where the black hole to galaxy bulge mass ratio is higher by a factor of 3-4 (Wang et al., 2013; Venemans et al., 2016) compared to local galaxies. This is counter to previous theoretical simulations that imply star formation and stellar mass build-up should occur during the gas-rich-merger phase, before the SMBH does its predominant growth when AGN feedback is suspected to transpire (i.e., Di Matteo et al. 2005; Hopkins 2012; Hopkins et al. 2016).

Models are still unclear about whether distant quasars should reside above, below or

even on an extension of the local SMBH-galaxy scaling relations. Hydrodynamical simulations of $z > 6$ quasars by Barai et al. 2017 suggest that negative feedback may drive quasars above the local scaling SMBH-galaxy relations. Barai et al. 2017 argue that conical, symmetric outflows can remove gas efficiently from galactic discs, while still allowing gas to accrete on to the SMBH perpendicular to the bi-conical outflow. Furthermore, the same simulations without quasar feedback tend to grow their stellar mass ahead of the SMBH, driving galaxies below the local correlations. Anglés-Alcázar et al. 2017b also find that the stellar bulges outpace the SMBH in the absence of feedback. Anglés-Alcázar et al. 2017b include feedback from bursty star formation, which can limit the growth of the SMBH and keeps the system lying below local SMBH-galaxy scaling relation.

3C 298 at z=1.439 (age 4.47 Gyr) has quasar negative feedback occurring in a conical outflow early in the gas-rich merger-phase, implying that the majority of the nucleus' stellar mass assembly must occur in later phases if it is to reach the scaling relations of today. Since the majority of the current gas supply in the host galaxy of 3C 298 is incapable of forming stars and will soon be removed from the galaxy through the quasar driven winds, perhaps this assembly happens through dry mergers or newly supplied IGM molecular gas. Even if all of the current gas supply in the molecular disc ($6.6\times10^{9}M_{\odot}$) turns into stars it will still be insufficient to bring the bulge of the 3C 298 host galaxy onto the local scaling relation. For the 3C 298 system this means that the SMBH mass is formed earlier and more efficiently than the host galaxy's stellar mass.

The host galaxy of 3C 298 could be a precursor to local galaxies that are significantly offset from the local scaling relation (e.g, NGC 1277). If there is insufficient accretion from the

intergalactic medium to fuel future star formation or if 3C 298 resides in a less dense environment than a typical quasar it could fail to form/accrete enough stars to fall on the local scaling laws. A natural way to limit the growth of the stellar bulge in a system with a powerful AGN is to have strong feedback on the ISM through a bi-polar outflow early in the lifetime of the system (Fabian et al., 2013).

In summary, the 3C 298 system shows strong evidence of negative feedback from powerful conical outflows that are halting star formation by driving extremely high velocity turbulence in the ISM and by ejecting large amounts of gas. The dynamical time scale of the outflow is $\sim$3-6 Myr, suggesting that quenching of star formation must occur rapidly. In the 3C 298 system, strong feedback has started fairly early in the merger process, well before the final coalescence of the two galactic nuclei. The system shows multiple concurrent phases of the standard merger model (Sanders et al., 1988; Hopkins et al., 2008; Alexander and Hickox, 2012), with the co-existence of a luminous type-1 quasar, star formation in merger host galaxies, and candidate secondary AGN that is offset from the quasar. This implies that removal of gas and dust surrounding the SMBHs occurred rapidly and early during the merger phase. This early and short onset of quasar feedback compared to total time scale of the merger ($\sim$ 1 Gyr) may also partially explain why it has been difficult for measuring its effect on the star-forming ISM in distant galaxies.

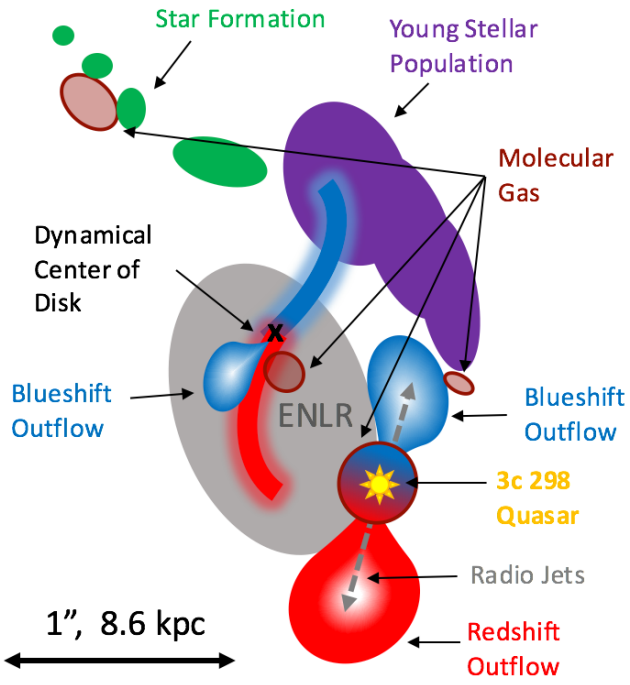

Figure 3.11 Cartoon illustration of the merger in the 3C 298 system that includes the results from OSIRIS, ALMA, HST, and VLA. The location of the quasar is distinguished by a yellow star. The large blue and red-shifted outflows emanating from the quasar observed in the nebular emission lines are co-aligned with the radio jet (indicated by a grey dashed arrow), where negative feedback is observed. The locations of the ALMA CO (3-2) and (5-4) emission are shown with red-brown ovals, representing molecular gas reservoirs. A molecular disc centered on the quasar is shown with a blue-red gradient. We find strong evidence for molecular outflow on the blueshifted side of the disc. The dynamical center of the secondary merging galaxy is shown with a black 'x' sign. The radial velocity map of this galaxy is well-fit to disc model. A secondary outflow region is found to reside near the dynamical center of the merging galaxy, providing tentative evidence for a secondary AGN in the system. The secondary AGN has spatially-concentrated elevated emission line ratios that are consistent with ionization from an AGN. A large area of the 3C 298 system is observed to have extended narrow line region (ENLR; grey) between both the quasar and putative AGN. The majority of the star formation (green) is occurring in compact clumps offset from both galaxies, which would be consistent with a tidal feature being induced by the merger. A young stellar population (purple) measured from the HST WFC3 colours is offset from both the outflows and molecular gas of the system.

3.7 Conclusion

We present integral field spectroscopy of resolved nebular emission lines; Hβ, [OIII] , Hα , [NII] , [SII]together with rotational CO (3-2) and (5-4) spatially resolved emission spectroscopy in the host galaxy of the radio loud quasar 3C 298 (z=1.439). These data are supplemented with archival HST-WFC3 and VLA observations of the rest frame UV and optical stellar continuum and jet/lobe synchrotron emission, respectively.

- We find strong evidence for negative feedback in the host galaxy of 3C 298. Dynamics of ionized gas traced through nebular emission lines show a significant quasar-driven outflow encompassing a large area of the host galaxy. We derive an ionized outflow rate of 467-1515$M_\odot$ yr^{-1} .

- Co-spatial with the powerful ionized gas outflow VLA imaging shows extended synchrotron emission from the quasar jet/lobes. Radio data suggests that the jet has sufficient energy to drive the outflow. A BAL wind also has the necessary energetics for potentially driving the outflow.

- We detect a molecular gas disc centered on the quasar with a total molecular gas of $6.6\times10^9 M_\odot$ and effective radius of 1.6 kpc.

- A powerful quasar driven molecular outflow is detected in the molecular disc with an $\dot{M}_{H_2}$ outflow rate of 2300 $M_\odot$ yr^{-1} . The molecular gas in the disc will be depleted by the outflow on a time scale of 3 Myr.

- Dynamical modeling of the molecular disc reveals that total mass enclosed in the disc

is 2-2.5 orders of magnitude below the expected value from local $\mathrm{M_{stellar-bulge}} - \mathrm{M_{BH}}$ relationship using the measured SMBH mass of the 3C 298 quasar.

- Several kiloparsecs away from the outflow path we find evidence of star forming regions based on BPT diagnostics, strong UV emission from O and B stars, and evidence for a molecular reservoir with a total mass of $1.4\times10^{9}\mathrm{M}_{\odot}$.

- Disc modeling of the velocity field traced by [OIII] emission shows a second rotating disc with a dynamical center offset from the quasar by 9 kpc. This suggests evidence for a late stage merger where the disc traces the second merging galaxy in the system. The dynamical center of the disc aligns well with a secondary outflow region seen in nebular emission that does not extend from the quasar and does not align with any structure in the radio map. This suggests a candidate secondary AGN in the 3C 298 system.

- These observations taken together imply an early onset of negative feedback with a short quenching time compared to time scale of the galactic merger. Feedback is also happening early in the 3C 298 merger process and is occurring well before the assembly of the 3C 298 host galaxy on the local $\mathrm{M_{stellar-bulge}} - \mathrm{M_{BH}}$ relationship.

Table 3.4 3C 298 Properties & Results

Parameter	Value
$z_{\rm quasar}$	1.439
RA	14:19:08.181
DEC	+06:28:34.79
λL_λ[a]	2.0×10^{46}erg s^{-1}
SFR Hα	$88\pm9 M_\odot$ yr^{-1}
SFR IR [b]	$930^{+40}_{-40} M_\odot$ yr^{-1}
$M_{\rm dust}$[b]	$3.8^{+0.3}_{-0.4}\times10^8 M_\odot$
$M_{H_2}^{\rm Total}$	$8.75\pm0.4\times10^9$ M$_\odot$
$M_{H_2}^{\rm MolDisc}$	$6.6\pm0.36\times10^9$ M$_\odot$
$M_{H_2}^{\rm SFRegion}$	$1.4\pm0.14\times10^9$ M$_\odot$
$\dot{M}_{\rm [OIII]}$	467 M$_\odot$ yr^{-1}
$\dot{M}_{H\alpha}$	1515 M$_\odot$ yr^{-1}
$\dot{M}_{H_2}$	2300 M$_\odot$ yr^{-1}
Outflow n_e[c]	272 cm^{-3}
$M_{\rm dyn,bulge}$	$1.35\pm0.5\times10^{10}$
$M_{\rm SMBH}$	$3.23\pm1.1\times10^9$

[a] Computed at rest-frame 3000 Å

[b] Value from (Podigachoski et al., 2015)

[c] Value based on [SII] line ratio measurment over blueshifted outflow region.

3.8 Acknowledgements

The authors wish to thank Randy Campbell and Jim Lyke with their assistance at the telescope to acquire the Keck OSIRIS data sets. We also appreciate valuable discussions with Dusan Keres and the constructive comments made by the anonymous referee. The data presented herein were obtained at the W.M. Keck Observatory, which is operated as a scientific partnership among the California Institute of Technology, the University of California and the National Aeronautics and Space Administration. The Observatory was made possible by the generous financial support of the W.M. Keck Foundation. The authors wish to recognize and acknowledge the very significant cultural role and reverence that the summit of Maunakea has always had within the indigenous Hawaiian community. We are most fortunate to have the opportunity to conduct observations from this mountain. This paper makes use of the following ALMA data: ADS/JAO.ALMA[2013.1.01359.S]. ALMA is a partnership of ESO (representing its member states), NSF (USA) and NINS (Japan), together with NRC (Canada), NSC and ASIAA (Taiwan), and KASI (Republic of Korea), in cooperation with the Republic of Chile. Based on observations made with the NASA/ESA Hubble Space Telescope, obtained from the Data Archive (Program GO13023) at the Space Telescope Science Institute, which is operated by the Association of Universities for Research in Astronomy, Inc., under NASA contract NAS 5-26555. A portion of the research was conducted at The Dunlap Institute for Astronomy and Astrophysics that is funded through an endowment established by the David Dunlap family and the University of Toronto. This research has made use of the NASA/IPAC Extragalactic Database (NED) which is operated by the Jet Propulsion Laboratory, California Institute of Technology, under contract

with the National Aeronautics and Space Administration.

Chapter 3, in full, is a reprint of the material as it appears in The Astrophysical Journal 2017. Vayner, A., Wright, S. A., Murray, N., Armus, L., Larkin, J. E., Mieda, E., 2017. The dissertation author was the primary investigator and author of this paper.

Chapter 4

A Spatially-Resolved Survey of Distant Quasar Host Galaxies: Kinematics and Energetics of Ionization Gas

4.1 Abstract

Using the OSIRIS integral field spectrograph behind the laser guide star adaptive optics system at the W.M. Keck Observatory we target nebular emission lines (Hβ,[OIII] ,Hα ,[NII] and [SII]) redshifted into the near infrared (1-2.4 μm), to study the distribution, kinematics, and dynamics of the ionized gas in 11 z$= 1.39 - 2.59$ radio-loud quasar host galaxies. We detect extended ionized emission on scales ranging from 1-30 kpc photoionized by a combination of stars, shocks, and AGN. Outflows are detected in all systems on scales ranging from < 1 kpc to 10 kpc with outflow rates from 8-2400 $M_\odot$ yr^{-1} . For 4/11 objects the momentum rates are 4-80

times L_{AGN}/c, consistent with being driven by an energy conserving shock, the rest are either driven by radiation pressure or an isothermal shock. The paths of the outflows are consistent with the direction of the jet. However, at present, we find the jets are not doing any work on the galactic outflows. If the jets were to drive the outflows, it had to happen in a dense environment, close to the supermassive black hole (SMBH). The outflows are the dominant source of gas depletion, with little evidence for star formation along the paths of the outflows. We find the quasar host galaxies to be under massive relative to the mass of the SMBH, with all systems residing off the local scaling ($M_\bullet - \sigma$) relationship. Gas phase metallicities are lower compared to galaxies with AGN in the nearby Universe. Taken together, we find the onset of feedback before the galaxies assemble onto the local scaling relation, and before chemical enrichment of gas to levels observed in nearby AGN. The galaxies require substantial growth, up to an order of magnitude in stellar mass if they are to grow into local massive elliptical galaxies.

4.2 Introduction

Today, in the nearby Universe, at most 10-20$\%$ of the baryonic matter resides in stars (Behroozi et al., 2010). In the most massive dark matter halos ($\mathrm{M_{dm}} > 10^{12}$ $\mathrm{M_\odot}$) the lack of baryons inside galaxies has been attributed to negative feedback from the active galactic nucleus (AGN) (Benson et al., 2003; Kormendy and Ho, 2013). Feedback from AGN is often used to explain the tight correlation between the mass of a supermassive black hole (SMBH) and the velocity dispersion ($M_\bullet - \sigma$) or mass of the bulge/galaxy ($M_\bullet - M_*$) (Ferrarese and Merritt, 2000; Gebhardt et al., 2000; McConnell and Ma, 2013). In the current theoretical framework,

the SMBH and galaxy grow until they reach a mass ratio close to what is observed in the nearby Universe ($\frac{M_\bullet}{M_*} \sim 5 \times 10^{-3}$). Afterward, the accretion disk surrounding the SMBH is capable of driving a wind that extends deep enough into the host galaxy to drive a shock that may expand adiabatically (Zubovas and King, 2012, 2014; Faucher-Giguère et al., 2012). The expanding shock produces a galaxy scale outflow that both removes material from the host galaxy and also drives turbulence preventing gas from collapsing and cooling on regular time scales.

In essence, AGN feedback both prolongs the time necessary for gas to collapse and form stars and removes the fuel for future star formation and SMBH growth. The feedback processes start near the vicinity of the SMBH, where radiation pressure from the accretion disk drives powerful winds. These nuclear winds are commonly observed as highly blueshifted absorption lines in UV spectra and are called Broad Absorption Line winds (BAL) (Chamberlain et al., 2015) or in X-ray spectra as "Ultra Fast Outflows" (Tombesi et al., 2010). From herein "winds" will be referred to as "small" scale (a few pc to a kpc) structures/events while "outflows" will refer to galaxy scale (>1kpc). Alternatively, the feedback process can also start with jets launched from the accretion disk. Similarly to BAL and UFO winds, jets can drive outflows that sweeps material out of the galaxy (Wagner et al., 2012; Mukherjee et al., 2016).

To effectively expel the gas from a galaxy and establish the observed local relationships ($M_\bullet - \sigma$,$M_\bullet - M_*$) the BAL or UFO type wind that drives a galaxy scale outflow needs to transfer at least $0.1 - 5\%$ of the quasar bolometric luminosity into the kinetic luminosity of the outflow (Hopkins and Elvis, 2010a; Zubovas and King, 2012). While for jets, the ratio of the power (P_{jet}) to the Eddington luminosity of the SMBH accretion disk needs to be higher than 10^{-4} (Wagner et al., 2012). Another proposed way of clearing gas in galaxies is through

radiation pressure on dust grains in the nuclear region of AGN (Thompson et al., 2015; Costa et al., 2018a). Although this mode of feedback is not as strong as the other proposed methods, it can still be powerful enough to disrupt star formation within the host galaxy.

Often feedback during luminous AGN phases has been described as transformative, where the galaxy goes from being star-forming to quiescent after episodes of AGN feedback. In the past decade, there is growing evidence for feedback from SMBH, yet there appear to be discrepancies between the theoretical predictions and observations. These disagreements can stand from observational bias or missing physics within galactic feedback models. Majority of studies have focused on detecting and characterizing nearby (Greene et al., 2012; Rupke and Veilleux, 2011; Liu et al., 2013a; Harrison et al., 2014) and distant (Nesvadba et al., 2008; Steinbring, 2011; Cano-Díaz et al., 2012; Harrison et al., 2012; Brusa et al., 2016; Carniani et al., 2015) outflows through nebular emission lines (e.g, Hβ, [OIII] , Hα), primarily focusing on the [OIII] emission line as a tracer of the ionized gas in the outflows. There is growing evidence of galaxy-scale outflows; however, it has been challenging to measure accurate outflow rates and energetics for comparison with theoretical predictions (Harrison et al., 2018). Detected outflows in quasar host galaxies show a large range in their kinetic luminosity, spanning from 0.001$\%$ to 5% of the quasar's bolometric luminosity. Often the measured energetics fall short of the predicted values from theoretical work, with about half of the detected ionized outflows show $\dot{E}_{outflow} < 0.1\%$ L_{Bol} (Carniani et al., 2015). Furthermore, the ratio of momentum flux $\dot{P}_{\rm outflow} = \dot{M} \times v$ to the $\dot{P}_{QSO}$ have been far lower than what is predicted by theoretical work (Zubovas and King, 2012) for high redshift ionized outflows. In contrast, in the nearby Universe, molecular outflows found in systems with AGN have shown energetics consistent with the theoretical predictions Cicone

et al. (2014). Several solutions have been brought up to reconcile differences between ionized and molecular outflows. Ionized outflows might constitute only a small fraction of the gas phase in the outflow (Carniani et al., 2015; Richings and Faucher-Giguère, 2018). The number of observed systems with both ionized and molecular outflows in the distant and nearby Universe is very small. For systems where the multi-phase outflow have been detected they show that the largest fraction of the gas is indeed in a molecular state (Vayner et al., 2017; Brusa et al., 2018; Herrera-Camus et al., 2019). More extensive studies with ALMA and JWST are necessary to confirm the multi-phase nature of quasar driven outflows.

Following episodes of transformative feedback during luminous AGN phase it has been proposed that to keep the galactic halos hot, “maintenance" feedback takes over in forms of large scale jets formed from a low Eddington accretion AGN. Often, these large scale jets carve out bubbles in the hot halo (Fabian, 1994; McNamara et al., 2000; Hlavacek-Larrondo et al., 2013), inducing turbulence and preventing the halo from cooling to fuel future generation of star formation. Understanding both transformative and maintenance mode feedback is essential to understanding the formation of massive galaxies.

One question arises; at what points does the AGN drive an outflow powerful enough to clear the galaxy of its gas? According to the theoretical work, this happens once the galaxy reaches the $M_\bullet - \sigma$ relationship (Zubovas and King, 2014). However, there has been growing evidence for galaxies with massive SMBH and powerful outflows that are offset from the local scaling relationship (Vayner et al., 2017). When are the scaling relations established? The origin and evolution of the local scaling relationships with redshift have been a hot topic of debate over the last decade. Are the local scaling relationships the end product of galaxy evolution?

Meaning, as galaxies form and evolve, do they fall in and out of the relationships due to rapid growth or feedback process? Do galaxies eventually end up on the local scaling relations once the galaxy or SMBH catch up and finish growing (Volonteri, 2012)? Alternatively, is there an inherit evolution in the scaling relationship with redshift and a symbiosis between the galaxy and SMBH growth? (i.e., evolution in slope, offset and scatter). From a sample of AGN in the COSMOS field (Merloni et al., 2010) finds an offset in the local scaling relationship between redshift 0 and 2. These authors use SED decomposition with numerous spectral bands to measure the stellar mass of the AGN host galaxy in the redshift range of $1 < \mathrm{z} < 2.2$. From a sample of lensed quasars at $1 < z < 4.5$ and broadband HST imaging, Peng et al. (2006) also finds an offset in the local scaling relationship. While Sun et al. (2015) using multi-band SED fitting of galaxies in the COSMOS field finds that z$\sim 0.2 - 2$ galaxies are consistent with being on the local scaling relationship. Schramm and Silverman (2013) using HST imaging in the Chandra Extended Deep Field also finds that galaxies at z$\sim 0.6 - 1$ are also consistent with being on the local scaling relationship. In the nearby Universe, there is tentative evidence that all of the most massive black holes ($> 10^9$ $\mathrm{M}_{\odot}$) are systematically more massive relative to their host galaxies (Martín-Navarro et al., 2018). Fields such as COSMOS or the Extended Chandra Deep Field-South are relatively small on the sky; hence, the number of luminous quasars with massive SMBH is small. Studies which explored the evolution of the local scaling relationships have generally focused on lower mass black holes with masses $< 10^9$ $\mathrm{M}_{\odot}$. A large fraction of these studies used broadband HST imaging to study the host galaxies of their quasars/AGN. Often it is difficult to disentangle the bright AGN emission from the host galaxy at smaller angular separations ($<0.5''$), and these studies have a limited number of filters to measure the age of

the stellar population and the mass to light ratio to extract the stellar mass of the host galaxy. Alternatively, mm-interferometry observations have become an essential tool in measuring the dynamical masses of quasar host galaxies across different redshift ranges. At the highest redshifts (z$>$ 4) the [CII] 158μm line has been the most commonly used tracer of the dynamics of the ISM. There is growing evidence that the most massive ($> 10^9$ $M_\odot$) SMBH in the highest redshift quasars known to date (z$>$ 6) appear to be over massive for the mass of their host galaxies (Wang et al., 2013; Venemans et al., 2016; Decarli et al., 2018), indicating that the most SMBHs grow first. At more intermediate redshifts 1$<$z$<$3 some systems also appear to have overly massive SMBH relative to their stellar/dynamical mass (Shields et al., 2006; Trakhtenbrot et al., 2015; Vayner et al., 2017). While a significant fraction of galaxies with lower SMBH $< 10^9$ $M_\odot$ appear closer or within the scatter of the local scaling relations, it appears that galaxies with the most massive SMBH appear to be under massive relative to the mass of their SMBH.

Interestingly surveys where a more substantial fraction of the systems are above $z \sim 1$ find an offset from the local scaling relation, while studies that include sources with $z < 1$ are finding a smaller or no offset from the local scaling relations. The redshift of the sources in the sample might play an important role in determining whether there is an offset or not. However, given the large uncertainties of both SMBH and galaxy masses and the limited sample size, it is difficult to test whether there is a statistically significant offset between z$<$ 1 and z$>$ 1 sources at the present time. In addition, there is a difference in the range of black hole masses that are probed by lower and higher redshift surveys which can play a critical role determining whether or not an offset exists for the sample.

Integral field spectroscopy (IFS) behind adaptive optics is another method with which it is possible to disentangle the bright quasar emission from the extended emission of the host galaxy. A point spread function can be constructed using data channels confined to the broad emission line of the quasar. After the point spread function is normalized, it is subtracted from the rest of the data channels in the cube. This technique was first shown to be able to resolve host galaxies of low redshift ($z < 0.2$) luminous type-1 quasars in seeing limited observations (Jahnke et al., 2004a). Later, when the first near-infrared IFS came online along with their own adaptive optics system this technique was expanded to samples of higher redshift quasars (Inskip et al., 2011; Vayner et al., 2016) and has shown to work on all the 8-10m class near-infrared IFS (e.g., SINFONI, NIFS, and OSIRIS). This PSF subtraction routine provides better contrast at smaller angular separations than HST, with an inner working angle of 0.1-0.2$''$, compared to HST's of about 0.5$''$(Vayner et al., 2016)(Chapter 2). Although today's near-infrared IFSs are not sensitive enough to detect the stellar continuum from the quasar/AGN host galaxies, they are still capable of detecting extended ionized emission, enabling us to extract the dynamical properties of the galaxy (Inskip et al., 2011).

There are vital open questions regarding the gas phase properties of the ISM in quasar host galaxies. What are the metallicities of the gas in quasar hosts? How does the metallicity in quasar host galaxies evolve with redshift? What is the dominant source of ionization in quasar hosts? What are the star formation rates? One of the best ways to measure the ionization properties of the gas in galaxies is through the BPT (Baldwin, Phillips & Terlevich) diagram (Baldwin et al., 1981; Veilleux and Osterbrock, 1987). The traditional BPT diagram plots the ratio of log([OIII] /Hβ) vs. log([NII]/Hα) and contains two clearly defined sequences: the star-

forming sequence and the mixing sequence. The star-forming sequence provides information about the metallicity of HII regions, the stellar ionizing radiation field as well as information on the gas condition in star-forming regions. The mixing sequence, on the other hand, consists of gas photoionized by AGN and shocks and can provide information on the hardness of the AGN ionizing radiation and the metallicity of the gas photoionized by the quasar/AGN (Groves et al., 2006). Studies consisting of high redshift star-forming galaxies have shown evidence for elevated line ratios relative to low redshift galaxies. At z$\sim$2 the observed elevated line ratios have been attributed to denser ISM conditions (Sanders et al., 2016) and harder ionizing radiation fields at fixed N/O and O/H abundances relative to typical z=0 galaxies (Strom et al., 2017). Evolutionary BPT models by Kewley et al. (2013a) are consistent with these observations. Also, the evolutionary BPT models provide a prediction on the evolution of the mixing sequence between z=0 and 3. The location of the mixing sequence moves to lower log([NII]/Hα) value at a relatively fixed log([OIII] /Hβ) value, primarily due to lower on average gas phase metallicity at higher redshift (Groves et al., 2006; Kewley et al., 2013a). There is tentative evidence that gas photoionized by AGN is consistent with this picture, as there are several galaxies with AGN which have emission line ratios offset from the local mixing sequence (Juneau et al., 2014; Coil et al., 2015; Strom et al., 2017; Nesvadba et al., 2017c; Law et al., 2018). Given the numerous sources of ionization in quasar host galaxies; star formation, quasar and shocks it is crucial to spatially resolve the quasar host galaxy to understand the various contributions to gas ionization. In the distant Universe, this generally requires observations with an IFS and adaptive optics. Resolved BPT diagnostics in both nearby and distant AGN/quasar host galaxies have found regions with distinct photoionization mechanisms (Davies et al., 2014; Williams et al.,

2017; Vayner et al., 2017). The question remains whether the condition of the ISM in the most luminous high redshift quasar host galaxies is different from local AGN.

We have begun a survey to study the host galaxies of z$= 1.4 - 2.6$ radio-loud quasars, which are the most likely systems to evolve into the most massive elliptical galaxies in the nearby Universe. The observations consist of near-infrared IFS observation behind laser-guide-star adaptive optics (LGS-AO) at the W.M. Keck Observatory with the OSIRIS instrument. The survey aims to understand the gas phase conditions and ionization in high redshift quasar host galaxies, along with searching for evidence of quasar feedback and weighing the masses of the quasar hosts. The observations target nebular emission lines (Hβ,[OIII] ,Hα ,[NII] ,[SII]) redshifted in the near-infrared bands ($1 - 2.4$ μm) at a spatial resolution of $\sim$1.4 kpc. We describe our sample selection in §4.3, we summarise the observations in §4.4, data reduction and analysis is outlined in §4.5, we describe how we identify spatially-resolved distinct regions in each quasar host galaxy in §4.7, resolved BPT diagrams and our interpretation of the line ratios are present in §4.8, outflow rates, energetics and the driving sources of outflows is presented in §4.9, dynamical masses of the quasar host galaxies and their place on local scaling relations is presented in §4.11 & §4.10, we discuss our results in broader context of massive galaxy evolution in §4.12 and present our conclusions in §4.13. Notes on individual sources are presented in §4.15. Throughout the paper we assume a Λ-dominated cosmology (Planck Collaboration et al., 2014) with Ω_M=0.308, Ω_Λ=0.692, and H$_o$=67.8 km s^{-1} Mpc^{-1}. All magnitudes are on the AB scale unless otherwise stated.

4.3 Sample Selection

Sources were selected from the Sloan Digital Sky Survey (SDSS) data release 10 (Ahn et al. (2014)). Quasars with a magnitude brighter than 17.5 at R band or those that have nearby stars with R magnitude < 17.5 within $45''$ were cross-correlated with the FIRST catalog (Becker et al., 1995) and NASA Extra-galactic Database (NED). Sources with radio flux of 0.3 Jy and greater at 1.4 GHz were selected based on their available archival VLA/MERLIN observations. We then selected targets with the most optimal tip/tilt star configuration that have jet sizes < 20 kpc. These sources fall in the compact steep spectrum (CSS) family except for 3C446, which is a Gigahertz peaked source (GPS). We added 4C09.17 and 4C05.84, which were not observed with SDSS, however, satisfies the radio, tip/tilt star criteria, and archival imaging and spectroscopic data. Table 4.4 summarizes the general properties of our sample.

4.4 Observations

In this section we outline the observations that were taken as part of our survey. This includes OSIRIS adaptive optics (AO) observations at the W.M Keck observatory of nebular emission lines, ALMA observations of the synchrotron emission from the radio jet, archival VLA and HST data.

4.4.1 Keck OSIRIS

OSIRIS (Larkin et al., 2006; Mieda et al., 2014) observations were performed during semesters 2015A - 2017B[1] on the Keck I telescope behind the laser guide star (LGS) adaptive optics system Wizinowich et al. (2006). For tip/tilt corrections, we used a nearby bright star (R magnitude < 17.5) or the quasars itself if it was sufficiently bright. For higher order corrections, a laser tuned to the Sodium line at 589.2 nm was used to create an artificial star at an altitude of 90 km centered on our object. The observing sequence was as follows: first, we acquired the tip/tilt star with a short exposure and centered it in the OSIRIS IFS field-of-view (FOV). For off-axis tip/tilt correction, we offset to the quasar using known shifts from archival SDSS or HST imaging with observations after September 2016 utilizing the new Gaia astrometric catalogs (Gaia Collaboration et al., 2016, 2018). We took a second short exposure to make sure the quasar was centered and began science observations with 600-second exposure for individual frames. We dithered each source by a few lenslets between science exposures and observed a pure sky region once an hour. Each quasar was observed in multiple filters to cover key nebular emission lines, with the goal to at least cover the wavelength range of redshifted Hα , [NII] , and [OIII] lines. Choices between FOV and wavelength coverage prevented us from obtaining a consistent line coverage for all sources. Table 4.1 includes the nebular lines observed for each quasar.

Each source was observed at least once in photometric conditions. Data for sources taken in non-photometric conditions had flux scaled to photometric nights. We find the scaling factor by constructing a 2D quasar image by taking an average along the spectral axis of the data cube and performing aperture photometry with an aperture correction from a curve of growth. We

[1]Program ID: U072OL, U90OL, U121OL, U184OL, U154OL, U110OL, U122OL, PI: S. Wright

use flux conversions from DN/s to cgs from photometric nights. Non-photometric nights had a maximum extinction of 1 magnitude as measured from the CFHT sky-probe[2].

For some sources, we took observations in both narrow and broadband filter modes. The combined data cubes for these sources have variable noise properties as a function of wavelength and spatial location. Furthermore, the PSF for these sources varies between overlapping and non-overlapping spectral regions.

[2] www.cfht.hawaii.edu/Instruments/Elixir/skyprobe/home.html

Table 4.1 OSIRIS-LGS Observational Summary

Name	Observing Dates UT	Observing Mode	Integration time $N_{frames} \times s$	Nebular Lines	PSF FWHM $''$
3C 9	150809	Kn1	6×600	Hα ,[NII]	0.14″×0.14″
	150809	Hn1	6×600	[OIII]	0.15″×0.16″
4C 09.17	160918	Hn2	10×600	[OIII]	0.11″×0.093″
	160919	Kn1	12×600	Hα ,[NII]	0.071″×0.079″
3C 268.4	150405	Hn2	6×600	Hα ,[NII] ,[SII]	0.19×0.17″
	150406	Jn1	7×600	[OIII]	0.3″×0.27″
	150406	Hbb	3×600	Hα ,[NII] ,[SII]	0.19″×0.17″
7C 1354+2552	160619	Hn1	11×600	[OIII]	0.18″×0.14″
	160620	Kn1	8×600	Hα ,[NII]	0.13″×0.12″
3C 298	140519	Hn3	4×600	Hα ,[NII] ,[SII]	0.113″×0.113″
	140520	Jn1	4×600	Hβ,[OIII]	0.127″×0.127″
3C 318	160619	Jbb	4×600	Hβ,[OIII]	0.34″×0.26″
	160620	Jn3	4×600	[OIII]	0.34″×0.26″
	170717	Hn4	11×600	Hα ,[NII] [SII]	0.25″×0.22″
	170718	Hn4	9×600	Hα ,[NII] ,[SII]	0.25″×0.22″
4C 57.29	150809	Hn2	7×600	[OIII] ,Hβ	0.11″×0.11″
	150809	Kn2	5×600	Hα ,[NII] ,[SII]	0.13″×0.13″
4C 22.44	160919	Jn2	7×600	Hβ,[OIII]	0.11″×0.13″
	170718	Hn4	10×600	Hα ,[NII] ,[SII]	0.094″×0.12″
4C 05.84	151009	Hn3	6×600	Hβ,[OIII]	0.11″×0.10″
	160619	Kn3	8×600	Hα ,[NII] ,[SII]	0.11″×0.10″
	160619	Jn2	4×600	[OII]	–
3C 446	160620	Jn1	9×600	[OIII]	0.16″×0.18″
	160918	Hn2	7×600	Hα ,[NII] ,[SII]	0.14″×0.14″
	160919	Hn2	5×600	Hα ,[NII] ,[SII]	0.14″×0.14″
4C 04.81	170610	Hn5	5×600	Hβ,[OIII]	0.17″×0.2″
	170717	Kn5	8×600	Hα ,[NII]	0.09″×0.12″
	170901	Kn5	6×600	Hα ,[NII]	0.09″×0.12″

Table 4.2. Archival VLA imaging

Object	Date	Project Code	Central frequency (GHz)	Beam
3C318	1990 May 5	AB568	8.4399	$0.24'' \times 0.24''$
4C04.81	1985 February 26	AL93	4.86	$0.43'' \times 0.40''$
3C9	1993 January 4	AK307	8.4399	$0.22'' \times 0.21''$
3C268.4	1991 November 13	AW249	8.2649	$0.72'' \times 0.58''$
4C57.29	1986 May 18	AG220	1.490	$1.53'' \times 1.0''$
3C298	1991 August 6	AJ206	8.4851	$0.32'' \times 0.25''$

4.4.2 Archival VLA observations

A large fraction of our sources have been observed with the Very Large Array (VLA) over the past 30 years. We scoured the VLA data archive for readily available high-quality images of the quasar jets in our systems. We downloaded data sets that were reduced with the VLA AIPS automated pipeline. We chose data sets that had an angular resolution close to or better than an arc-second with integration long enough to fill the uv-space to produce high fidelity images. Table 4.2 describes the observations.

4.4.3 ALMA

For objects where there is no available VLA imaging with our search criteria, we have used our observations at shorter radio wavelength (mm) to construct images of the radio jets. We have a concurrent ALMA program to study the molecular gas content of several quasars within this survey. We are targeting rotation CO lines redshifted into the band 4 (125–163 GHz, 1.8–2.4 mm) of ALMA. The quasar jet still dominates the continuum emission at these wavelengths. For

sources 4C05.84, 3C318, 4C09.17, 4C22.44, and 7C 1354+2552 we can produce high-quality continuum maps of the quasar jets. Data reduction was performed using CASA (Common Astronomy Software Applications (McMullin et al., 2007)). There is sufficient SNR to perform self calibrations directly on 3C318, 4C05.84 and 4C09.17. We used the CASA *CLEAN* function to establish a model for the synchrotron continuum through several interactive runs with clean masks centered on high SNR features. Cleaning is performed with Briggs weighting using a robust value of 0.5 with a pixel scale of $0.05''$. We used the *gaincal* function to perform self-phase calibration. The self-calibrated data was then cleaned again with further phase calibration until we did not see a significant improvement in the SNR on the continuum. The final root mean square (rms) improved by a factor of 3-8 in the continuum images. A single round of amplitude self-calibration was successfully only for 3C318. The typical spatial resolution of the ALMA observations is $0.4''$.

4.4.4 Archival *HST* imaging

For sources with available HST imaging we download fully-reduced data from the Barbara A. Mikulski Archive for Space Telescopes (MAST). Table 4.3 list the archival HST observations used in this study.

Table 4.3 Archival HST imaging

Object	Proposal ID	Instrument	Filter	Exposure time (s)
3C446	12975	ACS-WFC	F814W	2200
3C298	13023	WFC3-UV	F606W	1100
3C268.4	13023	WFC3-UV	F606W	1100
4C09.17	5393	WFPC2	F555W	2100
3C9	13945	ACS-WFC	F814W	2040

4.5 Data Reduction & Analysis

4.5.1 OSIRIS data reduction

Data reduction was performed using the standard OSIRIS data reduction pipeline version 4.1.0 Larkin et al. (2013). The pipeline performs standard near-infrared data reduction procedures. First, we constructed a master dark for each observing night by median combining 3-5 600s darks taken before/after our observing night. We subtract each master dark from the raw 2D spectra. “Adjust channel levels", “Remove Crosstalk" and “Glitch Identification" routines were only run on data taken before the detector upgrade in early 2016. The new Hawaii-2RG detector does not have the same artifacts which these modules were designed to correct, see Boehle et al. (2016) for further discussion. The pipeline performs a Lucy-Richardson deconvolution to extract raw spectra by using unique rectification matrixes for each observing mode. The rectification matrices are calibration files that contain the instrumental PSF for each lenslet at each wavelength location. Finally, the “Assemble Data Cube" routine is run to place the extracted spectra in the correct spatial location and construct a three-dimensional data cube. Sky cubes were subtracted from the science observations using the “Scaled Sky" module, which scales OH-lines in the sky data cube to that of the science frame before subtraction. The cubes were then combined

using the “Mosaic Frames" routine which registers cube to the same coordinate system based on AO offset header keywords and uses a 3σ clipping algorithm for combining.

An A-type star is observed either preceding or succeeding each science observation for both telluric and flux calibration. We select a star brighter than eighth magnitude from the 2MASS catalog for flux calibrations. The star is selected not to be variable or a known optical/spectroscopic binary. We select stars to have coordinates that when observed, will have an air mass roughly matching the average air mass of our science observations. The observations are taken in NGS mode with a typical exposure time of 1.4-10s depending on stellar brightness and observational mode. For each star, we obtain a pure sky observation by offsetting to an empty sky region a few arcseconds away.

We reduce the standard star in the same manner as for regular science observations. We produce a 2D image of the star by averaging the data cube along the spectral axis. We construct a curve of growth using the 2D stellar image and extract the spectrum using a small radius, approximately the 34% of star's spatial width. We apply an aperture correction to each spectrum based on the curve of growth to obtain the total stellar counts. Hydrogen absorption lines in the stellar spectra are fit with a Lorentz profile and are removed from each spectrum. We construct a model stellar spectrum using the Planck function normalized to the average flux of the star in the broad J, H, or K flux from 2MASS. We sample the (J, H or K) 1D model spectrum to the OSIRIS spectral sampling and then divide the model into the observed stellar spectrum. This provides us with a conversion factor between DN/s and at each channel in the data cube. We estimate the absolute flux accuracy to be at $\sim 10\%$.

4.5.2 PSF subtraction

The broad line region of a quasar is spatially unresolved to our observations since the emission happens on small scales, 10-400 light days (Peterson et al., 2004). Therefore, an integral field spectrograph is capable of constructing a PSF image from the data cube using only channels confined to the broad line region. Jahnke et al. (2004b) conducted some of the first IFS observations of low-redshift (z$\sim$ 0.2) quasar host galaxies to search for extended emission in nebular emission lines. With the deployment of near-infrared IFS and adaptive optics, the search for extended emission from quasar host galaxies shifted to higher redshifts (z$>$ 1). Inskip et al. (2011) presents detection of a quasar host galaxy in Hα for a z=1.3 quasar using SINFONI on VLT. Our team shortly followed up an observational program to detect nebular emission from quasar host galaxies at z$\sim$2 with OSIRIS at Keck and NIFS on Gemini. We demonstrated that we could detect extended emission on scales $\gtrsim$0.2$''$ from the quasar down to flux levels of a few $\times 10^{-17}$ erg s^{-1} cm^{-2}. We present a detailed description of our PSF subtraction routine in Vayner et al. (2016)(Chapter 2). Herein we provide an overview and some additional improvements that we have made to our PSF subtraction routine.

We select channels that are part of the quasar broad line emission and quasar continuum that do not overlap with strong OH emission from the sky. We avoid regions within $\pm$2000 km s^{-1} from the peak of a broad-line Hα or NLR [OIII] emission to avoid including potentially extended emission from the quasar host galaxy, since we expect the majority of the extended gas to emit close to the redshift of the quasar. Previously we only selected groups of channels between OH lines that are close to the peak of the broad emission line or [OIII] emission (within

$\pm$10,000 km s^{-1} from the peak of a line). With further testing and a more extensive data set, we found that selecting more data channels for constructing the PSF image caused less noise in the PSF subtracted data cube. So now we select all available channels that do not coincide with OH emission, low atmospheric transparency, spectral edge channels (due to filter transmission artifacts) or near ($< \pm$2000 km s^{-1}) the peak of a broad-line Balmer line (e.g., Hα , Hβ) or forbidden [OIII] , [SII] emission lines. We still do not perform any continuum subtraction to remove extended continuum emission from host galaxies' stellar component before selecting channels from the broad emission line as the sensitivity of OSIRIS is still below the flux expected from continuum emission from the host galaxy at these redshifts.

After subtracting the PSF from the data cube, we apply minor cosmetic smoothing with a 2D Gaussian to the datasets to improve spaxel-spaxel flux variations and to bring the data sets to the same angular resolution. When computing any sizes of extended emission, we remove in quadrature the size of the Gaussian kernel that was convolved with the data cube.

4.5.3 Emission Line Fitting

In this section, we outline how the nebular emission lines are detected and fit to construct integrated intensity, radial velocity, and dispersion maps.

For PSF subtracted data cube, we construct a spectrum in a large aperture centered on the quasar. We collapse the cube along the spectral axis using the channels near the peak of the identified emission line, effectively creating a moment zero map for that line. Some data cubes show multiple emission line peaks, from distinct kinematic structures in the galaxy, either from bi-conical outflows, merging galaxies or rotating discs. By distinct here we refer to spectrally

resolved emission line peaks resolved into individual emission line components. We then create a moment map for each one. We select a sky region in each map, where we do not see any strong emission, to estimate the background noise. The moment zero maps are divided by the background noise to construct a signal-to-noise ratio (SNR) map for each velocity component.

We fit the emission lines in spaxel that have a significance above 2σ in the SNR maps. Each emission line is fitted with a Gaussian model. For the [OIII] 500.7 nm line, we simultaneously fit the [OIII] 495.9 nm line as well. The position and width of the 495.9 nm line are held fixed to the redshift and width of 500.7 nm line. The line ratio between the [OIII] lines is held fixed at 1:2.98 (Storey and Zeippen, 2000). Spaxels where Hα and [NII] SNR maps both show a significant detection have the lines fit simultaneously. All the parameters on the Hα line are free while for the [NII] 658.4 lines the width and redshift are held fixed to the Hα line, and only the peak of the emission is a free parameter. The 654.8 [NII] line has no free parameters with the width and redshift held fixed to the Hα line, and the intensity ratio between the [NII] 654.9, 658.5 nm lines is held fixed at 1:2.95.

A fit to an emission line is deemed successful and is considered "real" if the peak is above 3σ and the width of the emission line is broader than the width of an OH sky emission line in the data cube. We compute the width of the OH sky line by fitting a Gaussian profile to an isolated sky line.

Each emission line is integrated from -3σ to +3σ to construct integrated line intensity maps. We compute the error by taking a standard deviation in a sky region at each spectral channel. The errors are simply an addition in quadrature of the error array over the same spectral range as the integration of the emission line. We construct radial velocity maps by measuring

the Doppler shift of the emission line from the redshift of the source, which we assume to be the rest frame of each system. We generate a velocity dispersion map from the best fit σ value of the Gaussian fit. The errors on the radial velocity and σ values are from the least squares Gaussian fit.

We create three color composite maps from the integrated nebular emission line maps, with the green color assigned to [OIII] , red to Hα and blue to [NII] . We utilize the *make Lupton rgb* routine within *astropy* visualization package (Lupton et al., 2004). Three color composite images for each source are presented in Figure 4.1. The radial velocity and dispersion maps for individual sources are present in the appendix. For each velocity dispersion map, we overlay the radio-maps of the quasars' jets. The two images are aligned by matching the optical/near-IR location of the quasar with the component in the radio maps that shows spectrally flat ($S_\nu \sim \nu^0$) spatially compact emission (Lonsdale et al., 1993; Fanti et al., 2002).

4.6 Quasar sample properties

We calculate redshifts from the Hα emission line that originates in the NLR of these quasars. We extract the spectra of the quasar emission by performing aperture photometry on the unresolved point-source emission in each data cube. Each spectrum has the broad Hα emission fit with multiple Gaussian profiles. The number of Gaussian emission lines is selected to minimize χ^2. Most sources only required two broad profiles for the broad-line region emission and one narrow component that signifies the quasar NLR. The centroid of the Gaussian profile associated with the NLR component in the multi-line fit is used to calculate the redshift quoted

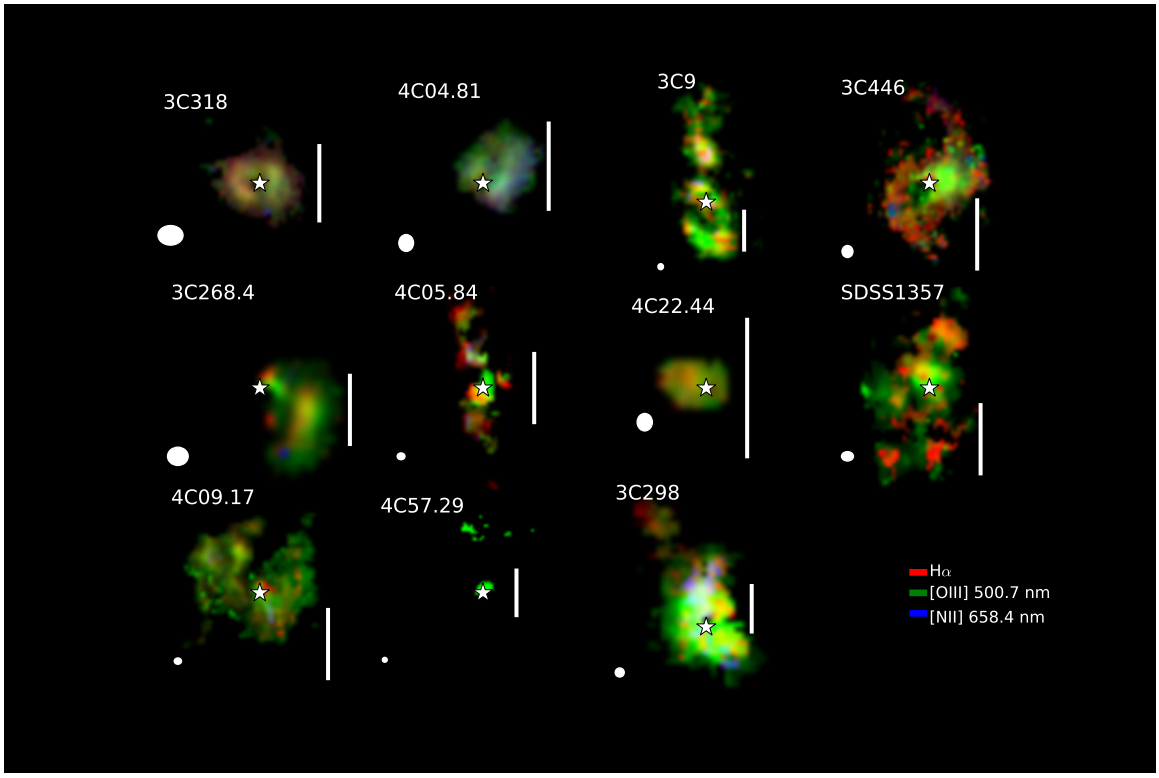

Figure 4.1 OSIRIS - LGS observations of 11 quasar host galaxies in our QUART sample. Each image is a three-color composite showcasing the distribution of ionized gas in these galaxies detected on scales ranging from 1.6-30 kpc after the quasar emission has been removed. Red is color-coded to Hα , green to [OIII] and blue to [NII] . The star represents the location of the subtracted quasar, the ellipse in the lower left corner is the measured FWHM of the PSF computed from the quasar-PSF image, and the scale bar to the right of each source represents $1''$ or approximately 8.4 kpc

in 4.4. In cases where no narrow line component is detected, we select the centroid of the brightest Gaussian component in the fit for the redshift. For 3C9 the broad Hα line is significantly contaminated by telluric absorption, and we cannot perform a good fit on this spectrum; hence, we quote the SDSS redshift for this source.

The bolometric luminosities are computed from monochromatic luminosity at either 1450Å, 3000Å or 5100Å for each object, depending on the available spectral coverage. We use the methodology described in Runnoe et al. (2012) and include the correction for average orientation angle towards the accretion disk of the quasar. Both 1450Å and 3000Å luminosities are taken from SDSS spectroscopy. For the majority of sources, we use SDSS data release 7 spectra instead of BOSS spectroscopy, as the later is not properly flux calibrated (Dawson et al., 2013). The quoted uncertainties are from the global fit to the linear correlation between monochromatic and bolometric luminosities from Runnoe et al. (2012). Only 4C04.81 and 4C22.44 have their bolometric luminosities computed from BOSS spectra and hence could have larger uncertainties. The bolometric luminosity for 3C446 is from an integrated SED from Runnoe et al. (2012). All quoted luminosity values are in Table 4.4.

Black hole masses are either calculated from the broad-line region Hα emission line using the single epoch black hole mass Hα luminosity and FWHM scaling relation from Greene and Ho (2005). For 3C9, 3C298, there is strong telluric/filter transmission issues that prevent accurate measurement of the FWHM for the emission line. For these targets, we use the Mg II single epoch black hole mass estimate from Shen et al. (2011).

Table 4.4. QUART Sample properties

Name	RA J2000	DEC J2000	z	L_{bol} (10^{46} erg s^{-1})	L_{178MHz} (10^{44} erg s^{-1})	M_{BH} $M_\odot$
3C 9	00:20:25.22	+15:40:54.77	2.0199	8.17±0.31	9.0	9.87
4C 09.17	04:48:21.74	+09:50:51.46	2.1170	2.88±0.14	2.6	9.11
3C 268.4	12:09:13.61	+43:39:20.92	1.3987	3.57±0.14	2.3	9.56
7C 1354+2552	13:57:06.54	+25:37:24.49	2.0068	2.75±0.11	1.4	9.86
3C 298	14:19:08.18	+06:28:34.76	1.439	7.80±0.30	12	9.51
3C 318	15:20:05.48	+20:16:05.49	1.5723	0.79±0.04	4.0	9.30
4C 57.29	16:59:45.85	+57:31:31.77	2.1759	2.1±0.1	1.9	9.10
4C 22.44	17:09:55.01	+22:36:55.66	1.5492	0.491±0.019	0.6	9.64
4C 05.84	22:25:14.70	+05:27:09.06	2.320	20.3±1.00	4.5	9.75
3C 446	22:25:47.26	-04:57:01.39	1.4040	7.76	4.4	8.87
4C 04.81	23:40:57.98	+04:31:15.59	2.5883	0.62±0.02	9.3	9.58

4.7 Spatially-Resolved Regions

In this section, we define how we select different regions in our quasar host galaxies and differentiate between gas in different components of a merger system. We define a distinct region as a portion of the data cube that shares similar radial velocity, velocity dispersion, ionized gas morphology, or similar nebular line ratios. These regions may be a part or entirety of a quasar host galaxy or a nearby merging system. The number of distinct regions varies depending on how diverse the kinematics and gas morphology are in a given system.

We define a dynamically “quiescent" region of our data set that contains gas with a velocity dispersion (V_σ) less than 250 km s^{-1} . A quiescent region which belongs to the host galaxy of the quasar must have a radial velocity < 400 km s^{-1} as we expect the maximum rotational velocity for a given host galaxy to be at most 400 km s^{-1} . The maximum rotational velocity found

for the most massive galaxies studied with IFS at z$\sim$2 is about 400 km s^{-1} (Förster Schreiber et al., 2018). Gas with $V_r > |400|$ km s^{-1} and $V_\sigma < 250$ km s^{-1} is labeled as belonging to a merger system. A system is defined to be a merger if there are components with $V_r > |400|$ km s^{-1} or there is more than one distinct kinematic component. In the 3C298 system, for example, two galactic disks are found to be offset by less than 400 km s^{-1} . All radial velocity and velocity dispersion are measured relative to the redshift of the quasar. We label quiescent regions in the following manner: source name + direction + component A or B where A = component associated with the quasar, B = component associated with the galaxy merging with the quasar host galaxy. We follow these with a one or two-word comment about the region. Examples of description words are clump, diffuse, or tidal feature. Where clump referrers to a typical few kpc in size compact ionized emission typically seen in high redshift star-forming galaxies. Diffuse referrers to gas that has a surface density less than typical clumpy star-forming regions. A tidal feature refers to ionized gas associated with a tidal tail in a merging system which may contain both diffuse and clumpy ionized gas morphology.

We define “turbulent outflow" regions of each galaxy that contains gas with velocity dispersion (V_σ) > 250 km s^{-1} . We select this velocity cut-off since massive disk galaxies at z$\sim$1-3 show maximum rotational velocities of 400 km s^{-1} (Förster Schreiber et al., 2009, 2018), which is close to the maximum rotational and dispersion velocities in nearby galaxies (Kormendy and Bender, 2011). For an isothermal galactic potential with circular velocity V_c, the escape velocity is $\sqrt{2}V_c$. Hence selecting a velocity dispersion cut-off at 250 km s^{-1} , means at least 50$\%$ of the gas is moving at speeds greater than the escape velocity for the inner regions of the galaxy. This velocity cut-off is likely not large enough to only encompass gas that will escape the dark matter

halo. Star-forming galaxies with a star formation rate of >1 $M_{\odot}$ yr^{-1} will drive outflows with velocities > 200 km s^{-1} Murray et al. (2005). This is the minimum outflow velocity expected from any energy injecting source; star formation or AGN. Similar to the quiescent regions, we label the turbulent outflow regions in the following manner: source name + direction + component A/B + outflow.

In some cases, there may be several outflow regions per component per object. In more rare situations there may be outflows associated with multiple components of the merger. For example, in 3C 298 there is an outflow associated with the host galaxy of the quasar and the merging galaxy at 9 kpc from the quasar. We made the distinction by identifying two rotating disks in the system's radial velocity maps. For each region, we construct a 1D spectrum by integrating over its spaxels, as presented in Figures 4.5, 4.6, 4.7, 4.8, 4.9, 4.10, 4.11, 4.12, 4.13, 4.14, 4.15. The emission lines in each spectrum are fit with multi-Gaussian profiles in the same manner as described in section 4.5.3. The flux of each emission line along with the uncertainty is presented in Table 4.5. We further describe each of the individual sources in §4.15.

Table 4.5 Fluxes of distinct regions in individual sources

Source	Region	$F_{[OIII]}$	$F_{H\alpha}$	$F_{[NII]}$
				10^{-17} erg s^{-1} cm^{-2}
3C9	SE-SW component A	199±20	65±7	21±2
	SE component A outflow	42±4	10±1	10±1
	N component B	127±13	40±4	15±1
4C09.17	SW component A	9.55±0.98	3.37±0.35	1.32±0.2
	S/E component A outflow	71±7	6±1	–
	W component B clumps	26±3	10±1	0.77±0.13
	W component B diffuse	92±9	25±2	3.5±0.4
3C268.4	SW component A outflow	98±10	–	–
	SW component B	245±25	51±5	9±1
7C1354	component A	46±1	12±1	–
	E component B	6.2±0.6	4.7±0.5	<0.7
3C 298	W component A outflow	1276±130	204 ±20	88±9
	E component A outflow	178±20	52±5	16±2
	SE component B outflow	27±3	14±2	–
	SE component B ENLR	649±65	188±20	65±7
	SE component B tidal feature	55±5	20±2	3.6±0.5
3C318	E,W component A outflow	206±21	197±20	98±10
4C57.29	NE component A	26±3	–	–
	N component A/B(?)	12±1	–	–
4C22.44	N,S component A	54±5	25±2	3.5±0.3
4C05.84	S component A Outflow	22±2	8.1±0.8	0.3±0.03
	NE component A Outflow	22±2	5.7±0.6	2.8±.3
	SW component A clump	7.7±0.8	3.3±0.3	0.48±0.05
3C446	NW component A tidal feature	11±1	5.9±0.6	<0.15
	E-W component B	132±10	48±4	6.9±1.0
4C04.81	E component A outflow	453±45	127±13	51±5

4.8 Nebular Emission Line Diagnostics and Sources of Gas Excitation

In this section, we explore the photoionization mechanism in distinct regions of each quasar host galaxy. The Baldwin, Phillips & Terlevich (BPT) diagram is used to differentiate between different gas photoionization sources (Baldwin et al., 1981). We plot ratios of log([OIII] /Hβ) and log([NII]/Hα) against each other. A different region of this diagram corresponds to different sources of photoionization (e.g., star formation, AGN, shocks, or a mix).

To construct the BPT diagram for our sources, we integrated each emission line over the same velocity width (ΔV) and velocity offset relative to the [OIII] emission line. We integrate the maps relative to [OIII] since it is typically the brightest emission line in any given spaxel. The higher signal-to-noise [OIII] emission line leads to a smaller spaxel-spaxel variation in the radial velocity and dispersion maps, creating a more consistent log([OIII] /Hβ) and the log([NII]/Hα) ratio between neighboring spaxels. We find that for the entire sample, the standard deviation on the log([OIII] /Hβ) ratio decreases by 0.2 dex compared to when integrating the maps relative to Hα .

A resolved BPT diagram allows us to investigate the source of ionization of distinct, resolved regions in each quasar host galaxy. Due to sensitivity and in some cases, wavelength coverage, we cannot create an integrated emission line map for Hβ on a similar scale to Hα , [OIII] , or [NII] maps. For our BPT diagrams, we construct our Hβ map by simply assuming case B recombination (Hβ=Hα /2.86) with a gas temperature of 10^4 K and an electron density of 10^2 cm^{-3}. Assuming other recombination cases and ISM conditions with reasonable temperatures

and densities would not change our results by a significant amount as the ratios between Hβ and Hα would only change at most by a factor of $\sim$1.3 (Osterbrock and Ferland, 2006).

Only spaxels where at least Hα and [OIII] were detected are analyzed and presented here. Typically [NII] is detected in far fewer spaxels compared to Hα and [OIII] . For spaxels where only Hα and [OIII] are detected, we calculate a limit on [NII] by integrating a sky spectrum over the same velocity width as [OIII] at the expected wavelength location of [NII] . In Figure 4.2 we plot the ratios from each spaxel. Diamonds are regions where [NII] , Hα and [OIII] were detected, and triangles are regions where only Hα and [OIII] were detected with a limit on the [NII] flux. A total of 3160 spaxels are plotted corresponding to 21 distinct galactic regions.

For each distinct regions identified in section 4.7 we over plot their line ratios and label them with a star. Individual spaxels typically have high uncertainties in their ratios but tend to cluster together on the BPT diagram. Integrating over distinct regions and re-calculating the ratios from a high SNR spectrum confirms the true ratio of that region.

To conserve space, we do not over-plot the error bars on points from individual spaxels in Figure 4.2, we only show the error bars of ratios computed for integrated values of the distinct regions. In Figures 4.3 we plot points of individual spaxel along with the error bars.

4.8.1 Ionization Diagnostic Models

We find that a large portion of our line ratios values lie outside the two typical sequences of the BPT diagram (Figure 4.2). At a fixed log([NII]/Hα) nearly all values are above both the local mixing and star-forming sequence. At a fixed log([OIII] /Hβ) value, nearly all values are outside the local mixing sequence. A large portion of points fall between the star-forming

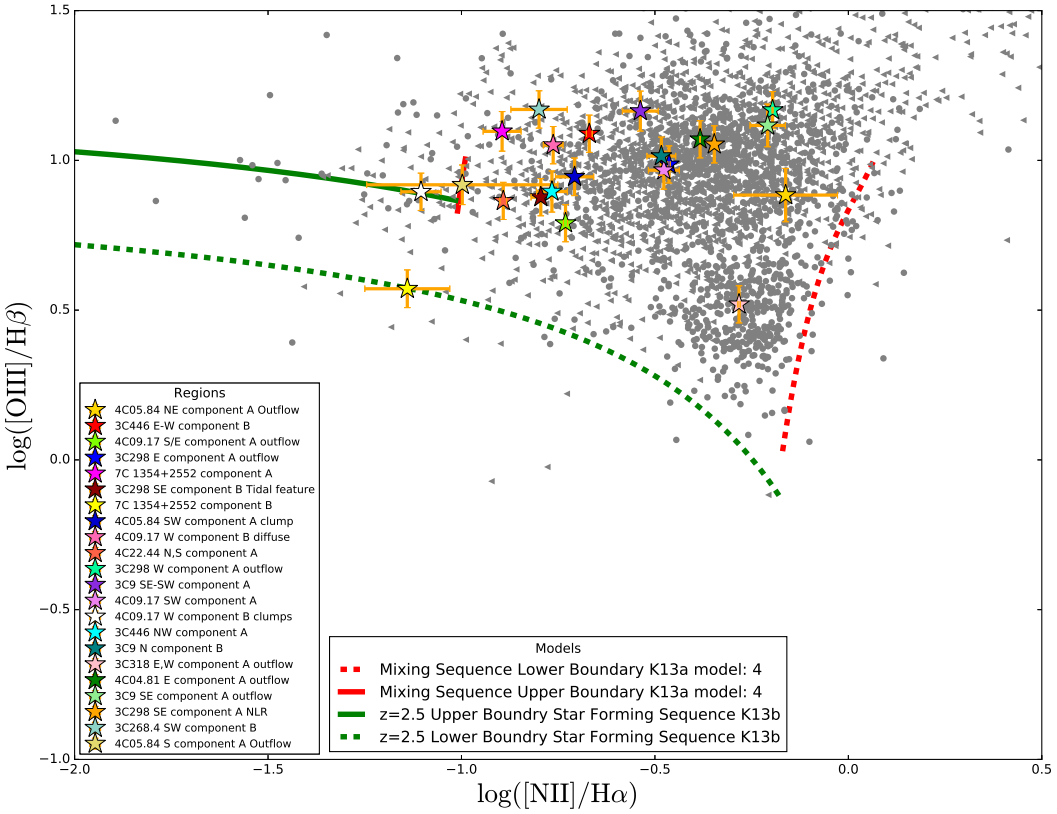

Figure 4.2 Line ratio diagnostics of individual resolved distinct regions. In grey, we plot the line ratios of individual spaxels where at least [OIII] and Hα was detected at an SNR>3. Uncertainties on these line ratios are generally large; hence, we also integrate over all spaxels in individual regions to increase the SNR and lower the uncertainties on the line ratios. We show region-integrated line ratios with a star. The names of the distinct region are present in the lower left corner, and these match the names given in Table 4.5. We present the evolutionary models of the mixing and star-forming sequence with red and green curves from Kewley et al. (2013a). We show the upper limit of a sequence with a straight line, and the lower boundary of each sequence with a dashed curve. Our line ratios are consistent with a model where gas photoionized by the quasar is denser, has lower metallicity and experiencing harder ionization compared to the gas photoionized by AGN in nearby galaxies.

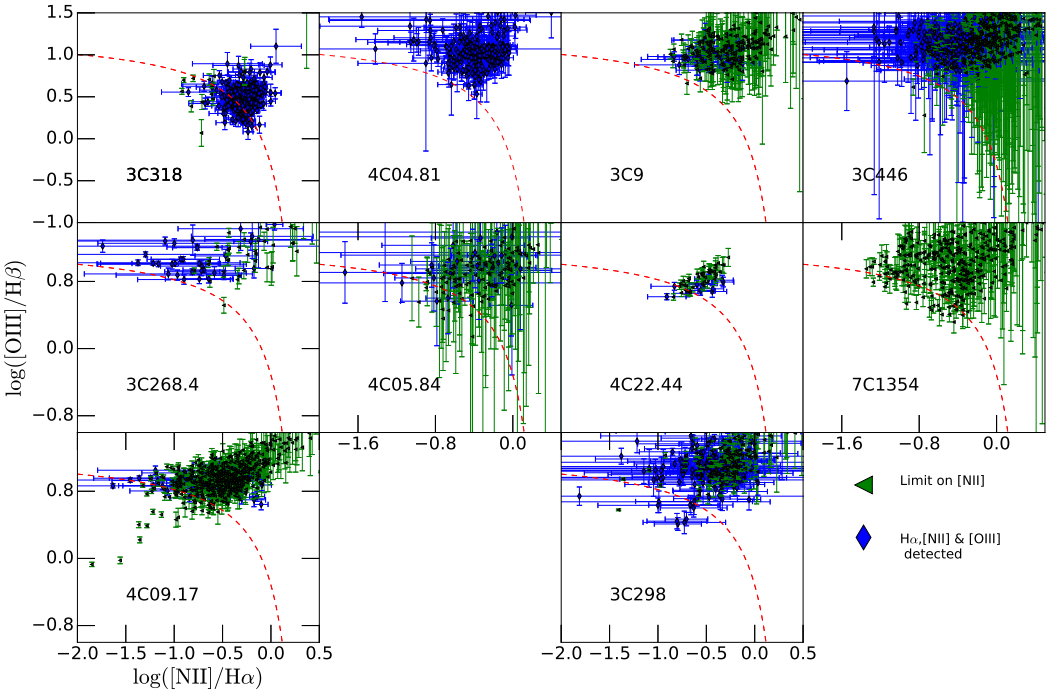

Figure 4.3 We present line ratio diagnostics for spaxels in each source where at least [OIII] and Hα were detected at SNR great than 3. We show the uncertainties on line ratio, which were omitted from figure 4.2 to conserve space. The dashed red line in each panel shows the theoretical separation between gas photoionized by star formation and AGN from Kewley et al. (2013a). Points above the line are photoionized by the quasar, while regions below are photoionized by O and B stars.

and mixing sequence, with relatively high log([OIII] /Hβ) values. Metallicity, electron density, the hardness of the ionization field and the ionization parameter determines the location of the galaxy/region on a given sequence. With changing conditions in the ISM between z=0 and the median redshift of our sample, the locus of both the star-forming and mixing sequence can change locations (Kewley et al., 2013a).

Galaxies at a fixed stellar mass have lower metallicities at high redshift compared to galaxies today (Yuan et al., 2013). Near the peak of the star formation rate density at z$\sim 1-3$, the ISM conditions and star formation histories of star-forming galaxies may differ from local systems. Star formation appears to happen in denser environments in the distant Universe with higher electron densities (Sanders et al., 2016), akin to conditions seen in local ULIRGs. According to Steidel et al. (2014); Strom et al. (2017) ISM in high redshift galaxies experiences harder ionization at a fixed N/O and O/H abundances compared to z=0 star-forming galaxies. On the other hand, galaxies at higher redshift have elevated N/O rations (Shapley et al., 2015). Taken together, Kewley et al. (2013a) shows that such changes in ISM conditions can alter the location of the star formation sequence between z=0 and z=2.5. Notably, the combination of harder ionization, electron density, and ionization parameter can shift the locus of the star-forming sequence to higher log([NII]/Hα) and log([OIII] /Hβ) values. It appears that UV/emission line selected galaxy samples tends to show a more significant shift from the SDSS star formation locus as evident in a large sample of 377 star-forming galaxies explored by Strom et al. (2017). Nearly all their galaxies have higher log([OIII] /Hβ) value at a fixed log([NII]/Hα) compared to local galaxies studied in SDSS. Various galaxy selection techniques may lead to samples of galaxies with inherently different ionization properties. However, the overall conclusion from

studying star-forming galaxies in the distant Universe is that the line ratios of these systems lie on different star formation locus compared to the local Universe.

Changes in the ISM conditions of distant galaxies may also lead to changes in the location of the mixing sequence in the distant Universe. Kewley et al. (2013a) and Groves et al. (2006) show that for galaxies with lower metallicities the mixing sequences shifts to lower log([NII]/Hα) values with relatively small changes in the log([OIII] /Hβ) value. We explore the various evolutionary models of the star-forming and mixing sequence with redshift and ISM conditions proposed by Kewley et al. (2013a). The best fit model to our sample is the one where the ISM of high redshift galaxies have more extreme condition (higher electron density, harder ionization field, and larger ionization parameters) and the metallicity of the gas photoionized by the quasar is at a lower metallicity compared to the gas ionized by local AGN in the SDSS sample. The median log([NII]/Hα) value is about 1.0 dex lower than that of the mixing sequence at z=0. If the primary source in the shift of the mixing sequence from z=0 to z=1.5-2.5 is a change in the gas phase metallicity, then the gas photoionized by the quasar in our sample has a metallicity a $5^{\rm th}$ of that in narrow line regions of z=0 AGN on the Kewley and Dopita (2002) metallicity scale. One of the consequences of the shift in the mixing sequence is that it becomes harder to distinguish between gas photoionized by AGN vs. star formation, especially in systems with potentially multiple ionization sources.

Majority of the gas in our quasar host galaxies lies on the mixing sequence where the gas is photoionized by a combination of quasar ionization and radiative shocks. However, A number of our distinct regions appear to have low log([NII]/Hα) values ($<$0.5) that showcase low-velocity dispersion gas ($V_\sigma < 250$ km s^{-1}). Morphologically these regions appear to be

clumpy in their Hα maps reminiscent of typical star-forming regions in galaxies at $z > 1$. The line ratios of these points do not coincide with regions of fast or slow shocks photoionization on the BPT diagram (Allen et al., 2008; Newman et al., 2014). Archival HST data of 3C9, 3C298, 4C09.17, 3C268.4, 3C446 all showcase that the dynamically “quiescent" regions in these galaxies have clumpy morphology in rest-frame UV continuum data, showcasing continuum emission from massive hot-young stars. In Figure 4.4 we overlay the Hα emission from dynamically quiescent regions onto archival HST observations at rest frame UV wavelength. Combining these clues suggests that the quasar does not entirely photoionize the gas in these regions. The elevated log([OIII] /Hβ) in these regions compared to local and distant star-forming regions may be from a harder ionization field due to the quasar. This gives rise to strong [OIII] emission relative to Hα , Hβ, and [NII] , whereas a part or majority of the emission from the Balmer and low ionization lines ([NII]) is from star formation. There is some evidence for this based on the morphology of the ionized gas and their respective log([OIII] /Hβ) ratios. For example, in 4C09.17, we see that more diffuse emission with low-velocity dispersion tends to have a higher log([OIII] /Hβ) value compared to clumpier regions where there evidence for recent star formation activity.

Using the empirical star formation rate Hα luminosity relationship from Kennicutt (1998), we convert the Hα luminosity of the distinct quiescent regions to star formation rates. Most likely majority of these regions are photoionized by a combination of AGN and star formation, hence the derived star formation rates are upper limits. Regions “3C298 SE component B Tidal feature" and “4C09.17 W component B clumps" have line rations most consistent with photoionization by O/B stars, the star formation rates derived in these regions are closer to their actual value. We also measure the metallicities of these regions using the Pettini and Pagel (2004) em-

Table 4.6 Star formation rates and metallicities of distinct star forming regions

Source	Region	$L_{H\alpha}$ 10^{43}erg s^{-1}	Star formation rate $M_\odot$ yr^{-1}	12+log(O/H)	σ_{gas} km s^{-1}
3C9	SE-SW component A	2±0.2	160±16	8.6	173.1±25.7
	N component B	1.2±0.1	99±10	8.6	200.5±5
4C09.17	SW component A	0.12±0.01	9±1	8.6	126.6±3
	W component B clumps	0.35±0.04	28±3	8.2	136±4.7
	W component B diffuse	0.86±0.09	68±7	8.4	146.2±7
3C268.4	SW component B	0.64±0.06	51±5	8.45	144.6±5
7C 1354	component A	0.37±0.04	29±3	<8.5	182.16±38.2
3C298	SE component B tidal	0.47±0.05	37±3	8.5	109.6±5.5
4C22.44	N,S component A	0.40±0.04	32±3	8.4	184.6±6.5
4C05.84	SW component A clump	0.14±0.01	11±1	8.5	198.7±16
3C446	NW component A tidal	0.07±0.001	6 ±1	<8.4	167.9±0.7
	E-W component B	0.48±0.05	38±4	8.5	204.3 ± 15

pirical gas phase metallicity - log([NII]/Hα) relationship. Given that log([NII]/Hα) is elevated in the presence of an AGN/quasar ionization field, the metallicities for the majority of the regions are also upper limits. We present quantitative values of these regions in Table 4.6, where we show the Hα luminosity of each quiescent region, along with the star formation rate and metallicities.

4.9 Outflow rates & energetics

In this section, we outline how we derive the outflow rates, energetics, and momentum fluxes for individual outflow regions detected in our sources. We later compare these values to predicted energy and momentum deposition from various origins (e.g., SNe, stellar winds, quasar) to establish the dominant source for driving the galaxy scale outflows.

First, we estimate the ionized gas mass of individual outflow regions. We assume constant density across each outflow and assume that each cloud inside the outflow has the same

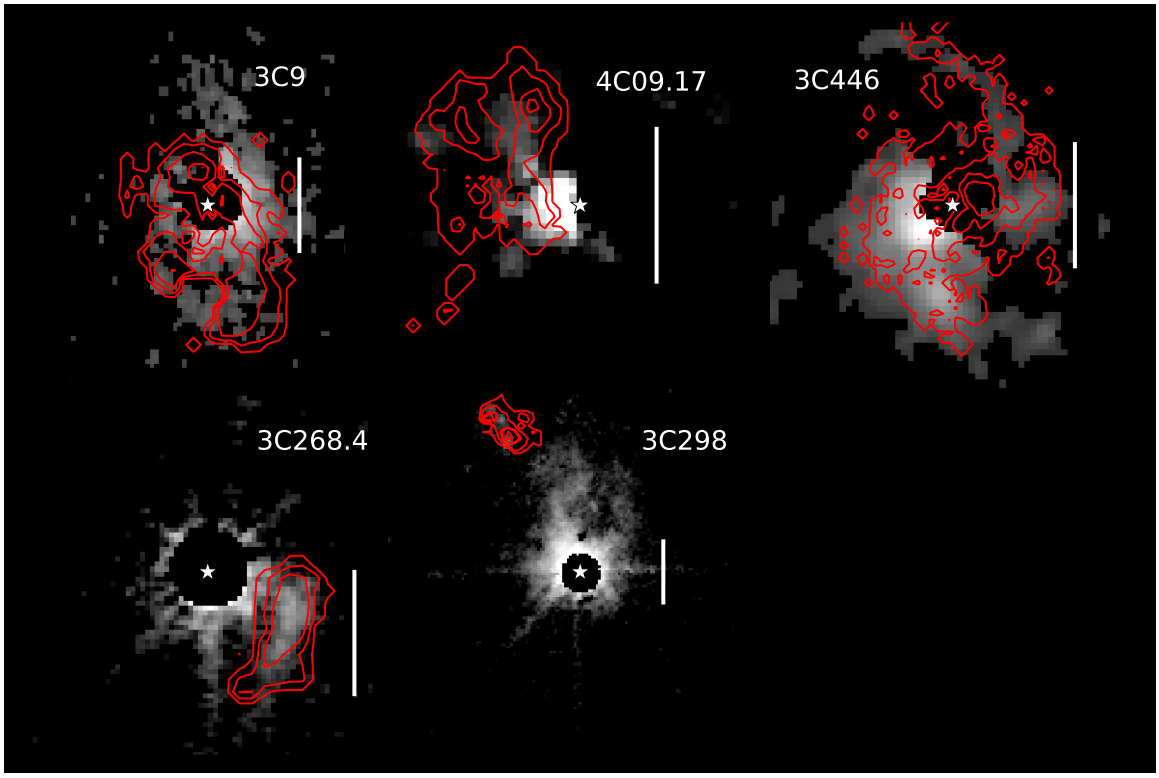

Figure 4.4 Detection of dynamically quiescent regions in archival *Hubble Space Telescope* observation. In the background, we show PSF-subtracted images of rest-frame UV emission in the quasar host galaxy. Overlaid in contours is the extended Hα emission of the dynamically quiescent regions detected with OSIRIS. Note the similarities in both morphology and extent. The bar represents a spatial scale of 1″ or about 8.5 kpc.

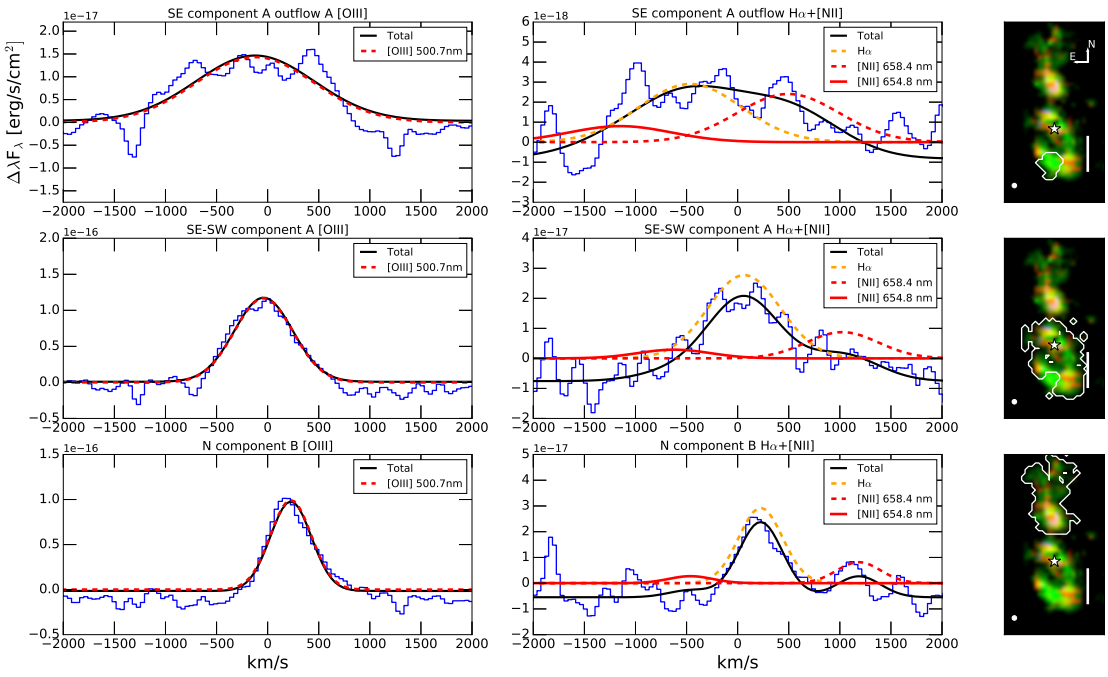

Figure 4.5 Spectra of distinct regions along with fits to individual emission lines for the 3C 9 system.

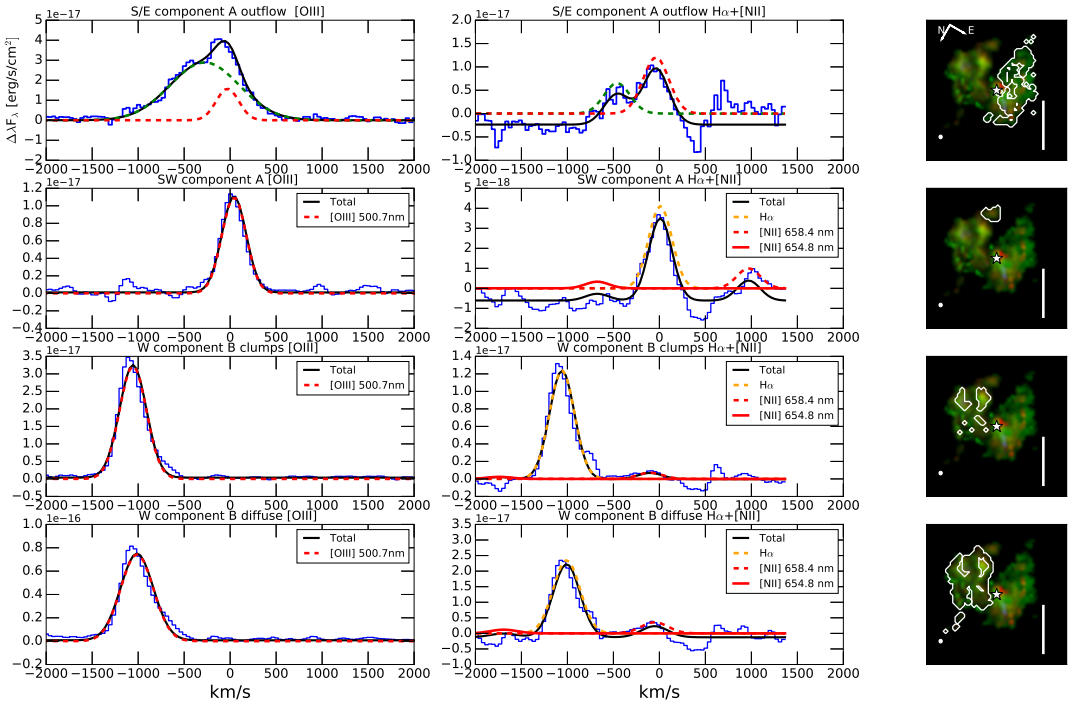

Figure 4.6 Spectra of distinct regions along with fits to individual emission lines for the 4C09.17 system.

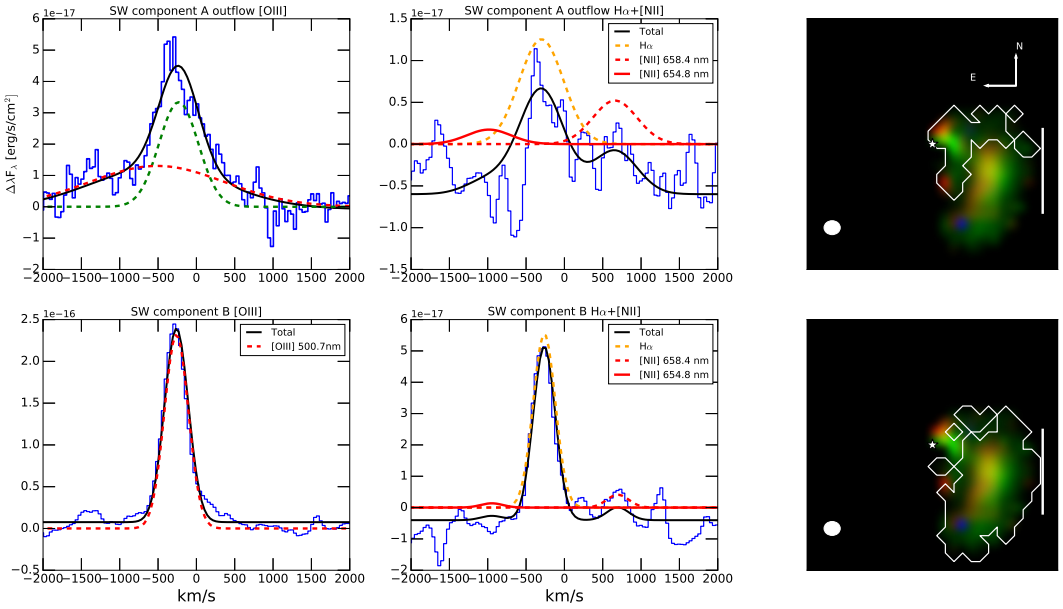

Figure 4.7 Spectra of distinct regions along with fits to individual emission lines for the 3C268.4 system.

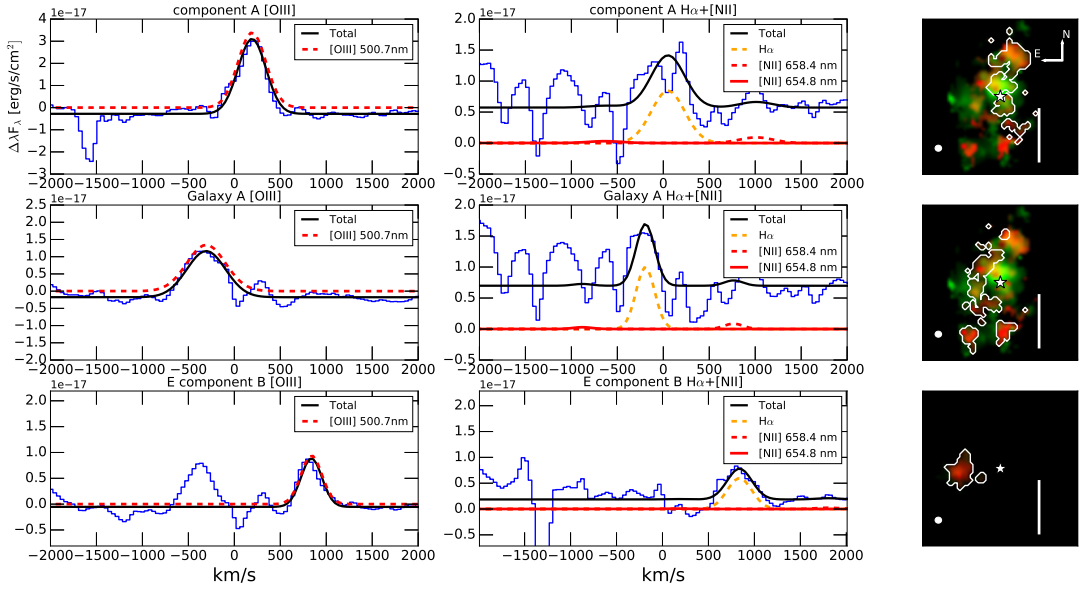

Figure 4.8 Spectra of distinct regions along with fits to individual emission lines for the 7C 1354+2552 system.

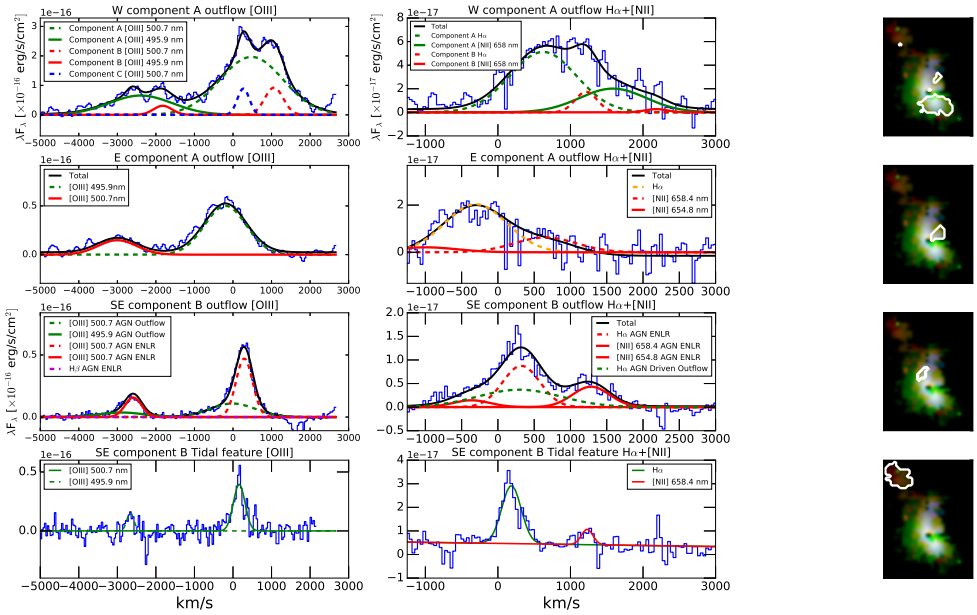

Figure 4.9 Spectra of distinct regions along with fits to individual emission lines for the 3C 298 system.

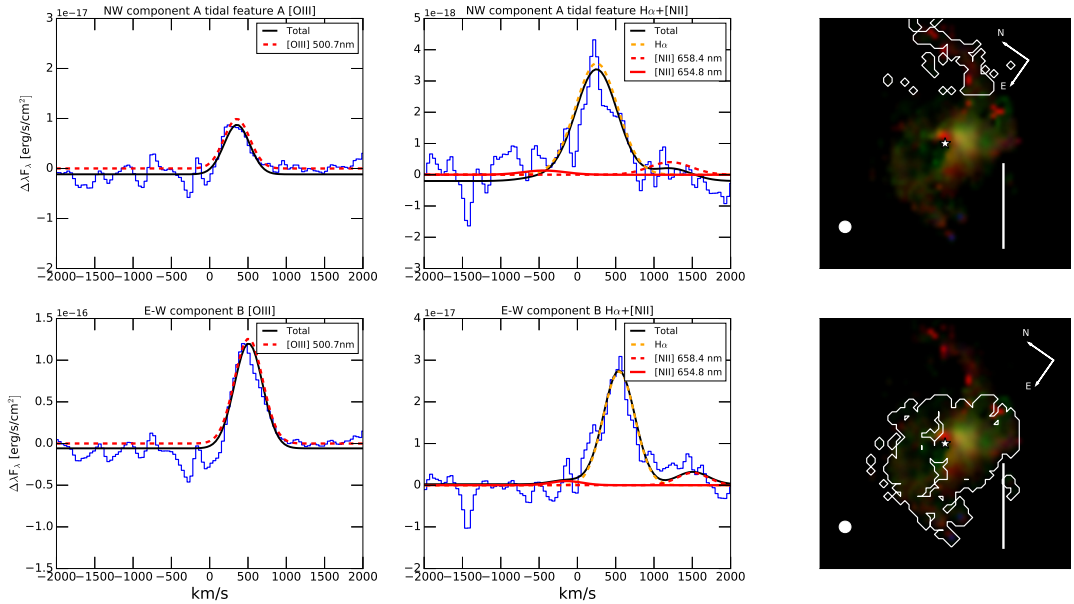

Figure 4.10 Spectra of distinct regions along with fits to individual emission lines for the 3C 446 system.

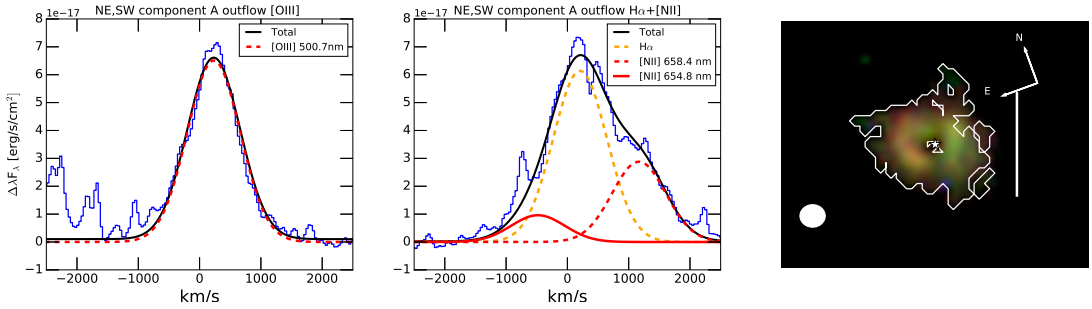

Figure 4.11 Spectra of distinct regions along with fits to individual emission lines for the 3C 318 system.

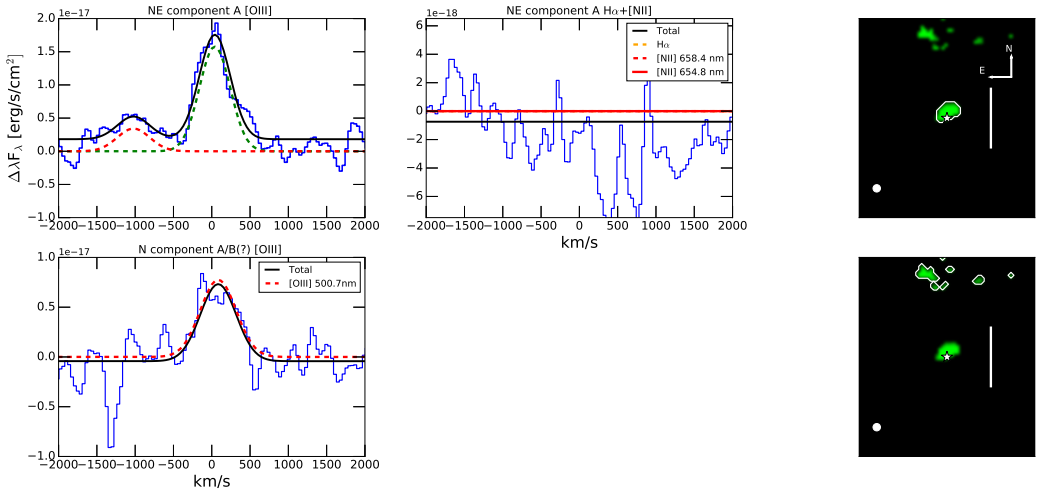

Figure 4.12 Spectra of distinct regions along with fits to individual emission lines for the 4C 57.29 system.

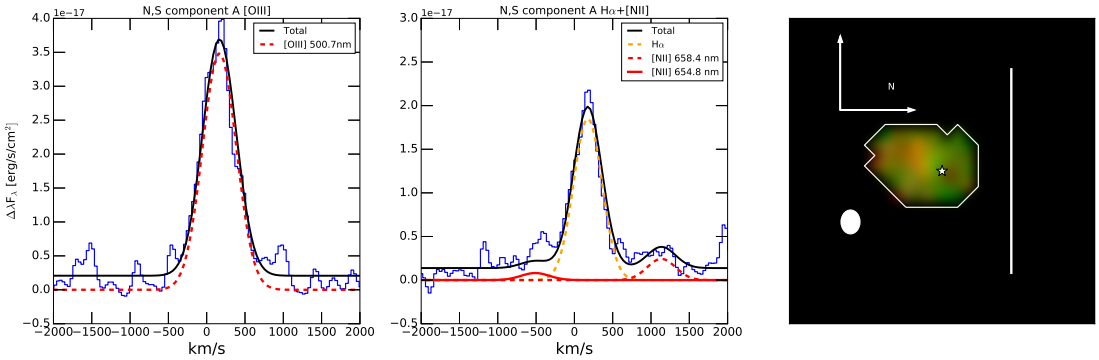

Figure 4.13 Spectra of distinct regions along with fits to individual emission lines for the 4C 22.44 system.

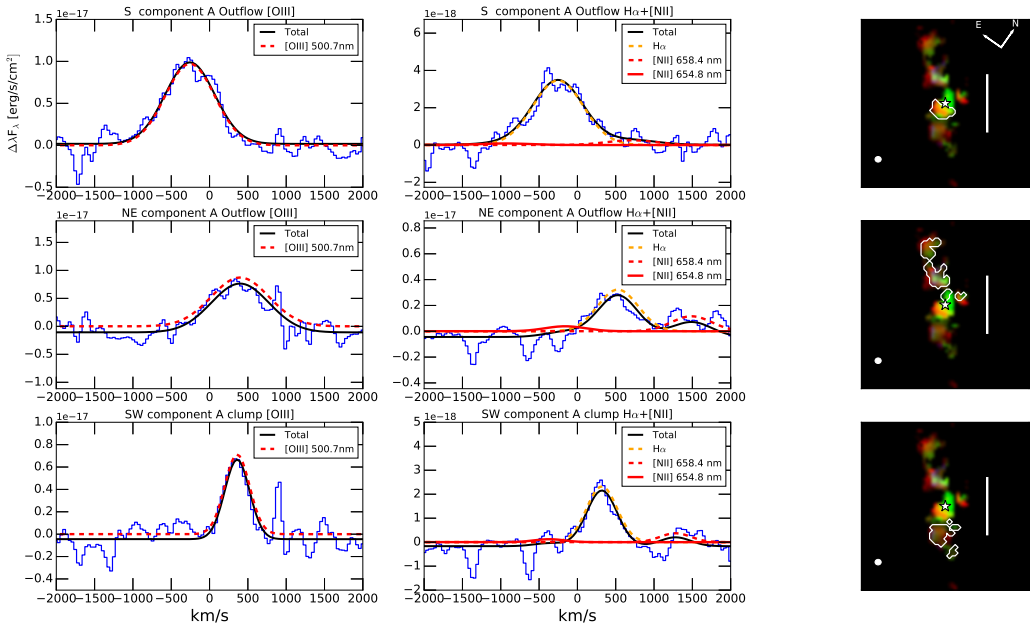

Figure 4.14 Spectra of distinct regions along with fits to individual emission lines for the 4C 05.84 system.

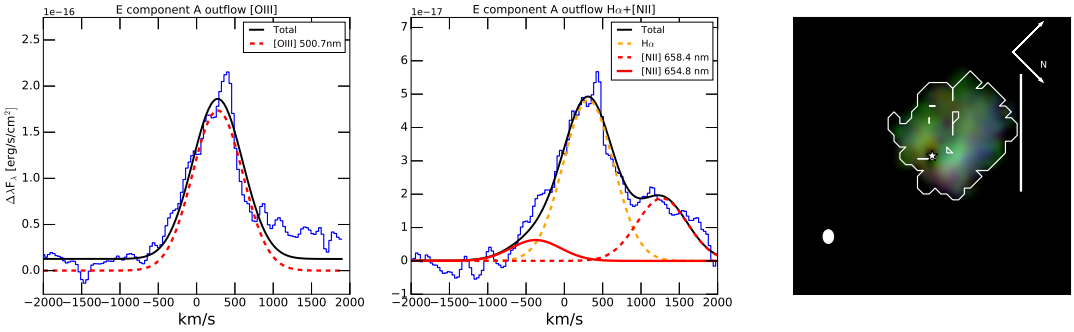

Figure 4.15 Spectra of distinct regions along with fits to individual emission lines for the 4C 04.81 system.

density. Under these assumptions, the ionized gas mass can be written as,

$$M_{gas\ ionized} = (n_p m_p + n_{He} m_{He}) V f. \tag{4.1}$$

Where V is the volume of the emitting region, f is the fill factor; the ratio of the size of emitting clumps to the total volume of the region and n_p is the proton number. Finally, n_{He} and m_{He} are the number density of Helium and the mass of a helium atom. We assume a solar abundance for Helium. We assume the gas in the outflow region is fully ionized where Helium is an equal mix of HeII and HeIII. Under these assumptions, we get the following relationships:

$$\begin{aligned} n(He) &= 0.1 n_p \\ n_e &= n_p + \frac{3}{2} n(He) \\ n_e &= 1.15 n_p \end{aligned} \tag{4.2}$$

Using the formulation of Osterbrock and Ferland (2006) Hα emission due to recombination is given by the following formula:

$$L(H_\alpha) = n_e n_p j_{H_\alpha} V f \tag{4.3}$$

where j_{H_α} is the emission line emissivity assuming Case B recombination. Under case B recombination the Hydrogen gas is optically thick to ionizing radiation, and all photons produced from an excited to the ground state are immediately reabsorbed. Hence, we omit downward radiative transitions to the ground state. Isolating Vf in equation 4.3 and substituting into equation 4.1 along with relationships from equation 4.2 we obtain the following equation for the

total ionized gas mass:

$$M_{gas\ ionized} = 1.27\left(\frac{m_p L_{H\alpha}}{j_{H_\alpha} n_e}\right) \tag{4.4}$$

where $\mathrm{L_{H\alpha}}$ and $\mathrm{n_e}$ are the integrated Hα luminosity and the average electron density over the outflow region. Since we cannot measure the electron temperature for our objects, we assume a range of 1-2$\times10^4$ K, which constrains the Hα line emissivity to 3.53-1.8$\times10^{-25}$ $\mathrm{erg\ cm^3\ s^{-1}}$ (Osterbrock and Ferland, 2006) for an electron density of $\sim 10^{2-3}$ $\mathrm{cm^{-3}}$. Missing information about the electron density can lead to an order of magnitude uncertainties on the ionized gas mass, while uncertainties on the electron temperature add a factor of a few. However, for two objects (3C318 and 3C298), we were able to measure the electron density from the 671.7 nm & 673.1 nm [SII] lines ratios directly. For the rest of the targets we assume an electron density of 500$\mathrm{cm^{-3}}$ with an uncertainty range of 100-1000 $\mathrm{cm^{-3}}$. Another way to compute the ionized gas mass is from the [OIII] line luminosity and electron density as presented in Cano-Díaz et al. (2012), however, this adds extra uncertainty as this method requires an assumption on the metallicity of the gas in the outflow region. We compute the ionized gas through this method by assuming solar metallicity. If the metallicity is lower than solar, then the ionized gas mass and subsequently the outflow rates computed from [OIII] line are effectively a lower limit as the ionized gas mass measured from [OIII] is inversely proportional to gas metallicity. Given that we do not have a proper measurement of the ionization parameter over the outflow regions, we have no way of knowing which oxygen ion contains the majority of the mass. For the masses measured from [OIII] , the assumption is that all of the oxygen in the outflow is doubly ionized.

The most straightforward outflow rate formula that we can use to estimate the outflow rate is given by the following equation:

$$\dot{M} = \frac{Mv}{R}. \tag{4.5}$$

where we assume no prior information about the geometry of the outflow and simply measure how long it takes the total gas (M) to reach an average radius R moving at constant velocity v. However, with the assistance of AO, we can resolve each outflow, typically with several beams across each region. We find that the majority of the outflows resemble a cone-like structure with evidence for either a bi-conical shape with blue and redshifted outflows in the same system or one-sided cones. We find bi-conical outflows in 3C318, 3C298 and 4C05.84 while we see one-sided conical outflows in 3C9, 4C04.81, 3C268.4 and 409.17. None of the outflows appear to cover a sold angle of 4pi steradians as seen from the center of each galaxy suggesting for cone-like structure as opposed to spherical shells.

A more fitting way to calculate the mass outflow rates for our objects is to assume a conical thin shell model with a constant density as presented in Cano-Díaz et al. (2012):

$$\dot{M} = vR^2\Omega\overline{\rho}, \tag{4.6}$$

where the density is given by $\overline{\rho} = M/V = \frac{3M}{R^3\Omega}$. The velocity of the material in the outflow is v, assumed to be moving at a constant rate over the cone, R is the radial extent of the cone, and Ω is the opening angle of the cone. Substituting the density formula into equation 4.6 yields the following outflow rate formulation:

$$\dot{M} = 3\frac{Mv}{R}. \tag{4.7}$$

This outflow rate is a factor of 3 larger than the simple outflow rate formula given by equation 4.5. The wings of the emission lines most likely give the true average velocity of the outflow, as the lower velocities seen in the line profiles are probably due to projection effects of the conical structure (Cano-Díaz et al., 2012; Greene et al., 2012). To measure the velocity in the wings of the emission line we use a non-parametric approach by first constructing a normalized cumulative velocity distribution:

$$F(v) = \int_{-\infty}^{v} f(v')/\int_{-\infty}^{\infty} f(v')dv' \tag{4.8}$$

on individual Gaussian fits where v=0 is where the Gaussian profile peaks. For a Gaussian, $F(v)$ is a smooth monotonically increasing function, v_{10} is defined where $F = 0.1$ (i.e., the velocity where 10% of the line is integrated). In Table 4.7 v_{10} is presented under the $\mathrm{V_{out}}$ column. For the outflow radius (R), we use the radius of the largest extent of the outflow on the sky. To compute R, we construct a curve of growth on the extended [OIII] emission line map, integrating from the centroid of the quasar for each outflow region. Individual outflow regions are isolated from the rest of the host galaxy emission using a mask that includes spaxels with broad emission lines (see section 4.7 for identifying extended outflow regions). The outflow radius is taken to be the radius where we spatially sum up 90% of the [OIII] flux in the outflow region. In this assumption, the outflow began near the quasar and had been expanding outwards. There could be the possibility that the outflow started at some $R_{initial}$ away from the quasar, in such a scenario it would be

more appropriate to use $\Delta R = R_{outflow} - R_{initial}-$ as the radial extent of the cone. However for all sources but 3C9 we see that the outflow extends all the way to the inner working angle (0.2″ from the quasar) of our PSF subtracted data cubes, indicating that potentially the outflow extends to the inner regions of the each galactic nucleus, so using R vs ΔR would not make a significant difference in the outflow rates. In fact, in 4C05.84, 4C04.81, and 4C09.17 we find that the outflow extends within the inner working angle of our OSIRIS observations, due to the detection of unresolved outflows, after subtracting all the extended emission.

We present the outflow rates from extended outflows in Table 4.7, they range from 23-700 $M_\odot$ yr^{-1} for masses derived from Hα luminosity and 5-460 $M_\odot$ yr^{-1} for masses derived from [OIII] . The error bars quoted in Table 4.7 on the outflow rates include the photon counting statistics and flux calibration uncertainties but are dominated by our missing information on the electron density over the outflow regions. For 3C298 and 3C318, we can directly measure the electron density from the ratio of the [SII] doublet by fitting a double Gaussian profile to the emission lines (Figure 4.16). We use the *getTempDen* routine part of *PyNeb* (Luridiana et al., 2015) package to derive the electron density. For 3C318 and 3C298, the largest uncertainty on the electron density comes from measuring the [SII] line ratios, for which the uncertainty is dominated by the limited spectral resolving power of OSIRIS (R$\sim$3800). For all the other sources we assume an electron density of 500 cm^{-3} with a range of 100-1000 cm^{-3} , which dominates the uncertainty on the outflow rate. The selected electron density is within the range of values found in AGN driven outflows in the distant and nearby Universe (Harrison et al., 2014; Kakkad et al., 2018; Förster Schreiber et al., 2019). The study by Carniani et al. (2015) also assumes the same electron density for outflows in type-1 quasars at z$\sim$ 2.4, so for direct

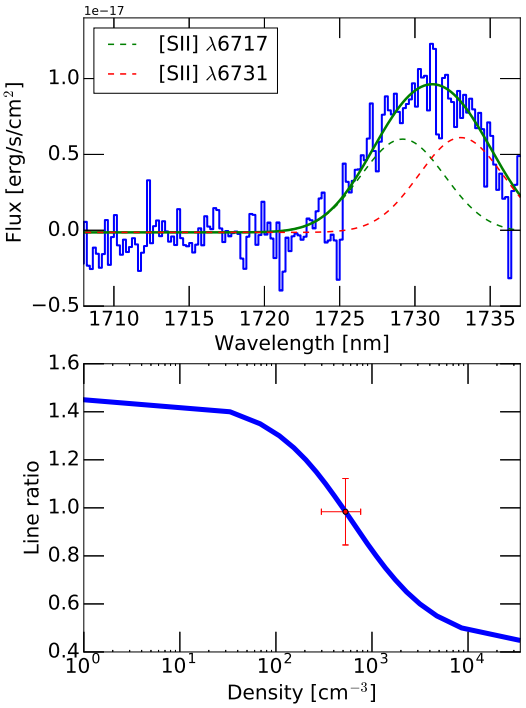

Figure 4.16 Measuring the electron density for the outflow region in the host galaxy of 3C 318. Top panel shows the spectrum in the vicinity of the [SII] doublet along with a double Gaussian fit to each emission line. Bottom panel shows the line ratio vs density from PyNeb for an electron temperature of 1×10^4 K. Red point represent the measured value on the ratio along with the uncertainty on the electron density as measured from this line ratio. We obtain an electron density of 529 ± 232 cm^{-3}

comparison; we chose this electron density as well.

To improve the uncertainties on outflow rates requires observations at a higher spectral resolving power. Since the emission lines are generally very broad, and the [SII] doublet is hard to separate, future IFS instruments with higher spectral resolving power are crucial to measuring accurate electron densities over outflow regions.

For each object, we search for nuclear outflows by subtracting the extended emission. The removal is done by subtracting a model cube of the extended emission from the PSF un-

subtracted data cubes. We then perform aperture photometry on the point source emission. We fit the broad Hα and Hβ emission from the broad-line region with a combination of broad Gaussian profiles (similar to section 4.3) and include intermediate width emission lines ($250 < V_\sigma < 2000$ km s^{-1}) in [OIII] and Hα when present to account for emission from the narrow-line region and nuclear outflows. For 4C09.17, 4C57.29, 3C268.4, 4C04.81, 4C57.29, and 7C 1354+2552 we detect broad spatially-unresolved asymmetric emission lines. Because we detect [OIII] , we believe that these outflows extend far beyond the broad line region for each quasar. In 4C09.17, 4C05.84, 3C268.4, and 4C04.81 we think the unresolved outflows are connected to the galaxy-wide outflows since they show similar emission line profiles. Most-likely these are the base of the galaxy-scale outflow at small separations ($<$ 1kpc) from the quasar, within the inner working angle of our LGS-AO observations. We set a limit on the radius of these regions by measuring the FWHM of the PSF by first integrating the data cube along the spatial axis and fitting a Gaussian plus Moffat profile to the image. For 7C 1354+2552 and 4C57.29, no extended outflows are detected at separations ($>$ 1kpc). We assume an electron density in the range of 500-1500 cm^3, slightly higher than our assumption on extended outflows since the nuclear outflows might be denser due to their smaller sizes. Their outflow rates are recorded in Table 4.8.

4.9.1 The driving source of the outflows

To test the driving mechanism for the outflows, we measure the momentum flux of each outflow region. We compare the measured momentum flux and kinetic luminosity of the outflow to predicted energy and momenta depositions from radiation pressure of the quasar's accretion disk, outflows driven by BAL and or UFO winds, radiation pressure from stars on dust grains

in the host galaxy, or mechanical feedback from supernovae explosions. The following formula gives the total measured momentum flux for the outflow:

$$\dot{P}_{\rm outflow} = \dot{M} \times v \tag{4.9}$$

and the momentum flux of the quasar accretion disk's radiation field is given by:

$$\dot{P}_{\rm quasar} = \frac{L_{\rm bolometric}}{c} \tag{4.10}$$

where $L_{\rm bolometric}$ is the bolometric luminosity of the quasar from Table 4.4 and c is the speed of light. We provide the ratio of these values in Tables 4.7,4.8 and range from 0.004 - 80. We interpret these values in the discussion section below. For each outflow region, we also measure the kinetic luminosity of the outflow, given by

$$L_{\rm kinetic} = \frac{1}{2}\dot{M} \times v_{out}^2. \tag{4.11}$$

To understand the driving mechanism for the galaxy scale outflows, we compare the outflows' kinetic luminosity and momentum fluxes to the momentum and energy deposition from AGN and stellar sources. For radiation pressure driven wind by the SMBH accretion disk, we compare the momentum flux of the outflow to the momentum flux of the quasar accretion disk: $\dot{P}_{QSO}$ = L_{bolQSO}/c. To investigate whether radiation pressure from massive young stars is driving the outflows, we take the stellar population's bolometric luminosity and convert it into a momentum flux (L_{SFR}/c). The bolometric luminosity is taken as the integrated infrared

luminosity from 8-1000 μm measured by fitting the mid to far infrared SED. The quasars 3C9, 3C298, 3C318, and 3C268.4 are modeled with AGN and star formation SED from Herschel and Spitzer photometry presented in Podigachoski et al. (2015). Only the SEDs for 3C298 and 3C318 contain points with significant detections at wavelengths from the mid-infrared to sub-mm, for the rest of the sources the total infrared luminosity due to star formation is an upper limit. In these works, the SED is fit with a model including emission from the dusty torus as well as far infrared emission produced by reprocessed UV emission from young stars. The best fit mid-infrared SED model is subtracted, leaving behind emission from dust associated with reprocessed stellar light. However, these models do not take into account far-infrared emission associated with cooler emission from the torus and dust on kpc scales heated by the quasar. Several studies have found the quasar itself can heat dust on kpc scales to temperatures similar to dust heated by young stars. The star formation rates derived from total infrared emission should be taken as upper limits in systems with powerful QSOs (Symeonidis et al., 2016). For luminous quasars there may be no wavelength where the emission “purely" comes from stellar activity, it is safe to assume that the quasar contributes to radiation at all wavelength. A second way to compute the stellar bolometric luminosity is to convert the Hα flux to a star formation rate of each distinct quiescent region (see section 4.7), and then convert this star formation rate to a total infrared luminosity. We use the star formation rate derived from Hα and far-infrared luminosity as prescribed in Kennicutt (1998). The total infrared luminosity measured from Hα should be taken as a lower limit because of dust extinction effects. As discussed in section 4.8, Hα is most likely not entirely produced by recombination from photoionization by O stars, there is a non-negligible contribution from quasar photoionization. The choice of initial mass

function (IMF) will add a factor of $\sim$1.3 uncertainty on the star formation rates. We use both the Hα and the SED derived momentum fluxes for comparison with the outflows' momentum flux and momentum deposition. The following equations provide the momentum flux from the radiation pressure of stellar systems:

$$\dot{\mathrm{P}}_{\mathrm{SFR}} = 5.827 \times 10^{34} \frac{\mathrm{L}_{\mathrm{H}\alpha}}{1 \times 10^{43} \mathrm{erg/s}} \mathrm{dynes} \tag{4.12}$$

$$\dot{\mathrm{P}}_{\mathrm{SFR}} = 3.336 \times 10^{35} \frac{\mathrm{L}_{\mathrm{IR}}}{1 \times 10^{46} \mathrm{erg/s}} \mathrm{dynes} \tag{4.13}$$

or in terms of a star formation rate:

$$\dot{\mathrm{P}}_{\mathrm{SFR}} = 7.34 \times 10^{32} \frac{\dot{\mathrm{M}}_{\mathrm{SFR}}}{1 \mathrm{M}_{\odot} \mathrm{yr}^{-1}} \mathrm{dynes} \tag{4.14}$$

We compute the momentum and energy deposition from supernovae driven winds using equations (10) and (34) presented in Murray et al. (2005):

$$\dot{P}_{SNe} = 2 \times 10^{33} \frac{\dot{M}_{SFR}}{1 M_{\odot} yr^{-1}} \mathrm{dyne} \tag{4.15}$$

$$\dot{E}_{SNe} = \xi E_{SN} \dot{M}_{SFR} f_{SN} \sim 3 \times 10^{40} \frac{\dot{M}_{SFR}}{1 M_{\odot} yr^{-1}} \mathrm{ergs}^{-1} \tag{4.16}$$

For momentum deposition, equation 4.15 assumes each supernova explosion produces 10M$_{\odot}$ of ejected all moving at $\sim$3000 km s^{-1} . It assumes a supernovae rate of 1 per 100 years per

$1M_{\odot}$ yr^{-1} of star formation. For energy deposition, equation 4.16 assumes each supernova explosion yields 10^{51} erg of energy, an energy coupling fraction to the ISM of $\xi = 0.1$, and a supernovae rate per unit rate of star formation $f_{SN} = 10^{-2}$, similar to the assumption for momentum deposition. In table 4.9, we present the momentum flux and energy deposition values derived from the star formation rates in dynamically quiescent regions associated with the quasar host galaxy. When available, we also derive these values from the far-infrared luminosity obtained from SED fitting.

4.9.2 Condition for star formation as a potential driver of outflow:

During the first 4 Myr after a burst of star formation, radiation pressure from massive stars dominates the energy and momentum deposition from stellar feedback. After about 3-4 Myr contribution from SNe is about the same as radiation pressure from stars (Leitherer et al., 1992, 1999; Murray et al., 2005). The SNe rate peaks at about 10 Myr after the burst (Leitherer et al., 1999), after which point feedback from stellar populations ceases to be important. Stellar feedback can drive the outflow if $\dot{P}_{SFR}$ is greater than or comparable to $\dot{P}_{outflow}$, either from supernovae (SNe) driven winds or radiation pressure driven on dust grains by the stellar population. Radiation pressure on dust grains surrounding star-forming regions can drive outflows with $\dot{P}_{outflow}$ up to $\times 2$ that of $\dot{P}_{SFR}$ on kpc scale (Thompson et al., 2015) through trapping of far infrared photons in the outflow. For the extent of the outflows in our sample with $\dot{P}_{outflow} > 2\times\dot{P}_{SFR}$, the primary driving source cannot be from star formation. If $\dot{E}_{SNe}$ is also higher than or comparable to $\dot{E}_{outflow}$, then the outflow may be powered by both energy and momentum deposition from SNe feedback or radiation pressure from massive stars. Even if $\dot{E}_{SNe}$ is

less than $\dot{E}_{outflow}$, there can still be sufficient momentum flux from star formation to drive the outflow as momentum deposition can couple much better to the outflow than energy (Murray et al., 2005).

The momentum deposition from radiation pressure by the quasar is almost always higher than the momentum deposition by star formation. Hence all the outflows except for 3C 318 may be driven by radiation pressure from the quasar accretion disk. In section 4.9.6, we discuss why we exclude star formation as the primary source for driving the outflow in 3C318 due to the geometry of the outflow.

4.9.3 Condition for AGN as potential driver of outflow:

If $\dot{P}_{SFR}$ is much smaller than $2\times$ $\dot{P}_{outflow}$, then the outflow cannot be driven by star formation, and we look to the quasar as a primary driving source. There are multiple ways that a quasar can drive a galaxy scale outflow. First is through radiation pressure on either dust grains or electrons in the host galaxy. If $\dot{P}_{QSO}$ is greater than $\dot{P}_{outflow}$, then the outflow can be driven by radiation pressure. In fact, for the radial extent of the outflows in our sample, through trapping of infrared photons in the outflow $\dot{P}_{outflow}$ can be at most $2\times$ higher than $\dot{P}_{QSO}$ and the outflow can still be driven by radiation pressure (Thompson et al., 2015; Costa et al., 2018a). However, in the scenario that the outflow has a very high infrared optical depth, the amount of gas these simulations predict in the outflow is significantly larger than what we observe.

The second type of an AGN driven outflow is when a broad absorption line wind, ultra-fast outflow, quasar jet or a warm absorber type wind drives a powerful shock in the host galaxy of the quasar. In simulations where a fast (v $>$ 30,000 km s^{-1}) wind drives the shock, Faucher-

Giguère and Quataert (2012) finds that the rate-limiting step in cooling the shocked bubble is due to Coulomb heating of the electrons to the same temperature as the protons past the shock. If the shock rapidly expands past a few kpc the timescale to do this can reach up to a few Gyr. Once the electrons are at the same temperature as the protons, they can cool through inverse Compton scattering or from free-free emission and the protons cool through Coulomb collisions with the cooling electrons. For these reasons the shocked bubble expands adiabatically sweeping material from the inner regions of the galaxy before the shock can cool, providing a momentum boost to the galaxy scale wind. For shocks driven by slower winds, the shocks are primarily cooled by inverse Compton scattering and free-free emission. The condition for an energy conserving shock is if the cooling time scale (t_c) is longer than the flow time scale ($t_{flow} = R_s/v_s$) and much longer than the initial crossing time scale ($t_{cr} = R_{SW}/v_{wind}$) at the radius where the gas is shocked. Where v_s is the velocity of the shock, R_s is the radius of the shock, v_{wind} is the velocity of the wind responsible for the shock, and R_{SW} is the radius where the initial shock occurs. $t_{cool} >> t_{flow} > t_{cr}$ implies energy conservation while $t_{cool} << t_{cr} < t_{flow}$ implies, the wind cools and only the ram-pressure is communicated to the ISM, only momentum is conserved (Faucher-Giguère and Quataert, 2012). In the energy conserving scenario, The shocked bubble expands adiabatically in a Sedov-Taylor phase and will maintain a large proportion of the energy provided to it by either one of the AGN driving mechanisms. The ratio between $\dot{P}_{outflow}$ and $\dot{P}_{QSO}$ for such outflow is expected to be >2-10$\times\dot{P}_{QSO}$ (Faucher-Giguère and Quataert, 2012; Zubovas and King, 2012) on kpc scales. Energy conserving or adiabatic shocks are one of the most efficient ways to remove gas from a massive galaxy at high redshift, drive turbulence in the host galaxy's ISM and prolong the time necessary for gas to cool and form stars. In the case of an

isothermal shock, $\dot{P}_{outflow}$ will be smaller than $\dot{P}_{QSO}$ on kpc scales, decreasing as a function of radius (Faucher-Giguère and Quataert, 2012; Zubovas and King, 2012; King and Pounds, 2015). Given that the same condition is true for a radiation pressure wind, with present data, we cannot distinguish between these two driving mechanisms (an isothermal shock vs. radiation pressure).

Wagner et al. (2012) also finds a considerable momentum boost for jet driven outflows. In their simulations, a powerful quasar jet slams into the ISM and drives a hot shock. The shocked wind is at a temperature of 10^7 K and expands adiabatically. Mukherjee et al. (2016) finds similar results. These simulations do not treat the protons and electrons as having different temperatures past the shock, and they do not have a luminous quasar on while the shocked bubble expands in comparison to Faucher-Giguère et al. (2012). The temperature of the shocked bubble is about two orders of magnitude lower than that in Faucher-Giguère and Quataert (2012). The question is, can the quasar radiation field cool the gas through inverse Compton scatting or free-free emission, in which case the momentum flux would drop as the shocked gas will radiate a portion of the energy provided to it by the jet. Using equation 15 from Faucher-Giguère et al. (2012) inverse Compton scattering can cool the gas in 18 Gyr at a kpc from the quasar for an AGN with a bolometric luminosity of 1×10^{46}erg s^{-1}, and an electron temperature of 10^7 K. Using equation 24 from Faucher-Giguère and Quataert (2012) the estimated cooling time scale from free-free emission is much shorter, about 15-150 Myr for an electron density of 0.1 - 1 cm^{-3} (Wagner et al., 2012). Even the 15 Myr time scale to cool the gas is much longer than the flow time of the shock. For example, in Mukherjee et al. (2016) the shocked bubble propagates from 1 kpc to 3 kpc in a matter of only 1 Myr. These results indicate that even with the presence of an intense radiation field from the quasar or free-free emission, the cooling time

scale for the shocked bubble is longer than the flow time. These results indicate that the bubble will expand adiabatically while sweeping the material from the inner few kpc of the galaxy, providing a significant momentum boost to the galactic wind. The temperature and phase map in Mukherjee et al. (2016) indicate the presence of gas at temperatures $> 10^7$ with densities 0.1-0.01 cm^{-3} . These higher temperatures can prolong the free-free cooling time scale by 1-2 orders of magnitude and decrease the inverse Compton cooling by about an order of magnitude. However, even this time scale will be too long for the flow time of the hot energy bubble at distances greater than 1 kpc.

4.9.4 Outflow Comparisons

Figure 4.17 is a diagnostic diagram that distinguishes between the driving mechanism for the outflows (star formation vs. AGN) based on the above-defined criteria. In figure 4.18 we distinguish whether radiation pressure from the quasar or an isothermal vs. adiabatic shock is driving the outflow. Points that are below the 1:2 line ratio between $\dot{P}_{QSO}$ and $\dot{P}_{outflow}$ are outflows that are driven by either radiation pressure or an isothermal shock, points that are above the line are outflows that are most-likely driven by an adiabatic shock.

The galaxy-scale outflows in 3C318, 3C 298 and 4C04.81, are consistent with energy conserving shock as a driving mechanism within the error bars on the ratio between $\dot{P}_{QSO}$ and $\dot{P}_{outflow}$. The nuclear outflows in 4C04.81 and 4C57.29 are consistent with either being driven by an adiabatic shock or from radiation pressure in a very optically thick environment with a high column density ($\mathrm{N_H} > 10^{24}$ cm^{-2}). For 4C09.17, 4C05.84 and 3C268.4 the extended outflow is consistent with either being driven by an isothermal shock or through radiation pressure by

the AGN. The nuclear outflow in 4C05.84 is consistent with either being driven by radiation pressure or an isothermal shock. For 3C9 the outflow can either be driven by star formation or by an isothermal shock or through radiation pressure by the AGN. The most likely driving source for 3C9 is star formation given the geometry of the outflow and the fact that it does not extend to the quasar. The outflow propagates along the minor axis of the rotation disk, similar to star formation driven outflow in M82. Furthermore, the wind in 3C9 is emanating from the location where star formation has recently occurred based on nebular emission line ratios for 3C9 and from the presence of extended UV emission in a galactic ring (see Figure 4.4).

In 4C05.84, 4C04.81, 3C298, 3C268.4, 3C318 and 3C9 the path of the jet correlates with the direction of the outflow (e.g. see Figures 4.28, 4.34). Indicating that the jet could be responsible for driving the outflow. In section 3.6 we further discuss this scenario.

4.9.5 Sample comparison

We collate data from the literature on both ionized and molecular outflows in the low and high redshift Universe. We attempt to make a comparison to various AGN host galaxy surveys, both type 1 and type 2 AGN and QSOs that are radio quiet and loud. To perform a direct comparison between the ionized outflows in our sample and the ionized outflows in literature we re-derive the outflow rates and bolometric luminosities (when possible) of the AGN in the same manner as we have in our paper. From each paper, we extract the luminosity of a Balmer emission line (either Hβ or Hα), and when possible the electron density to estimate the ionized gas mass with the similar assumption that we made for our sample using Equation 4.4. In cases where the electron density was not measured, similar to our sample, we assume an electron

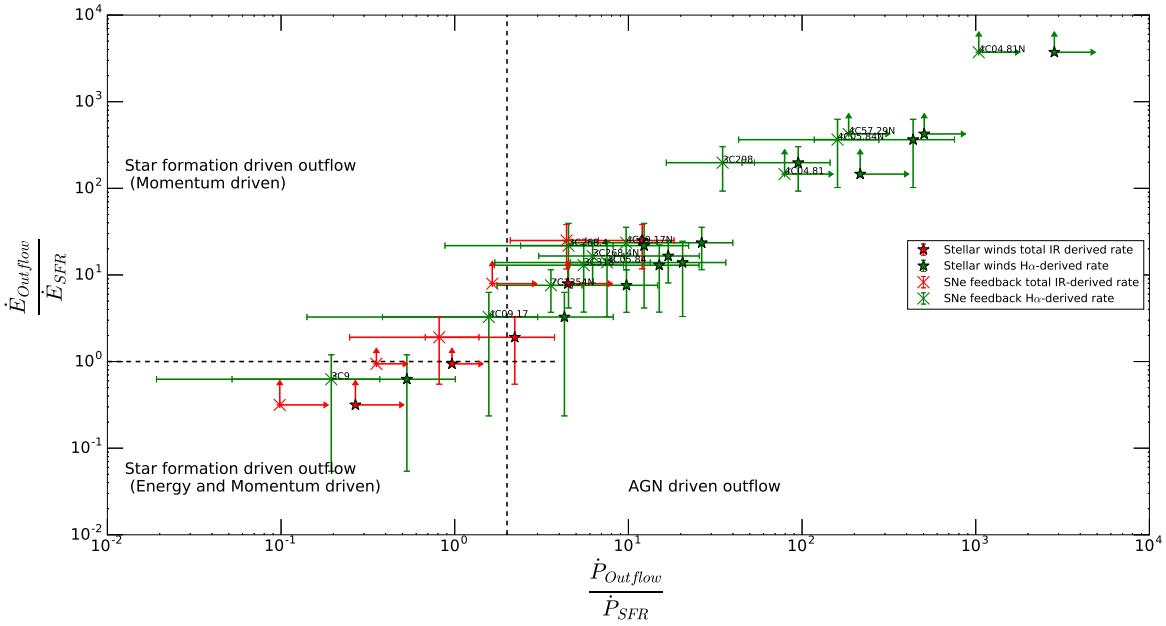

Figure 4.17 Diagnostic diagram distinguishing between AGN or Star formation as the main driving mechanism of the galaxy outflows. On the Y-axis, we plot the ratio of the kinetic luminosity of the outflow to the energy deposition from stellar feedback, and on the X-axis, we plot the ratio of the momentum flux of the outflow to the momentum deposition from stellar feedback. Points, where energy and momentum deposition are calculated from star formation rates derived from Hα emission line, are shown in green. Red points represent energy and momentum deposition derived from total infrared luminosity. The stars represent stellar feedback models from stellar winds, while the green Xs represent SNe feedback models. We show the division between AGN vs. Star formation as the main driving mechanism with dashed lines. These criteria are outlined in section 4.9.2,4.9.3.

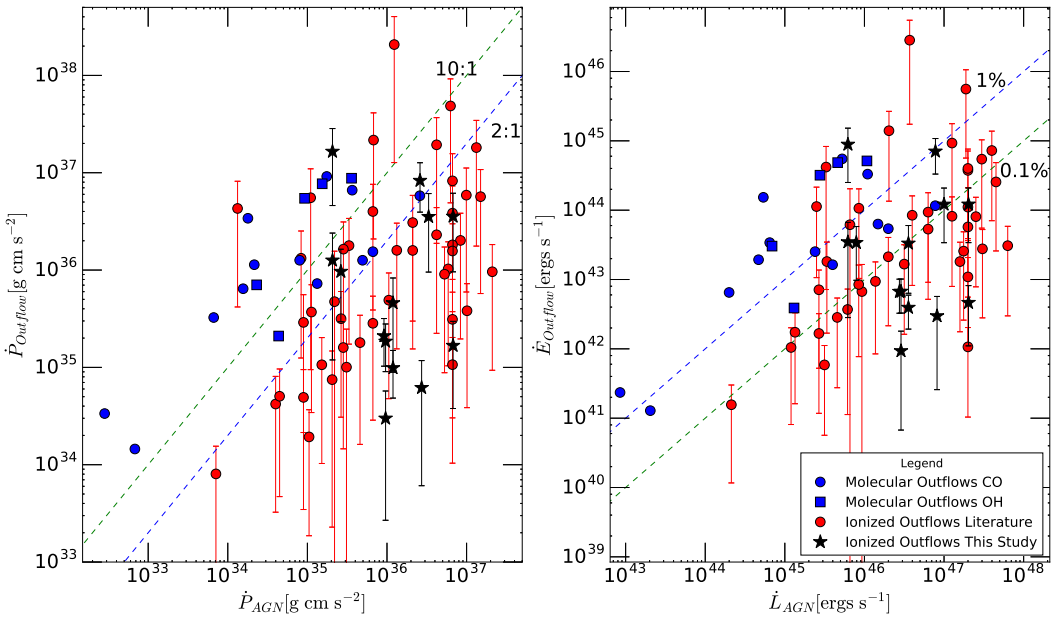

Figure 4.18 Diagnostic diagram distinguishing between different AGN components that may have driven the outflows. On the left, we plot the momentum flux of the outflow against the radiation momentum flux from the quasar. Red points represent outflows detected in ionized gas emission. Black stars represent points from our sample. Blue squares represent galaxies where a molecular outflow was detected through OH absorption while blue circles represent molecular outflows detected through CO emission. We plot lines of constant ratios of 2:1 and 10:1 between $\dot{P}_{outflow}$ and $\dot{P}_{AGN}$ as these ratios distinguishing between different driving mechanism. Points below the 2:1 line represent outflows that may have been driven either by an isothermal momentum conserving shocks or through radiation pressure on dust grains by the AGN or quasar. Points above the 2:1 line represent galactic outflows that were driven by a hot adiabatic shock if the radius of the outflow is $>$ 1 kpc. Points above the 2:1 line may also be driven by radiation pressure in very confined $<$1 kpc regions where there is very high opacity to infrared photons. On the right, we plot the kinetic luminosity of the outflow against the bolometric luminosity of the AGN. Green dashed curve represents the minimum coupling efficiency (0.01%) prescribed by theoretical work necessary to clear the galaxy of its gas and establish the observed local $M_\bullet - \sigma$ relationship. Points on the right plot are color-coded to the points on the left plot.

density in the range of 100-1000 cm^{-3} . We obtain the radius and velocity of the outflow, and along with the ionized gas mass, we estimate the ionized gas outflow rate with Equation 4.7.

For the type-1 radio-quiet quasar sample from Carniani et al. (2015) we use the Hβ emission line luminosity to derive the ionized gas mass and the radius and velocity from their Table 2 to derive the outflow rates. We assume electron density in the range of 100-1000cm^{-3} . We assume a conical geometry which leads to outflow rates 3 times higher than the original paper. For radio-loud type 2 AGN we extract data from Nesvadba et al. (2017b). We use their Table 4 to extract the velocity of the outflowing gas and the radial extent, which is taken to be half the major axis of the [OIII] emitting gas. We use either the extinction corrected (when available in Table 6) Hα or Hβ line luminosity to compute the mass of the ionized gas. For the radio loud type 2 AGN sample we use the bolometric luminosities presented in (Nesvadba et al., 2017c) computed from mid and far infrared Herschel observations (Drouart et al., 2014). Since these are obscured AGN measuring their bolometric luminosities from UV spectroscopy is difficult and would most likely underestimate the true luminosity of the object. For less luminous AGN at redshift ~ 2 we use the Genzel et al. (2014) sample of AGN select from star-forming galaxies observed with near-infrared IFS. We use the Hα line luminosity of the outflow component in their Table 4 along with the velocity and radial extent. The AGN bolometric luminosity for this sample are presented in Table 1 of the paper and are derived from rest-frame 8μm luminosity or absorption corrected X-ray luminosity. We only include targets for which both an outflow was detected, and the bolometric luminosity was measured. For one target (GS3-19791) the outflow may not be AGN driven as the system's bolometric luminosity is dominated by star formation. We add all detected outflows in galaxies with AGN from MOSDEF survey (Leung et al., 2019),

where we have re-calculated the ionized outflow rates with similar assumptions to our sample using the Hα lines to calculate the ionized gas mass. The bolometric luminosities of AGN in the MOSDEF survey span a range of 10^{44-47} erg s^{-1}and are calculated from the [OIII] line luminosity. The sample includes both type 1 and type 2 AGN and quasars.

We also include outflows from papers on individual sources. From Cresci et al. (2015) we include the properties of the outflow detected in the obscured AGN XID2028 at z=1.59. We use an outflow velocity of 1500 km s^{-1} and a radius of 13 kpc along with ionized gas mass derived from the Hβ luminosity for a typical range in electron density of 100-1000 cm^{-3} . For XID2028, the bolometric luminosity of 2×10^{46} erg/s is derived from SED modeling. From Brusa et al. (2016) we include the ionized outflow detected in XID5395 at z=1.472. We use the Hα emission line to derive the ionized gas mass using an electron density of 780$\pm$300 cm^{-3} measured from [SII] line ratios, along with the measured radius of 4.3 kpc and an outflow velocity of 1300 km/s. XID5395 has a bolometric luminosity of 8×10^{45} erg/s derived from SED fitting similar to XID2028.

We also make a comparison between the ionized outflows detected at z$>$1 to molecular outflows detected in the nearby and high redshift Universe. To date, the majority of the molecular outflows have been detected and studied in detail in nearby systems. With the advent of ALMA, the number of molecular outflows detected at high redshift is growing, but the majority of the sample still consists only of nearby systems. AGN that have bolometric luminosities in the quasar regime are extremely rare in the nearby Universe compared to $z \sim 2$ where they are nearly 1000 times more prevalent. As a result of this, the majority of the molecular outflows have been studied in systems with lower bolometric luminosities on average compared to the

systems with ionized outflows. From low redshift we include molecular outflows detected and studied in CO from Cicone et al. (2014); Alatalo et al. (2011); Aalto et al. (2012); Feruglio et al. (2013); Morganti et al. (2013); Veilleux et al. (2017) and in OH from Sturm et al. (2011). For comparison we only include objects where the bolometric luminosity of the AGN is greater than 10% of the total bolometric luminosity of the object, this is selected to avoid including objects where the outflow may primarily be driven by star formation and not AGN activity. The bolometric luminosity of the nearby AGN with molecular outflows spans a range of $10^{43} - 10^{46}$ erg/s. For molecular outflows seen at higher redshift we include our detection in the quasar host galaxy of 3C 298 (Vayner et al., 2017) along with a recent discovery in the star-forming/AGN galaxy zC400528 (Herrera-Camus et al., 2019) with an AGN bolometric luminosity of $10^{45.5}$ erg/s and in the obscured AGN XID2028 (Brusa et al., 2018) with an AGN bolometric luminosity of $10^{46.3}$ erg/s.

4.9.6 Special Note: 3C318 Outflow

If we assume that all of the far-infrared emission comes from cool dust heated by a recent starburst, then the recent star formation rate in the host galaxy of 3C 318 is about 580$M_{\odot}$ yr^{-1} . Within the observed error bars on $\dot{P}_{outflow}$, stellar feedback either through radiation pressure or from mechanical feedback from SNe has sufficient energy and momentum deposition to drive the galaxy scale outflow that we observe. The far infrared emission data comes from Herschel observations. The PSF of the PACS instrument is $>$17.5 arcseconds or about 150 kpc at the redshift of the quasar. Hence the cold dust emission is not well localized. Interferometric observations of molecular gas through CO emission indicate that there is an offset of 3 kpc between

the quasar and the molecular gas reservoir based on observations of CO 1-0 and CO 2-1 (Willott et al., 2007; Heywood et al., 2013). Our ALMA observations of CO 3-2 also confirms this offset (Vayner et al. 2019, in-prep). The outflow detected in ionized gas resembles a bi-conical structure centered on the quasar. The outflow emanates from the nuclear region of the system. If the distribution of dust is similar to the molecular gas, the outflow cannot be star formation driven as it does not originate from the region where star formation may have recently occurred.

Furthermore, we do not see any evidence for extended narrow Hα emission in the host galaxy that would be consistent with star formation. There is evidence for spatially unresolved narrow Hα and [OIII] emission from the nuclear region. The unresolved [OIII] is much broader than the unresolved narrow Hα emission; this is most likely due to PSF differences between the J and H band data for 3C 318. The J band data for 3C318 has a larger PSF compared H band. Most likely a larger fraction of the extended broad emission from the ionized outflow seen in nebular emission is unresolved in J band making the [OIII] line appear broader. However, a single Gaussian fit to the unresolved [OIII] emission provides a poor fit to the data. A second narrower emission line component is required. This second narrower line matches the width and redshift of the narrow Hα component, suggesting a common origin. The Hα emission is relatively narrow (FWHM of 440.24 $\pm$ 19.93 km s^{-1}) with [NII] lines undetected with a line ration limit of log([NII]/Hα)$<$ -1.1. With a log([OIII] /Hβ) ratio is about 0.3, places this region firmly inside the star-forming region on the BPT diagram. We compute the log([OIII] /Hβ) ratio from the two narrow (Hα and [OIII]) components with the broader [OIII] emission line from the galaxy scale outflow subtracted out.

The Hα line luminosity for this nuclear regions is $1.1\pm0.1\times10^{43}$ erg s^{-1}which translates

into a star formation rate of 88$\pm$9 $M_\odot$ yr^{-1} . Most likely at least some portion of the Hα flux could be due to photoionization from the quasar, so this star formation rate is an upper limit. Stellar feedback from this rate would produce about 1.8×10^{35} dynes of momentum deposition, which is 5 times smaller than the momentum flux measured in the outflow. The energy and momentum deposition is still insufficient to drive the galaxy scale outflow that we observe in this object, either from radiation pressure by the nuclear starburst (stellar winds) or SNe explosions. Taken together, we do not consider star formation as the primary driver of the outflow. The more likely scenario is the galaxy scale outflow is driven by quasar activity, both on energetic and geometric arguments.

Table 4.7 Extended outflow regions properties

Source	$L_{[OIII]}$	$L_{H\alpha}$	R_{out}	V_{out}	$t_{outflow}$	$dM/dt_{[OIII]}$	$dM/dt_{H\alpha}$	$\dot{P}$	$\frac{\dot{P}_{outflow}}{\dot{P}_{AGN}}$
	10^{43} erg s^{-1}	10^{43} erg s^{-1}	kpc	km s^{-1}	Myr	$M_\odot$ yr^{-1}	$M_\odot$ yr^{-1}	10^{35}dyne	
3C9	1.3±0.14	0.31±0.04	10.2±1	964± 50	10	4±3	10.2±9	0.6±0.5	0.03±0.03
4C09.17	2.5±0.2	0.21±0.02	5.9±1	623.3±50	9.2	9±7	8±7	0.3±0.3	0.08±0.02
3C268.4	1.9±0.1	–	5.5±1	1446±50	3.73	16.8±13.5	-	4.6±4	0.4±0.3
3C298									
W component A	17±2	2.8±0.3	4.4±0.7	1703±10	2.5	401±164	745±400	6.5±4	2.5±1.6
E component A	2.4	0.2±0.1	3.94±0.8	1403	2.75	63±27	143±94	1.3±0.8	0.5±0.3
3C318	3.5±0.3	6.48±2	3.19± 0.26	703.5±10	4.44	20.5±6.0	217±148	9.6±7	4±3
4C05.84									
SW component A	0.95±0.1	0.36±0.1	1.6±1	542.45±40	2.9	10.5±9	41.5±37	1.4±1.3	0.03±0.015
NE component A	0.95±0.1	0.24±0.2	8.3±1	618.68±40	13.2	2.3±1.9	6.4±6	0.25±0.2	0.004±0.003
4C04.81	26±3	7.2±0.7	3.8±1	552±20	6.74	122±100	361±325	12.6±11	6±5
3C268.4	1.95±0.1	–	5.5±1	1446±50	3.73	16.8±13.5	-	4.6±4	0.4±0.3

Table 4.8 Nuclear outflow regions properties

Source	$L_{[OIII]}$ 10^{43} erg s^{-1}	$L_{H\alpha}$ 10^{43} erg s^{-1}	R_{out} kpc	V_{out} km s^{-1}	$t_{outflow}$ Myr	$dM/dt_{[OIII]}$ $M_\odot$ yr^{-1}	$dM/dt_{H\alpha}$ $M_\odot$ yr^{-1}	$\dot{P}$ 10^{35}dyne	$\frac{\dot{P}_{outflow}}{\dot{P}_{AGN}}$
4C09.17	3±0.3	–	< 0.92	726±10	<1.3	40±20	–	1.8±0.9	0.16±0.08
3C268.4	2.5±0.25	–	<1.7	797±50	<2.0	19±10	-	1±0.5	0.08±0.04
7C1354	5.5±1	–	<1.0	636±10	<1.7	52±27	-	2±1	0.2±0.1
4C57.29	15±2	7±1	<1	686±20	<1.3	184±94	816±586	35±26	5±4
4C05.84	5±0.5	7±0.8	<1	683±20	< 1.4	60±30	825±590	35±26	0.5±0.4
4C04.81	10±1	14±1	<1	1073±20	<1	187±95	2440±1750	165±119	80±58

4.10 SMBH-galaxy scaling relationships

In this section, we place our galaxies on the velocity dispersion and galaxy mass vs. SMBH mass plots, comparing their locations to the local scaling relations ($M_\bullet - \sigma$ and $M_\bullet - M_*$). We calculate the SMBH masses from the broad Hα luminosity and line width using the methodology presented in Greene and Ho (2005). The SMBH masses span a range of $10^{8.87-9.87}$ $M_\odot$. The velocity dispersions are taken from dynamically quiescent regions, while the galaxy masses are calculated from the virial equation and from modeling the radial velocity of targets with rotating disks and extracting a dynamical mass.

4.10.1 Host Galaxy Velocity Dispersion

We identify several dynamically quiescent regions within most of the quasar host galaxies in our sample. These regions show relatively lower log([NII]/Hα) line ratios and typically have clumpy morphology, reminiscent of the general star-forming regions seen in nebular emission and UV continuum in high redshift galaxies. In most galaxies, these regions lie away from any galactic-scale outflows. Hence their observed dynamics could be a probe of the galactic gravitational potential. These regions can be used to measure the velocity dispersion of our quasar host galaxies. In combination with the measured black hole masses, we can compare them to the local scaling relation between the mass of the SMBH and the velocity dispersion of the galaxy/bulge. In Figure 4.19, we plot the mass of the SMBH presented in Table 4.4 against the velocity dispersion of distinct quiescent regions measured with the Hα line. Also, we include the velocity dispersion measured from CO (3-2) emission for 3C 298 from Vayner et al.

Table 4.9 Momentum and flux deposition from wind driving mechanisms

Source	$\dot{P}_{QSO}$ $\times 10^{36}$dyne	$\dot{P}_{SFR,rad,T_{ir}}$ $\times 10^{36}$dyne	$\dot{P}_{SFR,rad,H\alpha}$ $\times 10^{36}$dyne	$\dot{P}_{SNe,T_{ir}}$ $\times 10^{36}$dyne	$\dot{P}_{SNe,H\alpha}$ $\times 10^{36}$dyne	$\dot{E}_{SNe,T_{ir}}$ $\times 10^{42}$erg/s	$\dot{E}_{SNe,H\alpha}$ $\times 10^{42}$erg/s	SFR or AGN?
3C9	2.7	<0.23	0.12	<0.63	0.12	<9.4	4.8	SFR/AGN
4C09.17	0.96	–	0.007	–	0.019	–	0.29	AGN
3C298	2.6	0.69	0.087	1.9	0.24	28	3.6	AGN
3C318	0.26	0.44	0.064	1.2	0.18	18	0.26	AGN
4C05.84	6.8	–	0.0082	–	0.022	–	0.33	AGN
4C04.81	0.21	–	<0.0058	–	<0.016	–	<0.24	AGN
3C268.4	1.2	<0.1	0.037	<0.28	0.1	<4.2	1.5	AGN
4C57.29	0.7	–	<0.0064	-	<0.02	–	0.3	AGN

(2017)(Chapter 3). We find a significant offset from the local scaling relation between the mass of the SMBH and the velocity dispersion of the galaxy/bulge ($M_\bullet - \sigma$) (Gültekin et al., 2009; McConnell and Ma, 2013).

There have been numerous discussion in the literature, whether the velocity dispersion measured from gas traces the stellar velocity dispersion. The gas and stars might not have the same uniform distribution, and winds can contribute to broadening the nebular emission lines. Furthermore, the line of sight absorption and emission lines from which the velocity dispersion is calculated are luminosity weighted subject to galactic dust extinction. Because of the different light distribution between stars and gas, the measured velocity dispersion can be quiet different. These arguments can lead to increased scattering in any correlation between σ_* and σ_{gas} . Data-sets that spatially resolve the gas and stellar components as well as having enough resolving power to separate multi-component emission from different regions (e.g., outflowing/in-flowing gas vs. galactic disk rotation) are important when making a comparison between σ_* and σ_{gas} . In Bennert et al. (2018) for large sample local AGN when fitting a single Gaussian component to the [OIII] emission line, they find that they can overestimate the stellar velocity dispersion by about 50-100$\%$. Only by fitting multiple Gaussian components to account for both the narrow core and the broader wings of the [OIII] line profile can they adequately match the velocity dispersion from the narrow component of the [OIII] line to that of the stellar velocity dispersion. For their entire sample, the average ratio between the velocity dispersion of narrow Gaussian component and the stellar velocity dispersion is $\sim$1. The 1 σ scatter on the ratio between $\sigma_{[OIII],narrow}$ and σ_* is about 0.32 with a maximum measured ratio of about a factor of 2 which translates to a scatter in $\Delta\sigma = \sigma_{[OIII]} - \sigma_*$ of 43.22 km s^{-1} with a maximum difference of about $\pm$100

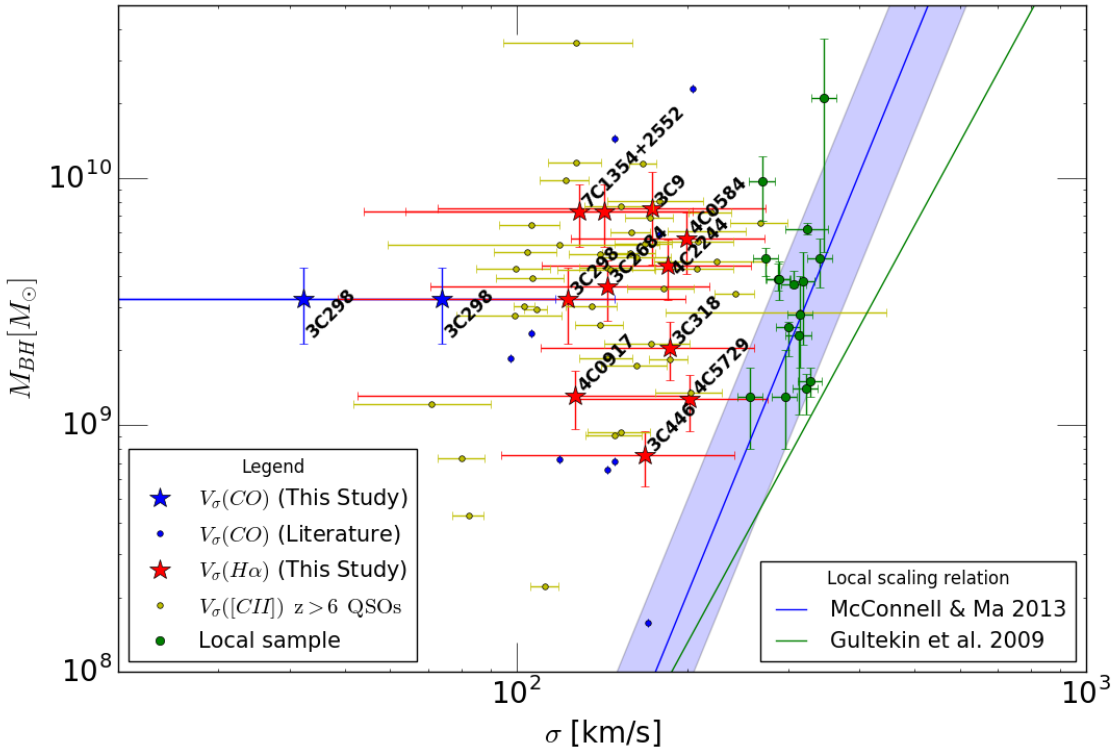

Figure 4.19 The location of our galaxies on the velocity dispersion vs. SMBH mass plot compared to the local $M_\bullet - \sigma$ relationship. Red stars are the measurements from our sample, where we measure the velocity dispersion from the Hα emission line. We measure the black hole masses using the broad Hα line from the broad-line-region discussed in section 4.3. The two blue stars represent the velocity dispersion measured in the disk of the host galaxy of 3C 298 and the tidal tail feature nearly 21 kpc away from the quasar (Vayner et al., 2017). Blue circles are quasars from the Shields et al. (2006) sample where they measure the velocity dispersion from CO emission lines. The yellow points are from quasars at z$>$ 6 where they measure the velocity dispersion from the 158μm [CII] emission line (Decarli et al., 2018). Green points represent the local sample of all the bright cluster galaxies with SMBH greater than 10^9 M$_\odot$ taken from McConnell and Ma (2013). The blue curve represents the best fit to the entire galaxy sample from McConnell and Ma (2013) while the green curve is the fit to the sample studied in Gültekin et al. (2009). The blue shaded region represents the intrinsic scatter on the $M_\bullet - \sigma$ relationship as measured by McConnell and Ma (2013). We find a significant offset between the galaxies in our sample and those of local BCG and the general local $M_\bullet - \sigma$ relationship. This large offset indicates that the host galaxies appear to be under-massive for their SMBHs.

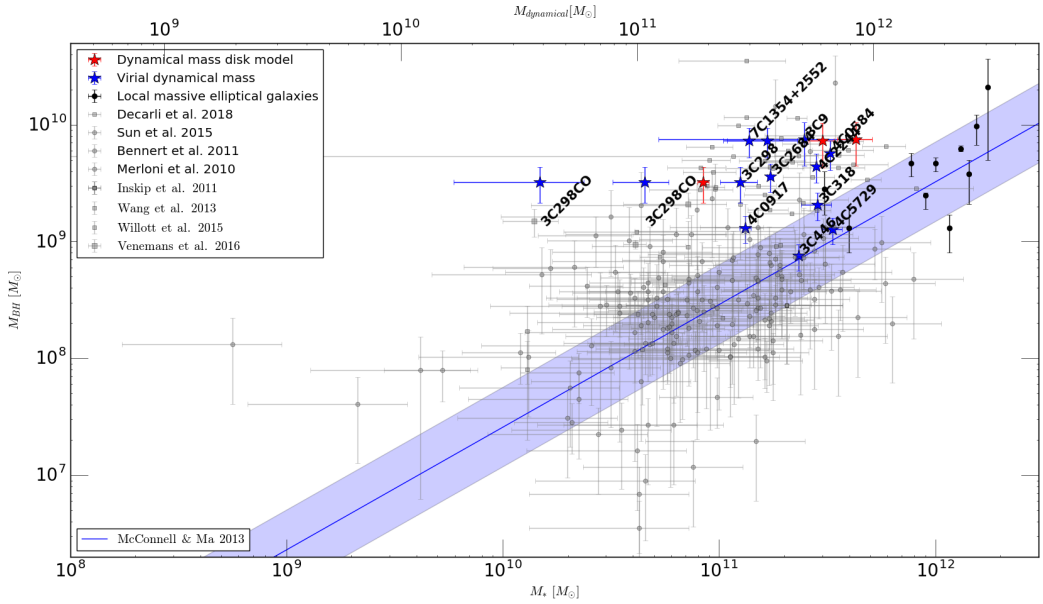

Figure 4.20 We present the location of individual galaxies compared to the local scaling relation between the mass of the SMBH and mass of the galaxy/bulge shown with a blue curve. Blue points represent systems with virial dynamical masses. Red points represent systems where we calculate the dynamical mass by modeling the radial velocity maps with an inclined disk model. Gray points show the location of galaxies at z>0.5, with lower SMBH masses and lower AGN luminosity compared to our sample. The blue curve represents the local scaling relationship as measured in McConnell and Ma (2013), with the shaded region representing the intrinsic scatter. We find the majority of our points are offset from the local scaling relationship, outside the observed scatter.

km s^{-1} . However, only a few sources show such drastic velocity differences ($\sim$ 2.5% of the entire sample, 82% of the sources show $\sigma_{[OIII]} - \sigma_* < \pm$50 km s^{-1}). In addition, when fitting for the $M_\bullet - \sigma$ relationship with the narrow [OIII] emission as a proxy for stellar velocity dispersion, the resultant fit agrees with that of quiescent galaxies and reverberation-mapped AGNs. These results indicate that for the sample as a whole Bennert et al. (2018) finds that both the stars and gas follow the same gravitation potential. We attempted to the best of our ability to separate regions that contain galactic scales winds from those with more quiescent kinematics both spectrally and spatially with OSIRIS. Hence similar to Bennert et al. (2018) we think that the measured velocity dispersions in quiescent regions are good tracers of the galactic potential on average. We still find a significant offset for our sample after applying the observed scatter in the difference between σ_* and σ_{gas} . This is also true when applied to the more distant quasar host galaxies studied with 158μm [CII] emission.

Using N-body smoothed-particle hydrodynamics simulations Stickley and Canalizo (2014) examines how the stellar velocity dispersion evolves in a binary galaxy merger. At various stages in the merger (e.g., a close passage, nucleus coalescence) they measure the stellar velocity dispersion along 10^3 random lines of sight. Near each close passage and during coalescence they find that the scatter on the velocity dispersion significantly increases from $\sim$ 5 $-$ 11 km s^{-1} to about 60 km s^{-1} with the average velocity dispersion a factor of $\sim$1.7 higher than after the galaxies have finished merging. For several sources in our sample (3C9, 3C298 and 3C446) the measured velocity dispersion might be higher than what it will be once the galactic merger is complete adding an uncertainty due to projection effects. Following the results from the simulations, we add in quadrature an additional uncertainty on the velocity dispersion of 60 km s^{-1}

given that majority of our mergers are near coalescence or a close passage ($\Delta R < 10$ kpc). It should be noted that this is near the maximum scatter seen in the simulations on σ. These simulations also find that for merging galaxies at their maximum separation, the measured velocity could be a factor of ~ 1.7 times smaller compared to the final system. They find that for a 1:1 merger the maximum separation after first passage is 10-100 kpc which is much larger than any separation that we find in our systems from observed projected separations and measured relative velocities. No obvious merging companions are found for 3C318, 4C22.44 or 4C05.84 hence for these systems the mergers might be past their coalescence stage where the measured velocity dispersion is close to its final value, and the scatter due to the line of sight effects is minimal ($\sim$ a few km s^{-1}). However, we still apply an additional 60 km s^{-1} uncertainty on these regions.

We still find that all of our systems are offset from the local scaling relation between the mass of the SMBH and the velocity dispersion of the bulge/galaxy. Even after incorporation additional uncertainties on σ due to projection effects and from observed statistical differences in σ_* and σ_* . Given that we are dealing with relatively small sample size, we performed statistical tests to confirm the validity of the offset between the local scaling relation and our sample. For each object, we measure the offset between the observed and predicted velocity dispersion for SMBH mass of our systems. We use the local scaling relation fit from (McConnell and Ma, 2013) and Hα measured SMBH masses. We construct a data set consisting of velocity differences. From bootstrap re-sampling of the velocity difference data set, we find that the average offset of 188.7 km s^{-1} is significant at the 3.25σ level. Using jackknife re-sampling similarly, we find that the offset is significant at the 3.3σ level with the 95$\%$ confidence intervals of 154.4 km s^{-1} to 223.0 km s^{-1} on the velocity dispersion offset. Performing similar statistical

tests on the Decarli et al. (2018) sample, we find an average offset of 178.8 $\mathrm{km\,s^{-1}}$ with a significance of the shift at 2.7σ and 2.8σ for Jackknife and bootstrap re-sampling, respectively from the local relationship. We also measure the offsets of massive BCGs in the local Universe from the $M_\bullet - \sigma$ relationship. Using a two-sided Kolmogorov-Smirnov test we can ask if the observed offsets of the local and high redshift data sets are drawn from the same continuous distribution. We find a p-value of 5.7×10^{-9}, indicating that the two populations are not drawn from the same distribution. Applying the Kolmogorov-Smirnov test to the velocity dispersion offsets from our sample and that found in the higher redshift quasar we find a p-value of 0.84 indicating that these two data sets could be drawn from the same continuous distribution. We find similar results by comparing the Shields et al. (2006) sample at $z \sim 2$ to our own and that of Decarli et al. (2018).

4.11 Dynamical mass measurements

We can also test whether these systems lie off the local scaling relationship between the mass of the SMBH and the dynamical mass of the bulge/galaxy. First by using a virial estimator for the dynamical mass of the galaxy $\mathrm{M_{virial}} = \frac{\mathrm{C}\sigma^2\mathrm{r}}{\mathrm{G}}$ where C=5 for a uniform rotating sphere (Erb et al., 2006a). We assume 7 kpc for the radius, which is the median effective radius of massive quiescent galaxies in the local Universe (Ene et al., 2019). Here σ is derived from a Gaussian fit to the integrated spectra over the distinct region. For galaxies with multiple distinct regions, we derive two or more dynamical masses as there may be a dependence on the velocity dispersion as a function of position with the galaxy. In nearby galaxies, there is a very weak

dependence on the velocity dispersion with the radius from the galaxy center (Bennert et al., 2018; Ene et al., 2019). For systems, in a clear merger, the galactic component belonging to the quasar is used to estimate the dynamical mass, since we are interested in the correlation between the SMBH and the velocity dispersion of the quasar host galaxy.

For systems with velocity shear in the 2D radial velocity map, we fit a 2D inclined disk model to the kinematics data to measure the dynamical mass. The model is a 2D arctan function

$$V(r) = \frac{2}{\pi} V_{max} \arctan\left(\frac{r}{r_{dyn}}\right), \tag{4.17}$$

where V(r) is rotation velocity at radius r from the dynamical center, V_{max}, is the asymptotic velocity, and r_{dyn} is the radius at which the arc-tangent function transitions from increasing to flat velocity. The measured line-of-sight velocity from our observations relates to V(r) as

$$V = V_0 + \sin i \cos\theta V(r), \tag{4.18}$$

where

$$\cos\theta = \frac{(\sin\phi(x_0 - x)) + (\cos\phi(y_0 - y))}{r}. \tag{4.19}$$

Radial distance from the dynamical center to each spaxel is given by

$$r = \sqrt{(x - x_0)^2 + \left(\frac{y - y_0}{\cos i}\right)^2}, \tag{4.20}$$

where x_0, y_0 is spaxel location of the dynamical center, we quote the value relative to the centroid

of the quasar, V_0 is velocity offset at the dynamical center relative to the redshift of the quasar, ϕ is position angle in spaxel space, and i is the inclination of the disk. V_{max} is not the true "plateau" velocity of the galaxy's disk. V_{max} can have arbitrarily large numbers, especially when r_{dyn} is very small (Courteau, 1997). To fit the data we use the MCMC code *emcee*. We construct the model in a grid with a smaller plate scale than the observed data which gets convolved with a 2D Gaussian PSF with an FWHM measured from the quasar PSF image. The image is then re-sized to the plate scale of the data. We construct the priors on each of the seven free parameters. The prior on V_{max} is $300 < V_{max} < 1000$ km s^{-1} the prior on both x_0, y_0 is the boundary of the FOV of the imaged area, the prior on the position angle is $0 < \phi < 2\pi$, the prior on the inclination angle is $0 < i < \pi/2$, the prior on the radius is $0.5 < r_{dyn} < 10$ pixels and the prior on V_0 is $-100 < V_0 < 100$ km s^{-1} . We then sample this distribution with *emcee*. We initialize 1000 walkers for each free parameter using the best fit values from *leastsquares* fitting as the starting point, with a small random perturbation in each walker. We run MCMC for 500 steps starting from the perturbed initial value. The best-fit parameters, along with their confidence intervals, are presented in 4.10 for the quasar host galaxies of 7C 1354+2552, 3C9. For 3C 298 we do not see the disk in the ionized emission with the OSIRIS data, it is solely detected in CO (3-2) observations from ALMA, here we present the best fit values from Vayner et al. (2017) (Chapter 3).

Assuming a spherically symmetric system, we can compute the total enclosed mass using the following formula:

$$M(R) = 2.33 \times 10^5 r V_r^2 / \sin(i)^2 \tag{4.21}$$

Table 4.10 Best fit values for each inclined disk model parameter

Parameters	7C 1354+2552	3C9	3C298
V_{max} [km s^{-1}]	$449.67^{+0.24}_{-0.64}$	$442.0^{+23.9}_{-5.7}$	392^{+65}_{-65}
x_0 [kpc]	$-2.37^{+0.04}_{-0.03}$	0.5^{+2}_{-1}	$0.43^{+0.1}_{-0.1}$
y_0 [kpc]	$-0.93^{+0.08}_{-0.08}$	$-4.8^{+1.22}_{-1.5}$	$0\ ^{+0.1}_{-0.1}$
ϕ [°]	$75.68^{+0.47}_{-0.48}$	$74.10^{+3.5}_{-35.4}$	$5.3^{+1.28}_{-1.28}$
i [°]	$47.6^{+0.8}_{-0.8}$	$47.1^{+5.0}_{-3.7}$	$54.37^{+6.4}_{-6.4}$
r [kpc]	<0.017	$0.26^{+0.49}_{-0.14}$	$2.1^{+0.9}_{-0.9}$
V_0 [km s^{-1}]	$-93.9^{+1.2}_{-1.7}$	$-9.22^{+30.45}_{-86.46}$	$-13.0^{+3.15}_{-3.15}$

Where V_r is the radial velocity, i is the inclination angle from the disk fit. The radial velocity is chosen as the average between the maximum and minimum observed velocity along the major axis of the disk, defined by the phase angle (ϕ) from our fit. Similarly we assume a radius that is the median value of nearby BCGs. The selected radius should give us an absolute upper limit on the dynamical mass of the galaxy/bulge as this radius is much larger than the typical size of a galactic bulge at this redshift and is larger than the observed extent of the galactic disks. The reason for choosing a larger radius is to address the case where the quasar host galaxy extends to a larger radius and is not captured in our OSIRIS observations because they are not sensitive enough to low surface brightness emission at larger separation from the quasar.

Using the measured virial and disk fit dynamical masses and the SMBH masses, we can now compare our galaxies to the local $M_\bullet - M_*$ relationship. Not only are these galaxies offset from the local $M_\bullet - \sigma$ relationship, but we also find that these galaxies are offset from the local $M_\bullet - M_*$ relationship. The galaxies need about an order of magnitude of stellar growth if they are to evolve into the present-day massive elliptical galaxies.

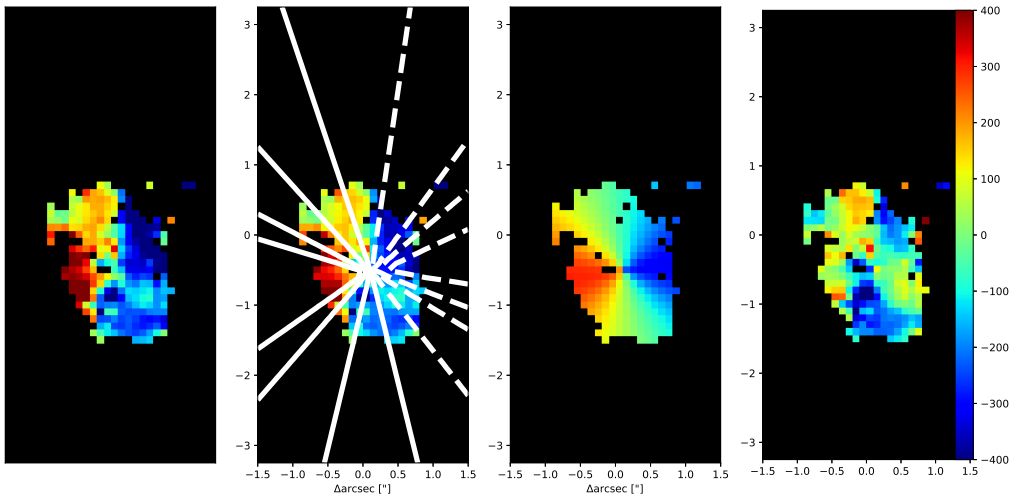

Figure 4.21 Fitting an inclined disk model to the radial velocity map of the 3C9 quasar host galaxy. Far left we plot the isolated radial velocity structure belonging to the quasar host galaxy of 3C9, middle left shows the best fit model overlaid as contours on top the radial velocity map, middle right is the best fit model, and on the right, we plot the residuals. Larger blue shifted residuals at $-1''$ south from the quasar are from the outflow (3C9 SE component A outflow A).

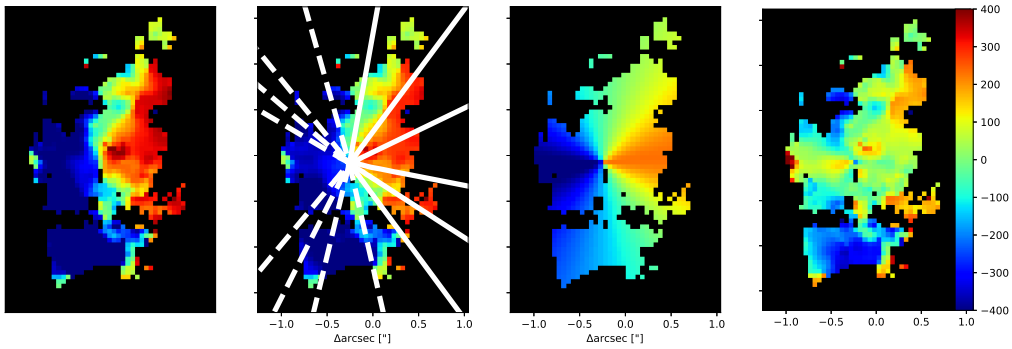

Figure 4.22 Fitting an inclined disk model to the radial velocity map of the 7C1354 quasar host galaxy. Far left we plot the isolated radial velocity structure belonging to the quasar host galaxy of 7C1354, middle left shows the best fit model overlaid as contours on top the radial velocity map, middle right is the best fit model, and on the right, we plot the residuals.

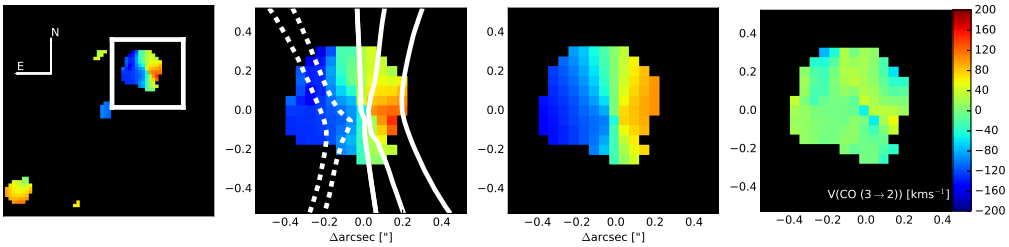

Figure 4.23 Fitting an inclined disk model to the radial velocity map of the 3C298 quasar host galaxy. Far left we plot the isolated radial velocity structure belonging to the quasar host galaxy of 3C298, middle left shows the best fit model overlaid as contours on top the radial velocity map, middle right is the best fit model, and on the right, we plot the residuals.

4.11.1 Some notes on disk fitting

Due to the limited sensitivity of OSIRIS to lower surface brightness emission, we are missing an accurate measurement of the plateau velocity for the galactic disks at large separations from the quasar. Hence, our fitting routine is unable to constrain V_{max} for 3C9 and 7C 1354. Also, it appears that the turn over radius is very small for these two systems, smaller than the resolution element of our observations. For this reason, we are unable to constrain the turn over radius, and we only provide a limit.

4.12 Discussion

Our survey aimed to study host galaxies of redshift 1.4 - 2.6 radio-loud quasars through rest frame nebular emission lines redshifted into the near infrared.

We place distinct regions of each quasar host galaxy on the traditional BPT diagram (log([OIII] /Hβ) vs. log([NII]/Hα)). Majority of the points for our sources lie outside the two local sequences (the mixing and star-forming sequence). In section 4.8, we introduce evolutionary BPT models from Kewley et al. (2013a) that indicate changes in the photoionization and metallicity conditions of the gas can shift both of the star-forming and mixing sequences. We fit these models to our data and find that the best fitting model is the one where the gas in our quasar host galaxies is at least five times less metal-rich compared to the narrow line regions of nearby (z<0.2) AGN. The best fitting model also indicates that the gas is ten times denser compared to nearby galaxies. In Figure 4.2, we show all of our points on the BPT diagram along with the best fitting model. Kewley et al. (2013b) studied a sample of star-forming galaxies and galaxies with AGN in the redshift range of 0.8<z<2.5. They also find that galaxies at z>2 show elevated line ratios, on average above the local star formation and mixing sequences. They find that normal ISM conditions similar to the SDSS sample transition to the more extreme conditions with elevated line ratios somewhere between redshift z=1.5 and z=2. This is an agreement with our results because the majority of our targets are at $z > 1.5$.

High redshift radio galaxies also appear to show ISM condition with metallicities that are lower compared to local AGN. In a study of a large sample of distant radio galaxies, Nesvadba et al. (2017a) finds that their gas phase metallicities are at least half of that seen in local AGN.

Nesvadba et al. (2017a) finds the same best fitting model from Kewley et al. (2013a) as we do for our sample to explain their observed nebular line ratios. The average log([NII]/Hα) value of our sample seems to be lower than that of Nesvadba et al. (2017a); this could be due to the lower metallicity of our sample. On the other hand, a different approach to how we compute our line ratios can cause the discrepancy. Nesvadba et al. (2017a) only presents source integrated line ratios, while we explore ratios of distinct regions because we typically have a factor of 5-10 better angular resolution due to adaptive optics and hence can resolve the different ionized/kinematics structures of our galaxies. In the majority of our sources, we see significant variations in log([NII]/Hα) and log([OIII] /Hβ) values across each system, hence why we explore distinct regions. Line ratios from integrated spectra that include regions with various ionization sources and from multiple components of a merger system may shift towards higher log([NII]/Hα), and log([OIII] /Hβ) values as the regions photoionized by the quasar/AGN tend to be brighter. Line ratios of galaxies with lower luminosity AGN compared to quasars/radio galaxies studied in Strom et al. (2017) are nearly all outside the local mixing sequence. These points overlap with the location of our line ratios and that of the radio galaxy sample. The MOSDEF survey finds similar results for their AGN sample at a range of bolometric luminosities (Coil et al., 2015). The ubiquity of elevated line ratios in host galaxies of AGN indicates that regardless of the active galaxy population selected at z$\sim$2 the conditions of the gas that is photoionized by an AGN may be similar.

Overall, this suggests that the ISM conditions in high redshift galaxies with powerful and even less luminous AGN are different from those in local systems. The ISM conditions appear to be far more extreme with gas phase metallicity lower than that of local AGN suggesting for

an evolution in the ISM gas that is photoionized by AGN from z=0 to z=2.5.

4.12.1 Star formation and quiescent regions in the host galaxies

The quasar most likely photoionizes majority of the gas in our systems. A large number of the points on the BPT diagram are within the predicted location of the mixing sequence from the evolutionary model by Kewley et al. (2013a) in Figure 4.2. Many regions show the morphology of clumpy star-forming regions seen in other galaxies at these redshifts. These regions also typically show lower velocity dispersion and lower log([NII]/Hα) values. We described them in more detail in section 4.7. These regions lie 1 - 21 kpc from the quasar and generally do not coincide with the location of galactic winds. For sources with available HST imaging of rest-frame UV continuum, these regions also appear bright and clumpy (see Figure 4.4). Taken these two results together indicates that O and B stars could photoionize a significant fraction of the gas in these regions. In section 4.8, we derive an upper limit on their star formation rates and gas phase metallicities.

4.12.2 Offset from local scaling relations

Majority of our systems appear to be offset from both local scaling relationships between the mass of the SMBH and mass and the velocity dispersion of the bulge (see Figures 4.19, 4.20). To explain the large offset from the local $M_\bullet - \sigma$ and $M_\bullet - M_*$ relationship, we could invoke a significant error in the estimated SMBH masses. The bolometric luminosities of some of our quasars are far greater than those used for reverberation mapping in the nearby Universe,

which intern is used in calibrating the single epoch SMBH mass (Greene and Ho, 2005). The SMBH masses would have to be off by 2-3 orders of magnitude to explain the observed offsets. By assuming that the SMBH grows primarily through gas accretion, we can use the Eddington luminosity formula to estimate the SMBH mass. Given that our quasars are most likely not all accreting at or close to the Eddington limit, this derived mass is effectively a lower limit.

$$\mathrm{M_{SMBH,min}} = \frac{\mathrm{L_{Eddington}}}{1.26 \times 10^{38}} \mathrm{M_{\odot}} \tag{4.22}$$

For the derived bolometric luminosities in Table 4.4 we find a range of minimum SMBH of $10^{7.5-9}\mathrm{M_{\odot}}$, consistent with what we measure from single epoch SMBH masses using the Hα emission line.

In Figure 4.24 we plot the offset from the local scaling relation against the redshift of each object from our sample, the local galaxies sample with SMBH $> 10^9$ $\mathrm{M_{\odot}}$ and higher redshift quasars. Quasars with SMBH $> 10^9$ $\mathrm{M_{\odot}}$ appear to be offset from the local scaling relationship, which indicates that SMBH growth appears to happen first in these systems. The SMBHs grow rapidly up to a mass of several times 10^9 $\mathrm{M_{\odot}}$ as early as a few 690 Myr after the Big Bang (Bañados et al., 2018), matching in mass to some of the most massive SMBH seen today. Some galaxies with lower luminosity AGN and lower mass SMBH also appear to be offset from the local scaling relation at z$>$ 1 (Merloni et al., 2010; Bennert et al., 2011). Given the typically large uncertainty on the measured values and generally small sample sizes, it is difficult today to say whether a different population of AGN/galaxies are offset differently from the local scaling relationships at z$>$ 1.

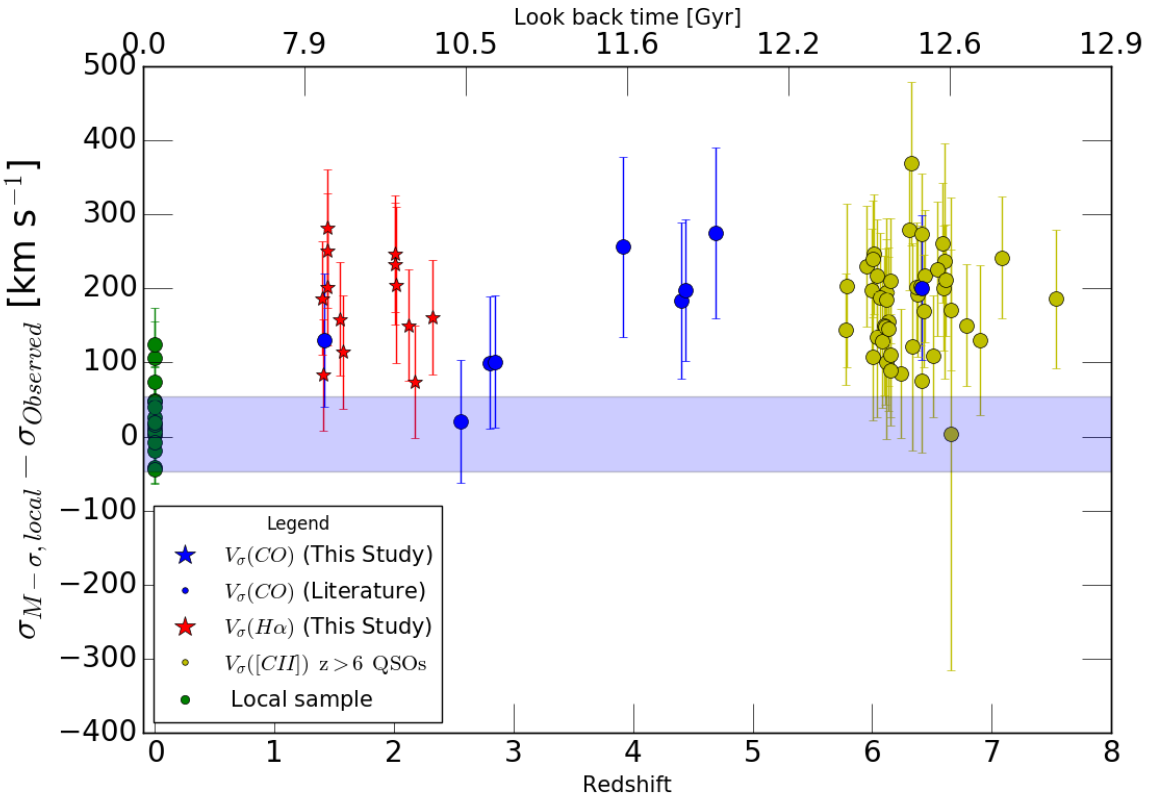

Figure 4.24 Measured offset of galaxies from the local $M_\bullet - \sigma$ scaling relationship (McConnell and Ma (2013), $\log_{10}(M_{BH}/M_\odot) = 8.32 + 5.64\log_{10}(\sigma/200\ \mathrm{km\ s^{-1}})$). On the y-axis, we quantify the offset as the difference between the observed and predicted velocity dispersion from the local scaling relation based on the observed SMBH mass. We plot the observed offset from the local scaling relation against the redshift for individual targets. The labels are similar to 4.19, where the blue circles are quasars from the Shields et al. (2006) sample, where the velocity dispersions are measured from CO emission lines. The yellow points are from quasars at z$>$ 6 where the velocity dispersion is measured from the 158 μm [CII] emission line (Decarli et al., 2018). The shaded blue region represents the intrinsic scatter in the $M_\bullet - \sigma$ relationship for black holes with a mass of $10^{9.5}$ M$_\odot$. There is an overall offset for galaxies with massive SMBH at z$>$1 from the local $M_\bullet - \sigma$ relationship. We find no statistically significant difference in the offset between any of the high redshift samples, while there is a statistically significant offset from the local BCG points (green).

Under the assumption that SMBH primarily grows through Eddington-limited gas accretion, the growth is expected to be exponential. The e-folding or “Salpeter" time scale is about 50-300 Myr, depending on the spin of the SMBH. At the mean redshift of our sample (z=1.87) the SMBHs are expected to experience 30-200 e-folds in mass growth. However, for a duty cycle of around 10% (Wang et al., 2006) the expected number of e-folds drops down to about 3-20. Furthermore, the quasars in our sample are not accreting near the Eddington limit and can eventually switch from high to low accretion-rate mode, further decreasing the Eddington ratio. The mass of the SMBH will grow at most by a factor of 1.2-7 under the assumption of an Eddington ratio of 10%, and a duty cycle of 10%. The SMBHs in our sample have nearly finished forming and will only further grow by a factor of a few. If these galaxies are to assemble onto the local scaling relation and to evolve into the most massive early-type galaxies that we see today, then the rapid SMBH growths at early times in the Universe must be followed by significant stellar growth. On average, the galaxies within our sample need to grow the stellar mass within a radius of 7 kpc at a constant rate of 100 $M_{\odot}$ yr^{-1} from z=2 to z=0.

In the host galaxy of 3C 298, there is currently an insufficient amount of molecular gas for the galaxy to grow in stellar mass to match the mass predicted by the local scaling relationship. Furthermore, the quasar 3C 298 does not appears to live in an over-dense environment based on the number count of galaxies seen with the Spitzer space telescope imaging data (Ghaffari et al., 2017). The open question is, how do these galaxies obtain the stellar mass necessary to grow into the massive galaxies we see today? Are minor mergers responsible for growing these galaxies? Alternatively, is the accretion of cool gas from the CGM responsible for providing the fuel necessary for future star formation? The results we find for the host galaxy of 3C 298

favors the scenario where cold accretion flows from the CGM will supply the majority of the fuel necessary for future star formation. Another scenario could be that the Spitzer observations are too shallow to see lower mass galaxies. If these systems are gas-rich, they can supply future fuel for star formation from merging the gas in their CGM and ISM with the quasar's host. Indeed in recent hydrodynamical simulation (Anglés-Alcázar et al., 2017a) found that for dark matter halos with masses $> 10^{12.5}$ $M_{\odot}$ majority of the mass build up happens from gas accreted from the CGM and transfer/exchange of gas from CGM and ISM of cannibalized low mass galaxies. These simulations also find that stellar build-up from dry mergers and just accretion of stars from merging galaxies is not significant to grow the stellar mass of galaxies in massive halos. If this is the case for the majority of our galaxies, this implies that they have enormous amounts of gas inside their CGM.

4.12.3 Galactic scale outflow, what is the main source of gas depletion?

In this section, we discuss the primary source of gas depletion in the quasar host galaxies in our sample. In several systems, we were able to measure upper limits on the star formation rates. We want to compare the star formation rates to the outflow rates to determine the primary source of gas depletion.

For 3C268.4, we only measure the outflow rate based on ionized gas mass derived from [OIII] . This ionized gas mass is most likely a lower limit, and if we scale it by a factor of 3; the smallest ratio that we find between ionized gas masses derived form [OIII] and Hα we find that the ionized outflow rate can be comparable to the star formation rate upper limit. If we also include the nuclear outflow (scaled for Hα) rate, then the total outflow rate can be as large as

$100M_{\odot}$ yr^{-1} , a factor of two larger than the star formation rate. For 4C09.17, we measure a higher outflow rate from the [OIII] emission line. Due to the difference in the FOV between the two modes used to observe [OIII] and Hα , we were unable to probe the entire extent of the outflow seen in [OIII] with Hα ; this leads to a smaller extended Hα flux.

For the case of 4C09.17, 3C298, 3C318, 4C05.84, 4C04.81, 3C268.4, 4C57.29, 7C1354+2552 the primary source of gas depletion is from the quasar driven outflows. These results indicate that the outflows are responsible at present for removing gas from the inner regions of the quasar host galaxies and are the dominant source of gas depletion. Furthermore, in the case of 3C298, the quasar is responsible for removing the molecular gas reservoir, indicating direct evidence for negative quasar feedback.

Our results can be in stark contrast to the predicted evolutionary paths of massive galaxies. In today's theoretical framework (Di Matteo et al., 2005; Hopkins et al., 2008; Zubovas and King, 2012, 2014), feedback from the SMBH is predicted to happen once the galaxy reaches the local $M_{\bullet} - \sigma$ relationship. However, our systems are experiencing quasar feedback when the mass of the galaxies is a fraction of their predicted final mass from the local scaling relations. Also, the gas-phase metallicities are far lower than those observed in nearby AGN. The kinetic luminosities for half of the outflows in our sample are far lower than the values predicted in simulations for the bolometric luminosities of our quasars. Ionized outflows in other samples show similar results, where about half the objects lie below the predicted minimum energy-coupling between the quasar and the outflow of 0.1% at z~ 2. If all these systems are offset from the local scaling relationship, it would be easier to launch the outflows, because their masses are smaller compared to if they were on the local scaling relations. This could lead to lower energy coupling

efficiency. On the other hand, we might be missing a significant fraction of the gas within the outflows because a large portion of the gas could be in either a molecular or neutral phase.

In the quasar host galaxy of 3C298 we find the majority of the gas in the outflow is in a molecular state, and once combined with the ionized kinetic luminosity we find values closer to those predicted in simulations. The kinetic luminosity in 3C298 is close to 1% of the quasar's bolometric luminosity. Regardless if we are accounting all the gas in the outflow, feedback is occurring before the galaxies are on the $M_{\bullet} - \sigma$ relationship. We might need to reconsider our theoretical framework for massive galaxy formation, where the gas is not cleared from the galaxy in a single "burst" of feedback once the galaxies reach the $M_{\bullet} - \sigma$ relationship. Instead, the SMBH grows first in massive dark matter haloes, followed by a delayed growth of the host galaxy with regulatory feedback from the SMBH and near-continuous accretion of gas from the CGM and nearby satellite galaxies. In such a scenario, the coupling efficiency might be lower per outflow event, compared to a single burst model where a single outflow-event clears all the gas. At later times, maintenance mode feedback from jets can heat the CGM, preventing gas from cooling and accreting onto the galaxy.

4.12.4 What is the main driving source of the ionized outflows and how does that compare to other galaxies in the local and distant Universe.

In this section, we discuss the driving mechanisms for the galaxy scale outflows. In section 4.9, we derived the outflow rates, momentum fluxes, and the kinetic luminosities of the

outflows. We also looked at the expected energy and momentum deposition from stellar feedback to see if they are sufficient or if a more powerful source is necessary to explain the observed momentum fluxes and kinetic luminosities of our outflows. These results are summarized in Table 4.7 and in Figure 4.17. We find that in the majority of the cases stellar feedback either from supernovae explosions or radiation pressure from stellar winds is insufficient to explain the observed momentum fluxes. Since recombination lines such as Hα probes star formation that happened in the past 6-10 Myr (Calzetti, 2013), given the observed dynamical time scales for the galactic outflows in our sample (3-10 Myr, see table 4.7) Hα probes the starburst event that would have driven these outflows (if it had enough energy and momentum). Hence we think that the momentum and energy deposition from stellar feedback is a good estimate from the star formation rate derived from Hα . Given the bursty nature of star formation in high redshift galaxies (Muratov et al., 2015), recombination lines are most likely the best way to estimate the amount of energy and momentum deposition from stellar feedback in the inner few kpc of a galaxy. Other star formation tracers such as UV or far infrared can trace star formation rates averaged over 100 Myr. Because UV and IR star formation tracers do not match to the dynamical time scales of our outflows and would provide a star formation rate averaged over several star formation episodes, for both of these reasons the computed stellar feedback energy and momentum depositions could be under or overestimated.

Within our sample, we find a mixture of sources with both high and low momentum flux ratios ($\frac{\dot{P}_{outflow}}{\dot{P}_{AGN}}$). For the extended outflows in 3C318, 3C298 and 4C04.81 we find $\frac{\dot{P}_{outflow}}{\dot{P}_{AGN}}$of 4-6 but, they can be as low as 0.5 or as high as 11 within the observed uncertainties. However, the more likely scenario is that they are all above 2. The momentum fluxes that we measure

in our outflows might be lower limits as we are not accounting for the neutral and molecular components of the outflow, except 3C 298 where we have measured both the molecular and ionized gas in the outflow but not the neutral. At the extent of these outflows (~ 3 kpc), radiation pressure is unlikely to drive the outflows. Thompson et al. (2015); Costa et al. (2018a) both find that on kpc scales the maximum observed $\frac{\dot{P}_{outflow}}{\dot{P}_{AGN}}$is about 1.5-2. To invoke radiation pressure as the primary driving mechanism for outflows with momentum flux $> 2 \times L_{AGN}/c$ and an extent > 1 kpc requires an extremely obscured ($\mathrm{N_H} > 10^{24}$ cm^{-2}) initial environments. However, Costa et al. (2018b) argues that driving outflows in much denser ($\mathrm{N_H} > 10^{24}$ cm^{-2}) regions through radiation pressure will most-likely not lead to much higher momentum fluxes on kpc scales and instead can produce outflows that barely escape the inner regions of their respective galaxies. Furthermore, the most obscured environments that we find AGN are on the order of $N_H \sim 10^{24}$ cm^{-2}.

The most likely scenario is that an energy conserving shock drives the outflows in 3C318, 3C298 and 4C04.81. Such shocks are produced by either UFO/BAL type winds or through quasar jets. Theoretical work on both of these driving mechanisms predicts $\frac{\dot{P}_{outflow}}{\dot{P}_{AGN}}>2$ on kpc scales (Wagner et al., 2012; Faucher-Giguère et al., 2012; Zubovas and King, 2012). In these scenarios the jet/UFO slams into the ISM and drives a hot shock. If this shock cools on a time scale much longer than the flow time then the “hot shocked bubble" will expand adiabatically sweeping material along the way. As the material is swept in a galaxy scale outflow, it gets provided with a significant momentum boost. The outflow that is driven by the shocked bubble also gets shocked, although at far lower temperatures, which allows it to cool through line emission down to perhaps a molecular phase (Richings and Faucher-Giguère, 2018). For both 3C298

and 3C318, we find that the nebular line ratios in the ionized outflow are consistent with being produced by radiative shocks (Vayner et al., 2017) and both systems are consistent with having an energy conserving shock drive the outflow.

Because the momentum fluxes in the nuclear outflows of 4C04.81 and 4C57.29 are $>$ $2 \times L_{AGN}/c$ an energy conserving shock can drive them, however, due to their smaller sizes ($<$ 1kpc), there is the possibility that they are driven through radiation pressure in a high column density environment. Both outflows show high column densities $N_H > 10^{22}$cm^{-2}, and their velocities are consistent with radiation pressure models on dust grains presented in Thompson et al. (2015). The nuclear outflow in 4C05.84 is also consistent with radiation pressure, however in a less dense environment compared to 4C04.81 and 4C57.29. An isothermal shock (Faucher-Giguère et al., 2012) can also drive the nuclear outflow in 4C05.84.

Nearly all of the detected ionized outflows in our sample align with the path of the jet, the only source that is the exception is 4C09.17. The jet could be the sole driving source of the galaxy scale outflows. However, in Vayner et al. (2017) (Chapter 3) we found that at present the jet is not doing any work on the extended ionized or molecular outflow in the host galaxy of the quasar 3C 298. This is because the jet pressure is orders of magnitude higher than the ISM pressure measured in both the ionized and molecular gas. Given the similarity in jet luminosity and ISM conditions between 3C 298 and the rest of the sample, we think this likely applies to the rest of the objects. If the jets were to drive the outflows in our systems, it would have had to be done in a denser environment closer to the quasar in the past. At present, the jet is most-likely merely following the path of least resistance as is the galaxy scale outflow. Since we have measured the electron density in the ionized outflow in 3C318, we can also perform

the same exercise as we have done for 3C298 in looking at whether the jet is currently doing any work on the outflow. To do this, we first extract all available radio fluxes of the object from NED. We construct a radio SED from 22 MHz to 353 GHz and fit it with a double power law. We integrate the fitted power law from rest-frame frequencies of 10 - 10000 MHz and obtain a total radio luminosity of $2.5 \pm 0.25 \times 10^{45}$ erg s^{-1}. We obtain a jet power for 3C318 on the order of 10^{46} erg s^{-1} using the relationship between total radio luminosity and jet power from Bîrzan et al. (2008). We obtain similar value using the monochromatic rest-frame 1400 MHz luminosity and jet power from the same study, where the 1400 MHz flux is taken from our best fit SED model. Following Vayner et al. (2017) we convert the jet power to jet pressure using the following equation:

$$\mathrm{P_{jet}} \approx \frac{\mathrm{L_{jet}} \times \mathrm{t}}{3\mathrm{V}}, \tag{4.23}$$

where L_{jet} is the jet luminosity (power), V is the confined volume of the jet for which we simply assume a cylindrical shape with a base radius of 1 kpc and height of 3 kpc, t is the propagation time for the jet for which we simply use the dynamical time scale of the outflow of 4 Myr. We obtain a jet pressure of 1×10^{-6} dynes/cm^2. The gas pressure ($P = nkT$) in the outflow 3C318 is on the order of 10^{-9} dynes/cm^2, much lower than the jet pressure, indicating that the two are not in pressure equilibrium. Similar to 3C298 the jet is venting out of the galaxy along the path of least resistance, and at present is not doing any work in driving the kpc-scale outflow in the system. On the other hand, another wind mechanisms such as an Ultra-Fast Outflow (UFO) could have driven the outflow first, and the jet turned on later and is now simply

following the path of least resistance and is escaping out of the galaxy. Both UFO and BAL type winds can provide a momentum flux of about L_{AGN}/c, sufficient to drive the observed galaxy-scale outflows in 3C318, 3C298 and 4C04.81 if shocks produced by the UFO/BAL are energy conserving (Faucher-Giguère and Quataert, 2012).

The rest of the objects in our sample show ionized outflows with $\frac{\dot{P}_{outflow}}{\dot{P}_{AGN}} << 1$. Combining our results with other studies of distant (z> 1) quasar host galaxies, a picture arises where the ionized outflow predominantly have $\frac{\dot{P}_{outflow}}{\dot{P}_{AGN}} < 2$ (Figure 4.18). There are several ways to drive such ionized outflows. First, if the shock produced by a UFO/BAL/Jet radiates its energy efficiently, then only the ram pressure is communicated to the ISM. Such a scenario can produce $\frac{\dot{P}_{outflow}}{\dot{P}_{AGN}} << 1$ (Zubovas and King, 2012; King and Pounds, 2015). Alternatively, if the outflow is driven by radiation pressure in a low-density environment, then the $\frac{\dot{P}_{outflow}}{\dot{P}_{AGN}}$ can also be very low (Thompson et al., 2015). Only a small fraction of all the ionized outflows show high $\frac{\dot{P}_{outflow}}{\dot{P}_{AGN}}$ (Figure 4.18). On the other hand, the majority of the molecular outflows have $\frac{\dot{P}_{outflow}}{\dot{P}_{AGN}} >> 1$. A significant fraction of molecular outflows are found and have been studied in nearby systems. Are there different driving mechanisms between the ionized and molecular outflows? Or are we missing a significant fraction of the gas in the outflows at high redshift by only studying the ionized component (Carniani et al., 2016)? The latter case would indicate that only a small fraction ($< 1\%$) of the total gas in an outflow can be in a warm ionized state, the rest has to be in either neutral, molecular or hot gas phase if all the outflows are “energy" conserving.

Interestingly a majority of the molecular outflows are much smaller in size compared to ionize outflows (Figure 4.25). The different sizes could indicate that they are probing different evolutionary phases of an AGN driven outflow. According to Thompson et al. (2015) for radia-

tion pressure driven outflow, initially, if the outflow is highly confined the $\frac{\dot{P}_{outflow}}{\dot{P}_{AGN}}$ and columns densities are very high, favoring molecular outflows on small scales. As the outflow expands, the momentum flux and column density drop rapidly, to a maximum $\frac{\dot{P}_{outflow}}{\dot{P}_{AGN}}$ of about 2 at 1 kpc and column densities $< 10^{20}$ cm^{-2}. For energy conserving outflows the momentum flux increases as the outflow expand peaking on kpc scales, opposite to radiation pressure driven winds. If the same mechanism drives the molecular and ionized outflows, then combining them leads to a picture where all the outflows are driven by radiation pressure. Even within our systems, nuclear outflows show larger $\dot{P}_{outflow}$ compared to the more extended outflows. However, we need to confirm this with better measurements of electron density in both nuclear and extended regions. On the other hand, it could be that the nearby AGN are fading quickly, and the $\frac{\dot{P}_{outflow}}{\dot{P}_{AGN}}$ are over-estimated if the AGN bolometric luminosity is smaller from when the outflow was driven vs. when it was measured.

The measured $\frac{\dot{P}_{outflow}}{\dot{P}_{AGN}}$ in nearby molecular outflows are still consistent with an energy conserving outflow scenario (Faucher-Giguère et al., 2012; Zubovas and King, 2012, 2014). While uncertainties on ionized outflows rates and dynamics need to be drastically improved, multi-phase studies of outflows will help address the driving source of galactic scale winds and whether there are any evolutionary effects in driving outflows in nearby and high redshift systems during a luminous quasar phase.

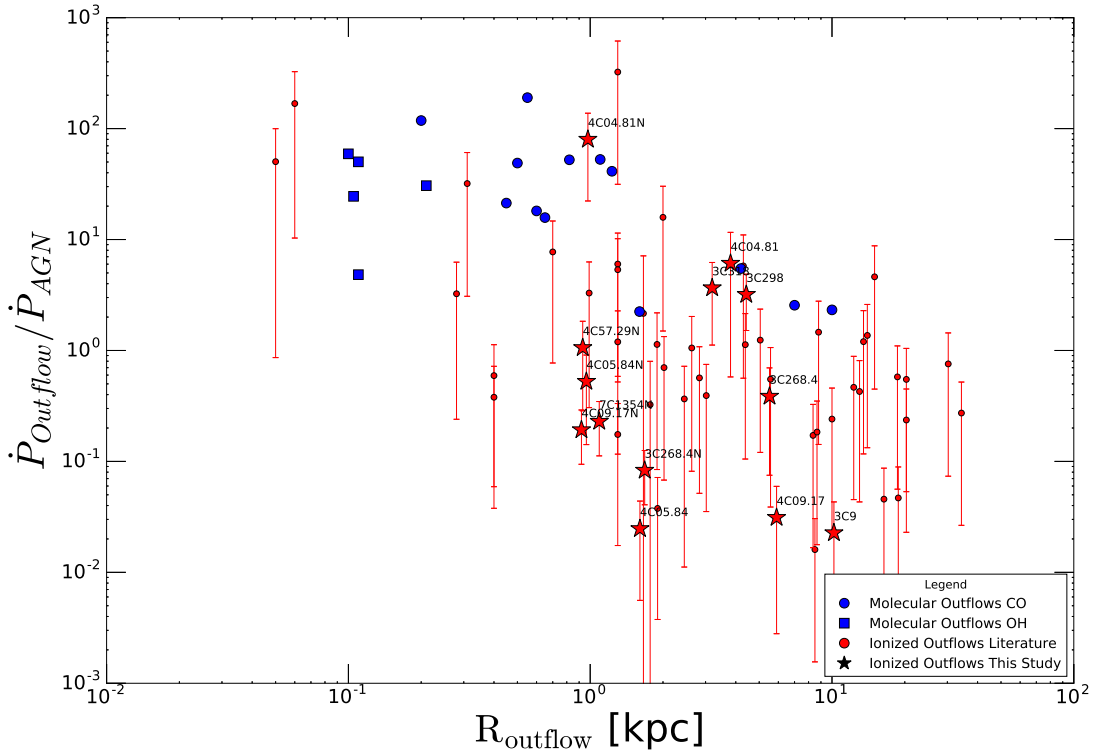

Figure 4.25 Outflow driving mechanism diagnostic diagram. We plot the $\frac{\dot{P}_{outflow}}{\dot{P}_{AGN}}$ ratio vs. the radius of the outflow. According to theoretical work on radiation pressure driven outflow the maximum ratio expected at separations $>$1 kpc is 2 and decreasing with radius. While $\frac{\dot{P}_{outflow}}{\dot{P}_{AGN}}$ for outflows driven by an energy conserving shock are expected to increase with radius. Red points represent outflows detected in ionized gas emission, and stars represent points from our sample. Blue squares represent galaxies where a molecular outflow was detected through OH absorption while blue circles represent molecular outflows detected through CO emission.

4.13 Conclusions

We have conducted a near diffraction limited survey of 11 quasar host galaxies, to study the distribution, kinematics, and dynamics of the ionized ISM using the OSIRIS IFS at the W.M. Keck Observatory. We detected extended emission in all objects on scales from 1-30 kpc.

- The AGN photoionizes the majority of the extended gas. A significant fraction of emission line ratios are found to reside between the two sequences on the traditional BPT diagram. By applying evolutionary models of the mixing and star-forming sequence from z=0 to z=2.5, we find that the gas within our systems is denser and has lower metallicity compared to the gas photoionized in local AGN.

- In 9 objects, we find dynamically quiescent regions, with on average lower log([OIII] /Hβ) ratios. For systems where Hubble Space Telescope imaging is available, their morphologies are consistent with clumpy star-forming regions commonly observed in the distant Universe, indicating the presence of recent star formation. We find these systems to be forming stars at a rate of 9-160 $M_\odot$ yr^{-1} based on the Hα luminosity.

- Outflows are detected in each object on spatial scales from $<$ 1 kpc to a 10 kpc. Outflow rates range from 8 - 2400 $M_\odot$ yr^{-1} , with momentum flux ranging from 0.03-80 L_{AGN}/c and energy rates of 0.01-1% L_{AGN}. For 4/11 sources the momentum flux is $4 - 80 \times L_{AGN}$/c and therefore the outflows are consistent with being driven by an energy conserving shock. In the rest of the objects, the outflows are either driven by star formation, radiation pressure on dust grains, or an isothermal shock. Their energetics fall short

of the predicted energy and momentum rates necessary to establish the $M_{\bullet} - \sigma$ relationship and clear galaxies of their gas reservoir predicted by theoretical work (Faucher-Giguère et al., 2012; Hopkins and Elvis, 2010a; Zubovas and King, 2014). Another possibility is that a large fraction of the gas inside the outflows is not in an ionized phase, but rather in either molecular or neutral, hence, we are drastically underestimating the gas rates and energetics.

- For the majority of the systems, the dominant source of gas depletion is due to the galaxy scale outflow. Along the path of the outflows, we see no strong evidence of active star formation.

- For 7/8 extended galactic outflow, the path of the jet is consistent with the direction of the outflow. However, we find that the jet pressure is orders of magnitude higher than that of the ionized galactic outflows. Because the jets and the ionized outflows are not in pressure equilibrium, the jets are not doing any work on the outflows. If the jet were to drive the outflows, it had to happen in dense environments close to the SMBH.

- We compare nine objects to the local scaling relation between the mass of SMBH and the mass or velocity dispersion of the galaxy. We calculate the SMBH masses from the broad Hα emission line intensity and width using the empirical single epoch SMBH mass - Hα line relationship. The velocity dispersions are taken from the dynamically quiescent regions where we do not see the presence of powerful outflows. The velocity dispersions range from 36-200 km s^{-1} . Galaxy masses are calculated in two ways, first, through virial mass equation for a rotating sphere. Second, we fit an inclined disk model for objects

with evidence of shear in their radial velocity maps. We find galaxy masses ranging from 1-10$\times 10^{10}$ M$_{\odot}$. Our systems are both offset from the $M_{\bullet} - \sigma$ and $M_{\bullet} - M_{*}$ relationship.

- We find evidence for the onset of feedback before the galaxies are on the local $M_{\bullet} - \sigma$ relationship, in disagreement with theoretical predictions. Luminous type-1 quasars are not the end phase of massive galaxy formation. Substantial growth is still necessary if these systems are to evolve into the present day massive elliptical galaxies. Gas accretion from the CGM and gas-rich minor mergers are necessary to grow the stellar mass and increase the metallicity of the ISM. On average the galaxies need to grow by at least an order of magnitude in stellar mass if they are to assemble onto the local scaling relations. A near constant mass growth rate of $\sim$100 M$_{\odot}$ yr^{-1} is necessary within a radius of 10 kpc from the quasar from z$\sim$ 2 to 0.

4.14 Acknowledgements

The authors wish to thanks Jim Lyke, Randy Campbell, and other SAs with their assistance at the telescope to acquire the Keck OSIRIS data sets. The data presented herein were obtained at the W.M. Keck Observatory, which is operated as a scientific partnership among the California Institute of Technology, the University of California and the National Aeronautics and Space Administration. The Observatory was made possible by the generous financial support of the W.M. Keck Foundation. The authors wish to recognize and acknowledge the very significant cultural role and reverence that the summit of Maunakea has always had within the indigenous Hawaiian community. We are most fortunate to have the opportunity to conduct observations

from this mountain. This research has made use of the NASA/IPAC Extragalactic Database (NED) which is operated by the Jet Propulsion Laboratory, California Institute of Technology, under contract with the National Aeronautics and Space Administration.

Chapter 4, in full, currently being prepared for submission for publication of the material in The Astrophysical Journal 2019. Vayner, A., Wright, S. A., Murray, N., Armus, L., Cosens, M., Walth, G., Boehle, A., Larkin, J. E., Mieda, 2019. The dissertation author was the primary investigator and author of this paper.

4.15 Appendix

4.16 3C 9

For this source, we identify three distinct regions. “SE-SW component A" is a region with a ring-like morphology associated with the 3C9 quasar host galaxy. We measure a velocity dispersion from a Gaussian fit to the nebular emission lines of 407.6$\pm$12.9km s^{-1} and the kinematics resembling a rotating disk. “SE component A" is classified as an outflow region with a very high emission line FWHM of 1362.7$\pm$60.5 km s^{-1} and elevated log([OIII] /Hβ) and log([NII]/Hα) ratios relative to the rest of the system. “N component B" is the merging galaxy in the 3C9 system showcasing a line FWHM of 472.15$\pm$11.8 km s^{-1} and a velocity offset of $\sim$200 km s^{-1} from the quasar.

3C9 is a luminous quasar at z = 2.019922 with a prominent blue rest-frame UV continuum. The 3C9 system is a merger of two galaxies. The velocity offset is $\sim$ 200 km s^{-1} with a

projected spatial offset of 9 kpc between the two apparent nuclei. The quasar lies in the galaxy with a ring-like morphology showing the kinematic structure of a disk. Archival HST imaging of rest-frame UV continuum shows the ring morphology as well (see Figure 4.4), indicating very recent star formation activity in the ring. The merging galaxy “N component B" appears to be dispersion dominated system with active star formation and also appears in rest-frame UV emission. The 3C9 system best resembles the local galaxy merger system Arp 148 (z=0.036) also known as Mayall’s Object. The outflow in this systems appears to be emanating from the ring of the galaxy with the quasar. The jet extends to 7.8″ to the southeast and 5″ to the northwest and is detected in both radio and X-ray observations (Fabian et al., 2003). The path of jet appears to follow the path of the ionized outflow.

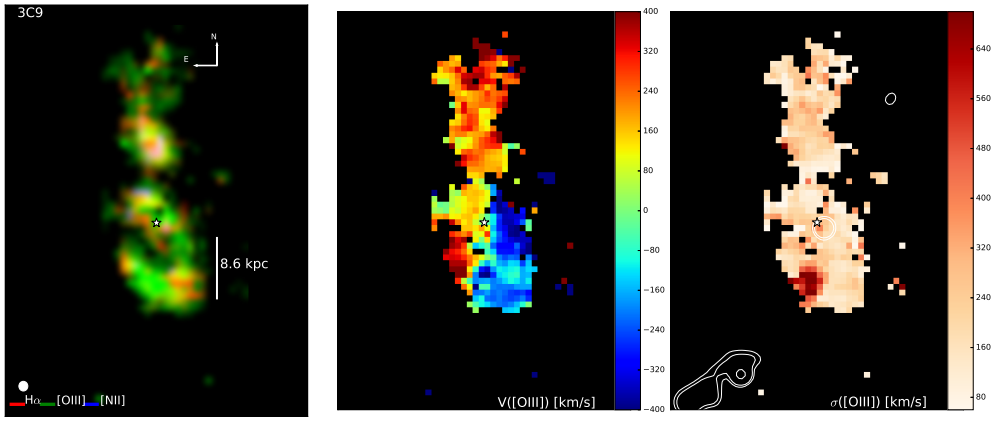

Figure 4.26 OSIRIS observations of 3C 9 nebular emission line distribution and kinematic maps. (Left) Three color intensity map of nebular emission lines: Hα (red), [OIII] (green), and [NII] (blue). Ellipse in the lower left corner showcases the spatial resolution of the observations. (Middle) Radial velocity offset (km s^{-1}) of the [OIII] line relative to the redshift of the quasar. The white star shows the location of the subtracted quasar. (Right) Velocity dispersion (km s^{-1}) map of [OIII] emission. The white contours are 8439.100 MHz VLA observations of radio synchrotron emission from the quasar jet and lobes.

4.17 4C 09.17

For this source, we identify four distinct regions. “SW component A" is a star-forming clump associated with the quasar host galaxy. The spectrum of this region shows a single narrow emission line with an FWHM of 312.0$\pm$7 km s^{-1} . “S/E component A" is an outflow region driven by the quasar, the nebular emission lines for this region have an FWHM of 887.2$\pm$22.4 km s^{-1} . A second narrow component is required for a good fit to each emission line in this region, with a line FWHM of 290.4$\pm$29.9 km s^{-1} . “W component B clumps" is a region part of the merging galaxy within the 4C09.17 system. The region consists of clumpy emission selected by isolating spaxels with an Hα line surface density $> 6 \times 10^{-16}$ erg s^{-1} cm^{-2}arcsec^{-2}. “W

component B diffuse" is emission associated with “diffuse" ionized emission in the merging galaxy selected by isolating spaxels with an Hα spatial line surface density $< 6 \times 10^{-16}$ erg s^{-1} cm^{-2}arcsec^{-2}. The diffuse region shows higher log([OIII] /Hβ) and log([NII]/Hα) line ratios associated with both AGN and star formation photoionization while the clumpy regions of the merging galaxy showcase lower ionization levels consistent with photoionization by star formation. This region is associated with bright UV emission in HST imaging of this object (Lehnert et al., 1999). “S/E component A outflow" shows high log([NII]/Hα) and log([OIII] /Hβ) values relative to the rest of the system indicating this region is predominantly photoionized by the quasar.

4C 09.17 is a luminous quasar at z=2.117 with a blue UV continuum. The 4C09.17 system is a merger of two galaxies with a velocity offsets of $\sim$1000 km s^{-1} and a projected separation of $\sim$ 4 kpc. HST imaging of rest-frame UV continuum (see Figure 4.4) shows evidence for a population of young hot stars indicating recent star formation activity. Majority of the star formation activity is confined to the merging galaxy, where lower log([OIII] /Hβ) values and clumpy morphology seen in nebular emission line is reminiscent of typical star-forming regions in the distant Universe. Star formation in the galaxy associated with the quasar appears to be confined to a single clump seen in Hα and UV. The kinematics of the merging galaxy appears to be dispersion dominated with no strong evidence for rotation. The clumps in the merging galaxy showcase photoionization consistent with star formation, while the more diffuse emission is consistent with photoionization by the quasar due to higher log([OIII] /Hβ) values compared to that of the clumps. Differences in gas column densities in clumps vs. the diffuse gas can explain the differences in photoionization. The higher column densities in clumps more easily self shield

from the quasar ionization field. Alternatively, the clumps have a higher concentration of young stars that dominate the photoionization of the gas relative to the quasar field, whereas the region with diffuse nebular emission has a different recent star formation history with no active star formation in the last few Myr. A combination of these two scenarios can also exist. We detect an outflow in the quasar host galaxy; however, the path of the outflow does not match that of the jet. A one-sided jet extends 12 kpc from the quasar.

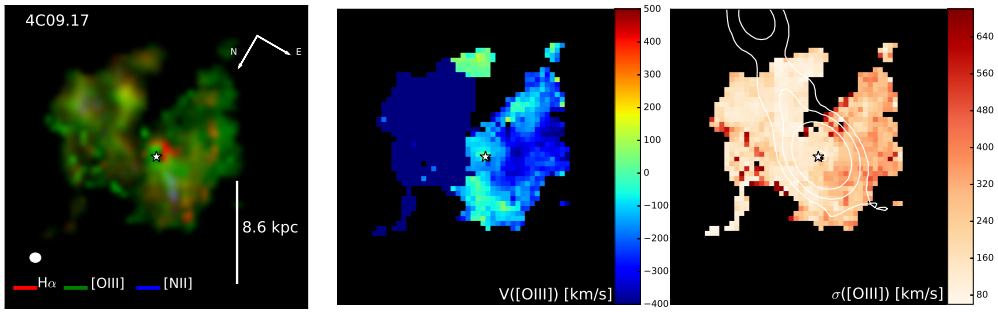

Figure 4.27 OSIRIS observations of 4C09.17 nebular emission line distribution and kinematic maps. (Left) Three color intensity map of nebular emission lines: Hα (red), [OIII] (green), and [NII] (blue). Ellipse in the lower left corner showcases the spatial resolution of the observations. (Middle) Radial velocity offset (km s^{-1}) of the [OIII] line relative to the redshift of the quasar. The white star shows the location of the subtracted quasar. (Right) Velocity dispersion (km s^{-1}) map of [OIII] emission. The white contours are ALMA band 4 observations of radio synchrotron emission from the quasar jet and lobes.

4.18 3C 268.4

For this target, we identified two distinct regions. “SW component A" is an outflow driven by the quasar. The FWHM of the emission lines is 2075±354 km s^{-1} as measured from the Gaussian fit to the [OIII] line. The spectrum extracted over this region also shows a narrow component with an FWHM of 603.7±54.9 km s^{-1} most likely signaling emission from an extended narrow line region close to the quasar. Because of issues with miss-assignment of flux in the OSIRIS pipeline (Lockhart et al., 2019), the rows below and above the centroid of the quasar do not have properly extracted spectra in the H band observations of this object. Hence we do not have a good spectrum of the extended emission in a 0.2-0.3″ radius around the quasar in the H band, which covers the Hα and [NII] emission lines of the ionized outflow. “SW component B" is a region associated with the merging galaxy, showcasing clumpy morphology in ionized gas emission. The emission lines have an FWHM of 367.7 ± 3.9 km s^{-1} and an offset of -300 km s^{-1} relative to the redshift of the quasar. The log([OIII] /Hβ) line ratios are lower for this region compared to the rest of the system, consistent with a mixture of AGN and star formation photoionization. This region is also associated with bright rest-frame UV continuum emission, seen with HST observations of this target Hilbert et al. (2016).

3C 268.4 is a luminous quasar at z=1.39, with a slightly reddened UV continuum compared to the average type-1 quasar. The system is a merger of two galaxies with a velocity offset of $\sim$300 km s^{-1} and a projected separation of $\sim$ 4kpc. Majority of the ionized emission that we detect is associated with the merging galaxy. The kinematics appears to be dispersion dominated for this galaxy. The morphology is consistent with a clumpy ISM with a tidal feature. An out-

flow is emanating from the quasar to a projected radius of about 3 kpc, the jet follows the path of the outflow out to 4.4″, beyond the FOV shown in Figure 4.28.

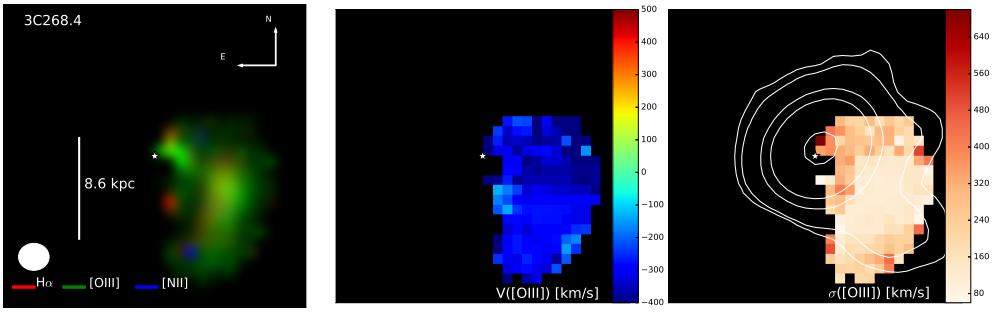

Figure 4.28 OSIRIS observations of 3C268.4 nebular emission line distribution and kinematic maps. (Left) Three color intensity map of nebular emission lines: Hα (red), [OIII] (green), and [NII] (blue). Ellipse in the lower left corner showcases the spatial resolution of the observations. (Middle) Radial velocity offset (km s^{-1}) of the [OIII] line relative to the redshift of the quasar. The white star shows the location of the subtracted quasar. (Right) Velocity dispersion (km s^{-1}) map of [OIII] emission. The white contours are VLA 8264.9 MHz observations of radio synchrotron emission from the quasar jet and lobes.

4.19 7C 1354+2552

7C 1354+2552 is a luminous quasar at z=2.0064 with a blue UV continuum. For this target, we identify two distinct regions. “Component A" is the extended emission associated with the quasar host galaxy. The kinematics show a smooth velocity gradient, indicating the presence of a galactic disk. The size, morphology, and kinematics of the disk are similar to that of star-forming galaxies on the more massive end of the star formation main sequence at $z \sim 2$ (Förster Schreiber et al., 2018). We measure an emission line FWHM of 357.2±2.0 km s^{-1}

on the redshifted side of the disk and 497.7$\pm$6.5 km s^{-1} on the blueshifted side of the disk. Although this region only has a single label (“component A"), in Figure 4.8 rows one and two show the fits to the red, and blue shifted sides of the disk that are part of this region. This region is selected based on the location where Hα emission is detected. This is done to boost the SNR in the Hα line as it appears to be, clumpier, more compact, and less extended compared to [OIII] . In Table 4.5 we provide values integrated over the entire galactic disk. “E component B " is a region associated with the merging galaxy at a projected separation of 6-7 kpc. The kinematics are consistent with a dispersion dominated galaxy. The entire “component A" is consistent with quasar photoionization. The gas in “E component B" is photoionized by star formation. The system has two sets of symmetric jets that are perpendicular to each other. One set propagates parallel to the rational axis of the disk, while the other is perpendicular. The parallel axis jet extends 1.5$''$ while the perpendicular extends 3$''$, which extends beyond the FOV of Figure 4.29.

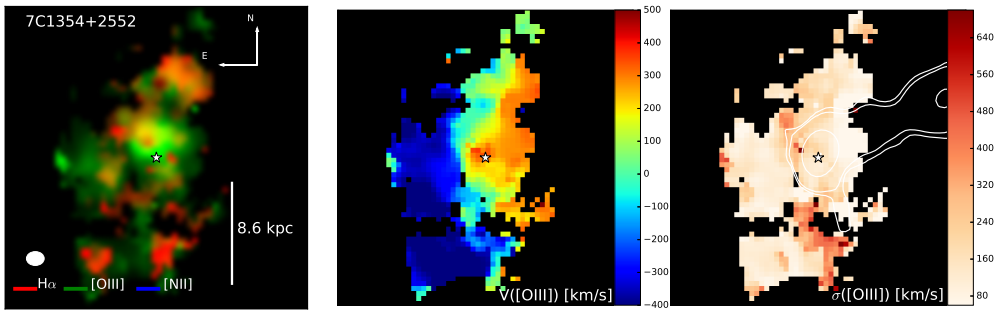

Figure 4.29 OSIRIS observations of 7C1354+2552 nebular emission line distribution and kinematic maps. (Left) Three color intensity map of nebular emission lines: Hα (red), [OIII] (green), and [NII] (blue). Ellipse in the lower left corner showcases the spatial resolution of the observations. (Middle) Radial velocity offset (km s^{-1}) of the [OIII] line relative to the redshift of the quasar. The white star shows the location of the subtracted quasar. (Right) Velocity dispersion (km s^{-1}) map of [OIII] emission. The white contours are ALMA Band 4 observations of radio synchrotron emission from the quasar jet and lobes.

4.20 3C 298

For this target, we identify five distinct regions. We present a detailed discussion of each region in Vayner et al. (2017) (Chapter 3). “W/E component A" are outflow regions with a biconical morphology, where the western (W) is the redshifted receding cone, and the eastern (E) is the approaching cone. In Vayner et al. (2017)(Chapter 3) they are referred to as the red(blue) shifted outflow region. The emission lines over the outflows are very broad with FWHM up to $\sim$1500 km s^{-1} . A combination of shocks and quasar activity are responsible for photoionizing the gas. “SE component B outflow" is an outflow region belonging to a merging galaxy. “SE component B ENLR" is an extended narrow line region belonging to the disk of the merging galaxy, with gas photoionized by the quasar or secondary AGN. “SE component B Tidal feature" is a region of the merging galaxy with active/recent star formation as evident by lower log([NII]/Hα) and log([OIII] /Hβ) values compared to the rest of the regions.

3C298 is a luminous quasar at z=1.439 with a slightly reddened UV continuum. 3C298 was the first source observed in our sample. The system is a merger of two disk galaxies separated by a projected distance of 8 kpc with a velocity offset of 250 km s^{-1} . The galaxy associated with the quasar shows a biconical outflow with a receding redshifted cone and an approaching blueshifted cone. The redshifted cone extends to about 4.42 kpc and shows evidence for expansion along our line of sight. The blueshifted cone extends to 3.9 kpc. A two-sided jet extends along the two outflow regions. The merging galaxy also shows an outflow extending about 2 kpc from its center. This source is the best candidate in our sample for a dual AGN. Majority of the star formation is occurring in a tidal feature that is 16-21 kpc from the quasar, where we see low

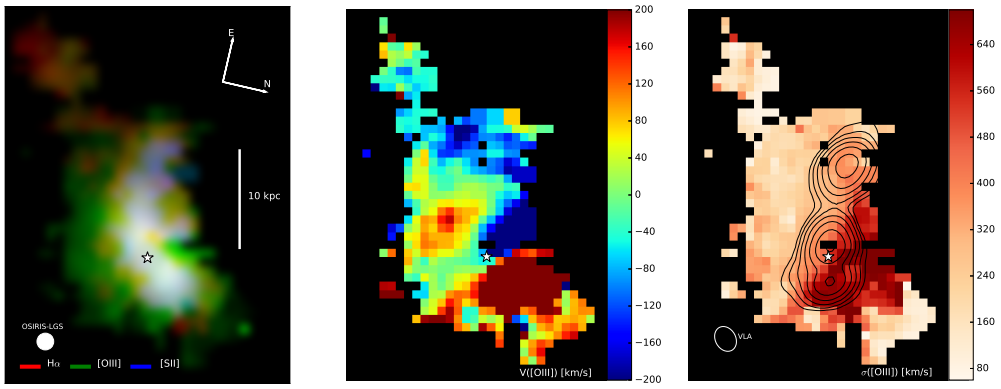

Figure 4.30 OSIRIS observations of 3C298 nebular emission line distribution and kinematic maps. (Left) Three color intensity map of nebular emission lines: Hα (red), [OIII] (green), and [SII](blue). Ellipse in the lower left corner showcases the spatial resolution of the observations. (Middle) Radial velocity offset (km s^{-1}) of the [OIII] line relative to the redshift of the quasar. The white star shows the location of the subtracted quasar. (Right) Velocity dispersion (km s^{-1}) map of [OIII] emission. The white contours are VLA observations of radio synchrotron emission from the quasar jet and lobes.

ionization from recently formed O stars, clumpy Hα , and rest-frame UV morphology. Majority of the molecular gas in this system detected with ALMA resides near the tidal feature and the quasar.

4.21 3C 318

For this target, we identify a single region. “E, W component A outflow", the kinematics show blue and red shifted broad (FWHM$\sim$1000 km s^{-1}) emission, similar to 3C 298 indicating

a bi-conical outflow. The ionized gas morphology is ring-like, suggesting that we are seeing the base of the receding and approaching side of a biconical outflow. Similar to the kinematic and morphology of the bipolar outflow seen in supernova 1987 A. The gas is photoionized by a combination of shock heating and quasar activity. We do not detect any narrow extended emission in this object.

3C318 is a luminous quasar at z=1.5723 with a reddened UV continuum. Willott et al. (2000) found a V band extinction value of 0.5 magnitude. The merger status of this object is unclear. Two nearby galaxies to the north and west of the quasar are visible in archival HST imaging (Willott et al., 2000). We do not detect the western object that is $2''$ away from the quasar in our OSIRIS observations in any emission line. Willott et al. (2007) studied this object with PdBI through CO 2-1 emission at a fairly coarse ($\sim$8 arcseconds) resolution. There appears to be CO emission that could plausibly be associated with the western object. We have recently obtained much higher angular resolution CO 3-2 spectroscopy of this target that will be discussed in detail in a forthcoming paper. We confirm the existence of CO 3-2 emission associated with the CO 2-1 emission. We resolve the molecular emission into multiple components. However, the CO 3-2 emission is not associated with either one of the galaxies seen in the HST data. We obtained a wide field of view IFS observations of this target with KCWI aimed at attempting to measure the redshifts of the nearby galaxies and to confirm the merger scenario of this object. We detect both the northern and western object in the continuum. We confirm that the northern target is at a different redshift than the quasar from the detection of [OII] emission while for the western object a reliable redshift is difficult to determine with the current data set. Hence no clear evidence of a companion galaxy that is part of a merger is detected for this quasar that would

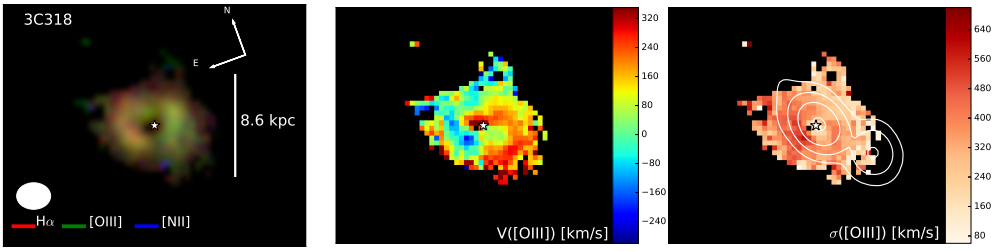

Figure 4.31 OSIRIS observations of 3C318 nebular emission line distribution and kinematic maps. (Left) Three color intensity map of nebular emission lines: Hα (red), [OIII] (green), and [NII] (blue). Ellipse in the lower left corner showcases the spatial resolution of the observations. (Middle) Radial velocity offset (km s^{-1}) of the [OIII] line relative to the redshift of the quasar. The white star shows the location of the subtracted quasar. (Right) Velocity dispersion (km s^{-1}) map of [OIII] emission. The white contours are VLA observations of radio synchrotron emission from the quasar jet and lobes.

be associated with the brightest galaxies seen in optical imaging within a few arcseconds from the quasar. The entire extended ionized gas emission detected in this object is from a bi-conical outflow driven by the quasar. 3C 318 contains a two-sided jet that extends along with the ionized outflow. There is evidence for a spatially unresolved nuclear star-burst with an upper limit on the star formation rate of $88\pm9 M_{\odot}$ yr^{-1} . This star formation rate is far lower than the far infrared derived rate of $580 M_{\odot}$ yr^{-1} . The extinction towards the nuclear region measured from Willott et al. (2000) alone cannot explain the mismatch between the Hα and far infrared derived SFR. Either a larger fraction of the far-infrared emission is from dust that is being heated by the AGN or the far infrared emission traces a different star formation history than Hα (Calzetti, 2013).

4.22 4C 57.29

4C 57.29 is a luminous quasar at z=2.1759 with a blue UV continuum. For this target, we identify two regions. Region “NE component A" belongs to the host galaxy of the quasar. The relatively high log([OIII] /Hβ) value indicates that this region is consistent with being photoionized by the quasar. The 500.7 nm [OIII] is the only emission line detected for this region. The region is marginally resolved, making it hard to measure the kinematic structure. We require a double Gaussian fit to the [OIII] emission in this region to obtain a good fit, and we measure an FWHM of 474.3 and 502.5 km s^{-1} with offsets of 35.0 km s^{-1} and -1050.1 km s^{-1} relative to the redshift of the quasar. We identify a second region north of the quasar. It is unclear if it belongs to a merging galaxy or the quasar host galaxy. There is a $\sim$ 100 km s^{-1} offset from the quasar, and the line has an FWHM of 550.13$\sim$19 km s^{-1} . This region is also only detected in [OIII] . The SNR is too low to measure any kinematics structure. After subtracting all the extended emission, we detect a spatially unresolved outflow that is driven by the quasar. The jet of this quasar is two-sided, extending north-east and south-west. The northern/southernmost extents are 5$''$ and 3$''$ respectively.

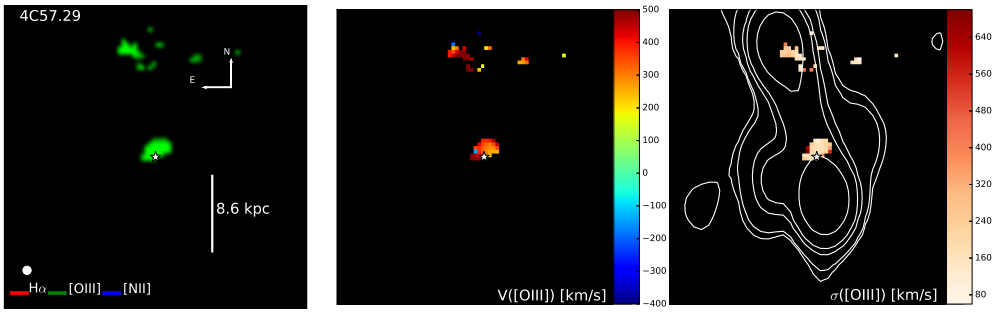

Figure 4.32 OSIRIS observations of 4C57.29 nebular emission line distribution and kinematic maps. (Left) Three color intensity map of nebular emission lines: Hα (red), [OIII] (green), and [NII] (blue). Ellipse in the lower left corner showcases the spatial resolution of the observations. (Middle) Radial velocity offset (km s^{-1}) of the [OIII] line relative to the redshift of the quasar. The white star shows the location of the subtracted quasar. (Right) Velocity dispersion (km s^{-1}) map of [OIII] emission. The white contours are VLA observations of radio synchrotron emission from the quasar jet and lobes.

4.23 4C 22.44

4C22.44 is a luminous quasar at z=1.5492 with a reddened UV continuum. Similar to 3C318 we do not detect any evidence for a merging galaxy for this system. For this target, we identify a single region, “N, S component A". The kinematics of this region may be consistent with a galactic disk belonging to the quasar host galaxy. We see evidence for a smooth gradient in the radial velocity map, however, the region is marginally resolved. We measure an emission line FWHM of 434.8 km s^{-1} . The region is consistent with being ionized by star formation with some contribution from quasar photoionization. The jet from the quasar is two-sided with both

sides extending about $\pm 5''$ from the quasar in the east and west directions.

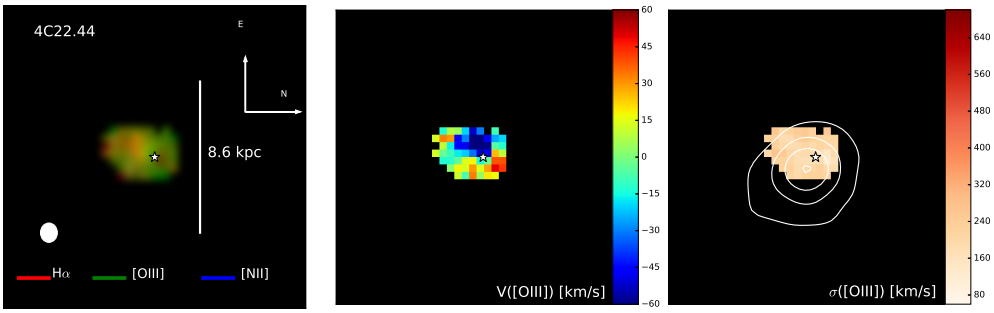

Figure 4.33 OSIRIS observations of 4C2244 nebular emission line distribution and kinematic maps. (Left) Three color intensity map of nebular emission lines: Hα (red), [OIII] (green), and [NII] (blue). Ellipse in the lower left corner showcases the spatial resolution of the observations. (Middle) Radial velocity offset (km s^{-1}) of the [OIII] line relative to the redshift of the quasar. The white star shows the location of the subtracted quasar. (Right) Velocity dispersion (km s^{-1}) map of [OIII] emission. The white contours are ALMA band 4 observations of radio synchrotron emission from the quasar jet and lobes.

4.24 4C 05.84

For this target, we identify three distinct regions. Regions “S component A" and “NE component A" are the blue(red) shifted outflow regions resembling a bi-conical outflow. They showcase broad extended emission with a line FWHM of $\sim$800 km s^{-1} . The quasar photoionizes these regions. Region “SW component A clump", shows a line FWHM of 467.9$\pm$3.0 km s^{-1} and is photoionized by a combination of star formation and the quasar.

4C05.84 is a luminous quasar at z=2.323 with a slightly reddened UV continuum. We find no evidence for a merging galaxy within our OSIRIS observations. The extended emission near the quasar is dominated by emission from a bi-conical outflow. The blue-shifted side of the cone extends 2 kpc southeast of the quasar, while the redshifted cone extends to nearly 9 kpc in the north-western direction. Southwest of the quasar a clump is evident in both Hα and [OIII] emission with ionization consistent with star formation with a non-negligible contribute from quasar photoionization. This clump is also detected in NIRC2 imaging of this object studied by Krogager et al. (2016), where they consider this clump to be associated with a damped Lyα system. However here we confirm that this objected is part of the quasar host galaxy. The one-sided jet for quasar extends in the southern direction and shows a strong bend in the south-western direction near the location of the south-western star-forming clump.

After subtracting the entire extended emission from the data cube, we detect unresolved emission associated with an outflow. This outflow appears to be connected to the extended outflow, where the unresolved emission arises from emission within the inner working angle of our observations.

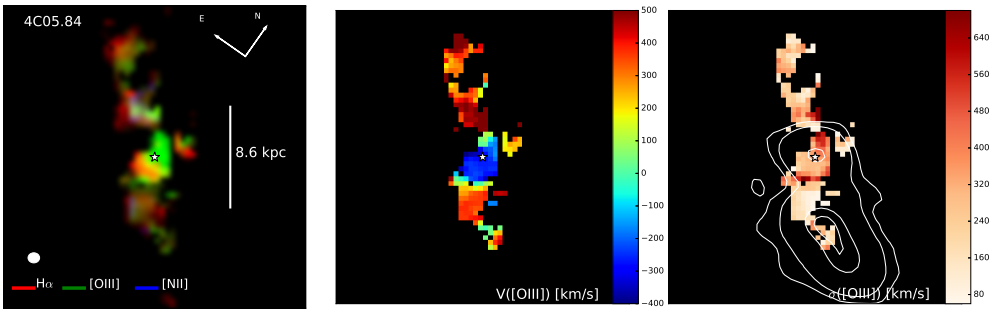

Figure 4.34 OSIRIS observations of 4C05.84 nebular emission line distribution and kinematic maps. (Left) Three color intensity map of nebular emission lines: Hα (red), [OIII] (green), and [NII] (blue). Ellipse in the lower left corner showcases the spatial resolution of the observations. (Middle) Radial velocity offset (km s^{-1}) of the [OIII] line relative to the redshift of the quasar. The white star shows the location of the subtracted quasar. (Right) Velocity dispersion (km s^{-1}) map of [OIII] emission. The white contours are ALMA Band 4 observations of radio synchrotron emission from the quasar jet and lobes.

4.25 3C 446

For this target we identify two regions, “N component A tidal feature" is a region belonging to the quasar host galaxy, resembling a tidal feature that is most likely induced by the merger. We measure an FWHM of 395.14$\pm$2.0 km s^{-1} for this region. “E-W component B" belongs to the merging galaxy, a portion of it resembles a tidal feature, counter to the tidal arm of “N component A tidal feature." For this region, we measure a line FWHM of 558.5$\pm$63 km s^{-1} however, it appears to be a blend of two velocity components. It is unclear where the nucleus of the merging galaxies resides. It could be that it has already merged with that of the quasar host galaxy. The two galaxies appear to be offset by at least 500 km s^{-1} in velocity, and there is a possibility that a portion of the merging galaxy lays on top of the quasar host galaxy.

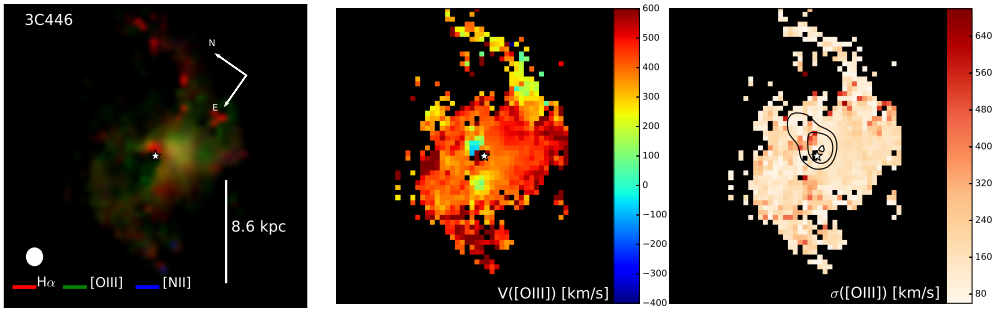

Figure 4.35 OSIRIS observations of 3C446 nebular emission line distribution and kinematic maps. (Left) Three color intensity map of nebular emission lines: Hα (red), [OIII] (green), and [NII] (blue). Ellipse in the lower left corner showcases the spatial resolution of the observations. (Middle) Radial velocity offset (km s^{-1}) of the [OIII] line relative to the redshift of the quasar. The white star shows the location of the subtracted quasar. (Right) Velocity dispersion (km s^{-1}) map of [OIII] emission. The white contours are ALMA Band 8 observations of radio synchrotron emission from the quasar jet.

4.26 4C 04.81

For this target, we identify a single region, “E component A outflow". The kinematics show blue and red shifted broad (FWHM$\sim$800 km s^{-1}) emission. The quasar mainly photoionizes the gas. We do not identify any narrow extended emission in this object.

4C04.81 is a luminous quasar at z=2.5883 with a reddened UV continuum. We find no evidence for a merging galaxy for this system in our OSIRIS observations. Lehnert and Becker (1998) identified a Lyα emitter 29$''$ away from the quasar at a position angle of 135 degrees, indicating that this quasar may be part of a galaxy group. The extended emission detected in multiple nebular emission lines is from an extended ionized outflow driven by the quasar. The

outflow extends 7 kpc from the quasar. A single-sided jet from the quasar extends in the eastern direction, eventually slightly bending southwards. The jet primarily extends along the path of the ionized outflow. After subtracting all the extended emission, we detected a nuclear, unresolved outflow. This outflow appears to be connected to the extended outflow, perhaps residing within the inner working angle of our OSIRIS observations and gets subtracted out after removing the point-source emission.

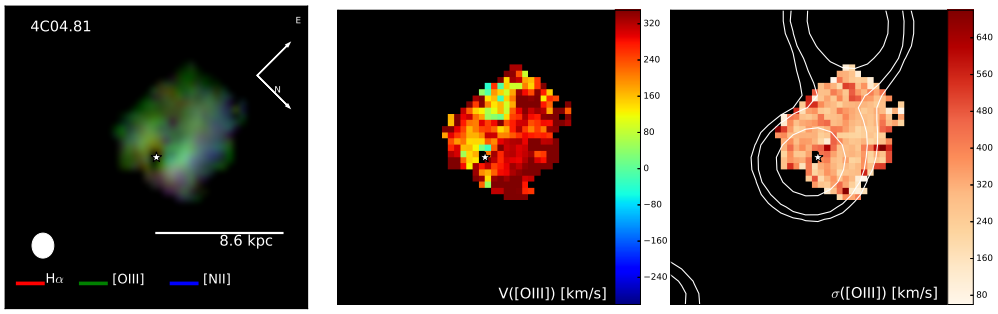

Figure 4.36 OSIRIS observations of 4C04.81 nebular emission line distribution and kinematic maps. (Left) Three color intensity map of nebular emission lines: Hα (red), [OIII] (green), and [NII] (blue). Ellipse in the lower left corner showcases the spatial resolution of the observations. (Middle) Radial velocity offset (km s^{-1}) of the [OIII] line relative to the redshift of the quasar. The white star shows the location of the subtracted quasar. (Right) Velocity dispersion (km s^{-1}) map of [OIII] emission. The white contours are VLA observations of radio synchrotron emission from the quasar jet.

Chapter 5

Conclusions and Future Directions

To-date, we have conducted the largest AO-assisted IFS survey of luminous-quasar host galaxies during the peak epoch of galaxy and SMBH growth. These observational results put constraints on theoretical models of massive galaxy formation. We found that galaxies hosting the most massive SMBH in the distant Universe still have to acquire substantial stellar-mass if they evolve into present-day massive elliptical galaxies. Winds driven by the SMBH appear to happen before the galaxy and SMBH have finished their present-day mass assembly. The observed outflow rates and energetics of ionized gas often fall short of theoretical predictions. The ISM is yet to be enriched to the level observed in massive local galaxies. In this chapter, I outline several future projects that will help understand processes by which galaxies may obtain the gas and stars necessary to grow to their present-day stellar mass. I additionally explore how future multi-wavelength observations can better measure outflow rates and energetics of quasar host galaxies. I will also discuss some upcoming flagship missions that will revolutionize our understanding of galaxy formation across cosmic time.

5.1 The Circumgalactic Medium of Quasar Host Galaxies at z$\sim$2

Simulations have indicated that accretion through cold streams is likely responsible for providing the majority of baryonic matter into galaxies (Kereš et al., 2009; van de Voort et al., 2011). These streams connect galaxies to their circumgalactic medium (CGM), which contain a significant fraction of a galaxy's gas reservoir. Understanding the accretion processes is crucial to understanding galaxy formation and evolution. The highly diffuse nature of the accreting material has made it very difficult to study. Until recently the two dominant ways of studying the CGM in the distant universe have been through transverse absorption line surveys (Zhu and Ménard, 2013; Prochaska et al., 2014) using background quasars, and galaxies as continuum sources to probe absorbing gas in foreground galaxies' CGM , and "down-the-barrel" spectroscopy using galaxies' own starlight as a background source (Steidel et al., 2010; Rubin et al., 2012). Narrowband imaging of Lyα emission in the CGM of high-redshift galaxies has also spurred in the last two decades (Cantalupo, 2017). The recent advent of a large field of view optical IFSs has opened a new window for studying the CGM in emission (Borisova et al., 2016), allowing us to map the distribution of gas around bright quasars and AGN, previously restricted to specific lines of sight where background objects were present.

Quasars are thought to illuminate the CGM through gas photoionization, making it detectable with modern-day IFS. The expected $\mathrm{Ly}\alpha$emission from the CGM surrounding a luminous quasar is on the order of 5-100$\times 10^{-19}$erg s^{-1} cm$^{-2}\mathrm{arcsec}^{-2}$. In the absence of quasar photoionization, it is possible to map the CGM with fluorescence emission due to the cosmic ul-

traviolet background. However, $\mathrm{Ly}\alpha$emission at z$\sim$ 2 produced by the cosmic UV background is 1-5$\times 10^{-19}$erg s^{-1} cm$^{-2}\mathrm{arcsec}^{-2}$ fainter than can be detected with ground and space-based observatories.

The exquisite sensitivity of KCWI and MUSE enables us to now study the distribution and kinematics of gas in the CGM through quasar fluorescence emission of $\mathrm{Ly}\alpha$, HeII and CIV to a flux density surface limit of 5×10^{-19}erg s^{-1} cm$^{-2}\mathrm{arcsec}^{-2}$ within the virial radius of the dark matter halo. The radiative mechanism(s) that generates $\mathrm{Ly}\alpha$ are still poorly constrained, making it challenging to fully interpret the observed radial velocity maps and determining the available gas in the CGM since it is optically thick to $\mathrm{Ly}\alpha$ radiation. The unprecedented sensitivity of KCWI allows the study of non-resonant 1640Å HeII emission line which provides far better constraints on the kinematics of the gas relative to $\mathrm{Ly}\alpha$ and allows for a better estimate of the available CGM gas.

We have begun a survey to study the CGM around six quasar host galaxies that are drawn from our OSIRIS sample in Chapter 4. The goal is to spatially map the CGM in rest-frame UV lines ($\mathrm{Ly}\alpha$, HeII , and CIV) to measure the gas transport from the CGM to galaxy scales. The aim is to understand whether accretion from the CGM provides enough gas supply to grow the stellar mass of the host galaxy to the expected z=0 value. Additionally, we would like to conduct a future study to understand the role of dry mergers in growing the stellar mass of the quasar host galaxies. This can be determined by linking the spatial location of satellite galaxies relative to the quasar host galaxy and measuring their stellar masses. Another observational method is by searching for tidal stripping of stars during mergers and measuring the mass in tidal streams.

Measuring the stellar masses of satellite galaxies and searching for stellar streams will

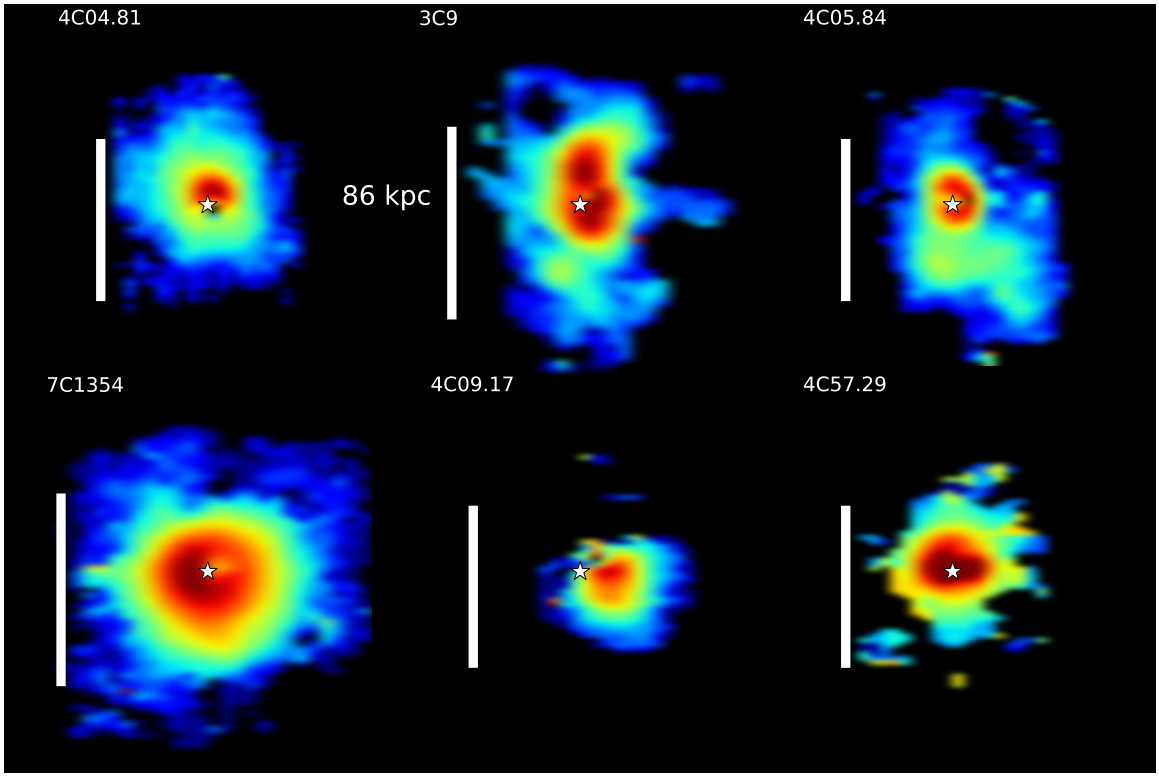

Figure 5.1 KCWI integrated Lyα intensity maps of the six sources in our sample. The bar represents 10″ or approximately 86 kpc at the redshift of these quasars. The star represents the location of the quasar which has been subtracted out to see the faint extended emission from the CGM.

require observations from space-based observatories. The majority of the stars in the stellar streams will be older, less massive stars which emit a significant fraction of their light past the Balmer break. At z$\sim$2 the Balmer break is redshifted into the near-infrared, where it is very challenging to obtain deep observations sensitive to low surface brightness emission. Ground-based near-infrared cameras struggle to reach magnitudes of about 25-26$''^{-2}$ at an angular resolution of 0.1-0.2$''$. To detect these faint tidal features requires space-based observations. Archival WFC3-IR F160W imaging of the field around 3C9 indicates that the tidal features are fainter than m_{140} of 25 magnitudes arcsec^{-2} (Figure 5.2). In Figure 5.2, we show how our survey will directly link the position of the stellar streams and nearby galaxies to the CGM morphology and kinematic structures. KCWI observations of nearby galaxies and streams will be compared to hydrodynamical simulations to confirm their nature. Combining the projected location of satellite galaxies in the environment of the quasar host galaxy can further help interpret the kinematic structures seen in KCWI data.

While detecting emission line and continuum in massive ($> 10^{10}M_{\odot}$) star-forming galaxies is feasible from the ground with near-IR spectrographs on 10-meter class telescopes, these instruments struggle to detect quiescent galaxies at these redshifts. The sensitivity typically does not allow detection of the continuum at high enough SNR to detect spectral absorption features indicative of the redshift and star formation history (e.g, from the Balmer break) of the target. Kriek et al. (2015) finds a spectroscopic success rate of 9-50$\%$ for quiescent galaxies at 1<z<3. Given that at z$\sim$ 2 about half of the observed galaxies near the break in the galaxy mass function are quiescent galaxies, only space-based observations today can detect their stellar continuum to measure the redshift and star formation history (Tomczak et al., 2014). To study the

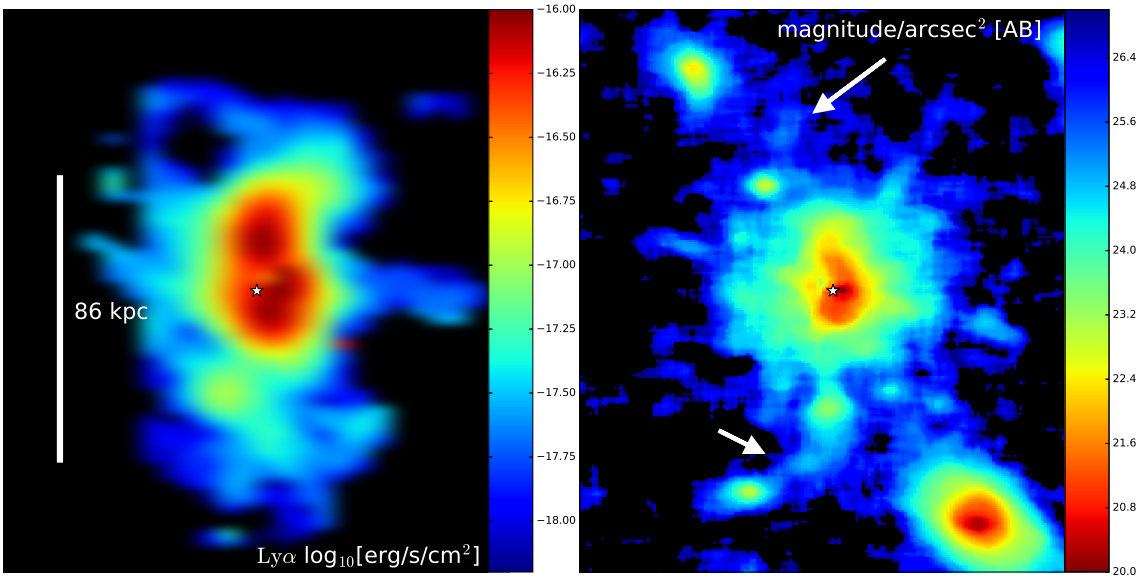

Figure 5.2 Left: KCWI integrated $\mathrm{Ly}\alpha$ intensity map showcasing the distribution of cool gas in the CGM of the host galaxy of the quasar 3C9 (z=2.0). Right: Rest-frame V band image of the stellar light in the environment around 3C9 with a 9-pixel median filter applied to improve SNR in the faint diffuse stellar emission. In both images, the bright quasar has been subtracted out. Arrows point towards two candidate tidal tails caused by the interaction of satellite galaxies with the quasar host. It is interesting to note that the extent of the tidal tail matches that of the cool CGM seen in UV emission. Note that these features are fainter than 25^{th} magnitude arcsec^{-2}, and can only be detected with space observations in the near-infrared.

role of dry mergers in growing the stellar mass of the quasar host galaxies will require space-based slitless or multi-object spectroscopy of the full satellite galaxy population at $z \sim 2$ with HST or JWST.

5.2 The Molecular Gas in Quasar Host Galaxies

As we learned in Chapter 3, galaxies with quasar driven outflows often exhibit energetics that are below the predicted values from simulations. To clear a galaxy of its molecular gas reservoir requires an energy rate coupling efficiency between the quasar and the galaxy scale outflow of at least 0.1% (Hopkins and Elvis, 2010a). Often simulations predict that energy-conserving outflows are important in clearing a galaxy of its gas, which results in $\dot{P}_{outflow}$ values $> 2 \times L_{AGN}/c$. However, combining our observations with results from the literature, we find a significant fraction of outflows detected in ionized emission have $\dot{P}_{outflow} < L_{AGN}/c$. Molecular outflows studied in the local Universe, on the other hand, find energy and momentum rates that are consistent with the theoretical predictions. Either different mechanisms drive molecular and ionized outflows, or we are significantly under-estimating the gas mass in quasar driven outflows by only studying the ionized component.

Furthermore, there has been missing critical observations that link both the spatial distribution and dynamics of ionized gas in outflows with properties of the molecular gas in high-redshift quasar host galaxies. Connecting both resolved molecular and ionized gas observations is crucial for understanding the role of quasars in regulating star formation.

In Chapter 2 we found a molecular outflow in 3C298 emanating from the galactic disk

with an outflow rate of 2300$M_\odot$ yr^{-1} and a total molecular (M_{H_2}) gas in the outflow of 3.3×10^9 $M_\odot$, about 50% of the total molecular gas in the disk. We found the majority of the gas in the outflow to be in a molecular state, with energy and momentum fluxes consistent with the theoretical prediction. The work on the host galaxy of 3C 298 was one of the first cases where AO-assisted IFS observations of the ionized ISM were linked to that of the molecular gas at z>1, hence enabling us to study the multi-phase ISM at similar angular resolution. 3C298 is the first source with detection of molecular gas in an outflow state in the distant Universe (z> 1), with strong evidence that the powerful outflows that we see in ionized nebular emission are directly affecting the molecular ISM. We found that the molecular and ionized outflows are emanating from the molecular disc centered on the quasar.

I led a cycle 5 ALMA program (PI: Vayner) to target low CO transition (e.g., CO (3-2)) emission that measured the dynamics and distribution of molecular gas in five quasar host galaxies. The entire data set of 18 hours was observed and processed. The goal of these observations was to either detect molecular outflows over similar regions where we find ionized outflows or to put some of the most stringent limits on molecular gas in high redshift quasar host galaxy outflow regions. Combining the molecular gas limits with the lack of detected star formation down to a limit of 0.3$M_\odot$ yr^{-1} kpc^{-2} from OSIRIS Hα observation will suggest good evidence for quenching of star formation over regions with powerful outflows. This program builds upon our work on the host galaxy of 3C 298 studied with ALMA in cycles 2 and 3 (see Chapter 2).

Tentative molecular outflows have been detected in 4 sources thus far (see Figure 5.3), with outflow rates of 100-4000 $M_\odot$ yr^{-1} on scales of 2-21 kpc. These objects potentially constitute the largest fraction of molecular outflows known to date at z> 1. The eventual goal is to

combine the ALMA observation of the molecular ISM with OSIRIS observations of the ionized ISM and KCWI to better understand the gas transport and compare both inflow and outflow rates for the same systems (see Figure 5.4).

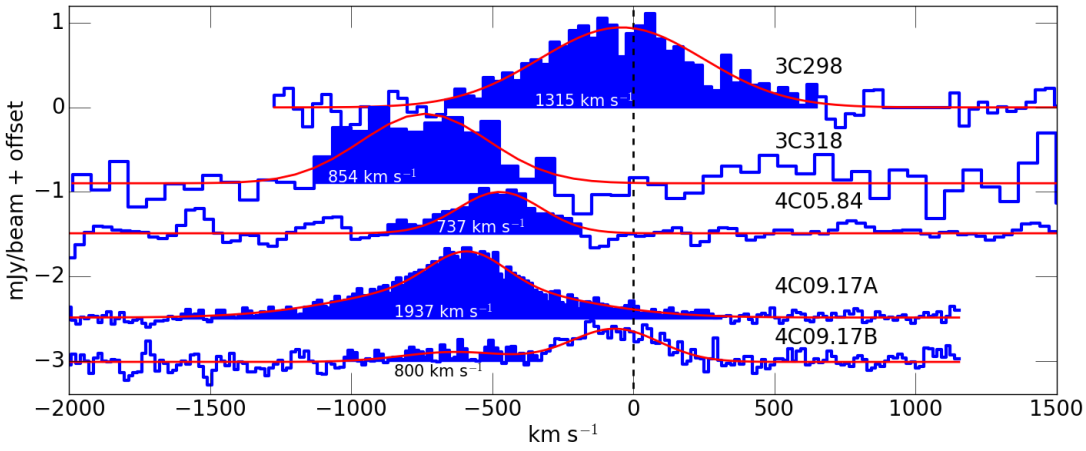

Figure 5.3 Spectra of galaxy scale (4-21 kpc) molecular outflows detected with ALMA cycles 3 and 5 data, in the host galaxies of our quasar sample. Outflow regions are selected from pixels in line-width (σ) maps that show velocity dispersion $>$250km s^{-1} . Highlighted in blue is the FWZI for each outflow($\gtrsim$ 700 km s^{-1}), much broader than what is expected from gravitational motion in these quasar host galaxies.

In hydrodynamical simulations that look at the cooling of the gas in quasar driven outflows, Richings and Faucher-Giguère (2018) finds that a significant fraction of the molecular gas in the quasar driven outflow is in a warm molecular gas phase at a temperature of about 500 K. Ro-vibrational molecular Hydrogen lines can trace the majority of this gas. The lines that trace the most significant fraction of the has are the pure-rotational vibrational lines in the mid-infrared. These have been extensively studied with the Spitzer space telescope in local galaxies, and indicate that they are produced in shock-heated regions within the galaxy (Hill and Zakamska, 2014). Both stellar and AGN feedback processes drive the shocks. With the launch of the JWST telescope it will be possible to extend the study of infrared Hydrogen lines out to z$\sim$2

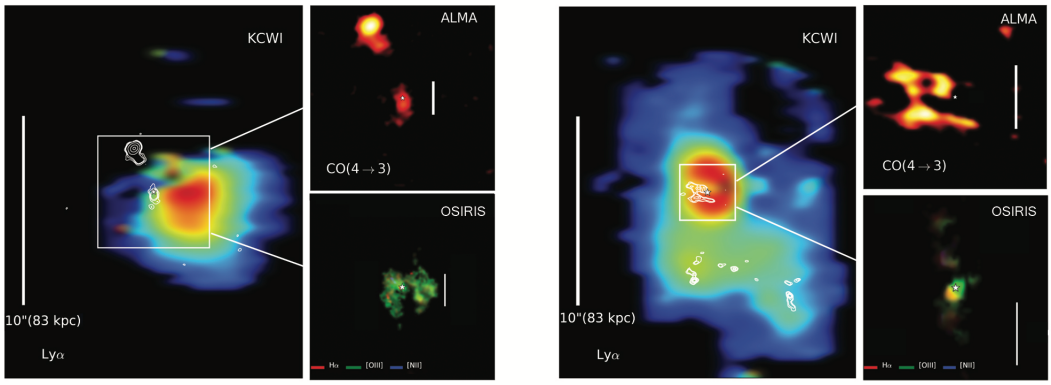

Figure 5.4 Example of our multiwavelength observations for 4C09.17 (left) and 4C05.84 (right). The left panel in each image shows the distribution of cool gas in CGM as traced by Lyα, taken with KCWI. ALMA Cycle 5 observations of molecular gas are shown in the upper right corner (inner few arcseconds) and with white contours (full FOV) as traced with CO (4-3), OSIRIS observations of ionized gas in the host galaxy are shown in the bottom right corner. OSIRIS-LGS is able to achieve sub-kiloparsec resolution in the inner 0.8 - 16 kpc from the center of the quasar. KCWI is capable of tracing the CGM of these quasar host galaxies on 200 kpc scale, with ALMA capable of tracing molecular gas on a similar a scale. Coupling KCWI to OSIRIS and ALMA observations will be incredibly powerful for deducing the accretion, star formation, and outflow history of these sources. In the future, we will be asking for ALMA time to obtain molecular gas observations for 4C04.81 and 3C9 to conduct a similar analysis for these two objects, for a total of 5 objects.

where the S(3) 9.66 μm line falls near the edge of the MIRI filter coverage and the near-infrared ro-vibrational lines of Hydrogen fall at the shorter end of the MIRI wavelength coverage. The rest-frame near-infrared ro-vibrational lines can still be used to study the warm molecular gas at higher redshifts, however they tracer a much warmer (>2000 K) component than the mid-infrared pure-rotational hydrogen lines (U et al., 2019). The much warmer, 2000 K component most likely constitutes a smaller fraction of the molecular gas in outflows.

Combining JWST MIRI observations with ALMA observations of cooler molecular hydrogen traced by rotational CO transitions will give a complete view of molecular gas in quasar driven outflows. Combining the molecular gas measurements with the ionized gas from nebular

emission lines will give a complete view of both ionized and molecular gas allowing for the first time to measure the total outflow rates and energetics for outflows near the peak epoch of galaxy and SMBH growth.

5.3 In The Era of Extremely Large Telescopes (ELTs)

Today, ionized outflow rates are plagued by uncertainty on the electron density. Typically the [SII] doublet at 6717Å, 6731Å is used to calculate the electron density. Often the line is detected at a low SNR, and the high-velocity dispersion of the emission line velocity cause them to blend. The dominant uncertainty in measuring the electron density is due to the lower spectral resolving power of near-infrared IFS today.

The first light Infrared Imaging Spectrograph (IRIS) on the Thirty Meter Telescope (TMT) paired with the adaptive optics system will provide diffraction-limited observations with spectral resolving power of 8000. The European Extremely Large Telescope (E-ELT) and the Giant Magellan Telescope (GMT) will also have similar spectroscopic and adaptive optics capabilities. The spectral resolution of first-generation IFS on ELTs will be sufficient to resolve the [SII] doublet with typical velocity dispersion of $\sim$500-900 km s^{-1} seen in the outflow regions of the quasar host galaxies studied in Chapter 3 and 4. Furthermore, the high spatial resolution of 70-160 pc will allow to detect individual clouds inside a galactic outflow and measuring their electron densities at z$\sim$2. This will significantly improve our uncertainties on the amount of mass in galactic outflows. Today we assume that each cloud inside the outflow has the same density, this assumption carries an inherent uncertainty which is hard to quantify since we have

yet to map the electron density at the resolution of individual clouds inside a quasar driven outflow at any redshift. The [SII] doublet is only able to probe the electron density in the range of $\sim 10^{1.3-3.6}$ cm^{-3} , other diagnostic line ratios are necessary to probe denser gas to understand the distribution of electron densities better. In the optical, the lines that provide diagnostic for higher electron density are typically much fainter, and today are impossible to detect in the distant Universe with 8-10 m class telescopes. With a 30-meter aperture, ELTs will have the necessary sensitivity to detect the doubly ionized Chlorine lines at 5517Å and 5537Å that will enable measurement of electron densities out to 10^5 cm^{-3} (Figure 5.5). In the outflow of Mrk 477 there appear to be regions with electron densities as high as 8,000 cm^{-3} as measured from line ratios of [Ar IV] 4711Å and 4740Å (Villar Martín et al., 2015). Such densities are much higher than what is typically assumed in outflows and higher than what can be measured with line ratios of [SII] and [OII] .

The high angular resolution of TMT and IRIS will provide us with a unique capability of measuring the SMBH of quasars at every redshift with SMBH masses $> 10^9$ M$_\odot$. This will be possible by measure the radial velocity of either gas or stars within the sphere of influence of the SMBH. For this science case to be successful, it is critical to adopt the PSF subtraction techniques developed in chapters 2 and 3 to future IFS and AO systems, to provide the highest possible contrast at small angular separations. The expected uncertainties will be significantly lower than what can be achieved today from single epoch SMBH mass estimates, which measure the SMBH with an uncertainty of about 0.5 dex.

The sensitivity of IFS on ELTs will also be sufficient to detect the stellar continuum on kpc scales in the host galaxy. This will allow us to measure the stellar velocity dispersion di-

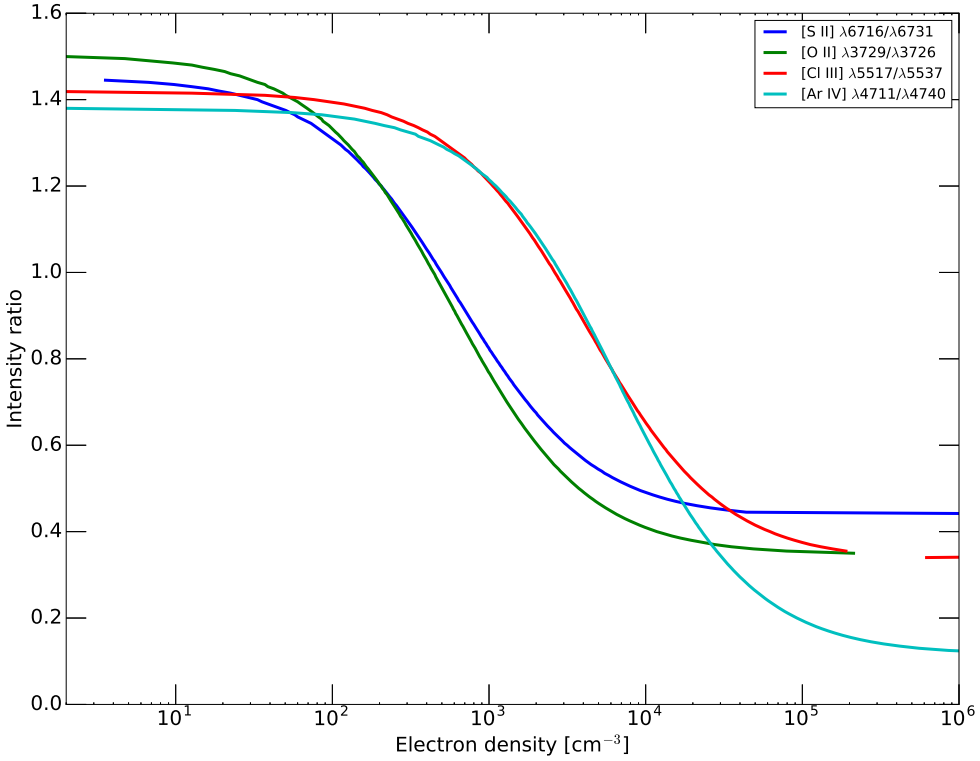

Figure 5.5 Deriving electron densities from ratios of optical emission lines. On the y-axis, we plot the ratio of emission line doublets as a function of electron density. Each pair of emission lines probes a range of electron densities. The values are computed using the Python module PyNeb (Luridiana et al., 2015).

rectly. As discussed in Chapter 4, today the IFS on 8-10 meter class telescopes are generally not sensitive enough to measure the stellar velocity dispersion, and often the gas velocity dispersion is used when comparing the galaxies to local scaling relation. The unknown uncertainty on assuming that gas velocity dispersion probes the stellar velocity dispersion cause challenges in comparing samples of higher redshift systems to the local scaling relationship. This further complicates testing whether there is an inherent redshift evolution in the slope and y-intercept of the local scaling relation between the mass of the SMBH and the velocity dispersion and mass of the bulge from z=0-2.

While the next generation of ELTs will provide a unique opportunity to measure the SMBH masses of massive black holes, future space-based gravitational wave experiments will allow for the measurement of lower mass black holes in the distant Universe. Today, seismic noise prevents the detection of gravitational waves from SMBH mergers with masses $> 10^5$ $M_\odot$, which produce their characteristic chirp at frequencies below 10^{-1} Hz. Space-based laser interferometers will enable this capability out to redshifts of 10, making it possible to detect gravitational wave signals from BH-BH mergers with masses in the range of 10^{5-7} $M_\odot$ (Amaro-Seoane et al., 2017). One of the currently planned missions is the Laser Interferometer Space Antenna (LISA). The challenge will be localizing these gravitational wave events since the beam area on the sky will be on the order of 100 deg^2 for LISA. The current proposed launch date for LISA is in 2034 coinciding with the time when ELTs will be fully operational. Furthermore, LSST will still be operational and will continue to provide wide-field time series observation of the entire visible sky in the southern hemisphere. Once the optical counterpart to the gravitational wave is determined, ground-based AO observation of their galaxy with IFS observations

such as IRIS will provide information about the stellar mass and velocity dispersion, enabling multi-messenger astronomy of nuclear regions in individual galaxies for the first time. Combining the stellar mass and velocity dispersion will enable us to compare these objects to the local scaling relations. Combining the sample of galaxies with lower mass SMBH to that of quasars hosting SMBH with masses of 10^9 $M_{\odot}$ will give a more complete demographic of the galaxy and SMBH masses at $z \sim 2$. This will enable us to study the evolution in the $M_{\bullet} - \sigma$ relationship from z=0 out to the peak epoch of SMBH and galaxy growth.

Bibliography

S. Aalto, S. Muller, K. Sakamoto, J. S. Gallagher, S. Martín, and F. Costagliola. Winds of change - a molecular outflow in NGC 1377?. The anatomy of an extreme FIR-excess galaxy. *AAP*, 546:A68, October 2012. doi: 10.1051/0004-6361/201118052.

C. P. Ahn, R. Alexandroff, C. Allende Prieto, F. Anders, S. F. Anderson, T. Anderton, B. H. Andrews, É. Aubourg, S. Bailey, F. A. Bastien, and et al. The Tenth Data Release of the Sloan Digital Sky Survey: First Spectroscopic Data from the SDSS-III Apache Point Observatory Galactic Evolution Experiment. *ApJS*, 211:17, April 2014. doi: 10.1088/0067-0049/211/2/17.

K. Alatalo, L. Blitz, L. M. Young, T. A. Davis, M. Bureau, L. A. Lopez, M. Cappellari, N. Scott, K. L. Shapiro, A. F. Crocker, S. Martín, M. Bois, F. Bournaud, R. L. Davies, P. T. de Zeeuw, P.-A. Duc, E. Emsellem, J. Falcón-Barroso, S. Khochfar, D. Krajnović, H. Kuntschner, P.-Y. Lablanche, R. M. McDermid, R. Morganti, T. Naab, T. Oosterloo, M. Sarzi, P. Serra, and A. Weijmans. Discovery of an Active Galactic Nucleus Driven Molecular Outflow in the Local Early-type Galaxy NGC 1266. *ApJ*, 735:88, July 2011. doi: 10.1088/0004-637X/735/2/88.

D. M. Alexander and R. C. Hickox. What drives the growth of black holes? *New Astronomy R.*, 56:93–121, June 2012. doi: 10.1016/j.newar.2011.11.003.

D. M. Alexander, A. M. Swinbank, Ian Smail, R. McDermid, and N. P. H. Nesvadba. Searching for evidence of energetic feedback in distant galaxies: a galaxy wide outflow in a z $\sim$2 ultra-luminous infrared galaxy. *MNRAS*, 402(4):2211–2220, Mar 2010. doi: 10.1111/j.1365-2966.2009.16046.x.

James T. Allen, Paul C. Hewett, Natasha Maddox, Gordon T. Richards, and Vasily Belokurov. A strong redshift dependence of the broad absorption line quasar fraction. *MNRAS*, 410(2): 860–884, Jan 2011. doi: 10.1111/j.1365-2966.2010.17489.x.

M. G. Allen, B. A. Groves, M. A. Dopita, R. S. Sutherland, and L. J. Kewley. The MAPPINGS III Library of Fast Radiative Shock Models. *Astrophys. J. Suppl.*, 178:20-55, September 2008. doi: 10.1086/589652.

Pau Amaro-Seoane, Heather Audley, Stanislav Babak, John Baker, Enrico Barausse, Peter Bender, Emanuele Berti, Pierre Binetruy, Michael Born, and Daniele Bortoluzzi. Laser Interferometer Space Antenna. *arXiv e-prints*, art. arXiv:1702.00786, Feb 2017.

D. Anglés-Alcázar, C.-A. Faucher-Giguère, D. Kereš, P. F. Hopkins, E. Quataert, and N. Murray. The cosmic baryon cycle and galaxy mass assembly in the FIRE simulations. *MNRAS*, 470: 4698–4719, October 2017a. doi: 10.1093/mnras/stx1517.

D. Anglés-Alcázar, C.-A. Faucher-Giguère, E. Quataert, P. F. Hopkins, R. Feldmann, P. Torrey, A. Wetzel, and D. Kereš. Black Holes on FIRE: Stellar Feedback Limits Early Feeding of Galactic Nuclei. *ArXiv e-prints*, July 2017b.

R. Antonucci. Unified models for active galactic nuclei and quasars. *ARAA*, 31:473–521, 1993. doi: 10.1146/annurev.aa.31.090193.002353.

R. R. J. Antonucci and J. S. Miller. Spectropolarimetry and the nature of NGC 1068. *ApJ*, 297: 621–632, October 1985. doi: 10.1086/163559.

Eduardo Bañados, Bram P. Venemans, Chiara Mazzucchelli, Emanuele P. Farina, Fabian Walter, Feige Wang, Roberto Decarli, Daniel Stern, Xiaohui Fan, and Frederick B. Davies. An 800-million-solar-mass black hole in a significantly neutral Universe at a redshift of 7.5. *Nature*, 553(7689):473–476, Jan 2018. doi: 10.1038/nature25180.

W. Baade and R. Minkowski. Identification of the Radio Sources in Cassiopeia, Cygnus A, and Puppis A. *ApJ*, 119:206, January 1954. doi: 10.1086/145812.

J. A. Baldwin, M. M. Phillips, and R. Terlevich. Classification parameters for the emission-line spectra of extragalactic objects. *PASP*, 93:5–19, February 1981. doi: 10.1086/130766.

P. Barai, S. Gallerani, A. Pallottini, A. Ferrara, A. Marconi, C. Cicone, R. Maiolino, and S. Carniani. Quasar outflows at $z \geq 6$: the impact on the host galaxies. *ArXiv e-prints*, July 2017.

R. S. Barrows, J. M. Comerford, J. E. Greene, and D. Pooley. Spatially Offset Active Galactic Nuclei. I. Selection and Spectroscopic Properties. *Astrophys. J.*, 829:37, September 2016. doi: 10.3847/0004-637X/829/1/37.

Robert H. Becker, Richard L. White, and David J. Helfand. The FIRST Survey: Faint Images of the Radio Sky at Twenty Centimeters. *ApJ*, 450:559, Sep 1995. doi: 10.1086/176166.

Peter S. Behroozi, Charlie Conroy, and Risa H. Wechsler. A Comprehensive Analysis of Uncertainties Affecting the Stellar Mass-Halo Mass Relation for 0 < z < 4. *ApJ*, 717(1): 379–403, Jul 2010. doi: 10.1088/0004-637X/717/1/379.

E. F. Bell, D. H. McIntosh, M. Barden, C. Wolf, J. A. R. Caldwell, H.-W. Rix, S. V. W. Beckwith, A. Borch, B. Häussler, K. Jahnke, S. Jogee, K. Meisenheimer, C. Peng, S. F. Sanchez, R. S. Somerville, and L. Wisotzki. GEMS Imaging of Red-Sequence Galaxies at z˜0.7: Dusty or Old? *Astrophys. J. Lett.*, 600:L11–L14, January 2004. doi: 10.1086/381388.

V. N. Bennert, M. W. Auger, T. Treu, J.-H. Woo, and M. A. Malkan. The Relation between Black Hole Mass and Host Spheroid Stellar Mass Out to z ˜ 2. *ApJ*, 742:107, December 2011. doi: 10.1088/0004-637X/742/2/107.

V. N. Bennert, D. Loveland, E. Donohue, M. Cosens, S. Lewis, S. Komossa, T. Treu, M. A. Malkan, N. Milgram, K. Flatland, M. W. Auger, D. Park, and M. S. Lazarova. Studying the [O III]λ5007 Å emission-line width in a sample of
80 local active galaxies: a surrogate for σ. *MNRAS*, 481:138–152, November 2018. doi: 10.1093/mnras/sty2236.

A. J. Benson, R. G. Bower, C. S. Frenk, C. G. Lacey, C. M. Baugh, and S. Cole. What Shapes the Luminosity Function of Galaxies? *ApJ*, 599:38–49, December 2003. doi: 10.1086/379160.

L. Bîrzan, B. R. McNamara, P. E. J. Nulsen, C. L. Carilli, and M. W. Wise. Radiative Efficiency and Content of Extragalactic Radio Sources: Toward a Universal Scaling Relation between Jet Power and Radio Power. *Astrophys. J.*, 686:859-880, October 2008. doi: 10.1086/591416.

R. D. Blandford and M. J. Rees. Some comments on radiation mechanisms in Lacertids. In A. M. Wolfe, editor, *BL Lac Objects*, pages 328–341, 1978.

A. Boehle, J. E. Larkin, S. M. Adkins, T. Aliado, M. P. Fitzgerald, C. A. Johnson, J. E. Lyke, K. G. Magnone, J. M. Sohn, E. Wang, and J. L. Weiss. Upgrade of the detector in the integral field spectrograph OSIRIS at the W. M. Keck Observatory. In *Ground-based and Airborne Instrumentation for Astronomy VI*, volume 9908 of *Proc. SPIE*, page 99082Q, August 2016. doi: 10.1117/12.2233100.

H. Boehringer, W. Voges, A. C. Fabian, A. C. Edge, and D. M. Neumann. A ROSAT HRI study of the interaction of the X-ray emitting gas and radio lobers of NGC 1275. *MNRAS*, 264: L25–L28, Oct 1993. doi: 10.1093/mnras/264.1.L25.

J. G. Bolton, G. J. Stanley, and O. B. Slee. Positions of Three Discrete Sources of Galactic Radio-Frequency Radiation. *Nature*, 164:101–102, July 1949. doi: 10.1038/164101b0.

E. Borisova, S. Cantalupo, S. J. Lilly, R. A. Marino, S. G. Gallego, R. Bacon, J. Blaizot, N. Bouché, J. Brinchmann, C. M. Carollo, J. Caruana, H. Finley, E. C. Herenz, J. Richard, J. Schaye, L. A. Straka, M. L. Turner, T. Urrutia, A. Verhamme, and L. Wisotzki. Ubiquitous Giant Lyα Nebulae around the Brightest Quasars at z
3.5 Revealed with MUSE. *ApJ*, 831:39, November 2016. doi: 10.3847/0004-637X/831/1/39.

C. S. Bowyer, M. Lampton, J. Mack, and F. de Mendonca. Detection of X-Ray Emission from 3c 273 and NGC 5128. *ApJL*, 161:L1, July 1970. doi: 10.1086/180559.

V. A. Bruce, J. S. Dunlop, R. J. McLure, M. Cirasuolo, F. Buitrago, R. A. A. Bowler, T. A. Targett, E. F. Bell, D. H. McIntosh, A. Dekel, S. M. Faber, H. C. Ferguson, N. A. Grogin, W. Hartley, D. D. Kocevski, A. M. Koekemoer, D. C. Koo, and E. J. McGrath. The decomposed bulge and disc size-mass relations of massive galaxies at 1 z 3 in CANDELS. *MNRAS*, 444:1660–1673, October 2014. doi: 10.1093/mnras/stu1537.

M. Brusa, M. Perna, G. Cresci, M. Schramm, I. Delvecchio, G. Lanzuisi, V. Mainieri, M. Mignoli, G. Zamorani, S. Berta, A. Bongiorno, A. Comastri, F. Fiore, D. Kakkad, A. Marconi, D. Rosario, T. Contini, and F. Lamareille. A fast ionised wind in a star-forming quasar

system at z$\sim$ 1.5 resolved through adaptive optics assisted near-infrared data. *Astron. & Astrop.*, 588:A58, April 2016. doi: 10.1051/0004-6361/201527900.

M. Brusa, G. Cresci, E. Daddi, R. Paladino, M. Perna, A. Bongiorno, E. Lusso, M. T. Sargent, V. Casasola, C. Feruglio, F. Fraternali, I. Georgiev, V. Mainieri, S. Carniani, A. Comastri, F. Duras, F. Fiore, F. Mannucci, A. Marconi, E. Piconcelli, G. Zamorani, R. Gilli, F. La Franca, G. Lanzuisi, D. Lutz, P. Santini, N. Z. Scoville, C. Vignali, F. Vito, S. Rabien, L. Busoni, and M. Bonaglia. Molecular outflow and feedback in the obscured quasar XID2028 revealed by ALMA. *AAP*, 612:A29, April 2018. doi: 10.1051/0004-6361/201731641.

E. M. Burbidge and G. R. Burbidge. Optical Evidence Suggesting the Occurrence of a Violent Outburst in NGC 1275. *ApJ*, 142:1351, November 1965. doi: 10.1086/148421.

D. Calzetti, L. Armus, R. C. Bohlin, A. L. Kinney, J. Koornneef, and T. Storchi-Bergmann. The Dust Content and Opacity of Actively Star-forming Galaxies. *Astrophys. J.*, 533:682–695, April 2000. doi: 10.1086/308692.

D. Calzetti, S. Y. Wu, S. Hong, R. C. Kennicutt, J. C. Lee, D. A. Dale, C. W. Engelbracht, L. van Zee, B. T. Draine, and C. N. Hao. The Calibration of Monochromatic Far-Infrared Star Formation Rate Indicators. *ApJ*, 714(2):1256–1279, May 2010. doi: 10.1088/0004-637X/714/2/1256.

Daniela Calzetti. *Star Formation Rate Indicators*, page 419. 2013.

M. Cano-Díaz, R. Maiolino, A. Marconi, H. Netzer, O. Shemmer, and G. Cresci. Observational evidence of quasar feedback quenching star formation at high redshift. *Astron. & Astrop.*, 537:L8, January 2012. doi: 10.1051/0004-6361/201118358.

S. Cantalupo. Gas Accretion and Giant Lyα Nebulae. In A. Fox and R. Davé, editors, *Astrophysics and Space Science Library*, volume 430 of *Astrophysics and Space Science Library*, page 195, 2017. doi: 10.1007/978-3-319-52512-9_9.

C. L. Carilli and F. Walter. Cool Gas in High-Redshift Galaxies. *Ann. Rev. Astron. Astrophys.*, 51:105–161, August 2013. doi: 10.1146/annurev-astro-082812-140953.

C. L. Carilli, R. A. Perley, and D. E. Harris. Observations of interaction between cluster gas and the radio lobes of Cygnus A. *MNRAS*, 270:173–177, Sep 1994. doi: 10.1093/mnras/270.1.173.

S. Carniani, A. Marconi, R. Maiolino, B. Balmaverde, M. Brusa, M. Cano-Díaz, C. Cicone, A. Comastri, G. Cresci, F. Fiore, C. Feruglio, F. La Franca, V. Mainieri, F. Mannucci, T. Nagao, H. Netzer, E. Piconcelli, G. Risaliti, R. Schneider, and O. Shemmer. Ionised outflows in z ˜ 2.4 quasar host galaxies. *Astron. & Astrop.*, 580:A102, August 2015. doi: 10.1051/0004-6361/201526557.

S. Carniani, A. Marconi, R. Maiolino, B. Balmaverde, M. Brusa, M. Cano-Díaz, C. Cicone, A. Comastri, G. Cresci, F. Fiore, C. Feruglio, F. La Franca, V. Mainieri, F. Mannucci, T. Nagao, H. Netzer, E. Piconcelli, G. Risaliti, R. Schneider, and O. Shemmer. Fast outflows and star formation quenching in quasar host galaxies. *Astron. & Astrop.*, 591:A28, June 2016. doi: 10.1051/0004-6361/201528037.

K. W. Cavagnolo, B. R. McNamara, P. E. J. Nulsen, C. L. Carilli, C. Jones, and L. Bîrzan. A Relationship Between AGN Jet Power and Radio Power. *Astrophys. J.*, 720:1066–1072, September 2010. doi: 10.1088/0004-637X/720/2/1066.

C. Chamberlain, N. Arav, and C. Benn. Strong candidate for AGN feedback: VLT/X-shooter observations of BALQSO SDSS J0831+0354. *Mon. Not. R. Astron. S.*, 450:1085–1093, June 2015. doi: 10.1093/mnras/stv572.

HongâYee Chiu. Chiu's views. *Physics Today*, 17(7):70–72, 1964. doi: 10.1063/1.3051721. URL `https://doi.org/10.1063/1.3051721`.

C. Cicone, R. Maiolino, E. Sturm, J. Graciá-Carpio, C. Feruglio, R. Neri, S. Aalto, R. Davies, F. Fiore, J. Fischer, S. García-Burillo, E. González-Alfonso, S. Hailey-Dunsheath, E. Piconcelli, and S. Veilleux. Massive molecular outflows and evidence for AGN feedback from CO observations. *AAP*, 562:A21, February 2014. doi: 10.1051/0004-6361/201322464.

Alison L. Coil, James Aird, Naveen Reddy, Alice E. Shapley, Mariska Kriek, Brian Siana, Bahram Mobasher, William R. Freeman, Sedona H. Price, and Irene Shivaei. The MOSDEF Survey: Optical Active Galactic Nucleus Diagnostics at z ∼2.3. *ApJ*, 801(1):35, Mar 2015. doi: 10.1088/0004-637X/801/1/35.

J. M. Comerford, D. Pooley, R. S. Barrows, J. E. Greene, N. L. Zakamska, G. M. Madejski, and M. C. Cooper. Merger-driven Fueling of Active Galactic Nuclei: Six Dual and Offset AGNs Discovered with Chandra and Hubble Space Telescope Observations. *Astrophys. J.*, 806:219, June 2015. doi: 10.1088/0004-637X/806/2/219.

C. Conroy and J. E. Gunn. The Propagation of Uncertainties in Stellar Population Synthesis Modeling. III. Model Calibration, Comparison, and Evaluation. *Astrophys. J.*, 712:833–857, April 2010. doi: 10.1088/0004-637X/712/2/833.

C. Conroy, J. E. Gunn, and M. White. The Propagation of Uncertainties in Stellar Population Synthesis Modeling. I. The Relevance of Uncertain Aspects of Stellar Evolution and the Initial Mass Function to the Derived Physical Properties of Galaxies. *Astrophys. J.*, 699:486–506, July 2009. doi: 10.1088/0004-637X/699/1/486.

T. Costa, D. Sijacki, and M. G. Haehnelt. Fast cold gas in hot AGN outflows. *MNRAS*, 448: L30–L34, March 2015. doi: 10.1093/mnrasl/slu193.

T. Costa, J. Rosdahl, D. Sijacki, and M. G. Haehnelt. Quenching star formation with quasar outflows launched by trapped IR radiation. *MNRAS*, 479:2079–2111, September 2018a. doi: 10.1093/mnras/sty1514.

T. Costa, J. Rosdahl, D. Sijacki, and M. G. Haehnelt. Driving gas shells with radiation pressure on dust in radiation-hydrodynamic simulations. *MNRAS*, 473:4197–4219, January 2018b. doi: 10.1093/mnras/stx2598.

Stephane Courteau. Optical Rotation Curves and Linewidths for Tully-Fisher Applications. *AJ*, 114:2402, Dec 1997. doi: 10.1086/118656.

G. Cresci, V. Mainieri, M. Brusa, A. Marconi, M. Perna, F. Mannucci, E. Piconcelli, R. Maiolino, C. Feruglio, F. Fiore, A. Bongiorno, G. Lanzuisi, A. Merloni, M. Schramm, J. D. Silverman, and F. Civano. Blowin' in the Wind: Both "Negative" and "Positive" Feedback in an Obscured High-z Quasar. *Astrophys. J.*, 799:82, January 2015. doi: 10.1088/0004-637X/799/1/82.

Scott M. Croom, Gordon T. Richards, Tom Shanks, Brian J. Boyle, Michael A. Strauss, Adam D. Myers, Robert C. Nichol, Kevin A. Pimbblet, Nicholas P. Ross, and Donald P. Schneider. The 2dF-SDSS LRG and QSO survey: the QSO luminosity function at 0.4 < z < 2.6. *MNRAS*, 399(4):1755–1772, Nov 2009. doi: 10.1111/j.1365-2966.2009.15398.x.

R. M. Cutri, M. F. Skrutskie, S. van Dyk, C. A. Beichman, J. M. Carpenter, T. Chester, L. Cambresy, T. Evans, J. Fowler, and J. Gizis. *2MASS All Sky Catalog of point sources.* 2003.

R. I. Davies. A method to remove residual OH emission from near-infrared spectra. *MNRAS*, 375(3):1099–1105, Mar 2007. doi: 10.1111/j.1365-2966.2006.11383.x.

R. L. Davies, J. A. Rich, L. J. Kewley, and M. A. Dopita. Starburst-AGN mixing - I. NGC 7130. *MNRAS*, 439:3835–3846, April 2014. doi: 10.1093/mnras/stu234.

K. S. Dawson, D. J. Schlegel, C. P. Ahn, S. F. Anderson, É. Aubourg, S. Bailey, R. H. Barkhouser, J. E. Bautista, A. Beifiori, A. A. Berlind, V. Bhardwaj, D. Bizyaev, C. H. Blake, M. R. Blanton, M. Blomqvist, A. S. Bolton, A. Borde, J. Bovy, W. N. Brandt, H. Brewington, J. Brinkmann, P. J. Brown, J. R. Brownstein, K. Bundy, N. G. Busca, W. Carithers, A. R. Carnero, M. A. Carr, Y. Chen, J. Comparat, N. Connolly, F. Cope, R. A. C. Croft, A. J. Cuesta, L. N. da Costa, J. R. A. Davenport, T. Delubac, R. de Putter, S. Dhital, A. Ealet, G. L. Ebelke, D. J. Eisenstein, S. Escoffier, X. Fan, N. Filiz Ak, H. Finley, A. Font-Ribera, R. Génova-Santos, J. E. Gunn, H. Guo, D. Haggard, P. B. Hall, J.-C. Hamilton, B. Harris, D. W. Harris, S. Ho, D. W. Hogg, D. Holder, K. Honscheid, J. Huehnerhoff, B. Jordan, W. P. Jordan, G. Kauffmann, E. A. Kazin, D. Kirkby, M. A. Klaene, J.-P. Kneib, J.-M. Le Goff, K.-G. Lee, D. C. Long, C. P. Loomis, B. Lundgren, R. H. Lupton, M. A. G. Maia, M. Makler, E. Malanushenko, V. Malanushenko, R. Mandelbaum, M. Manera, C. Maraston, D. Margala, K. L. Masters, C. K. McBride, P. McDonald, I. D. McGreer, R. G. McMahon, O. Mena, J. Miralda-Escudé, A. D. Montero-Dorta, F. Montesano, D. Muna, A. D. Myers, T. Naugle, R. C. Nichol, P. Noterdaeme, S. E. Nuza, M. D. Olmstead, A. Oravetz, D. J. Oravetz, R. Owen, N. Padmanabhan, N. Palanque-Delabrouille, K. Pan, J. K. Parejko, I. Pâris, W. J. Percival, I. Pérez-Fournon, I. Pérez-Ràfols, P. Petitjean, R. Pfaffenberger, J. Pforr, M. M. Pieri, F. Prada, A. M. Price-Whelan, M. J. Raddick, R. Rebolo, J. Rich, G. T. Richards, C. M. Rockosi, N. A. Roe, A. J. Ross, N. P. Ross, G. Rossi, J. A. Rubiño-Martin, L. Samushia, A. G.

Sánchez, C. Sayres, S. J. Schmidt, D. P. Schneider, C. G. Scóccola, H.-J. Seo, A. Shelden, E. Sheldon, Y. Shen, Y. Shu, A. Slosar, S. A. Smee, S. A. Snedden, F. Stauffer, O. Steele, M. A. Strauss, A. Streblyanska, N. Suzuki, M. E. C. Swanson, T. Tal, M. Tanaka, D. Thomas, J. L. Tinker, R. Tojeiro, C. A. Tremonti, M. Vargas Magaña, L. Verde, M. Viel, D. A. Wake, M. Watson, B. A. Weaver, D. H. Weinberg, B. J. Weiner, A. A. West, M. White, W. M. Wood-Vasey, C. Yeche, I. Zehavi, G.-B. Zhao, and Z. Zheng. The Baryon Oscillation Spectroscopic Survey of SDSS-III. *AJ*, 145:10, January 2013. doi: 10.1088/0004-6256/145/1/10.

R. Decarli, F. Walter, B. P. Venemans, E. Bañados, F. Bertoldi, C. Carilli, X. Fan, E. P. Farina, C. Mazzucchelli, D. Riechers, H.-W. Rix, M. A. Strauss, R. Wang, and Y. Yang. An ALMA [C II] Survey of 27 Quasars at z 5.94. *ApJ*, 854:97, February 2018. doi: 10.3847/1538-4357/aaa5aa.

I. Delvecchio, C. Gruppioni, F. Pozzi, S. Berta, G. Zamorani, A. Cimatti, D. Lutz, D. Scott, C. Vignali, G. Cresci, A. Feltre, A. Cooray, M. Vaccari, J. Fritz, E. Le Floc'h, B. Magnelli, P. Popesso, S. Oliver, J. Bock, M. Carollo, T. Contini, O. Le Févre, S. Lilly, V. Mainieri, A. Renzini, and M. Scodeggio. Tracing the cosmic growth of supermassive black holes to z 3 with Herschel. *MNRAS*, 439:2736–2754, April 2014. doi: 10.1093/mnras/stu130.

T. Di Matteo, V. Springel, and L. Hernquist. Energy input from quasars regulates the growth and activity of black holes and their host galaxies. *Nature*, 433:604–607, February 2005. doi: 10.1038/nature03335.

Michael A. Dopita, I. Ting Ho, Linda L. Dressel, Ralph Sutherland, Lisa Kewley, Rebecca Davies, Elise Hampton, Prajval Shastri, Preeti Kharb, and Jessy Jose. Probing the Physics of Narrow-line Regions in Active Galaxies. III. Accretion and Cocoon Shocks in the LINER NGC 1052. *ApJ*, 801(1):42, Mar 2015. doi: 10.1088/0004-637X/801/1/42.

A. Dressler and D. O. Richstone. Stellar dynamics in the nuclei of M31 and M32 - Evidence for massive black holes? *ApJ*, 324:701–713, January 1988. doi: 10.1086/165930.

G. Drouart, C. De Breuck, J. Vernet, N. Seymour, M. Lehnert, P. Barthel, F. E. Bauer, E. Ibar, A. Galametz, M. Haas, N. Hatch, J. R. Mullaney, N. Nesvadba, B. Rocca-Volmerange, H. J. A. Röttgering, D. Stern, and D. Wylezalek. Rapidly growing black holes and host galaxies in the distant Universe from the Herschel Radio Galaxy Evolution Project. *AAP*, 566:A53, June 2014. doi: 10.1051/0004-6361/201323310.

D. O. Edge, J. R. Shakeshaft, W. B. McAdam, J. E. Baldwin, and S. Archer. A survey of radio sources at a frequency of 159 Mc/s. , 68:37–60, 1959.

B. Elsmore, M. Ryle, and P. R. R. Leslie. The positions, flux densities and angular diameters of 64 radio sources observed at a frequency of 178 Mc/s. , 68:61–67, 1959.

Irina Ene, Chung-Pei Ma, Nicholas J. McConnell, Jonelle L. Walsh, Philipp Kempski, Jenny E. Greene, Jens Thomas, and John P. Blakeslee. The MASSIVE Survey XIII. Spatially Resolved

Stellar Kinematics in the Central 1 kpc of 20 Massive Elliptical Galaxies with the GMOS-North Integral Field Spectrograph. *ApJ*, 878(1):57, Jun 2019. doi: 10.3847/1538-4357/ab1f04.

D. K. Erb, C. C. Steidel, A. E. Shapley, M. Pettini, N. A. Reddy, and K. L. Adelberger. The Stellar, Gas, and Dynamical Masses of Star-forming Galaxies at z ˜ 2. *ApJ*, 646:107–132, July 2006a. doi: 10.1086/504891.

Dawn K. Erb, Charles C. Steidel, Alice E. Shapley, Max Pettini, Naveen A. Reddy, and Kurt L. Adelberger. Hα Observations of a Large Sample of Galaxies at z $\sim$2: Implications for Star Formation in High-Redshift Galaxies. *ApJ*, 647(1):128–139, Aug 2006b. doi: 10.1086/505341.

Event Horizon Telescope Collaboration, Kazunori Akiyama, Antxon Alberdi, Walter Alef, Keiichi Asada, Rebecca Azulay, Anne-Kathrin Baczko, David Ball, Mislav Baloković, and John Barrett. First M87 Event Horizon Telescope Results. I. The Shadow of the Supermassive Black Hole. *ApJ*, 875(1):L1, Apr 2019. doi: 10.3847/2041-8213/ab0ec7.

A. C. Fabian. Cooling Flows in Clusters of Galaxies. *ARAA*, 32:277–318, Jan 1994. doi: 10.1146/annurev.aa.32.090194.001425.

A. C. Fabian. Observational Evidence of Active Galactic Nuclei Feedback. *ARAA*, 50:455–489, Sep 2012. doi: 10.1146/annurev-astro-081811-125521.

A. C. Fabian, A. Celotti, and R. M. Johnstone. Chandra reveals X-rays along the radio axis in the quasar 3C 9 at z= 2.012. *MNRAS*, 338(1):L7–L11, Jan 2003. doi: 10.1046/j.1365-8711.2003.06111.x.

A. C. Fabian, J. S. Sanders, M. Haehnelt, M. J. Rees, and J. M. Miller. X-ray emission from the ultramassive black hole candidate NGC 1277: implications and speculations on its origin. *MNRAS*, 431:L38–L42, April 2013. doi: 10.1093/mnrasl/slt004.

R. Falomo, J. K. Kotilainen, R. Scarpa, and A. Treves. VLT adaptive optics imaging of QSO host galaxies and their close environment at z 2.5: Results from a pilot program. *Astron. & Astrop.*, 434:469–473, May 2005. doi: 10.1051/0004-6361:20041894.

C. Fanti, R. Fanti, D. Dallacasa, A. McDonald, R. T. Schilizzi, and R. E. Spencer. Multi-frequency analysis of the two CSS quasars 3C 43 & 3C 298. *Astron. & Astrop*, 396:801–813, December 2002. doi: 10.1051/0004-6361:20021410.

Duncan Farrah, Tanya Urrutia, Mark Lacy, Andreas Efstathiou, Jose Afonso, Kristen Coppin, Patrick B. Hall, Carol Lonsdale, Tom Jarrett, and Carrie Bridge. Direct Evidence for Termination of Obscured Star Formation by Radiatively Driven Outflows in Reddened QSOs. *ApJ*, 745(2):178, Feb 2012. doi: 10.1088/0004-637X/745/2/178.

E. A. Fath. The spectra of some spiral nebulae and globular star clusters. *Lick Observatory Bulletin*, 5:71–77, 1909. doi: 10.5479/ADS/bib/1909LicOB.5.71F.

C.-A. Faucher-Giguère and E. Quataert. The physics of galactic winds driven by active galactic nuclei. *MNRAS*, 425:605–622, September 2012. doi: 10.1111/j.1365-2966.2012.21512.x.

C.-A. Faucher-Giguère, E. Quataert, and N. Murray. A physical model of FeLoBALs: implications for quasar feedback. *MNRAS*, 420:1347–1354, February 2012. doi: 10.1111/j.1365-2966.2011.20120.x.

L. Ferrarese and D. Merritt. A Fundamental Relation between Supermassive Black Holes and Their Host Galaxies. *ApJL*, 539:L9–L12, August 2000. doi: 10.1086/312838.

C. Feruglio, F. Fiore, E. Piconcelli, C. Cicone, R. Maiolino, R. Davies, and E. Sturm. High resolution mapping of CO(1-0) in NGC 6240. *AAP*, 558:A87, October 2013. doi: 10.1051/0004-6361/201321275.

C. Feruglio, F. Fiore, S. Carniani, E. Piconcelli, L. Zappacosta, A. Bongiorno, C. Cicone, R. Maiolino, A. Marconi, N. Menci, S. Puccetti, and S. Veilleux. The multi-phase winds of Markarian 231: from the hot, nuclear, ultra-fast wind to the galaxy-scale, molecular outflow. *AAP*, 583:A99, Nov 2015. doi: 10.1051/0004-6361/201526020.

D. J. E. Floyd, J. S. Dunlop, M. J. Kukula, M. J. I. Brown, R. J. McLure, S. A. Baum, and C. P. O'Dea. Star formation in luminous quasar host galaxies at z = 1-2. *Mon. Not. R. Astron. S.*, 429:2–19, February 2013. doi: 10.1093/mnras/sts291.

N. M. Förster Schreiber, R. Genzel, N. Bouché, G. Cresci, R. Davies, P. Buschkamp, K. Shapiro, L. J. Tacconi, E. K. S. Hicks, and S. Genel. The SINS Survey: SINFONI Integral Field Spectroscopy of z ∼2 Star-forming Galaxies. *ApJ*, 706(2):1364–1428, Dec 2009. doi: 10.1088/0004-637X/706/2/1364.

N. M. Förster Schreiber, A. Renzini, C. Mancini, R. Genzel, N. Bouché, G. Cresci, E. K. S. Hicks, S. J. Lilly, Y. Peng, and A. Burkert. The SINS/zC-SINF Survey of z 2 Galaxy Kinematics: SINFONI Adaptive Optics-assisted Data and Kiloparsec-scale Emission-line Properties. *ApJS*, 238(2):21, Oct 2018. doi: 10.3847/1538-4365/aadd49.

N. M. Förster Schreiber, H. Übler, R. L. Davies, R. Genzel, E. Wisnioski, S. Belli, T. Shimizu, D. Lutz, M. Fossati, and R. Herrera-Camus. The KMOS^{3D} Survey: Demographics and Properties of Galactic Outflows at z = 0.62.7. *ApJ*, 875(1):21, Apr 2019. doi: 10.3847/1538-4357/ab0ca2.

J. P. U. Fynbo, J. K. Krogager, B. Venemans, P. Noterdaeme, M. Vestergaard, P. Møller, C. Ledoux, and S. Geier. Optical/Near-infrared Selection of Red Quasi-stellar Objects: Evidence for Steep Extinction Curves toward Galactic Centers? *ApJS*, 204(1):6, Jan 2013. doi: 10.1088/0067-0049/204/1/6.

Gaia Collaboration, A. G. A. Brown, A. Vallenari, T. Prusti, J. H. J. de Bruijne, F. Mignard, R. Drimmel, C. Babusiaux, C. A. L. Bailer-Jones, and U. Bastian. Gaia Data Release 1. Summary of the astrometric, photometric, and survey properties. *AAP*, 595:A2, Nov 2016. doi: 10.1051/0004-6361/201629512.

Gaia Collaboration, A. G. A. Brown, A. Vallenari, T. Prusti, J. H. J. de Bruijne, C. Babusiaux, C. A. L. Bailer-Jones, M. Biermann, D. W. Evans, and L. Eyer. Gaia Data Release 2. Summary of the contents and survey properties. *AAP*, 616:A1, Aug 2018. doi: 10.1051/0004-6361/201833051.

A. Gallazzi, J. Brinchmann, S. Charlot, and S. D. M. White. A census of metals and baryons in stars in the local Universe. *MNRAS*, 383:1439–1458, February 2008. doi: 10.1111/j.1365-2966.2007.12632.x.

Rajib Ganguly and Michael S. Brotherton. On the Fraction of Quasars with Outflows. *ApJ*, 672 (1):102–107, Jan 2008. doi: 10.1086/524106.

K. Gebhardt, R. Bender, G. Bower, A. Dressler, S. M. Faber, A. V. Filippenko, R. Green, C. Grillmair, L. C. Ho, J. Kormendy, T. R. Lauer, J. Magorrian, J. Pinkney, D. Richstone, and S. Tremaine. A Relationship between Nuclear Black Hole Mass and Galaxy Velocity Dispersion. *ApJL*, 539:L13–L16, August 2000. doi: 10.1086/312840.

R. Genzel, S. Newman, T. Jones, N. M. Förster Schreiber, K. Shapiro, S. Genel, S. J. Lilly, A. Renzini, L. J. Tacconi, and N. Bouché. The Sins Survey of z ∼2 Galaxy Kinematics: Properties of the Giant Star-forming Clumps. *ApJ*, 733(2):101, Jun 2011. doi: 10.1088/0004-637X/733/2/101.

R. Genzel, N. M. Förster Schreiber, D. Rosario, P. Lang, D. Lutz, E. Wisnioski, E. Wuyts, S. Wuyts, K. Bandara, R. Bender, S. Berta, J. Kurk, J. T. Mendel, L. J. Tacconi, D. Wilman, A. Beifiori, G. Brammer, A. Burkert, P. Buschkamp, J. Chan, C. M. Carollo, R. Davies, F. Eisenhauer, M. Fabricius, M. Fossati, M. Kriek, S. Kulkarni, S. J. Lilly, C. Mancini, I. Momcheva, T. Naab, E. J. Nelson, A. Renzini, R. Saglia, R. M. Sharples, A. Sternberg, S. Tacchella, and P. van Dokkum. Evidence for Wide-spread Active Galactic Nucleus-driven Outflows in the Most Massive z ˜ 1-2 Star-forming Galaxies. *ApJ*, 796:7, November 2014. doi: 10.1088/0004-637X/796/1/7.

Reinhard Genzel, Frank Eisenhauer, and Stefan Gillessen. The Galactic Center massive black hole and nuclear star cluster. *Reviews of Modern Physics*, 82(4):3121–3195, Oct 2010. doi: 10.1103/RevModPhys.82.3121.

Z. Ghaffari, Ch. Westhues, M. Haas, R. Chini, S. P. Willner, M. L. N. Ashby, and B. J. Wilkes. Galaxy overdensities around 3C radio galaxies and quasars at 1 < z < 2.5 revealed by Spitzer 3.6/4.5 m and Pan-STARRS. *Astronomische Nachrichten*, 338(7):823–840, Aug 2017. doi: 10.1002/asna.201713389.

A. M. Ghez, S. Salim, N. N. Weinberg, J. R. Lu, T. Do, J. K. Dunn, K. Matthews, M. R. Morris, S. Yelda, and E. E. Becklin. Measuring Distance and Properties of the Milky Way's Central Supermassive Black Hole with Stellar Orbits. *ApJ*, 689(2):1044–1062, Dec 2008. doi: 10.1086/592738.

E. Glikman, B. Simmons, M. Mailly, K. Schawinski, C. M. Urry, and M. Lacy. Major Mergers Host the Most-luminous Red Quasars at z ˜ 2: A Hubble Space Telescope WFC3/IR Study. *Astrophys. J.*, 806:218, June 2015. doi: 10.1088/0004-637X/806/2/218.

Karl D. Gordon, Geoffrey C. Clayton, K. A. Misselt, Arlo U. Land olt, and Michael J. Wolff. A Quantitative Comparison of the Small Magellanic Cloud, Large Magellanic Cloud, and Milky Way Ultraviolet to Near-Infrared Extinction Curves. *ApJ*, 594(1):279–293, Sep 2003. doi: 10.1086/376774.

Gravity Collaboration, E. Sturm, J. Dexter, O. Pfuhl, M. R. Stock, R. I. Davies, D. Lutz, Y. Clénet, A. Eckart, F. Eisenhauer, R. Genzel, D. Gratadour, S. F. Hönig, M. Kishimoto, S. Lacour, F. Millour, H. Netzer, G. Perrin, B. M. Peterson, P. O. Petrucci, D. Rouan, I. Waisberg, J. Woillez, A. Amorim, W. Brandner, N. M. Förster Schreiber, P. J. V. Garcia, S. Gillessen, T. Ott, T. Paumard, K. Perraut, S. Scheithauer, C. Straubmeier, L. J. Tacconi, and F. Widmann. Spatially resolved rotation of the broad-line region of a quasar at sub-parsec scale. *Nature*, 563:657–660, November 2018. doi: 10.1038/s41586-018-0731-9.

J. E. Greene and L. C. Ho. Estimating Black Hole Masses in Active Galaxies Using the Hα Emission Line. *ApJ*, 630:122–129, September 2005. doi: 10.1086/431897.

J. E. Greene, N. L. Zakamska, and P. S. Smith. A Spectacular Outflow in an Obscured Quasar. *ApJ*, 746:86, February 2012. doi: 10.1088/0004-637X/746/1/86.

Brent A. Groves, Timothy M. Heckman, and Guinevere Kauffmann. Emission-line diagnostics of low-metallicity active galactic nuclei. *MNRAS*, 371(4):1559–1569, Oct 2006. doi: 10.1111/j.1365-2966.2006.10812.x.

P. Guillard, F. Boulanger, M. D. Lehnert, P. N. Appleton, and G. Pineau des Forêts. Warm molecular Hydrogen at high redshift with the James Webb Space Telescope. In *SF2A-2015: Proceedings of the Annual meeting of the French Society of Astronomy and Astrophysics*, pages 81–85, Dec 2015.

Kayhan Gültekin, Douglas O. Richstone, Karl Gebhardt, Tod R. Lauer, Scott Tremaine, M. C. Aller, Ralf Bender, Alan Dressler, S. M. Faber, Alexei V. Filippenko, Richard Green, Luis C. Ho, John Kormendy, John Magorrian, Jason Pinkney, and Christos Siopis. The M-σ and M-L Relations in Galactic Bulges, and Determinations of Their Intrinsic Scatter. *ApJ*, 698:198–221, Jun 2009. doi: 10.1088/0004-637X/698/1/198.

N. Häring and H.-W. Rix. On the Black Hole Mass-Bulge Mass Relation. *ApJL*, 604:L89–L92, April 2004. doi: 10.1086/383567.

C. M. Harrison, D. M. Alexander, A. M. Swinbank, I. Smail, S. Alaghband-Zadeh, F. E. Bauer, S. C. Chapman, A. Del Moro, R. C. Hickox, R. J. Ivison, K. Menéndez-Delmestre, J. R. Mullaney, and N. P. H. Nesvadba. Energetic galaxy-wide outflows in high-redshift ultraluminous infrared galaxies hosting AGN activity. *Mon. Not. R. Astron. S.*, 426:1073–1096, October 2012. doi: 10.1111/j.1365-2966.2012.21723.x.

C. M. Harrison, D. M. Alexander, J. R. Mullaney, and A. M. Swinbank. Kiloparsec-scale outflows are prevalent among luminous AGN: outflows and feedback in the context of the overall AGN population. *MNRAS*, 441:3306–3347, July 2014. doi: 10.1093/mnras/stu515.

C. M. Harrison, T. Costa, C. N. Tadhunter, A. Flütsch, D. Kakkad, M. Perna, and G. Vietri. AGN outflows and feedback twenty years on. *Nature Astronomy*, 2:198–205, February 2018. doi: 10.1038/s41550-018-0403-6.

C. Hazard, M. B. Mackey, and A. J. Shimmins. Investigation of the Radio Source 3C 273 By The Method of Lunar Occultations. *Nature*, 197:1037–1039, March 1963. doi: 10.1038/1971037a0.

R. Herrera-Camus, L. Tacconi, R. Genzel, N. Förster Schreiber, D. Lutz, A. Bolatto, S. Wuyts, A. Renzini, S. Lilly, S. Belli, H. Übler, T. Shimizu, R. Davies, E. Sturm, F. Combes, J. Freundlich, S. García-Burillo, P. Cox, A. Burkert, T. Naab, L. Colina, A. Saintonge, M. Cooper, C. Feruglio, and A. Weiss. Molecular and Ionized Gas Phases of an AGN-driven Outflow in a Typical Massive Galaxy at z2. *ApJ*, 871:37, January 2019. doi: 10.3847/1538-4357/aaf6a7.

I. Heywood, A. Martínez-Sansigre, C. J. Willott, and S. Rawlings. Ground-state ^{12}CO emission and a resolved jet at 115 GHz (rest frame) in the radio-loud quasar 3C 318. *MNRAS*, 435:3376–3384, November 2013. doi: 10.1093/mnras/stt1530.

B. Hilbert, M. Chiaberge, J. P. Kotyla, G. R. Tremblay, C. Stanghellini, W. B. Sparks, S. Baum, A. Capetti, F. D. Macchetto, G. K. Miley, C. P. O'Dea, E. S. Perlman, and A. Quillen. Powerful Activity in the Bright Ages. I. A Visible/IR Survey of High Redshift 3C Radio Galaxies and Quasars. *Astrophys. J. Suppl.*, 225:12, July 2016. doi: 10.3847/0067-0049/225/1/12.

Matthew J. Hill and Nadia L. Zakamska. Warm molecular hydrogen in outflows from ultraluminous infrared Galaxies. *MNRAS*, 439(3):2701–2716, Apr 2014. doi: 10.1093/mnras/stu123.

J. Hlavacek-Larrondo, S. W. Allen, G. B. Taylor, A. C. Fabian, R. E. A. Canning, N. Werner, J. S. Sand ers, C. K. Grimes, S. Ehlert, and A. von der Linden. Probing the Extreme Realm of Active Galactic Nucleus Feedback in the Massive Galaxy Cluster, RX J1532.9+3021. *ApJ*, 777(2):163, Nov 2013. doi: 10.1088/0004-637X/777/2/163.

E. Holmberg. On the Apparent Diameters and the Orientation in Space of Extragalactic Nebulae. *Meddelanden fran Lunds Astronomiska Observatorium Serie II*, 117:3–82, January 1946.

P. F. Hopkins. Dynamical delays between starburst and AGN activity in galaxy nuclei. *MNRAS*, 420:L8–L12, February 2012. doi: 10.1111/j.1745-3933.2011.01179.x.

P. F. Hopkins and M. Elvis. Quasar feedback: more bang for your buck. *Mon. Not. R. Astron. S.*, 401:7–14, January 2010a. doi: 10.1111/j.1365-2966.2009.15643.x.

P. F. Hopkins and M. Elvis. Quasar feedback: more bang for your buck. *MNRAS*, 401:7–14, January 2010b. doi: 10.1111/j.1365-2966.2009.15643.x.

P. F. Hopkins, L. Hernquist, T. J. Cox, and D. Kereš. A Cosmological Framework for the Co-Evolution of Quasars, Supermassive Black Holes, and Elliptical Galaxies. I. Galaxy Mergers and Quasar Activity. *Astrophys. J. Suppl.*, 175:356-389, April 2008. doi: 10.1086/524362.

P. F. Hopkins, P. Torrey, C.-A. Faucher-Giguère, E. Quataert, and N. Murray. Stellar and quasar feedback in concert: effects on AGN accretion, obscuration, and outflows. *MNRAS*, 458: 816–831, May 2016. doi: 10.1093/mnras/stw289.

J. B. Hutchings, D. Frenette, R. Hanisch, J. Mo, P. J. Dumont, D. C. Redding, and S. G. Neff. Imaging of z˜2 QSO Host Galaxies with the Hubble Space Telescope. *The Astronomical Journal*, 123:2936–2944, June 2002. doi: 10.1086/340472.

M. Imanishi, K. Nakanishi, T. Izumi, and K. Wada. ALMA Reveals an Inhomogeneous Compact Rotating Dense Molecular Torus at the NGC 1068 Nucleus. *ApJL*, 853:L25, February 2018. doi: 10.3847/2041-8213/aaa8df.

K. J. Inskip, K. Jahnke, H.-W. Rix, and G. van de Ven. Resolving the Dynamical Mass of a z ˜ 1.3 Quasi-stellar Object Host Galaxy Using SINFONI and Laser Guide Star Assisted Adaptive Optics. *Astrophys. J.*, 739:90, October 2011. doi: 10.1088/0004-637X/739/2/90.

W. Jaffe, H. C. Ford, L. Ferrarese, F. van den Bosch, and R. W. O'Connell. A large nuclear accretion disk in the active galaxy NGC4261. *Nature*, 364:213–215, July 1993. doi: 10.1038/364213a0.

K. Jahnke, S. F. Sánchez, L. Wisotzki, M. Barden, S. V. W. Beckwith, E. F. Bell, A. Borch, J. A. R. Caldwell, B. Häussler, C. Heymans, S. Jogee, D. H. McIntosh, K. Meisenheimer, C. Y. Peng, H.-W. Rix, R. S. Somerville, and C. Wolf. Ultraviolet Light from Young Stars in GEMS Quasar Host Galaxies at 1.8<z<2.75. *Astrophys. J.*, 614:568–585, October 2004a. doi: 10.1086/423233.

K. Jahnke, L. Wisotzki, S. F. Sánchez, L. Christensen, T. Becker, A. Kelz, and M. M. Roth. Integral field spectroscopy of QSO host galaxies. *Astronomische Nachrichten*, 325:128–131, February 2004b. doi: 10.1002/asna.200310191.

Knud Jahnke and Andrea V. Macciò. The Non-causal Origin of the Black-hole-galaxy Scaling Relations. *ApJ*, 734(2):92, Jun 2011. doi: 10.1088/0004-637X/734/2/92.

S. Juneau, F. Bournaud, S. Charlot, E. Daddi, D. Elbaz, J. R. Trump, J. Brinchmann, M. Dickinson, P.-A. Duc, R. Gobat, I. Jean-Baptiste, É. Le Floc'h, M. D. Lehnert, C. Pacifici, M. Pannella, and C. Schreiber. Active Galactic Nuclei Emission Line Diagnostics and the Mass-Metallicity Relation up to Redshift z ˜ 2: The Impact of Selection Effects and Evolution. *ApJ*, 788:88, June 2014. doi: 10.1088/0004-637X/788/1/88.

Stéphanie Juneau, Mark Dickinson, David M. Alexander, and Samir Salim. A New Diagnostic of Active Galactic Nuclei: Revealing Highly Absorbed Systems at Redshift >0.3. *ApJ*, 736 (2):104, Aug 2011. doi: 10.1088/0004-637X/736/2/104.

D. Kakkad, V. Mainieri, M. Brusa, P. Padovani, S. Carniani, C. Feruglio, M. Sargent, B. Husemann, A. Bongiorno, M. Bonzini, E. Piconcelli, J. D. Silverman, and W. Rujopakarn. ALMA observations of cold molecular gas in AGN hosts at z 1.5 - evidence of AGN feedback? *MNRAS*, 468(4):4205–4215, Jul 2017. doi: 10.1093/mnras/stx726.

D. Kakkad, B. Groves, M. Dopita, A. D. Thomas, R. L. Davies, V. Mainieri, P. Kharb, J. Scharwächter, E. J. Hampton, and I. T. Ho. Spatially resolved electron density in the narrow line region of z < 0.02 radio AGNs. *AAP*, 618:A6, Oct 2018. doi: 10.1051/0004-6361/201832790.

G. Kauffmann, T. M. Heckman, C. Tremonti, J. Brinchmann, S. Charlot, S. D. M. White, S. E. Ridgway, J. Brinkmann, M. Fukugita, P. B. Hall, Ž. Ivezić, G. T. Richards, and D. P. Schneider. The host galaxies of active galactic nuclei. *Mon. Not. R. Astron. S.*, 346:1055–1077, December 2003. doi: 10.1111/j.1365-2966.2003.07154.x.

K. I. Kellermann. The discovery of quasars and its aftermath. *Journal of Astronomical History and Heritage*, 17(3):267–282, Nov 2014.

R. C. Kennicutt, Jr. The Global Schmidt Law in Star-forming Galaxies. *Astrophys. J.*, 498: 541–552, May 1998. doi: 10.1086/305588.

D. Kereš, N. Katz, M. Fardal, R. Davé, and D. H. Weinberg. Galaxies in a simulated ΛCDM Universe - I. Cold mode and hot cores. *MNRAS*, 395:160–179, May 2009. doi: 10.1111/j.1365-2966.2009.14541.x.

Roy P. Kerr. Gravitational field of a spinning mass as an example of algebraically special metrics. *Phys. Rev. Lett.*, 11:237–238, Sep 1963. doi: 10.1103/PhysRevLett.11.237. URL `https://link.aps.org/doi/10.1103/PhysRevLett.11.237`.

L. J. Kewley and M. A. Dopita. Using Strong Lines to Estimate Abundances in Extragalactic H II Regions and Starburst Galaxies. *ApJS*, 142:35–52, September 2002. doi: 10.1086/341326.

L. J. Kewley, M. A. Dopita, R. S. Sutherland, C. A. Heisler, and J. Trevena. Theoretical Modeling of Starburst Galaxies. *Astrophys. J.*, 556:121–140, July 2001. doi: 10.1086/321545.

L. J. Kewley, M. A. Dopita, C. Leitherer, R. Davé, T. Yuan, M. Allen, B. Groves, and R. Sutherland. Theoretical Evolution of Optical Strong Lines across Cosmic Time. *ApJ*, 774:100, September 2013a. doi: 10.1088/0004-637X/774/2/100.

L. J. Kewley, C. Maier, K. Yabe, K. Ohta, M. Akiyama, M. A. Dopita, and T. Yuan. The Cosmic BPT Diagram: Confronting Theory with Observations. *ApJL*, 774:L10, September 2013b. doi: 10.1088/2041-8205/774/1/L10.

Andrew King and Ken Pounds. Powerful Outflows and Feedback from Active Galactic Nuclei. *ARAA*, 53:115–154, Aug 2015. doi: 10.1146/annurev-astro-082214-122316.

J. Kormendy and L. C. Ho. Coevolution (Or Not) of Supermassive Black Holes and Host Galaxies. *ARAA*, 51:511–653, August 2013. doi: 10.1146/annurev-astro-082708-101811.

John Kormendy and Ralf Bender. Supermassive black holes do not correlate with dark matter haloes of galaxies. *Nature*, 469(7330):377–380, Jan 2011. doi: 10.1038/nature09695.

Jari K. Kotilainen, Renato Falomo, Roberto Decarli, Aldo Treves, Michela Uslenghi, and Riccardo Scarpa. The Properties of Quasar Hosts at the Peak of the Quasar Activity. *ApJ*, 703 (2):1663–1671, Oct 2009. doi: 10.1088/0004-637X/703/2/1663.

M. Kriek, A. E. Shapley, N. A. Reddy, B. Siana, A. L. Coil, B. Mobasher, W. R. Freeman, L. de Groot, S. H. Price, R. Sanders, I. Shivaei, G. B. Brammer, I. G. Momcheva, R. E. Skelton, P. G. van Dokkum, K. E. Whitaker, J. Aird, M. Azadi, M. Kassis, J. S. Bullock, C. Conroy, R. Davé, D. Kereš, and M. Krumholz. The MOSFIRE Deep Evolution Field (MOSDEF) Survey: Rest-frame Optical Spectroscopy for ˜1500 H-selected Galaxies at 1.37 z 3.8. *ApJS*, 218:15, June 2015. doi: 10.1088/0067-0049/218/2/15.

J. Kristian. Quasars as Events in the Nuclei of Galaxies: the Evidence from Direct Photographs. *ApJL*, 179:L61, January 1973. doi: 10.1086/181117.

J.-K. Krogager, J. P. U. Fynbo, P. Noterdaeme, T. Zafar, P. Møller, C. Ledoux, T. Krühler, and A. Stockton. A quasar reddened by a sub-parsec-sized, metal-rich and dusty cloud in a damped Lyman α absorber at z = 2.13. *MNRAS*, 455:2698–2711, January 2016. doi: 10.1093/mnras/stv2346.

Erini L. Lambrides, Andreea O. Petric, Kirill Tchernyshyov, Nadia L. Zakamska, and Duncan J. Watts. Mid-Infrared Spectroscopic Evidence for AGN Heating Warm Molecular Gas. *MNRAS*, page 1261, May 2019. doi: 10.1093/mnras/stz1316.

J. Larkin, M. Barczys, A. Krabbe, S. Adkins, T. Aliado, P. Amico, G. Brims, R. Campbell, J. Canfield, T. Gasaway, A. Honey, C. Iserlohe, C. Johnson, E. Kress, D. LaFreniere, J. Lyke, K. Magnone, N. Magnone, M. McElwain, J. Moon, A. Quirrenbach, G. Skulason, I. Song, M. Spencer, J. Weiss, and S. Wright. OSIRIS: a diffraction limited integral field spectrograph for Keck. In *Society of Photo-Optical Instrumentation Engineers (SPIE) Conference Series*, volume 6269 of *Proc. Soc. Photo-Opt. Instrum. Eng.*, page 62691A, June 2006. doi: 10.1117/12.672061.

James Larkin, Shelley Wright, Jason Weiss, Mike McElwain, Marshall Perrin, Christof Iserlohe, Alfred Krabbe, Tom Gasaway, Tommer Wizanski, Randy Campbell, and Jim Lyke. Keck osiris data reduction pipeline. `https://github.com/Keck-DataReductionPipelines/OsirisDRP/tree/master`, 2013.

D. R. Law, C. C. Steidel, Y. Chen, A. L. Strom, G. C. Rudie, and R. F. Trainor. Imaging Spectroscopy of Ionized Gaseous Nebulae around Optically Faint AGNs at Redshift z 2. *ApJ*, 866:119, October 2018. doi: 10.3847/1538-4357/aae156.

David R. Law, Charles C. Steidel, Dawn K. Erb, James E. Larkin, Max Pettini, Alice E. Shapley, and Shelley A. Wright. The Kiloparsec-scale Kinematics of High-redshift Star-forming Galaxies. *ApJ*, 697(2):2057–2082, Jun 2009. doi: 10.1088/0004-637X/697/2/2057.

David R. Law, Alice E. Shapley, Charles C. Steidel, Naveen A. Reddy, Charlotte R. Christensen, and Dawn K. Erb. High velocity dispersion in a rare grand-design spiral galaxy at redshift z = 2.18. *Nature*, 487(7407):338–340, Jul 2012. doi: 10.1038/nature11256.

M. D. Lehnert and R. H. Becker. Spectroscopy of the extended emission associated with two high-z quasars. *AAP*, 332:514–522, April 1998.

M. D. Lehnert, W. J. M. van Breugel, T. M. Heckman, and G. K. Miley. HUBBLE SPACE TELESCOPE Imaging of the Host Galaxies of High-RedshiftRadio-loud Quasars. *Astrophys. J. Suppl.*, 124:11–31, September 1999. doi: 10.1086/313252.

C. Leitherer, C. Robert, and L. Drissen. Deposition of mass, momentum, and energy by massive stars into the interstellar medium. *ApJ*, 401:596–617, December 1992. doi: 10.1086/172089.

C. Leitherer, D. Schaerer, J. D. Goldader, R. M. G. Delgado, C. Robert, D. F. Kune, D. F. de Mello, D. Devost, and T. M. Heckman. Starburst99: Synthesis Models for Galaxies with Active Star Formation. *ApJS*, 123:3–40, July 1999. doi: 10.1086/313233.

Gene C. K. Leung, Alison L. Coil, James Aird, Mojegan Azadi, Mariska Kriek, Bahram Mobasher, Naveen Reddy, Alice Shapley, Brian Siana, and Tara Fetherolf. The MOSDEF survey: a census of AGN-driven ionized outflows at $z = 1.4 - 3.8$. *arXiv e-prints*, art. arXiv:1905.13338, May 2019.

G. Liu, N. L. Zakamska, J. E. Greene, N. P. H. Nesvadba, and X. Liu. Observations of feedback from radio-quiet quasars - II. Kinematics of ionized gas nebulae. *MNRAS*, 436:2576–2597, December 2013a. doi: 10.1093/mnras/stt1755.

X. Liu, F. Civano, Y. Shen, P. Green, J. E. Greene, and M. A. Strauss. Chandra X-Ray and Hubble Space Telescope Imaging of Optically Selected Kiloparsec-scale Binary Active Galactic Nuclei. I. Nature of the Nuclear Ionizing Sources. *Astrophys. J.*, 762:110, January 2013b. doi: 10.1088/0004-637X/762/2/110.

Kelly E. Lockhart, Tuan Do, James E. Larkin, Anna Boehle, Randy D. Campbell, Samantha Chappell, Devin Chu, Anna Ciurlo, Maren Cosens, and Michael P. Fitzgerald. Characterizing and Improving the Data Reduction Pipeline for the Keck OSIRIS Integral Field Spectrograph. *AJ*, 157(2):75, Feb 2019. doi: 10.3847/1538-3881/aaf64e.

C. J. Lonsdale, P. D. Barthel, and G. K. Miley. The radio properties of high-redshift quasars. I - Dual-frequency observations of 79 steep-spectrum quasars at Z over 1.5. *ApJS*, 87:63–133, July 1993. doi: 10.1086/191799.

R. Lupton, M. R. Blanton, G. Fekete, D. W. Hogg, W. O'Mullane, A. Szalay, and N. Wherry. Preparing Red-Green-Blue Images from CCD Data. *PASP*, 116:133–137, February 2004. doi: 10.1086/382245.

V. Luridiana, C. Morisset, and R. A. Shaw. PyNeb: a new tool for analyzing emission lines. I. Code description and validation of results. *Astron. & Astrop.*, 573:A42, January 2015. doi: 10.1051/0004-6361/201323152.

D. Lynden-Bell. Galactic Nuclei as Collapsed Old Quasars. *Nature*, 223:690–694, August 1969. doi: 10.1038/223690a0.

P. Madau and M. Dickinson. Cosmic Star-Formation History. *ARAA*, 52:415–486, August 2014. doi: 10.1146/annurev-astro-081811-125615.

J. Magorrian, S. Tremaine, D. Richstone, R. Bender, G. Bower, A. Dressler, S. M. Faber, K. Gebhardt, R. Green, C. Grillmair, J. Kormendy, and T. Lauer. The Demography of Massive Dark Objects in Galaxy Centers. *AJ*, 115:2285–2305, June 1998. doi: 10.1086/300353.

R. Maiolino, S. Gallerani, R. Neri, C. Cicone, A. Ferrara, R. Genzel, D. Lutz, E. Sturm, L. J. Tacconi, F. Walter, C. Feruglio, F. Fiore, and E. Piconcelli. Evidence of strong quasar feedback in the early Universe. *MNRAS*, 425:L66–L70, September 2012. doi: 10.1111/j.1745-3933.2012.01303.x.

S. Manti, S. Gallerani, A. Ferrara, B. Greig, and C. Feruglio. Quasar UV luminosity function evolution up to z = 8. *MNRAS*, 466(1):1160–1169, Apr 2017. doi: 10.1093/mnras/stw3168.

F. Mantovani, A. Rossetti, W. Junor, D. J. Saikia, and C. J. Salter. Radio polarimetry of compact steep spectrum sources at sub-arcsecond resolution. *Astron. & Astrop.*, 555:A4, July 2013. doi: 10.1051/0004-6361/201220769.

I. Martín-Navarro, J. P. Brodie, A. J. Romanowsky, T. Ruiz-Lara, and G. van de Ven. Black-hole-regulated star formation in massive galaxies. *Nature*, 553:307–309, January 2018. doi: 10.1038/nature24999.

T. A. Matthews and A. R. Sandage. Optical Identification of 3C 48, 3C 196, and 3C 286 with Stellar Objects. *ApJ*, 138:30, July 1963. doi: 10.1086/147615.

N. J. McConnell and C.-P. Ma. Revisiting the Scaling Relations of Black Hole Masses and Host Galaxy Properties. *ApJ*, 764:184, February 2013. doi: 10.1088/0004-637X/764/2/184.

Peter J. McGregor, John Hart, Peter G. Conroy, Murray L. Pfitzner, Gabe J. Bloxham, Damien J. Jones, Mark D. Downing, Murray Dawson, Peter Young, and Mark Jarnyk. Gemini near-infrared integral field spectrograph (NIFS). In Masanori Iye and Alan F. M. Moorwood, editors, *Proc. SPIE*, volume 4841 of *Society of Photo-Optical Instrumentation Engineers (SPIE) Conference Series*, pages 1581–1591, Mar 2003. doi: 10.1117/12.459448.

R. J. McLure and J. S. Dunlop. The cosmological evolution of quasar black hole masses. *MNRAS*, 352:1390–1404, August 2004. doi: 10.1111/j.1365-2966.2004.08034.x.

J. P. McMullin, B. Waters, D. Schiebel, W. Young, and K. Golap. CASA Architecture and Applications. In R. A. Shaw, F. Hill, and D. J. Bell, editors, *Astronomical Data Analysis Software and Systems XVI*, volume 376 of *Astronomical Society of the Pacific Conference Series*, page 127, October 2007.

B. R. McNamara, M. Wise, P. E. J. Nulsen, L. P. David, C. L. Sarazin, M. Bautz, M. Markevitch, A. Vikhlinin, W. R. Forman, C. Jones, and D. E. Harris. Chandra X-Ray Observations of the Hydra A Cluster: An Interaction between the Radio Source and the X-Ray-emitting Gas. *ApJL*, 534:L135–L138, May 2000. doi: 10.1086/312662.

A. M. Medling, V. U, C. E. Max, D. B. Sanders, L. Armus, B. Holden, E. Mieda, S. A. Wright, and J. E. Larkin. Following Black Hole Scaling Relations through Gas-rich Mergers. *ApJ*, 803:61, April 2015. doi: 10.1088/0004-637X/803/2/61.

A. Merloni, A. Bongiorno, M. Bolzonella, M. Brusa, F. Civano, A. Comastri, M. Elvis, F. Fiore, R. Gilli, H. Hao, K. Jahnke, A. M. Koekemoer, E. Lusso, V. Mainieri, M. Mignoli, T. Miyaji, A. Renzini, M. Salvato, J. Silverman, J. Trump, C. Vignali, G. Zamorani, P. Capak, S. J. Lilly, D. Sanders, Y. Taniguchi, S. Bardelli, C. M. Carollo, K. Caputi, T. Contini, G. Coppa, O. Cucciati, S. de la Torre, L. de Ravel, P. Franzetti, B. Garilli, G. Hasinger, C. Impey, A. Iovino, K. Iwasawa, P. Kampczyk, J.-P. Kneib, C. Knobel, K. Kovač, F. Lamareille, J.-F. Le Borgne, V. Le Brun, O. Le Fèvre, C. Maier, R. Pello, Y. Peng, E. Perez Montero, E. Ricciardelli, M. Scodeggio, M. Tanaka, L. A. M. Tasca, L. Tresse, D. Vergani, and E. Zucca. On the Cosmic Evolution of the Scaling Relations Between Black Holes and Their Host Galaxies: Broad-Line Active Galactic Nuclei in the zCOSMOS Survey. *ApJ*, 708:137–157, January 2010. doi: 10.1088/0004-637X/708/1/137.

Charles Messier. Catalogue des Nébuleuses et des Amas d'Étoiles (Catalog of Nebulae and Star Clusters). Technical report, Jan 1781.

E. Mieda, S. A. Wright, J. E. Larkin, J. R. Graham, S. M. Adkins, J. E. Lyke, R. D. Campbell, J. Maire, T. Do, and J. Gordon. Efficiency Measurements and Installation of a New Grating for the OSIRIS Spectrograph at Keck Observatory. *Publications of the Astronomical Society*, 126:250–263, March 2014. doi: 10.1086/675784.

R. Minkowski. A New Distant Cluster of Galaxies. *ApJ*, 132:908–910, November 1960. doi: 10.1086/146994.

R. Morganti, W. Frieswijk, R. J. B. Oonk, T. Oosterloo, and C. Tadhunter. Tracing the extreme interplay between radio jets and the ISM in IC 5063. *AAP*, 552:L4, April 2013. doi: 10.1051/0004-6361/201220734.

D. Mudd, P. Martini, Y. Zu, C. Kochanek, B. M. Peterson, R. Kessler, T. M. Davis, J. K. Hoormann, A. King, C. Lidman, N. E. Sommer, B. E. Tucker, J. Asorey, S. Hinton, K. Glazebrook, K. Kuehn, G. Lewis, E. Macaulay, A. Moeller, C. O'Neill, B. Zhang, T. M. C. Abbott, F. B. Abdalla, S. Allam, M. Banerji, A. Benoit-Lévy, E. Bertin, D. Brooks, A. Carnero Rosell, D. Carollo, M. Carrasco Kind, J. Carretero, C. E. Cunha, C. B. D'Andrea, L. N.

da Costa, C. Davis, S. Desai, P. Doel, P. Fosalba, J. García-Bellido, E. Gaztanaga, D. W. Gerdes, D. Gruen, R. A. Gruendl, J. Gschwend, G. Gutierrez, W. G. Hartley, K. Honscheid, D. J. James, S. Kuhlmann, N. Kuropatkin, M. Lima, M. A. G. Maia, J. L. Marshall, R. G. McMahon, F. Menanteau, R. Miquel, A. A. Plazas, A. K. Romer, E. Sanchez, R. Schindler, M. Schubnell, M. Smith, R. C. Smith, M. Soares-Santos, F. Sobreira, E. Suchyta, M. E. C. Swanson, G. Tarle, D. Thomas, D. L. Tucker, A. R. Walker, and DES Collaboration. Quasar Accretion Disk Sizes from Continuum Reverberation Mapping from the Dark Energy Survey. *ApJ*, 862(2):123, Aug 2018. doi: 10.3847/1538-4357/aac9bb.

Dipanjan Mukherjee, Geoffrey V. Bicknell, Ralph Sutherland , and Alex Wagner. Relativistic jet feedback in high-redshift galaxies - I. Dynamics. *MNRAS*, 461:967–983, Sep 2016. doi: 10.1093/mnras/stw1368.

A. L. Muratov, D. Kereš, C.-A. Faucher-Giguère, P. F. Hopkins, E. Quataert, and N. Murray. Gusty, gaseous flows of FIRE: galactic winds in cosmological simulations with explicit stellar feedback. *MNRAS*, 454:2691–2713, December 2015. doi: 10.1093/mnras/stv2126.

N. Murray, J. Chiang, S. A. Grossman, and G. M. Voit. Accretion Disk Winds from Active Galactic Nuclei. *Astrophys. J.*, 451:498, October 1995. doi: 10.1086/176238.

N. Murray, E. Quataert, and T. A. Thompson. On the Maximum Luminosity of Galaxies and Their Central Black Holes: Feedback from Momentum-driven Winds. *ApJ*, 618:569–585, January 2005. doi: 10.1086/426067.

N. P. H. Nesvadba, M. D. Lehnert, C. De Breuck, A. M. Gilbert, and W. van Breugel. Evidence for powerful AGN winds at high redshift: dynamics of galactic outflows in radio galaxies during the "Quasar Era". *Astron. & Astrop.*, 491:407–424, November 2008. doi: 10.1051/0004-6361:200810346.

N. P. H. Nesvadba, C. De Breuck, M. D. Lehnert, P. N. Best, and C. Collet. The SINFONI survey of powerful radio galaxies at z 2: Jet-driven AGN feedback during the Quasar Era. *AAP*, 599: A123, March 2017a. doi: 10.1051/0004-6361/201528040.

N. P. H. Nesvadba, C. De Breuck, M. D. Lehnert, P. N. Best, and C. Collet. The SINFONI survey of powerful radio galaxies at z 2: Jet-driven AGN feedback during the Quasar Era. *AAP*, 599: A123, March 2017b. doi: 10.1051/0004-6361/201528040.

N. P. H. Nesvadba, G. Drouart, C. De Breuck, P. Best, N. Seymour, and J. Vernet. Gas kinematics in powerful radio galaxies at z 2: Energy supply from star formation, AGN, and radio jets$\star$. *AAP*, $600 : A121, April 2017c. doi : .$

S. F. Newman, P. Buschkamp, R. Genzel, N. M. Förster Schreiber, J. Kurk, A. Sternberg, O. Gnat, D. Rosario, C. Mancini, S. J. Lilly, A. Renzini, A. Burkert, C. M. Carollo, G. Cresci, R. Davies, F. Eisenhauer, S. Genel, K. Shapiro Griffin, E. K. S. Hicks, D. Lutz, T. Naab, Y. Peng, L. J. Tacconi, S. Wuyts, G. Zamorani, D. Vergani, and B. J. Weiner. Nebular Excitation in z ˜ 2 Star-forming Galaxies from the SINS and LUCI Surveys: The Influence of Shocks and Active Galactic Nuclei. *ApJ*, 781:21, January 2014. 10.1088/0004-637X/781/1/21.

D. E. Osterbrock and G. J. Ferland. *Astrophysics of gaseous nebulae and active galactic nuclei*. 2006.

C. Y. Peng, C. D. Impey, H.-W. Rix, C. S. Kochanek, C. R. Keeton, E. E. Falco, J. Lehár, and B. A. McLeod. Probing the Coevolution of Supermassive Black Holes and Galaxies Using Gravitationally Lensed Quasar Hosts. *ApJ*, 649:616–634, October 2006. 10.1086/506266.

Chien Y. Peng. How Mergers May Affect the Mass Scaling Relation between Gravitationally Bound Systems. *ApJ*, 671(2):1098–1107, Dec 2007. 10.1086/522774.

A. A. Penzias and R. W. Wilson. A Measurement of Excess Antenna Temperature at 4080 Mc/s. *ApJ*, 142:419–421, July 1965. 10.1086/148307.

B. M. Peterson, L. Ferrarese, K. M. Gilbert, S. Kaspi, M. A. Malkan, D. Maoz, D. Merritt, H. Netzer, C. A. Onken, and R. W. Pogge. Central Masses and Broad-Line Region Sizes of Active Galactic Nuclei. II. A Homogeneous Analysis of a Large Reverberation-Mapping Database. *ApJ*, 613(2):682–699, Oct 2004. 10.1086/423269.

Andreea O. Petric, Lee Armus, Nicolas Flagey, Pierre Guillard, Justin Howell, Hanae Inami, Vassillis Charmand aris, Aaron Evans, Sabrina Stierwalt, and Tanio Diaz-Santos. Warm Molecular Hydrogen in Nearby, Luminous Infrared Galaxies. *AJ*, 156(6):295, Dec 2018. 10.3847/1538-3881/aaca35.

M. Pettini and B. E. J. Pagel. [OIII]/[NII] as an abundance indicator at high redshift. *MNRAS*, 348:L59–L63, March 2004. 10.1111/j.1365-2966.2004.07591.x.

Planck Collaboration, P. A. R. Ade, N. Aghanim, C. Armitage-Caplan, M. Arnaud, M. Ashdown, F. Atrio-Barandela, J. Aumont, C. Baccigalupi, A. J. Banday, and et al. Planck 2013 results. XVI. Cosmological parameters. *Astron. & Astrop.*, 571:A16, November 2014. 10.1051/0004-6361/201321591.

P. Podigachoski, P. D. Barthel, M. Haas, C. Leipski, B. Wilkes, J. Kuraszkiewicz, C. Westhues, S. P. Willner, M. L. N. Ashby, R. Chini, D. L. Clements, G. G. Fazio, A. Labiano, C. Lawrence, K. Meisenheimer, R. F. Peletier, R. Siebenmorgen, and G. Verdoes Kleijn. Star formation in z > 1 3CR host galaxies as seen by Herschel. *Astron. & Astrop.*, 575:A80, March 2015. 10.1051/0004-6361/201425137.

J. X. Prochaska, M. W. Lau, and J. F. Hennawi. Quasars Probing Quasars. VII. The Pinnacle of the Cool Circumgalactic Medium Surrounds Massive z ˜ 2 Galaxies. *ApJ*, 796:140, December 2014. 10.1088/0004-637X/796/2/140.

J. A. Rich, L. J. Kewley, and M. A. Dopita. Galaxy Mergers Drive Shocks: An Integral Field Study of GOALS Galaxies. *ApJS*, 221(2):28, Dec 2015. 10.1088/0067-0049/221/2/28.

A. J. Richings and C.-A. Faucher-Giguère. The origin of fast molecular outflows in quasars: molecule formation in AGN-driven galactic winds. *MNRAS*, 474:3673–3699, March 2018. 10.1093/mnras/stx3014.

D. J. Rosario, B. Trakhtenbrot, D. Lutz, H. Netzer, J. R. Trump, J. D. Silverman, M. Schramm, E. Lusso, S. Berta, and A. Bongiorno. The mean star-forming properties of QSO host galaxies. *AAP*, 560:A72, Dec 2013. 10.1051/0004-6361/201322196.

M. Rowan-Robinson. On the unity of activity in galaxies. *ApJ*, 213:635–647, May 1977. 10.1086/155195.

Michael Rowan-Robinson. A new model for the infrared emission of quasars. *MNRAS*, 272(4): 737–748, Feb 1995. 10.1093/mnras/272.4.737.

K. H. R. Rubin, J. X. Prochaska, D. C. Koo, and A. C. Phillips. The Direct Detection of Cool, Metal-enriched Gas Accretion onto Galaxies at z ˜ 0.5. *ApJL*, 747:L26, March 2012. 10.1088/2041-8205/747/2/L26.

J. C. Runnoe, M. S. Brotherton, and Z. Shang. Updating quasar bolometric luminosity corrections. *Mon. Not. R. Astron. S.*, 422:478–493, May 2012. 10.1111/j.1365-2966.2012.20620.x.

D. S. Rupke, S. Veilleux, and D. B. Sanders. Keck Absorption-Line Spectroscopy of Galactic Winds in Ultraluminous Infrared Galaxies. *ApJ*, 570:588–609, May 2002. 10.1086/339789.

D. S. N. Rupke and S. Veilleux. Integral Field Spectroscopy of Massive, Kiloparsec-scale Outflows in the Infrared-luminous QSO Mrk 231. *ApJL*, 729:L27, March 2011. 10.1088/2041-8205/729/2/L27.

M. Ryle, F. G. Smith, and B. Elsmore. A preliminary survey of the radio stars in the Northern Hemisphere. *MNRAS*, 110:508, 1950. 10.1093/mnras/110.6.508.

S. Sachdeva, K. Saha, and H. P. Singh. Growth of Bulges in Disk Galaxies Since z
1. *ApJ*, 840:79, May 2017. 10.3847/1538-4357/aa6c61.

E. E. Salpeter. Accretion of Interstellar Matter by Massive Objects. *ApJ*, 140:796–800, August 1964. 10.1086/147973.

S. F. Sánchez, K. Jahnke, L. Wisotzki, D. H. McIntosh, E. F. Bell, M. Barden, S. V. W. Beckwith, A. Borch, J. A. R. Caldwell, B. Häussler, S. Jogee, K. Meisenheimer, C. Y. Peng, H.-W. Rix, R. S. Somerville, and C. Wolf. Colors of Active Galactic Nucleus Host Galaxies at 0.5<z<1.1 from the GEMS Survey. *Astrophys. J.*, 614:586–606, October 2004. 10.1086/423234.

A. Sandage. The Existence of a Major New Constituent of the Universe: the Quasistellar Galaxies. *ApJ*, 141:1560, May 1965. 10.1086/148245.

D. B. Sanders, B. T. Soifer, J. H. Elias, B. F. Madore, K. Matthews, G. Neugebauer, and N. Z. Scoville. Ultraluminous infrared galaxies and the origin of quasars. *Astrophys. J.*, 325:74–91, February 1988. 10.1086/165983.

R. L. Sanders, A. E. Shapley, M. Kriek, N. A. Reddy, W. R. Freeman, A. L. Coil, B. Siana, B. Mobasher, I. Shivaei, S. H. Price, and L. de Groot. The MOSDEF Survey: Electron Density and Ionization Parameter at z ˜ 2.3. *ApJ*, 816:23, January 2016. 10.3847/0004-637X/816/1/23.

E. Sani, A. Marconi, L. K. Hunt, and G. Risaliti. The Spitzer/IRAC view of black hole-bulge scaling relations. *MNRAS*, 413:1479–1494, May 2011. 10.1111/j.1365-2966.2011.18229.x.

M. Schmidt. 3C 273 : A Star-Like Object with Large Red-Shift. *Nature*, 197:1040, March 1963. 10.1038/1971040a0.

Donald P. Schneider, Gordon T. Richards, Patrick B. Hall, Michael A. Strauss, Scott F. Anderson, Todd A. Boroson, Nicholas P. Ross, Yue Shen, W. N. Brandt, and Xiaohui Fan. The Sloan Digital Sky Survey Quasar Catalog. V. Seventh Data Release. *AJ*, 139(6):2360, Jun 2010. 10.1088/0004-6256/139/6/2360.

M. Schramm and J. D. Silverman. The Black Hole-Bulge Mass Relation of Active Galactic Nuclei in the Extended Chandra Deep Field-South Survey. *ApJ*, 767:13, April 2013. 10.1088/0004-637X/767/1/13.

K. Sellgren, M. T. McGinn, E. E. Becklin, and D. N. Hall. Velocity dispersion and the stellar population in the central 1.2 parsecs of the Galaxy. *ApJ*, 359:112–120, August 1990. 10.1086/169039.

C. K. Seyfert. Nuclear Emission in Spiral Nebulae. *ApJ*, 97:28, January 1943. 10.1086/144488.

J. R. Shakeshaft, M. Ryle, J. E. Baldwin, B. Elsmore, and J. H. Thomson. A survey of radio sources between declinations 38° and +83°. , 67:106, 1955.

A. E. Shapley, N. A. Reddy, M. Kriek, W. R. Freeman, R. L. Sanders, B. Siana, A. L. Coil, B. Mobasher, I. Shivaei, S. H. Price, and L. de Groot. The MOSDEF Survey: Excitation Properties of z

2.3 Star-forming Galaxies. *ApJ*, 801:88, March 2015. 10.1088/0004-637X/801/2/88.

Y. Shen, G. T. Richards, M. A. Strauss, P. B. Hall, D. P. Schneider, S. Snedden, D. Bizyaev, H. Brewington, V. Malanushenko, E. Malanushenko, D. Oravetz, K. Pan, and A. Simmons. A Catalog of Quasar Properties from Sloan Digital Sky Survey Data Release 7. *ApJS*, 194:45, June 2011. 10.1088/0067-0049/194/2/45.

G. A. Shields, K. L. Menezes, C. A. Massart, and P. Vanden Bout. The Black Hole-Bulge Relationship for QSOs at High Redshift. *ApJ*, 641:683–688, April 2006. 10.1086/500542.

Gregory A. Shields. A Brief History of Active Galactic Nuclei. *PASP*, 111(760):661–678, Jun 1999. 10.1086/316378.

J. Silk and M. J. Rees. Quasars and galaxy formation. *AAP*, 331:L1–L4, March 1998.

V. M. Slipher. The spectrum and velocity of the nebula N.G.C. 1068 (M 77). *Lowell Observatory Bulletin*, 3:59–62, 1917.

Rachel S. Somerville, Philip F. Hopkins, Thomas J. Cox, Brant E. Robertson, and Lars Hernquist. A semi-analytic model for the co-evolution of galaxies, black holes and active galactic nuclei. *MNRAS*, 391(2):481–506, Dec 2008. 10.1111/j.1365-2966.2008.13805.x.

C. C. Steidel, D. K. Erb, A. E. Shapley, M. Pettini, N. Reddy, M. Bogosavljević, G. C. Rudie, and O. Rakic. The Structure and Kinematics of the Circumgalactic Medium from Far-ultraviolet Spectra of z ˜= 2-3 Galaxies. *ApJ*, 717:289–322, July 2010. 10.1088/0004-637X/717/1/289.

C. C. Steidel, G. C. Rudie, A. L. Strom, M. Pettini, N. A. Reddy, A. E. Shapley, R. F. Trainor, D. K. Erb, M. L. Turner, N. P. Konidaris, K. R. Kulas, G. Mace, K. Matthews, and I. S. McLean. Strong Nebular Line Ratios in the Spectra of z ˜ 2-3 Star Forming Galaxies: First Results from KBSS-MOSFIRE. *ApJ*, 795:165, November 2014. 10.1088/0004-637X/795/2/165.

E. Steinbring. Radio Galaxy 3C 230 Observed with Gemini Laser Adaptive-optics Integral-field Spectroscopy. *The Astronomical Journal*, 142:172, November 2011. 10.1088/0004-6256/142/5/172.

N. R. Stickley and G. Canalizo. Stellar Velocity Dispersion in Dissipative Galaxy Mergers with Star Formation. *ApJ*, 786:12, May 2014. 10.1088/0004-637X/786/1/12.

H. S. Stockman, R. L. Moore, and J. R. P. Angel. The optical polarization properties of 'normal' quasars. *Astrophys. J.*, 279:485–498, April 1984. 10.1086/161912.

M. Stone, S. Veilleux, M. Meléndez, E. Sturm, J. Graciá-Carpio, and E. González-Alfonso. The Search for Molecular Outflows in Local Volume AGNs with Herschel-PACS. *ApJ*, 826:111, August 2016. 10.3847/0004-637X/826/2/111.

P. J. Storey and C. J. Zeippen. Theoretical values for the [Oiii] 5007/4959 line-intensity ratio and homologous cases. *Mon. Not. R. Astron. S*, 312:813–816, March 2000. 10.1046/j.1365-8711.2000.03184.x.

A. L. Strom, C. C. Steidel, G. C. Rudie, R. F. Trainor, M. Pettini, and N. A. Reddy. Nebular Emission Line Ratios in z 2-3 Star-forming Galaxies with KBSS-MOSFIRE: Exploring the Impact of Ionization, Excitation, and Nitrogen-to-Oxygen Ratio. *ApJ*, 836:164, February 2017. 10.3847/1538-4357/836/2/164.

E. Sturm, E. González-Alfonso, S. Veilleux, J. Fischer, J. Graciá-Carpio, S. Hailey-Dunsheath, A. Contursi, A. Poglitsch, A. Sternberg, R. Davies, R. Genzel, D. Lutz, L. Tacconi, A. Verma, R. Maiolino, and J. A. de Jong. Massive Molecular Outflows and Negative Feedback in ULIRGs Observed by Herschel-PACS. *ApJL*, 733:L16, May 2011. 10.1088/2041-8205/733/1/L16.

A.-L. Sun, J. E. Greene, N. L. Zakamska, and N. P. H. Nesvadba. ALMA Observations of a Candidate Molecular Outflow in an Obscured Quasar. *ApJ*, 790:160, August 2014. 10.1088/0004-637X/790/2/160.

M. Sun, J. R. Trump, W. N. Brandt, B. Luo, D. M. Alexander, K. Jahnke, D. J. Rosario, S. X. Wang, and Y. Q. Xue. Evolution in the Black HoleGalaxy Scaling Relations and the Duty Cycle of Nuclear Activity in Star-forming Galaxies. *ApJ*, 802:14, March 2015. 10.1088/0004-637X/802/1/14.

M. Symeonidis, B. M. Giblin, M. J. Page, C. Pearson, G. Bendo, N. Seymour, and S. J. Oliver. AGN are cooler than you think: the intrinsic far-IR emission from QSOs. *MNRAS*, 459:257–276, June 2016. 10.1093/mnras/stw667.

H. Tananbaum, Y. Avni, G. Branduardi, M. Elvis, G. Fabbiano, E. Feigelson, R. Giacconi, J. P. Henry, J. P. Pye, A. Soltan, and G. Zamorani. X-ray studies of quasars with the Einstein Observatory. *ApJL*, 234:L9–L13, November 1979. 10.1086/183100.

T. A. Thompson, A. C. Fabian, E. Quataert, and N. Murray. Dynamics of dusty radiation-pressure-driven shells and clouds: fast outflows from galaxies, star clusters, massive stars, and AGN. *MNRAS*, 449:147–161, May 2015. 10.1093/mnras/stv246.

Kip S. Thorne. Disk-Accretion onto a Black Hole. II. Evolution of the Hole. *ApJ*, 191:507–520, Jul 1974. 10.1086/152991.

F. Tombesi, M. Cappi, J. N. Reeves, G. G. C. Palumbo, T. Yaqoob, V. Braito, and M. Dadina. Evidence for ultra-fast outflows in radio-quiet AGNs. I. Detection and statistical incidence of Fe K-shell absorption lines. *AAP*, 521:A57, October 2010. 10.1051/0004-6361/200913440.

F. Tombesi, M. Meléndez, S. Veilleux, J. N. Reeves, E. González-Alfonso, and C. S. Reynolds. Wind from the black-hole accretion disk driving a molecular outflow in an active galaxy. *Nature*, 519:436–438, March 2015. 10.1038/nature14261.

A. R. Tomczak, R. F. Quadri, K.-V. H. Tran, I. Labbé, C. M. S. Straatman, C. Papovich, K. Glazebrook, R. Allen, G. B. Brammer, G. G. Kacprzak, L. Kawinwanichakij, D. D. Kelson, P. J. McCarthy, N. Mehrtens, A. J. Monson, S. E. Persson, L. R. Spitler, V. Tilvi, and P. van Dokkum. Galaxy Stellar Mass Functions from ZFOURGE/CANDELS: An Excess of Low-mass Galaxies since z = 2 and the Rapid Buildup of Quiescent Galaxies. *ApJ*, 783:85, March 2014. 10.1088/0004-637X/783/2/85.

J. L. Tonry. A central black hole in M32. *ApJ*, 322:632–642, November 1987. 10.1086/165758.

B. Trakhtenbrot, C. M. Urry, F. Civano, D. J. Rosario, M. Elvis, K. Schawinski, H. Suh, A. Bongiorno, and B. D. Simmons. An over-massive black hole in a typical star-forming galaxy, 2 billion years after the Big Bang. *Science*, 349:168–171, July 2015. 10.1126/science.aaa4506.

E. Treister, K. Schawinski, C. M. Urry, and B. D. Simmons. Major Galaxy Mergers Only Trigger the Most Luminous Active Galactic Nuclei. *Astrophys. J. Lett.*, 758:L39, October 2012. 10.1088/2041-8205/758/2/L39.

J. Tumlinson, C. Thom, J. K. Werk, J. X. Prochaska, T. M. Tripp, D. H. Weinberg, M. S. Peeples, J. M. O'Meara, B. D. Oppenheimer, J. D. Meiring, N. S. Katz, R. Davé, A. B. Ford, and K. R. Sembach. The Large, Oxygen-Rich Halos of Star-Forming Galaxies Are a Major Reservoir of Galactic Metals. *Science*, 334(6058):948, Nov 2011. 10.1126/science.1209840.

Vivian U, Anne M. Medling, Hanae Inami, Lee Armus, Tanio Díaz-Santos, Vassilis Charmandaris, Justin Howell, Sabrina Stierwalt, George C. Privon, and Sean T. Linden. Keck OSIRIS AO LIRG Analysis (KOALA): Feedback in the Nuclei of Luminous Infrared Galaxies. *ApJ*, 871 (2):166, Feb 2019. 10.3847/1538-4357/aaf1c2.

Tanya Urrutia, Mark Lacy, Henrik Spoon, Eilat Glikman, Andreea Petric, and Bernhard Schulz. Spitzer Observations of Young Red Quasars. *ApJ*, 757(2):125, Oct 2012. 10.1088/0004-637X/757/2/125.

C. M. Urry and P. Padovani. Unified Schemes for Radio-Loud Active Galactic Nuclei. *PASP*, 107:803, September 1995. 10.1086/133630.

F. van de Voort, J. Schaye, C. M. Booth, M. R. Haas, and C. Dalla Vecchia. The rates and modes of gas accretion on to galaxies and their gaseous haloes. *MNRAS*, 414:2458–2478, July 2011. 10.1111/j.1365-2966.2011.18565.x.

A. Vayner, S. A. Wright, T. Do, J. E. Larkin, L. Armus, and S. C. Gallagher. Providing Stringent Star Formation Rate Limits of z $\sim$ 2 QSO Host Galaxies at High Angular Resolution. *Astrophys. J.*, 821:64, April 2016. 10.3847/0004-637X/821/1/64.

A. Vayner, S. A. Wright, N. Murray, L. Armus, J. E. Larkin, and E. Mieda. Galactic-scale Feedback Observed in the 3C 298 Quasar Host Galaxy. *ApJ*, 851:126, December 2017. 10.3847/1538-4357/aa9c42.

S. Veilleux, A. Bolatto, F. Tombesi, M. Meléndez, E. Sturm, E. González-Alfonso, J. Fischer, and D. S. N. Rupke. Quasar Feedback in the Ultraluminous Infrared Galaxy F11119+3257: Connecting the Accretion Disk Wind with the Large-scale Molecular Outflow. *ApJ*, 843:18, July 2017. 10.3847/1538-4357/aa767d.

Sylvain Veilleux and Donald E. Osterbrock. Spectral Classification of Emission-Line Galaxies. *ApJS*, 63:295, Feb 1987. 10.1086/191166.

B. P. Venemans, F. Walter, L. Zschaechner, R. Decarli, G. De Rosa, J. R. Findlay, R. G. McMahon, and W. J. Sutherland. Bright [C ii] and Dust Emission in Three z 6.6 Quasar Host Galaxies Observed by ALMA. *ApJ*, 816:37, January 2016. 10.3847/0004-637X/816/1/37.

M. Vestergaard and P. S. Osmer. Mass Functions of the Active Black Holes in Distant Quasars from the Large Bright Quasar Survey, the Bright Quasar Survey, and the Color-selected Sample of the SDSS Fall Equatorial Stripe. *ApJ*, 699:800–816, July 2009. 10.1088/0004-637X/699/1/800.

Marianne Vestergaard and Bradley M. Peterson. Determining Central Black Hole Masses in Distant Active Galaxies and Quasars. II. Improved Optical and UV Scaling Relationships. *ApJ*, 641(2):689–709, Apr 2006. 10.1086/500572.

M. Villar Martín, E. Bellocchi, J. Stern, C. Ramos Almeida, C. Tadhunter, and R. González Delgado. Deconstructing the narrow-line region of the nearest obscured quasar. *MNRAS*, 454 (1):439–456, Nov 2015. 10.1093/mnras/stv1864.

C. Villforth, J. Heidt, and K. Nilsson. Quasar host galaxies in the FORS deep field. *AAP*, 488 (1):133–143, Sep 2008. 10.1051/0004-6361:200809712.

M. Volonteri. The Formation and Evolution of Massive Black Holes. *Science*, 337(6094):544, Aug 2012. 10.1126/science.1220843.

A. Y. Wagner, G. V. Bicknell, and M. Umemura. Driving Outflows with Relativistic Jets and the Dependence of Active Galactic Nucleus Feedback Efficiency on Interstellar Medium Inhomogeneity. *ApJ*, 757:136, October 2012. 10.1088/0004-637X/757/2/136.

M. F. Walker. Studies of Extragalactic Nebulae. V. Motions in the Seyfert Galaxy NGC 1068. *ApJ*, 151:71, January 1968. 10.1086/149420.

E. J. Wampler, L. B. Robinson, E. M. Burbidge, and J. A. Baldwin. The nebulosity around 3C 48. *ApJL*, 198:L49–L52, June 1975. 10.1086/181808.

Jian-Min Wang, Yan-Mei Chen, and Fan Zhang. Cosmological Evolution of the Duty Cycle of Quasars. *ApJL*, 647(1):L17–L20, Aug 2006. 10.1086/507271.

R. Wang, J. Wagg, C. L. Carilli, F. Walter, L. Lentati, X. Fan, D. A. Riechers, F. Bertoldi, D. Narayanan, M. A. Strauss, P. Cox, A. Omont, K. M. Menten, K. K. Knudsen, R. Neri, and L. Jiang. Star Formation and Gas Kinematics of Quasar Host Galaxies at z ˜ 6: New Insights from ALMA. *ApJ*, 773:44, August 2013. 10.1088/0004-637X/773/1/44.

D. W. Weedman. High-Velocity Gas Motions in Galactic Nuclei. *ApJ*, 159:405, February 1970. 10.1086/150318.

J. K. Werk, M. E. Putman, G. R. Meurer, and N. Santiago-Figueroa. Metal Transport to the Gaseous Outskirts of Galaxies. *ApJ*, 735(2):71, Jul 2011. 10.1088/0004-637X/735/2/71.

R. J. Williams, R. Maiolino, Y. Krongold, S. Carniani, G. Cresci, F. Mannucci, and A. Marconi. An ultra-dense fast outflow in a quasar at z = 2.4. *MNRAS*, 467:3399–3412, May 2017. 10.1093/mnras/stx311.

C. J. Willott, S. Rawlings, and M. J. Jarvis. The hyperluminous infrared quasar 3C 318 and its implications for interpreting submm detections of high-redshift radio galaxies. *MNRAS*, 313: 237–246, April 2000. 10.1046/j.1365-8711.2000.03267.x.

C. J. Willott, J. Bergeron, and A. Omont. Star Formation Rate and Dynamical Mass of 10^8 Solar Mass Black Hole Host Galaxies At Redshift 6. *ApJ*, 801:123, March 2015. 10.1088/0004-637X/801/2/123.

Chris J. Willott, Alejo Martínez-Sansigre, and Steve Rawlings. Molecular Gas Observations of the Reddened Quasar 3C 318. *ApJ*, 133(2):564–567, Feb 2007. 10.1086/510291.

Chris J. Willott, Alain Omont, and Jacqueline Bergeron. Redshift 6.4 Host Galaxies of 10^8 Solar Mass Black Holes: Low Star Formation Rate and Dynamical Mass. *ApJ*, 770(1):13, Jun 2013. 10.1088/0004-637X/770/1/13.

P. L. Wizinowich, D. Le Mignant, A. H. Bouchez, R. D. Campbell, J. C. Y. Chin, A. R. Contos, M. A. van Dam, S. K. Hartman, E. M. Johansson, R. E. Lafon, H. Lewis, P. J. Stomski, D. M. Summers, C. G. Brown, P. M. Danforth, C. E. Max, and D. M. Pennington. The W. M. Keck Observatory Laser Guide Star Adaptive Optics System: Overview. *PASP*, 118:297–309, February 2006. 10.1086/499290.

L. Woltjer. Emission Nuclei in Galaxies. *ApJ*, 130:38, July 1959. 10.1086/146694.

O. I. Wong, K. Schawinski, S. Kaviraj, K. L. Masters, R. C. Nichol, C. Lintott, W. C. Keel, D. Darg, S. P. Bamford, D. Andreescu, P. Murray, M. J. Raddick, A. Szalay, D. Thomas, and J. Vandenberg. Galaxy Zoo: building the low-mass end of the red sequence with local post-starburst galaxies. *Mon. Not. R. Astron. S.*, 420:1684–1692, February 2012. 10.1111/j.1365-2966.2011.20159.x.

Renbin Yan, Luis C. Ho, Jeffrey A. Newman, Alison L. Coil, Christopher N. A. Willmer, Elise S. Laird, Antonis Georgakakis, James Aird, Pauline Barmby, and Kevin Bundy. AEGIS: Demographics of X-ray and Optically Selected Active Galactic Nuclei. *ApJ*, 728(1):38, Feb 2011. 10.1088/0004-637X/728/1/38.

T.-T. Yuan, L. J. Kewley, and J. Richard. The Metallicity Evolution of Star-forming Galaxies from Redshift 0 to 3: Combining Magnitude-limited Survey with Gravitational Lensing. *ApJ*, 763:9, January 2013. 10.1088/0004-637X/763/1/9.

Y. B. Zel'dovich. The Fate of a Star and the Evolution of Gravitational Energy Upon Accretion. *Soviet Physics Doklady*, 9:195, September 1964.

G. Zhu and B. Ménard. Calcium H K Induced by Galaxy Halos. *ApJ*, 773:16, August 2013. 10.1088/0004-637X/773/1/16.

K. Zubovas and A. King. Clearing Out a Galaxy. *ApJL*, 745:L34, February 2012. 10.1088/2041-8205/745/2/L34.

K. Zubovas and A. R. King. Galaxy-wide outflows: cold gas and star formation at high speeds. *MNRAS*, 439:400–406, March 2014. 10.1093/mnras/stt2472.
[heading=none]